

On-bearing Vibration Response Integration for Condition Monitoring of Rotating Machinery

A thesis submitted to The University of Manchester for the degree of

Doctor of Philosophy (PhD)

in the Faculty of Engineering and Physical Science

2015

Adrian D. Nembhard

School of Mechanical, Aerospace and Civil Engineering

(This page is intentionally left blank)

Table of Content

List of Tables	7
List of Figures	8
Nomenclature	14
List of Abbreviations	16
List of Publications	18
Abstract	19
Declaration	20
Copyright statement	21
Acknowledgement	22
Dedication	23
1 INTRODUCTION	24
1.1 Introduction	25
1.2 Aims and Objectives	27
1.3 Contributions to knowledge	29
1.4 Report Layout	32
1.5 Report linkages	33
2 LITERATURE REVIEW	36
2.1 Introduction	37
2.2 Machinery failure patterns	37
2.3 Condition monitoring	38
2.4 Vibration-based condition monitoring of rotating machinery	39
2.5 Vibration-based condition monitoring for rotor fault diagnosis	41
2.5.1 Data acquisition	42
2.5.2 Data manipulation	43
2.5.3 Health assessment	44
2.6 Standard practices in vibration-based rotor fault diagnosis	44
2.6.1 Simple spectrum analysis	44
2.6.2 Orbit plot analysis	45
2.6.3 Overview of standard practices	49
2.7 Research on alternative methods to standard practices	50
2.7.1 Data acquisition	50
2.7.2 Data manipulation	52
2.7.3 Health assessment	53
2.8 Vibration-based fault diagnosis for transient operation	58
2.9 Simple mathematical modelling in vibration-based fault diagnosis	60
2.10 Summary	62
3 EXPERIMENTAL APPROACH	63

3.1	Introduction	64
3.2	Experimental set up	64
3.2.1	Rigid support.....	64
3.2.2	Flexible support.....	66
3.3	Experiments conducted	73
3.3.1	Rigid set up	73
3.3.2	Flexible set up	74
3.4	Summary	75
4	EXPERIMENTAL OBSERVATIONS IN THE SHAFT ORBITS OF RELATIVELY FLEXIBLE MACHINES WITH DIFFERENT ROTOR-RELATED FAULTS.....	77
4.1	Introduction	78
4.2	Experimental Set Up	82
4.2.1	Mechanical Layout and Instrumentation.....	82
4.2.2	Dynamic Characterization of Experimental Rig.....	86
4.3	Experiments conducted	89
4.4	Data processing	93
4.5	Shaft orbit observations.....	95
4.5.1	Residual Misalignment with Residual Unbalance - Baseline	95
4.5.2	Added Unbalance	97
4.5.3	Bow	98
4.5.4	Crack	99
4.5.5	Looseness	102
4.5.6	Misalignment	103
4.5.7	Rub.....	105
4.5.8	General Observations of Orbit Shapes on a different Flexible Machine (with 6mm supports)	109
4.6	Summary	110
5	COMBINED VIBRATION AND THERMAL ANALYSIS FOR THE CONDITION MONITORING OF ROTATING MACHINERY.....	111
5.1	Introduction	112
5.2	Experimental set up and data collection.....	116
5.3	Simulated faults and experiments.....	118
5.4	Vibration spectrum analysis	120
5.4.1	Results: Spectrum analysis - 40 Hz (2400 rev/min).....	122
5.4.2	Results: Spectrum analysis - 50 Hz (3000 rev/min).....	125
5.5	Combined vibration and thermal analysis	127
5.5.1	Theory: Computation of steady-state temperatures	127
5.5.2	Simple linear analysis	129
5.5.3	PCA-based analysis.....	132
5.6	Summary	138

6	UNIFIED MULTI-SPEED ANALYSIS (UMA) FOR THE CONDITION MONITORING OF AERO-ENGINES.....	140
6.1	Introduction	141
6.2	Experimental set up	143
6.3	Spectrum analysis.....	146
6.3.1	Effect of speed change on spectral features	146
6.4	Application of principal component analysis (PCA)	151
6.5	Feature selection.....	153
6.5.1	Root mean square (r.m.s.) vibration amplitude.....	153
6.5.2	Crest factor	154
6.5.3	Kurtosis	155
6.5.4	Spectrum energy (SE)	155
6.5.5	Feature selection summary.....	156
6.6	Data processing	157
6.7	Results and discussion.....	158
6.7.1	Analysis of features from a single speed at a single bearing	159
6.7.2	Analysis of integrated features from multiple speeds at a single bearing	164
6.7.3	Analysis at a single speed for integrated features from multiple bearings ..	166
6.7.4	Unified Multi-speed analysis (integrated features from multiple speeds and multiple Bearings)	168
6.8	Summary	170
7	DEVELOPMENT OF A GENERIC ROTATING MACHINERY FAULT DIAGNOSIS APPROACH INSENSITIVE TO MACHINE SPEED AND SUPPORT TYPE	171
7.1	Introduction	172
7.2	Experimental set up and experiments conducted	177
7.2.1	Mechanical layout and instrumentation	178
7.2.2	Experiments conducted	181
7.3	Observations on orbit analysis and spectrum analysis	186
7.3.1	Orbit plots – time domain analysis.....	186
7.3.2	Amplitude spectra analysis – frequency domain analysis.....	189
7.4	Proposed approach - data processing and analyses	193
7.4.1	Application of principal component analysis.....	193
7.4.2	Feature selection.....	194
7.4.3	Data processing	195
7.5	Fault diagnosis - flexible support 1 (FS1)	199
7.5.1	Individual speed individual foundation (ISIF) analysis on FS1.....	199
7.5.2	Multi-speed individual foundation (MSIF) analysis on FS1.....	203
7.6	Fault diagnosis – flexible support 2 (FS2)	204
7.7	Fault Diagnosis - combined foundations; FS1 and FS2	206
7.7.1	Individual speed multi-foundation (ISMF) analysis on FS1 and FS2	207
7.7.2	Multi-speed multi-foundation (MSMF) analysis on FS1 and FS2	209
7.8	Global observations	210

7.9	Summary	211
8	COMPARISON OF EXPERIMENTAL OBSERVATIONS IN ROTATING MACHINES WITH SIMPLE MATHEMATICAL SIMULATIONS	213
8.1	Introduction	213
8.2	Earlier experimental study [13]	217
8.2.1	Experimental rig	217
8.2.2	Experiments conducted	218
8.2.3	Experimental observations in orbit plots and simple spectra	218
8.2.4	Fault classification method with earlier proposed approach	222
8.3	Mathematical modelling – Jeffcott rotor	223
8.4	Fault simulation and response	225
8.4.1	Healthy	226
8.4.2	Added unbalance	230
8.4.3	Crack	233
8.4.4	Misalignment	238
8.4.5	Rub	242
8.4.6	Summary of fault simulations	247
8.5	Fault classification – simulated data	250
8.5.1	Single speed (SS) classification with simulated data	250
8.5.2	Multi-speed (MS) classification with simulated data	253
8.6	Summary	254
9	CONCLUSIONS AND FUTURE WORK	256
9.1	Conclusions	257
9.2	Future Work	260
	REFERENCES	261

List of Tables

Table 3.1 Details of main components used on mechanical rig with flexible supports	70
Table 3.2 Summary of experimental approach used in present study.....	76
Table 4.1 Summary of experiments conducted in present rotor orbit study	93
Table 5.1 Summary of experimental procedure used.....	120
Table 7.1 Summary of experiments conducted.....	185
Table 7.2 Summary of different approaches considered in the present study	194
Table 7.3 Features used in previous studies done	195
Table 8.1 Summary of model parameters	249

List of Figures

Figure 1.1 Flow diagram showing logical progression of research undertaken in the current study as presented in Chapters 4-8, part 1	34
Figure 1.2 Flow diagram showing logical progression of research undertaken in the current study as presented in Chapters 4-8, part 2	35
Figure 2.1 Trends in maintenance expectations [43]	38
Figure 2.2 Fundamental components in rotating machinery.....	40
Figure 2.3 Condition monitoring data processing flow diagram [51].....	41
Figure 2.4 Typical set up for a vibration-based condition monitoring system	43
Figure 2.5 One machine with possibilities for different foundation set up which results in different dynamic characteristics including different natural frequencies.....	58
Figure 3.1 Experimental rig mechanical layout with relatively rigid supports [20]	65
Figure 3.2 Experimental Rig with relatively rigid supports major dimensions	65
Figure 3.3 Schematic of software and instrumentation used in the experiment for the rigid support	66
Figure 3.4 Mechanical layout of experimental rig with relatively flexible supports	67
Figure 3.5 Dimensions of main components on rig with flexible supports	68
Figure 3.6 Close up of bearing pedestal from (a) rigid support and (b) flexible support	69
Figure 3.7 Schematic of instrumentation used for testing with flexible supports.....	71
Figure 3.8 Details of accelerometer and thermocouple configuration for: a) rigid supports and b) flexible supports	72
Figure 3.9 Details of instrumentation used at Bearing 1 (B1)	73
Figure 4.1 Mechanical layout of experimental rig	83
Figure 4.2 Close up of: a) Bearing 4 side view with Disc 3 and pedestal and b) Bearing 4 end view	84
Figure 4.3 Schematic of experimental rig instrumentation	85
Figure 4.4 Details of eddy current probe mounting at Bearing 1 of experimental rig	85
Figure 4.5 Schematic of rig dimensions and measurement location.....	86
Figure 4.6 Schematic of experimental rig set up for modal testing	87
Figure 4.7 Frequency Response Function (FRF) in the vertical direction at position 4 obtained during modal testing	88
Figure 4.8 Mode shapes of experimental rig with 10 mm supports for first two observed natural frequencies in: a) vertical and b) horizontal direction	89
Figure 4.9 Rub fault apparatus mounted near Bearing 1	90

Figure 4.10 Seeding of misalignment in vertical direction at Bearing 1 by 2×0.8 mm shims under Bearing 1	91
Figure 4.11 Details of looseness fault at Bearing 3	92
Figure 4.12 Details of crack showing close up of notch and shim	92
Figure 4.13 Sample of processing method for Rub showing: a) vertical response, b) horizontal response and c) tachometer reference signal with start and stop point for 1 cycle	94
Figure 4.14 RMRU unfiltered orbits for 10 mm supports at B1 for: a) 600 rev/min (10 Hz), b) 1200 rev/min (20 Hz), c) 1800 rev/min (30 Hz) and d) 2400 rev/min (40 Hz)	95
Figure 4.15 RMRU orbits for 10 mm supports at B1 for: a) 600 rev/min (10 Hz), b) 1200 rev/min (20 Hz), c) 1800 rev/min (30 Hz) and d) 2400 rev/min (40 Hz)	96
Figure 4.16 RMRU orbits for 10 mm supports at B4 for: a) 600 rev/min (10 Hz), b) 1200 rev/min (20 Hz), c) 1800 rev/min (30 Hz) and d) 2400 rev/min (40 Hz)	97
Figure 4.17 Added Unbalance orbits for 10 mm supports at B1 for: a) 600 rev/min (10 Hz), b) 1200 rev/min (20 Hz), c) 1800 rev/min (30 Hz) and d) 2400 rev/min (40 Hz)	97
Figure 4.18 Bow orbits for 10 mm supports at B1 for: a) 600 rev/min (10 Hz) and b) 1200 rev/min (20 Hz)	99
Figure 4.19 Crack orbits for 10 mm supports at B1 for : a) 600 rev/min (10 Hz), b) 1200 rev/min (20 Hz), c) 1800 rev/min (30 Hz) and d) 2400 rev/min (40 Hz)	100
Figure 4.20 Crack orbit for 10 mm supports at B1 for: a) 1710 rev/min (28.5 Hz); approx. half of the second natural frequency (56.67 Hz)	101
Figure 4.21 RMRU orbit at B1 for half of a) 50.66 Hz (1st) natural frequency and b) 56.76 Hz (2nd) natural frequency	101
Figure 4.22 Looseness orbits at B1 for: a) 600 rev/min (10 Hz), b) 1200 rev/min (20 Hz), c) 1800 rev/min (30 Hz) and d) 2400 rev/min (40 Hz)	103
Figure 4.23 Misalignment orbits at B1 for: a) 600 rev/min (10 Hz), b) 1200 rev/min (20 Hz), c) 1800 rev/min (30 Hz) and d) 2400 rev/min (40 Hz)	104
Figure 4.24 Rub orbits at B1 for: a) 600 rev/min (10 Hz), b) 1200 rev/min, (20 Hz), c) 1800 rev/min (30 Hz) and d) 2400 rev/min (40 Hz)	105
Figure 4.25 Rub orbits at B1 over 2 shaft rotations for: a) 600 rev/min (10 Hz), b) 1200 rev/min (20 Hz), c) 1800 rev/min (30 Hz) and d) 2400 rev/min (40 Hz)	107
Figure 4.26 Simple amplitude spectra at 40 Hz from B1 of 10 mm supports for: (a) RMRU vertical, (b) RMRU horizontal, (c) Rub vertical and (d) Rub horizontal	108
Figure 4.27 Residual Misalignment with Residual Unbalance orbits at B1 for: a) 600 rev/min (10 Hz), b) 1200 rev/min (20 Hz), c) 1800 rev/min (30 Hz) and d) 2400 rev/min (40 Hz);	109
Figure 4.28 Orbit for 6 mm supports at B1 for : a) Added Unbalance, b) Crack, c) Looseness, d) Misalignment, e) Rub at 1800 rev/min (30 Hz) and f) Bow at 600 rev/min (10 Hz);	110
Figure 5.1 Experimental rig mechanical layout	117
Figure 5.2 Schematic of software and instrumentation	117

Figure 5.3 Details of crack simulation: (a) locations tested, (b) crack dimensions and (c) shim details	118
Figure 5.4 Details of apparatus used for rub simulation	119
Figure 5.5 Details of Misalignment simulation at Bearing 3	119
Figure 5.6 Time waveform sample of the measured vibration data.....	121
Figure 5.7 Acceleration spectra at bearing 2 for all faults at 40 Hz.....	124
Figure 5.8 Comparison of spectral features for all conditions tested at 40 Hz	125
Figure 5.9 Acceleration spectra at bearing 2 for all faults at 50 Hz.....	126
Figure 5.10 Comparison of spectral features for all conditions tested at 50 Hz	127
Figure 5.11 Bearing heat transfer model.....	128
Figure 5.12 Sample showing progression of temperature trends in curve fitting process: a) transient curve fitting and b) generation of steady-state curves	130
Figure 5.13 Linear combined approach: a) Temperature and vibration scatter and b) Proposed linear combined diagnostic trend	131
Figure 5.14 PCA flow process	134
Figure 5.15 PCA-based approach without Temperature - 40 Hz.....	135
Figure 5.16 PCA-based approach with Temperature - 40 Hz	136
Figure 5.17 PCA-based approach without Temperature - 50 Hz.....	137
Figure 5.18 PCA-based approach with Temperature - 50 Hz	138
Figure 6.1 Layout of rotating machinery experimental rig.....	144
Figure 6.2 Measured mode shapes (dots represent measurement locations) of experimental rig: (a) mode 1: 67.14 Hz and (b) mode 2: 142.2	145
Figure 6.3 Sample of Frequency Response Function (FRF) in the horizontal direction; measured on long shaft near bearing 2 during modal testing	145
Figure 6.4 Amplitude Spectra from Bearing 2 at 2400 rev/min (40 Hz) for: a) healthy, b) crack near Bearing 1, c) crack near Bearing 2, d) crack near Bearing 3, e) misalignment and f) rub near Bearing 4	147
Figure 6.5 Amplitude Spectra from Bearing 2 at 3000 rev/min (50 Hz) for: a) healthy, b) crack near Bearing 1, c) crack near Bearing 2, d) crack near Bearing 3, e) misalignment and f) rub near Bearing 4	148
Figure 6.6 Comparison of spectral features at 2400 rev/min (40 Hz) for all conditions tested.....	150
Figure 6.7 Comparison of spectral features at all speeds for all conditions tested	151
Figure 6.8 Basic example of a Principal Component representation of two correlated variables X and Y	153
Figure 6.9 Time waveform sample of a measured vibration signal $y(t)$, where t is time in seconds.....	154
Figure 6.10 Actual sample of the amplitude spectrum Yf of function yt between frequencies f_1 and f_w	156

Figure 6.11 Sample showing variation of normalized PCA features for Bearing 3 at 2400 rev/min (40 Hz).....	158
Figure 6.12 Single speed analysis using only Bearing 1 features at: (a) 600 rev/min, (b) 1800 rev/min, (c) 2400 rev/min and (d) 3000 rev/min	160
Figure 6.13 Single speed analysis using only Bearing 2 features at: (a) 600 rev/min, (b) 1800 rev/min, (c) 2400 rev/min and (d) 3000 rev/min	161
Figure 6.14 Single speed analysis using only Bearing 3 features at: (a) 600 rev/min, (b) 1800 rev/min, (c) 2400 rev/min and (d) 3000 rev/min	162
Figure 6.15 Single speed analysis using only Bearing 4 features at: (a) 600 rev/min, (b) 1800 rev/min, (c) 2400 rev/min and (d) 3000 rev/min	163
Figure 6.16 Results of integrating features from all speeds from one bearing for (a) B1, (b) B2, (c) B3 and (d) B4.....	165
Figure 6.17 Samples of results from analysis at one speed for integrated features from all bearings for: (a) 600 rev/min, (b) 1800 rev/min, (c) 2400 rev/min and (d) 3000 rev/min	167
Figure 6.18 Results of proposed Unified Multi-speed Analysis comprised of features integrated from all speeds (600, 1200, 1800, 2400 and 3000 rev/min) and all bearings (B1–B4)	169
Figure 7.1 Mechanical layout of experimental Rig.....	179
Figure 7.2 Schematic of experimental rig with main dimensions.....	179
Figure 7.3 Schematic of experimental rig instrumentation and data acquisition (DAQ) system	180
Figure 7.4 Details of mounting for: (a) proximity probes and (b) accelerometer.....	181
Figure 7.5 Details of all faults seeded: (a) Crack, (b) Added unbalance, (c) Looseness at B3, (d) Misalignment at B1, (e) Blade rub near D1 and (f) Seal rub near D2.....	184
Figure 7.6 Schematic of experimental rig showing location of different fault conditions tested.....	185
Figure 7.7 Orbit plots of FS1 at Bearing 1 for all faults at 2400 rev/min (40 Hz).....	188
Figure 7.8 Sample of amplitude spectra for all faults of FS1 at B1 for 2400 rev/min (40 Hz)	191
Figure 7.9 Sample of amplitude spectra for all faults of FS1 at B2 for 2400 rev/min (40 Hz)	192
Figure 7.10 PCA flow process for vibration data acquired at a single steady-speed.....	198
Figure 7.11 Fault diagnosis with ISIF analysis for FS1 at 1200 rev/min (20 Hz) in (a) full view and (b) zoomed view of clustered section with baseline case	201
Figure 7.12 Fault diagnosis with ISIF analysis for FS1 at 1800 rev/min (30 Hz) in (a) full view and (b) zoomed view of clustered section with baseline case	202
Figure 7.13 Fault diagnosis with ISIF analysis for FS1 at 2400 rev/min (40 Hz) in (a) full view and (b) zoomed view of clustered section with baseline case	202

Figure 7.14 Fault Diagnosis with MSIF analysis (fusing data acquired at steady speeds of 20 Hz, 30Hz and 40 Hz combined) for FS1 in (a) full view and (b) zoomed view of clustered section with baseline case.....	204
Figure 7.15 Fault diagnosis with ISIF analysis for FS2 at 1800 rev/min (30 Hz) in (a) full view and (b) zoomed view of clustered section with baseline case	205
Figure 7.16 Fault Diagnosis with MSIF analysis (20 Hz, 30 Hz and 40 Hz combined) for FS2 in (a) full view and (b) zoomed view of clustered section with baseline case	206
Figure 7.17 Fault diagnosis with ISMF analysis combining FS1 and FS2 at 1200 rev/min (20 Hz) in (a) full view and (b) zoomed view of clustered section with baseline case	208
Figure 7.18 Fault diagnosis with ISMF analysis combining FS1 and FS2 at 1800 rev/min (30 Hz) in (a) full view and (b) zoomed view of clustered section with baseline case	208
Figure 7.19 Fault diagnosis with ISMF analysis combining FS1 and FS2 at 2400 rev/min (40 Hz) in (a) full view and (b) zoomed view of clustered section with baseline case	209
Figure 7.20 Fault diagnosis with MSMF combining FS1 and FS2 at all speeds (20 Hz, 30 Hz and 40 Hz) in (a) full view and (b) zoomed view of clustered section with baseline case	210
Figure 8.1 Mechanical layout of experimental rig used in earlier study [13]	218
Figure 8.2 Representative experimental orbits at B1 for: (a) RMRU (b) Added unbalance, (c) Bow, (d) Crack, (e) Looseness, (f) Misalignment and (g) Rub.....	220
Figure 8.3 Representative experimental spectrum at B1 for: (a) RMRU at 1800 rev/min (30 Hz) (b) Added unbalance at 1800 rev/min (30 Hz), (c) Bow at 1200 rev/min (20 Hz), (d) Crack at 1710 rev/min (28.5 Hz), (e) Looseness at 1800 rev/min (30 Hz), (f) Misalignment at 1800 rev/min (30 Hz) and (g) Rub at 2400 rev/min (40 Hz).....	221
Figure 8.4 Typical output of vibration-based fault classification technique developed in earlier experimental study showing PC plot in: a) full view and b) zoomed view [13]	223
Figure 8.5 Simple Jeffcott rotor model with flexible shaft and centrally located disc on rigid bearing supports	224
Figure 8.6 Healthy model showing disc with eccentric mass (m).....	227
Figure 8.7 Healthy orbit plot; filtered for $1\times$ and $2\times$ at: (a) 600 rev/min (10 Hz), (b) 1200 rev/min (20 Hz), (c) 1800 rev/min (30 Hz) and (d) 2400 rev/min (40 Hz)	229
Figure 8.8 Healthy amplitude spectra at 450 for: (a) 600 rev/min (10 Hz), (b) 1200 rev/min (20 Hz), (c) 1800 rev/min (30 Hz) and (d) 2400 rev/min (40 Hz).....	230
Figure 8.9 Added unbalance model showing mass of disc (m) and added mass (m_a).....	231
Figure 8.10 Added unbalance orbit plot; filtered for $1\times$ and $2\times$ at: (a) 600 rev/min (10 Hz), (b) 1200 rev/min (20 Hz), (c) 1800 rev/min (30 Hz) and (d) 2400 rev/min (40 Hz) .	232
Figure 8.11 Added unbalance amplitude spectrum at 45° for: (a) 600 rev/min (10 Hz), (b) 1200 rev/min (20 Hz), (c) 1800 rev/min (30 Hz) and (d) 2400 rev/min (40 Hz)	233
Figure 8.12 Crack model with cracked shaft section	234

Figure 8.13 Stiffness variation in a switching or hinge crack model.....	235
Figure 8.14 Crack orbit plot; filtered for $1\times$ and $2\times$ at: (a) 600 rev/min (10 Hz), (b) 1200 rev/min (20 Hz), (c) 1800 rev/min (30 Hz) and (d) 2400 rev/min (40 Hz)	236
Figure 8.15 Crack orbit plot; filtered for $1\times$ and $2\times$ at half rotor natural frequency; 1500 rev/min (25 Hz).....	237
Figure 8.16 Crack amplitude spectra at 45° for: (a) 600 rev/min (10 Hz), (b) 1200 rev/min (20 Hz), (c) 1800 rev/min (30 Hz) and (d) 2400 rev/min (40 Hz).....	237
Figure 8.17 Crack amplitude spectra at 450 for half resonant speed; 1500 rev/min (25 Hz)	238
Figure 8.18 Coupling misalignment model for parallel misalignment [140].....	239
Figure 8.19 Misalignment orbit plot; filtered for $1\times$ and $2\times$ at: (a) 600 rev/min (10 Hz), (b) 1200 rev/min (20 Hz), (c) 1800 rev/min (30 Hz) and (d) 2400 rev/min (40 Hz)	241
Figure 8.20 Misalignment amplitude spectra at 45° for: (a) 600 rev/min (10 Hz), (b) 1200 rev/min (20 Hz), (c) 1800 rev/min (30 Hz) and (d) 2400 rev/min (40 Hz)	242
Figure 8.21 Schematic of rub model showing contacting rotor-stator system.....	243
Figure 8.22 Rub orbit plot; filtered for $1\times$ and $2\times$ at: (a) 600 rev/min (10 Hz), (b) 1200 rev/min (20 Hz), (c) 1800 rev/min (30 Hz) and (d) 2400 rev/min (40 Hz)	246
Figure 8.23 Rub orbit plot; filtered for $0.5\times$ component at 2400 rev/min (40 Hz)	246
Figure 8.24 Rub amplitude spectra at 450 for: (a) 600 rev/min (10 Hz), (b) 1200 rev/min (20 Hz), (c) 1800 rev/min (30 Hz) and (d) 2400 rev/min (40 Hz).....	247
Figure 8.25 Single speed (SS) fault classification with data from mathematical simulations at 600 rev/min (10 Hz) in: a) full view and b) zoomed view	251
Figure 8.26 Single speed (SS) fault classification with data from mathematical simulations at 1200 rev/min (20 Hz) in: a) full view and b) zoomed view	252
Figure 8.27 Single speed (SS) fault classification with data from mathematical simulations at 1800 rev/min (30 Hz) in: a) full view and b) zoomed view	252
Figure 8.28 Single speed (SS) fault classification with data from mathematical simulations at 2400 rev/min (40 Hz) in: a) full view and b) zoomed view	253
Figure 8.29 Multi-speed (MS) fault classification with data from mathematical simulations from all speeds (10 – 40 Hz) in: a) full view and b) zoomed view	254

Nomenclature

a	Crack depth
A	Arbitrary variable
c	Damping coefficient of shaft
C_x	Covariance matrix
d	Rotor radial displacement
d_0	Rotor-stator radial clearance
e_a	Added mass eccentricity
e_d	Disc eccentricity
E	Modulus of elasticity
F_{nC}	Rub normal contact force
F_{tC}	Rub tangential friction force
F_x, F_y	General forces on rotor
F_{xM}, F_{yM}	Misalignment reaction forces on rotor (x and y)
F_{xR}, F_{yR}	Rub forces on rotor (x and y)
FX, FY, FZ	Coupling reaction forces
g	Acceleration due to gravity
k	Rotor (shaft) stiffness
k_C	Stator stiffness
K_b	Coupling bending spring rate
m	Rotor mass
m_a	Added mass
MX, MY, MZ	Coupling moments due to misalignment
P	Motor power
r_s	Shaft radius
R	Disc radius
S	A diagonal matrix containing the corresponding singular values

t	Time
T_{max}	Steady-state temperature
T_o	Ambient temperature
Tq	Drive torque
u, v	Rotor displacement (x and y)
\dot{u}, \dot{v}	Rotor velocity (x and y)
\ddot{u}, \ddot{v}	Rotor acceleration (x and y)
u', v'	Rotor displacement at 45° (x and y)
U	An orthonormal matrix
x, y	Coordinate directions
$Z1, Z2$	Shaft centreline (driver and driven)
$Z3$	Coupling centre of articulation
α	Added mass phase angle
β	Unbalance phase angle
γ	Misalignment phase angle
ζ	Damping ratio
μ	Friction coefficient
ρ	Rotor density
τ	Rotor-stator stiffness ratio
ψ	Velocity at rotor-stator contact point
ω	Angular velocity
ω_n	Natural frequency
ΔT	Temperature increase
$\Delta X, \Delta Y$	Misalignment offset (x and y)

List of Abbreviations

AC	Alternating Current
AI	Artificial Intelligence
A/D	Analogue to Digital
B1	Bearing 1
B2	Bearing 2
B3	Bearing 3
B4	Bearing 4
CBM	Condition-based Maintenance
CF	Crest Factor
C1	Coupling 1
C2	Coupling 2
DAQ	Data Acquisition
EMD	Empirical Mode Decomposition
D1	Balance disc 1
D2	Balance disc 2
D3	Balance disc 3
FD	Fault diagnosis
FFT	Fast Fourier Transform
FS1	Flexible support 1
FS2	Flexible support 2
IRT	Infrared Thermography
ISIF	Individual Speed Individual Foundation
ISMF	Individual Speed Multi-foundation
K	Kurtosis
MSIF	Multi-speed Individual Foundation
MSMF	Multi-speed Multi Foundation

OSV	On-shaft vibration
PC	Principal Component
PCA	Principal Component Analysis
r.m.s.	Root Mean Square
R1	Rotor 1
R2	Rotor 2
SE	Spectrum Energy
SVD	Singular Value Decomposition
SVM	Support Vector Machine
TG	Turbo generator
VCM	Vibration-based Condition Monitoring
VMS	Vibration Monitoring System
2D	Two dimensional

List of Publications

Journal publications

1. Nembhard, A. D., & Sinha, J. K. (2015). Comparison of experimental of observations in rotating machines with simple mathematical simulations. *Mechanical Systems and Signal Processing*, Submitted.
2. Nembhard, A. D., Sinha, J. K., & Yunusa-Kaltungo, A. (2015). Experimental observations in the shaft orbits of relatively flexible machines with different rotor related faults. *Measurement*, Under review.
3. Nembhard, A. D., Sinha, J. K., & Yunusa-Kaltungo, A. (2015). Development of a generic rotating machinery fault diagnosis approach insensitive to machine speed and support type. *Journal of Sound and Vibration*, **337**(0), 321-341.
4. Nembhard, A. D., & Sinha, J. K. (2015). Unified Multi-speed Analysis (UMA) for the condition monitoring of aero-engines. *Mechanical Systems and Signal Processing*, **2015**.
5. Nembhard, A. D., Sinha, J. K., Pinkerton, A. J., & Elbhah, K. (2014). Combined vibration and thermal analysis for the condition monitoring of rotating machinery. *Structural Health Monitoring*, **13**(3), 281-295.
6. Nembhard, A. D., Sinha, J. K., Pinkerton, A. J., & Elbhah, K. (2013). Fault Diagnosis of Rotating Machines using Vibration and Bearing Temperature Measurements. *Diagnostyka Science Journal*, **14**(3), 45-51.

Conference publications

1. Nembhard, A., & Sinha, J. (2015). Vibration-Based Condition Monitoring for Rotating Machinery with Different Flexible Supports. In J. K. Sinha (Ed.), *Vibration Engineering and Technology of Machinery* (Vol. 23, pp. 119-127): Springer International Publishing.
2. Nembhard, A. D., & Sinha, J. K. (2014). *Combined Vibration and Temperature Analysis for Condition Monitoring of Aero-engines (GT2014-25726)*. Paper presented at the Proceedings of ASME Turbo Expo 2014: Turbine Technical Conference and Exposition GT2014, Düsseldorf, Germany.
3. Nembhard, A., Sinha, J., Pinkerton, A. J., & Elbhah, K. (2014). Condition Monitoring of Rotating Machines Using Vibration and Bearing Temperature Measurements. In G. Dalpiaz, R. Rubini, G. D'Elia, M. Cocconcelli, F. Chaari, R. Zimroz, W. Bartelmus & M. Haddar (Eds.), *Advances in Condition Monitoring of Machinery in Non-Stationary Operations* (pp. 159-169): Springer Berlin Heidelberg.

Abstract

Adrian D. Nembhard - PhD in Mechanical Engineering,
The University of Manchester – July 2015,

“On-bearing Vibration Response Integration for Condition Monitoring of Rotating Machinery”

Vibration-based fault diagnosis (FD) with a simple spectrum can be complex, especially when considering FD of rotating machinery with multiple bearings like a multi-stage turbine. Various studies have sought to better interpret fault spectra, but the process remains equivocal. Consequently, it has been accepted that the simple spectra requires support from additional techniques, such as orbit analysis. But even orbit analysis can be inconclusive. Though promising, attempts at developing viable methods that rival the failure coverage of spectrum analysis without gaining computational complexity remain protracted. Interestingly, few researchers have developed FD methods for transient machine operation, however, these have proven to be involved. Current practices limit vibration data to a single machine, which usually requires a large unique data history. However, if sharing of data between similar machines with different foundations was possible, the need for unique histories would be mitigated. From readily available works, this has not been encountered. Therefore, a simple but robust vibration-based approach is warranted. In light of this, a novel on-bearing vibration response integration approach for condition monitoring of shaft-related faults irrespective of speed and foundation type is proposed in the present study. Vibration data are acquired at different speeds for: a baseline, unbalance, bow, crack, looseness, misalignment, and rub conditions on three laboratory rigs with dynamically different foundations, namely: rigid, flexible support 1 (FS1) and flexible support 2 (FS2). Testing is done on the rigid rig set up first, then FS1, and afterwards FS2. Common vibration features are computed from the measured data to be input to the proposed approach for further processing. First, the proposed approach is developed through its application to a machine at a steady speed in a novel Single-speed FD technique which exploits a single vibration sensor per bearing and fusion of features from different bearings for FD. Initially, vibration features are supplemented with bearing temperature readings with improved classification compared to vibration features alone. However, it is observed that temperature readings are insensitive to faults on the FS1 and FS2 rigs, when compared to vibration features, which are standardised for consistent classification on the different rigs tested. Thus, temperature is not included as a final feature. The observed fault classifications on the different rigs at different speeds with the standardised vibration features are encouraging. Thereafter, a novel Unified Multi-speed FD technique that is based on the initial proposed approach and which works by fusion of vibration features from different bearings at different speeds in a single analysis step for FD is proposed. Experiments on the different rigs repeatedly show the novel Multi-speed technique to be suitable for transient machine operation. Then, a novel generic Multi-foundation Technique (also based on the proposed approach) that allows sharing of vibration data of a wide range of fault conditions between two similarly configured machines with similar speed operation but different foundations is implemented to further mitigate data requirements in the FD process. Observations made with the rigs during steady and transient speed tests show this technique is applicable in situations where data history is available on one machine but lacking on the other. Comparison of experimental results with results obtained from theoretical simulations indicates the approach is consistent. Thus, the proposed approach has the potential for practical considerations.

Declaration

I hereby declare that no portion of the work referred to in the thesis has been submitted in support of an application for another degree or qualification of this or any other university or other institute of learning.

Copyright statement

- i. The author of this thesis (including any appendices and/or schedules to this thesis) owns certain copyright or related rights in it (the “Copyright”) and s/he has given The University of Manchester certain rights to use such Copyright, including for administrative purposes.
- ii. Copies of this thesis, either in full or in extracts and whether in hard or electronic copy, may be made **only** in accordance with the Copyright, Designs and Patents Act 1988 (as amended) and regulations issued under it or, where appropriate, in accordance with licensing agreements which the University has from time to time. This page must form part of any such copies made.
- iii. The ownership of certain Copyright, patents, designs, trademarks and other intellectual property (the “Intellectual Property”) and any reproductions of copyright works in the thesis, for example graphs and tables (“Reproductions”), which may be described in this thesis, may not be owned by the author and may be owned by third parties. Such Intellectual Property and Reproductions cannot and must not be made available for use without the prior written permission of the owner(s) of the relevant Intellectual Property and/or Reproductions.
- iv. Further information on the conditions under which disclosure, publication and commercialisation of this thesis, the Copyright and any Intellectual Property and/or Reproductions described in it may take place is available in the University IP Policy (see <http://documents.manchester.ac.uk/DocuInfo.aspx?DocID=487>), in any relevant Thesis restriction declarations deposited in the University Library, The University Library’s regulations (see <http://www.manchester.ac.uk/library/aboutus/regulations>) and in The University’s policy on Presentation of Theses

Acknowledgement

Dr Jyoti K. Sinha, my supervisor, has selflessly offered invaluable guidance and tuition over the course of this research, which significantly aided the development of the concepts presented and inevitably the writing of this thesis. I also wish to express sincere gratitude to the Commonwealth Scholarship and Fellowship Programme for affording me The 2012 PhD Commonwealth Scholarship from Jamaica to the UK to pursue this research.

Dedication

This thesis is dedicated to Mrs Glenice J. Nembhard, my wife and inspiration.

1 INTRODUCTION

1.1 Introduction

Rotating machinery is the most ubiquitous category of critical industrial equipment. It is to this end that condition monitoring is crucial for the maintenance of such assets in order to prevent costly catastrophic damages. In critical systems such as power generating turbines and aero-engines, rotor failure may have considerable implications to operating costs. Thus, given, the strong business case for improving rotor fault diagnosis it was selected as the object of the current research.

The vibration spectrum analysis is a mature FD technique that has low computational burden and is applicable to different machinery, but the process can be complex, especially when considering machines with multiple bearings, such as a multi-stage turbine. This results in large volumes of data sets needing processing and interpretation, because several vibration measurements are required at each bearing location [1]. Consequently the process mandates a highly trained and knowledgeable analyst [2], who despite training may still yield subjective and erroneous diagnosis. Inherently, because of such difficulties, the FD process can be lengthy and prove costly, or even worse, life threatening.

Various studies have been done to better comprehend the dynamic responses of common rotor faults [3-11], but there still exists ambiguity in the interpretation of data from same [3]. Consequently, it has been accepted that the simple spectra on its own may not be adequate for confident FD and might require support from additional techniques, such as the orbit plot [12]. But even orbit plot analysis can be inconclusive [13]. However, the usefulness of orbit analysis in providing information on the dynamic behaviour of a rotor was noted. Similar studies in readily available literature on the technique were mainly theoretical and done considering a few fault conditions on different machines. Therefore, an opportunity exists to provide further experimental insight to changes in the behaviour of a single machine when affected by a wider range of different rotor-related faults.

Recent efforts in FD research have focused on either improving traditional techniques or developing new techniques [14]. The usefulness of wireless sensors relative to conventional sensors [15] for remote condition monitoring [16] and on-shaft vibration

measurement [17] has been demonstrated. It was, however, noted that wireless sensors do not mitigate the aforementioned difficulties associated with traditional FD and may require special arrangement of the measurement instrumentation [17], which currently might not be practicable. It is opined in some studies that for complex systems a single sensor is incapable of collecting data requisite for accurate FD, and therefore, simultaneous application of multiple sensors is better able to comprehensively describe a machine state [18]. Researchers have been able to fuse different sensors [19, 20], but a fundamental challenge for fusion of different sensors has been to create a fusion technique that is simple but adequately robust for practical application. Encouraging results had from studies combining vibration and temperature that compared overall vibration r.m.s. with on-bearing temperature measurements suggest an opportunity still exists for multi-sensor fusion for effective FD [20].

Though promising, other attempts at developing viable alternatives to traditional practice [21-30], have led to advanced techniques with “high computational complexity” [21, 23]; therefore leaving a gap in the current body of research and the needs of industry. It was also interesting to note that despite the strong business case, few researchers have sought to develop methods that are applicable to critical machines like aero-engines during transient operations, which offer a fundamental challenge [31]. Methods developed to overcome this challenge have proven less than accurate [32-34] or too intricate [14, 35-37] for real life application.

Of the different alternative methods perused, attempts based on pattern recognition [38, 39] appeared most promising for simultaneous simplicity and robustness, but from readily accessible literature, this approach has not been attempted on commonly encountered rotor-related faults. Pattern recognition techniques require “a relatively large number of identified fault and non-fault samples” [40] in a unique data history. Needless to say, any attempt at a viable approach requires a feasible method to mitigate the need for large vibration data history without compromising diagnosis confidence. Current practices limit vibration data to a single machine. It is possible that the same design or model rotating machine when installed at different plant sites have different foundations with different natural frequencies and the vibration data history requisite for condition monitoring may exist at one site and be lacking in the other. Therefore, if sharing of vibration data between

similar machines was possible, the need for different large data histories unique to a machine would be mitigated or eliminated. From readily available works this has not been encountered.

For these reasons, a study proposing a viable alternative approach to traditional practices with documentation of experimental and theoretical validation of the proposed approach's ability to provide solutions to the issues and gaps identified is warranted.

1.2 Aims and Objectives

The aim of the current study is to propose an on-bearing vibration response integration approach for condition monitoring and diagnosis of a wide range of shaft-related faults on different rotating machinery irrespective of speed and foundation type. It is intended that the approach: requires significantly less data than spectrum analysis; bypasses the need for complex processing; offers moderate computational burden; produces easily interpreted results; and enables sharing of vibration data history between similarly configured machines with different foundations. In order to accomplish this approach, the following objectives are required:

1. Gain an appreciation of the dynamic effects of a wide range of common rotor faults from experiments on different machines with different foundations operating at different speeds.
2. Experimentally develop an on-bearing vibration response integration approach which uses a single vibration sensor per bearing and fusion of features from different bearings for the diagnosis of a wide range of rotor faults on different machines at different steady speeds.
3. Implement a novel Unified Multi-speed analysis technique based on the on-bearing vibration response integration approach (from Objective 2), which fuses vibration data from different speeds in a single analysis step for the diagnosis of a wide range of faults on different machines operating at different transient speed conditions.

4. Introduce a novel generic Multi-foundation technique which allows sharing of vibration data history of a wide range of rotor faults between two similarly configured machines irrespective of speed for FD in situations where data history is available on one machine but lacking on the other.
5. Compare the experimentally proposed approach with simple mathematical simulations and analyses.

1.3 Contributions to knowledge

The studies reported in this thesis are intended to propose and provide insight to a novel on-bearing vibration response integration approach for condition monitoring of rotating machinery. The contributions of this thesis can be listed as follows:

1. A novel, simple and robust On-bearing Vibration Response Integration Approach for condition monitoring and diagnosis of rotor faults was proposed in the current study. The on-bearing approach applies to a wide range of commonly encountered shaft-related faults; requires significantly less data than the traditional spectrum analysis as it exploits a single vibration sensor per bearing; produces an easily interpreted diagrammatical result; offers moderate computational load; and is applicable to different machines with different dynamic characteristics. The novel on-bearing vibration integration approach can be applied to rotating machinery fault classification in three novel techniques: Single-speed Analysis technique, Unified Multi-speed Analysis (UMA) technique, and a Multi-foundation Analysis technique.
2. The novel Single-speed technique works by fusion of vibration data from different bearings at a single speed in a single analysis step. The technique is initially proposed on an experimental rig with relatively rigid bearing supports, which was developed in an earlier study. Measured on-bearing vibration data from healthy, crack, misalignment and rub faults are used to compute commonly applied vibration indicators or features, namely: r.m.s.; and amplitudes of $1\times$, $2\times$, and $3\times$ spectral components. Bearing temperature measurements were also employed as a feature as it was expected that temperature would compensate for the reduction in vibration sensors while replacing the need for advanced and complex signal processing of the vibration data. Fault classification with vibration features alone was good. However, it was seen that the supplementing vibration data with bearing temperature readings improved the efficacy of the fault classification process achieved on the rigid rig.

3. The novel Single-speed technique was then trialled on different machines with a wider range of shaft fault conditions, namely: added unbalance, bow, crack, looseness, misalignment and rub with respect to a baseline residual misalignment with residual unbalance (RMRU) condition. Experiments were done on two dynamically different experimental rigs with relatively flexible supports, which were developed in the current study. Preliminary analysis showed that that temperature did not have an effect with either flexible support set up and, therefore, temperature was excluded from the set of features used, which were standardized to the following: r.m.s vibration amplitude; amplitudes of $1\times$, $2\times$, $3\times$, $4\times$ and $5\times$ spectral components; and spectrum energy (SE). Classification with the revised vibration features was good. This study is the first application of a simple but robust Principal Component Analysis based fault classification data fusion technique for rotating machinery shaft-related faults.
4. The novel Unified Multi-speed Analysis (UMA) technique is proposed in the current study with objective being the application of the novel On-bearing Vibration Response Integration Approach to variable speed machines or machines which operate constantly under transient speed conditions. The Multi-speed technique works by fusion of data different speeds and different bearings in a single analysis step. Initially, the technique was developed solely from vibration data obtained on the rigid rig support, as temperature did not have an effect on the classification. Results from the Multi-speed technique indicate that fusion of more dynamic features available at different speeds and different bearing locations improve the efficacy of the classification process. Fusion of vibration data from different speeds is would be difficult to achieve if not impossible with conventional vibration-based techniques. The Unified Multi-speed Analysis technique is suitable for variable speed machines including aero-engines.
5. The novel Unified Multi-speed Analysis technique was initially proposed in on the rigid set up, and then its transferability was tested on two experimental rigs with relatively flexible bearing supports that were developed in the current study. Preliminary analysis revealed that the initially used Multi-speed features of r.m.s. amplitude, crest factor (CF), kurtosis (K) and spectrum energy (SE) did not perform consistently on the rigs with flexible supports. Therefore, the features were

standardized to the said revised features used in the singles-speed technique: r.m.s, 1×, 2×, 3×, 4×, 5× and SE. The revised set of features performed effectively for both rigid and flexible set up. The test of transferability of the Multi-speed technique showed good fault classification on different rigs with flexible supports, thereby indicating the UMA technique is transferable to different machines with different dynamic characteristics.

6. A novel generic Multi-foundation technique for mitigating the need for unique data history in vibration-based FD, by enabling sharing of vibration data between two similarly configured machines that are dynamically different, is proposed in the current study. The technique is able to accurately classify mixed vibration data of the following conditions: unbalance, bow, crack, misalignment, rub and a baseline residual misalignment with residual unbalance. The technique is applied to two similarly configured machines either when both are operated at a steady speed or when both have variable speed operations. Therefore, the technique is not confined to machines with a particular speed operation. This is the first account of a vibration-based technique being able to accurately classify mixed vibration data from two dynamically different machines. Sharing of data with traditional means is not possible as different machine foundations result in different dynamic characteristics and hence different spectral features. The novel Multi-foundation technique is highly suited in situations where vibration data history for a machine is not readily available, but a similarly configured machine in a different physical location has readily accessible history.
7. For the first time, the proposed novel Single-speed and novel Multi-speed techniques are demonstrated with vibration features computed from data obtained from mathematical simulations of a healthy condition and added unbalance, crack, misalignment and rub. A Jeffcott rotor was used to model the different conditions. The outputs from the models were processed to compute the standardized vibration features of r.m.s.; amplitudes of the 1×, 2×, 3×, 4× and 5× spectral components; and SE, that were input to the Single-speed technique first and then to the Multi-speed technique. Results from experiments were compared to those obtained from the simulations and it was found that the fault classification in each case were consistent. Therefore, the results from the simulation-based analyses further

reinforced the posit that the proposed single-speed and Multi-speed techniques will perform with data from different sources.

8. The proposed novel single speed or Multi-speed techniques would require historical data, from say a database of known healthy and fault data. The historical data would establish healthy and fault clusters (such as clusters of misalignment separate from crack etc.) in the output. As new data become available, this would be fed into the database from which the algorithm mines and generates an input matrix. Continuous classification would be done. Therefore, if a fault does not exist with the machine being monitored, the input data would be grouped into the healthy cluster. This would continue until, say data with a fault occurrence is supplied to the tool, which would classify and group the fault into one of the predefined fault clusters. There also exists the possibility that new input data are not classified in the predefined healthy or fault clusters. This would therefore mean the fault was not previously classified and would warrant investigation to ascertain the cause of the fault. This new fault can then be updated to the database as reference for future classification.

1.4 Report Layout

The thesis is presented in the alternative format with its main content written in the form of published/submitted research papers of the candidate's own work. As would be in a traditional format thesis, Chapters 2 provides a review of relevant literature to establish the research context and Chapter 3 outlines the experimental approach employed in the study. However, Chapters 4-8 hold the main content of the paper comprising of the aforementioned published/submitted research papers. Conclusions are drawn and future works recommended, as would be in a traditional format thesis, in Chapter 9. Further details of the outline are provided:

- **Chapter 2** presents a critical review of literature and published works relevant to the current study in order to establish the research background and context.

- **Chapter 3** provides cursory descriptions of the experimental approach used; comprising of the experimental set up, instrumentation used and conditions tested.
- **Chapter 4** presents experimental observations made in the orbit plots for the different fault conditions tested on different machines with reference to a baseline condition.
- **Chapter 5** describes, in detail, the initial experimental works done to develop the on-bearing integration approach for rotor condition monitoring and FD of rotating machinery.
- **Chapter 6** introduces, in detail, the experimental implementation of the novel Unified Multi-speed Analysis (UMA) FD technique.
- **Chapter 7** holds detailed accounts of experiments done in the expansion of the on-bearing integration approach to different machines with different foundations and different speed operation. The Multi-foundation technique is also proposed here.
- **Chapter 8** offers the comparison of the various experimental results with theoretical simulations and analyses.
- **Chapter 9** has the conclusion of the present study. Salient observations made are outlined and future work is also recommended.

1.5 Report linkages

A flow process depicting the logical progression of the research undertaken in the current study is presented in two parts in Figures 1.1 and 1.2, respectively. The figures provide key details of the links between chapters 4-8, which are the main chapters with the novel contributions of the current study. cursory details of the methods used, decisions made and findings obtained are also presented. It is intended that the flow processes shown will provide an overall snapshot of the works done in the current study.

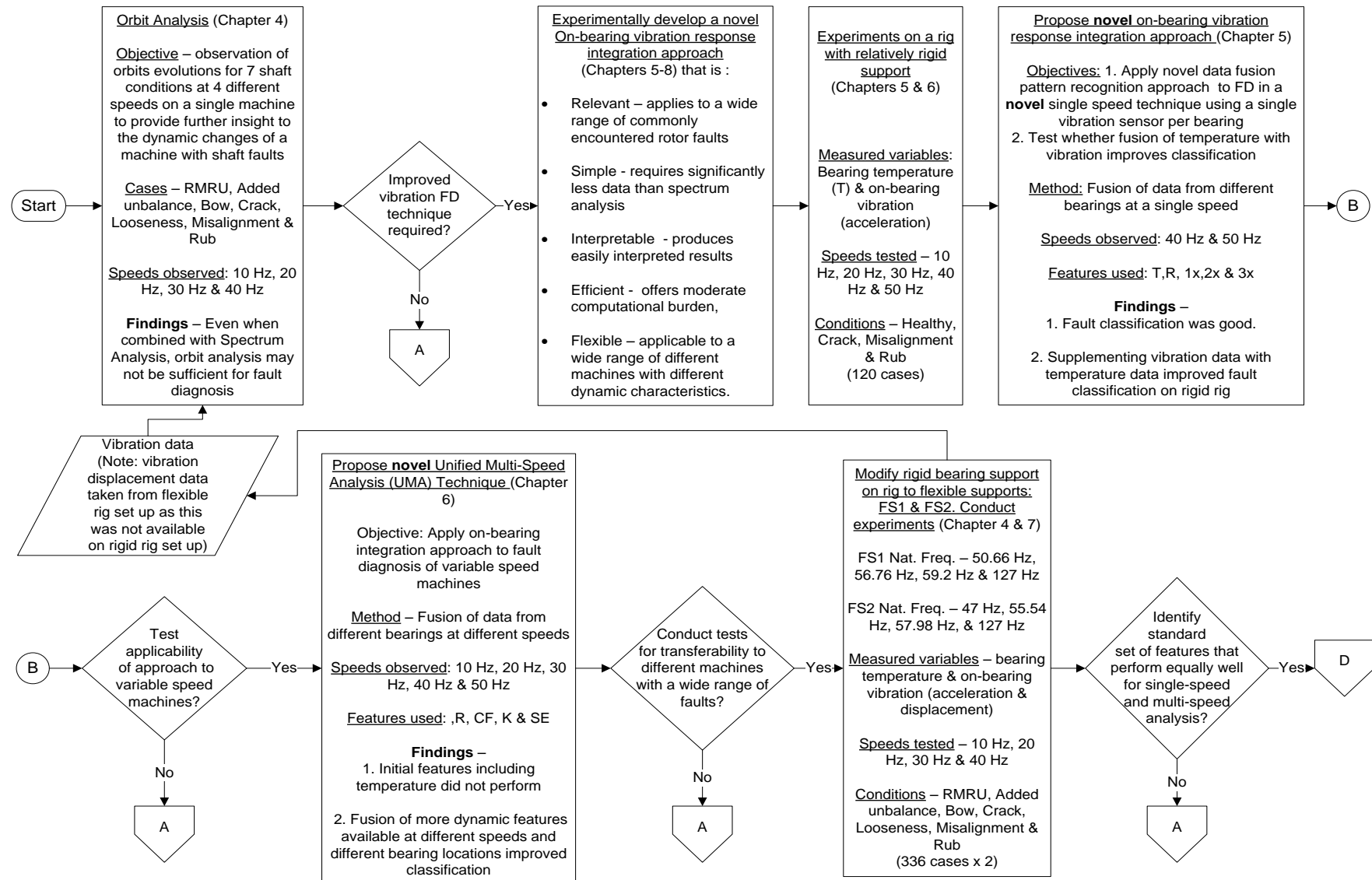


Figure 1.1 Flow diagram showing logical progression of research undertaken in the current study as presented in Chapters 4-8, part 1

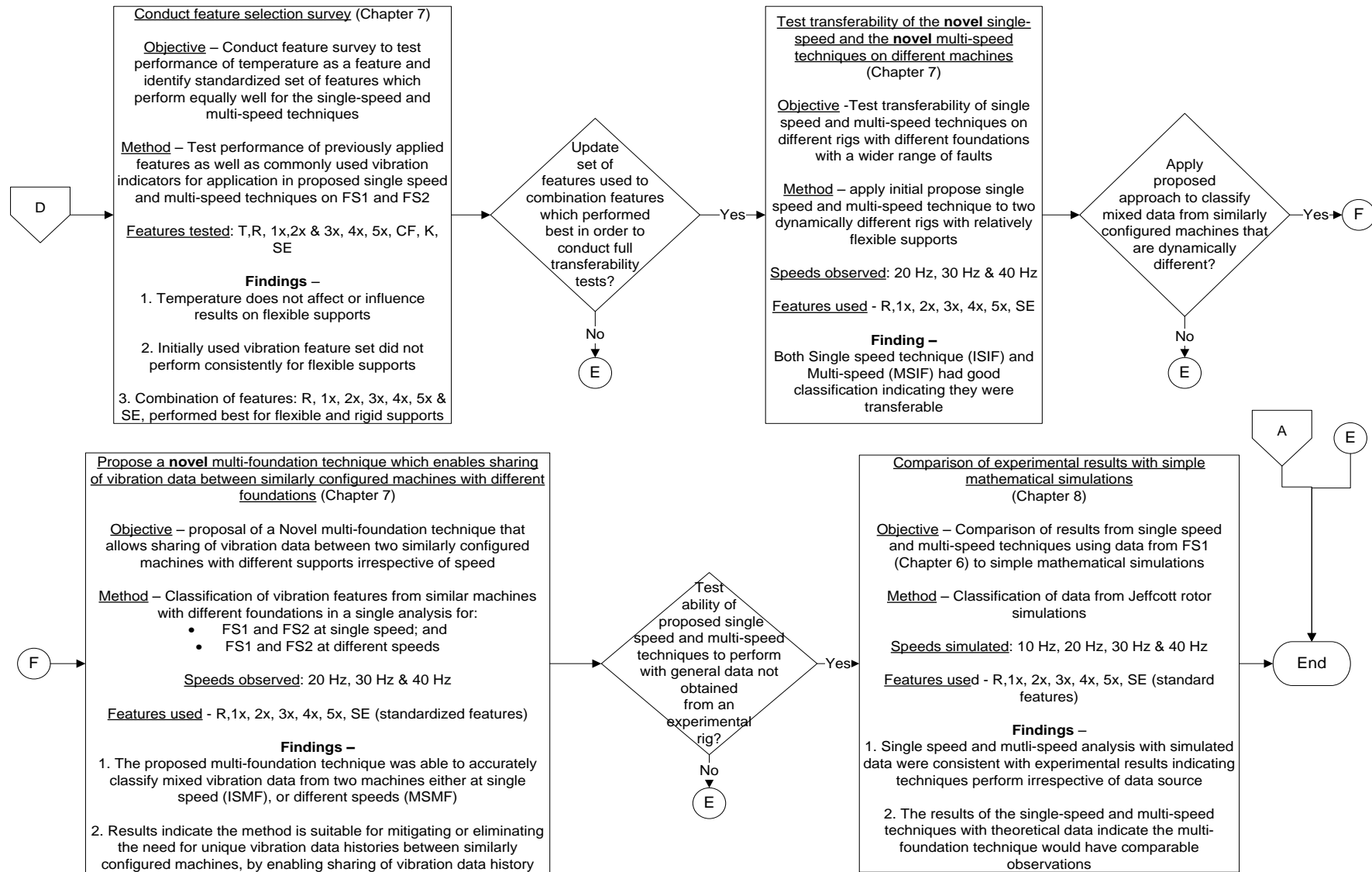


Figure 1.2 Flow diagram showing logical progression of research undertaken in the current study as presented in Chapters 4-8, part 2

2 LITERATURE REVIEW

2.1 Introduction

To establish the research context of the present study, a review of background literature and research papers relevant to the current study is given in this chapter. Condition monitoring is introduced and then standard practice in vibration-based fault diagnosis is reviewed. Finally recent research efforts in vibration-based condition monitoring for rotating machinery are critically assessed.

2.2 Machinery failure patterns

Failure is defined as the termination of the ability of an item (or the machine containing it) to perform a required function or meet a specified performance standard [41, 42]. A failure is an event, as opposed to a fault, which is a state of a machine or equipment, resulting from failure [42].

Prior to the 1970s it was accepted that equipment failure patterns were primarily age related [43]. Maintenance management practices employed strategies focussed on time based replacement of equipment and components with the aim of returning it to “as new” conditions before ending its useful life (preventive maintenance). It was not until the 1970s when a study of failure patterns was conducted in the airline industry, that it was found that only 11% of failures were age related [41]. The remaining 89% were random in nature and as such were impacted very little by time based maintenance interventions [43]. As shown in Figure 2.1, which illustrates the trend in maintenance expectations since the 1930s, the task of managing random non-age related failures has been an increasing challenge [43]. Numerous techniques have been developed to address this challenge. Amongst the different techniques used for equipment management, condition monitoring has proven itself formidable based on its technical feasibility and cost savings capabilities. This is predicated by the fact that 99% of all machinery failures are preceded by a measurable indicator [44], which is the basis of condition monitoring.

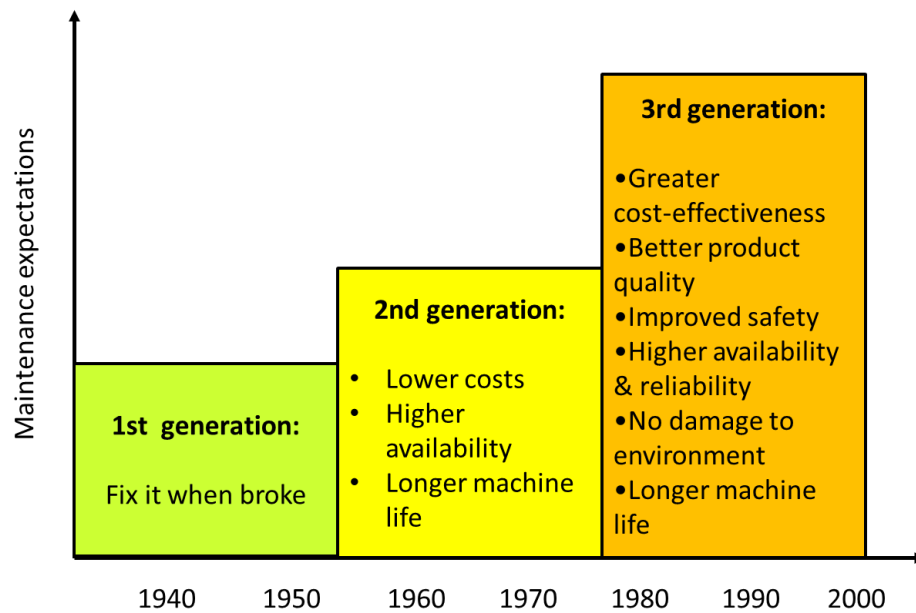


Figure 2.1 Trends in maintenance expectations [43]

2.3 Condition monitoring

In order to maximize return on investments, organizations perpetually push the operational boundaries of machinery. Increased output, availability and efficiency are mandated and as such the stresses and loads placed on bearings and rotors are ever increasing. Commensurate to this is the need for maintenance practitioners to sustain machinery health by confidently diagnosing and correcting faults as early as possible. Maintenance is a costly means to an end and if not done properly accounts for up to 60% of total production costs, with as much as a third of that squandered on ineffective work. Such counter-productive maintenance is caused by a lack of factual data that quantify the health of machinery in order to make timely decisions on requisite repairs [45]. As such, maintenance techniques, such as Condition Monitoring are widely employed. Condition monitoring is defined as the “acquisition and processing of data that indicate the state of a machine” [40]. It is a non-intrusive data driven technique, which involves checking for a measureable parameter which indicates the state of the equipment so that requisite maintenance action can be taken to mitigate or prevent the consequences of failure or costly equipment downtime [43]. That being said, condition monitoring itself is a relatively

costly venture, which is usually reserved for critical machinery in order to justify the cost of implementing and sustaining the venture [40, 43].

Condition monitoring techniques commonly used in practice include vibration analysis, infrared thermography, lubrication oil and wear debris analysis [46] and acoustic emissions analysis (AE) [31]; to name a few. There is no absolutely suitable technique [47]. An appropriate approach is chosen based on factors including equipment operating context, operating environment, cost and expected faults [31, 45]. But owing to its comprehensive failure mode coverage and applicability to diverse mechanical systems, vibration analysis is the preferred condition monitoring technique for critical systems [31]. Rotating machinery is the most ubiquitous category of critical industrial equipment, which is why vibration analysis is widely applied to such machinery in industry.

2.4 Vibration-based condition monitoring of rotating machinery

Vibration analysis is based on the premise that machinery failures may be indicated at least months in advance by a change in vibration [44]. The ability to detect such vibration changes in rotating machinery allows the maintenance practitioner to predict the time to failure and conduct corrective work. Considering the pump shown in Figure 2.2, fundamentally rotating machinery is comprised of three basic components; foundation, bearings and rotor (or shaft) [48].

Vibration analysis allows the detection, diagnosis and decision making towards the mitigation and or elimination of failures that would originate in any of these basic components. The bearing is a supportive connection to the rotor and the machine foundation. Bearing fault frequencies are impulsive and often contaminated with noise, which is why vibration research is generally focussed on the extraction of features representative of the bearing health from the noisy time-variant measured data [49]. The foundation offers structural support to hold the rotor-bearing assembly in place. Vibration studies for machinery foundations involve quantification of the dynamic characteristics of the machine support structure [50] and also for diagnosis of structural faults. The rotor or shaft in the system is the rotating component. Rotor faults include self-excited vibration

caused by system instability as well as those due to externally applied loads (such as cracked shafts and mass unbalance), thus works on rotor fault diagnosis aim to identify the cause and dynamic properties of such excitations. There is also a need for dynamic characterization [50] of the rotor to aid diagnosis.

In critical systems such as power generating turbines and aero-engines, rotor failure may have considerable implications to operating costs or even worse; loss of life. Thus, given, the strong business case for improving rotor fault diagnosis it was selected as the object of the current research.

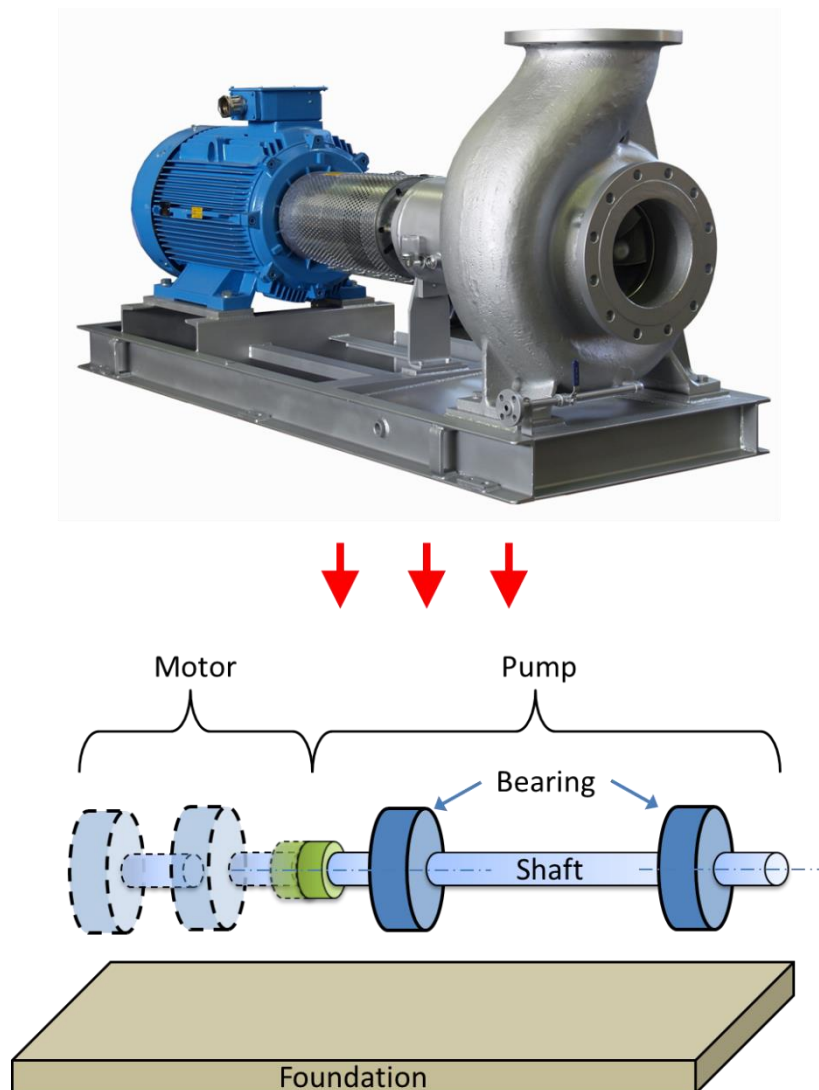


Figure 2.2 Fundamental components in rotating machinery

2.5 Vibration-based condition monitoring for rotor fault diagnosis

Figure 2.3 shows the condition monitoring data processing flow diagram, which illustrates how data transforms as it passes through the various stages of the process; from data acquisition through to fault diagnosis. Detailed description of the different stages of the process with respect to vibration analysis follows.

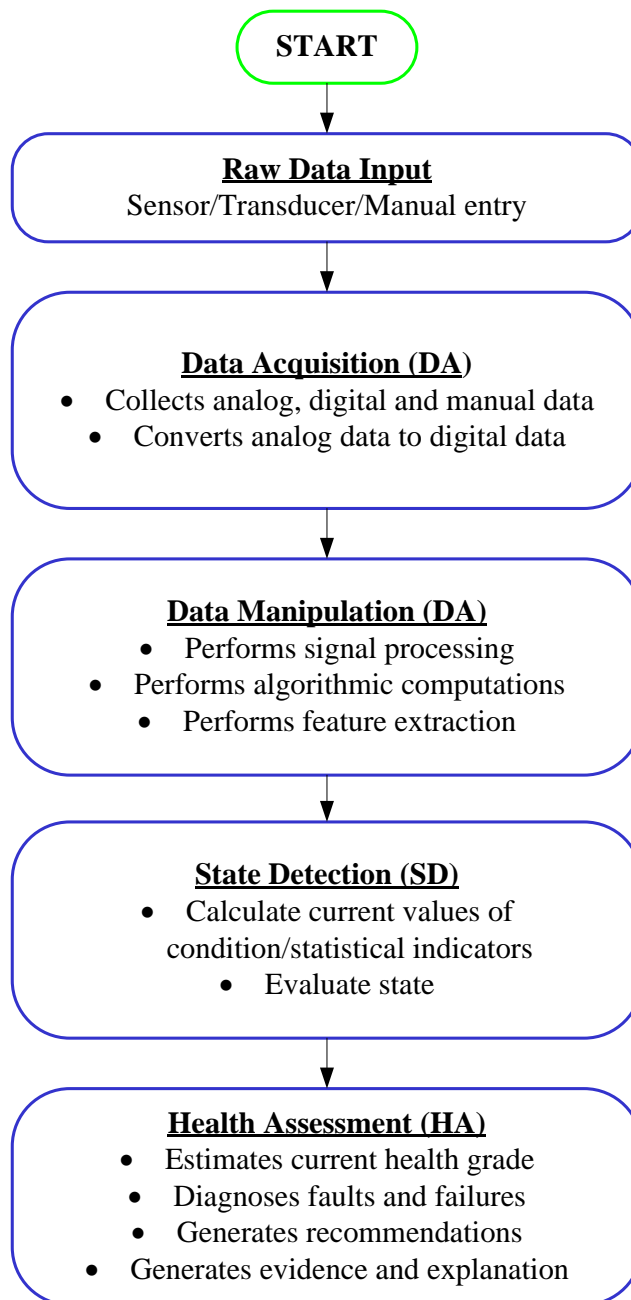


Figure 2.3 Condition monitoring data processing flow diagram [51]

2.5.1 Data acquisition

Data acquisition (DAQ) is “the process of measuring an electrical or physical phenomenon such as voltage, current, temperature, pressure, or sound” [52]. A typical set up of a vibration monitoring DAQ system is represented in Figure 2.4. The system comprises of three fundamental components: vibration transducers, DAQ device and the computer.

Selection of the type and location of transducers is based on the expected fault frequencies and parameters to be measured, respectively [53]. As shown, it is useful to observe the displacement of shaft centreline relative to the stationary bearing housing in large machinery such as power turbines. To do this, eddy current probes are mounted at mutually exclusive positions in the same transverse plane on the bearing housing and directed to the shaft. For vibration measurements on the non-rotating structure of the machinery, an accelerometer is widely used owing to its wide applicability in early detection of various faults occurring across a wide frequency range (1 to 10,000 Hz), reliability, and ability to provide velocity and displacement values with subsequent integration during data processing. In the traditional sense, monitoring of the absolute vibratory motion of the rotating element is less commonly employed [53].

The DAQ’s main function is to convert the analogue signal from the transducers to a digitized format that can be read by the personal computer which controls the DAQ device. The computer is also used after data acquisition for signal processing. Data acquisition and analysis of vibration data can be complex as data are usually required in three mutually perpendicular planes for accurate fault diagnosis [1].

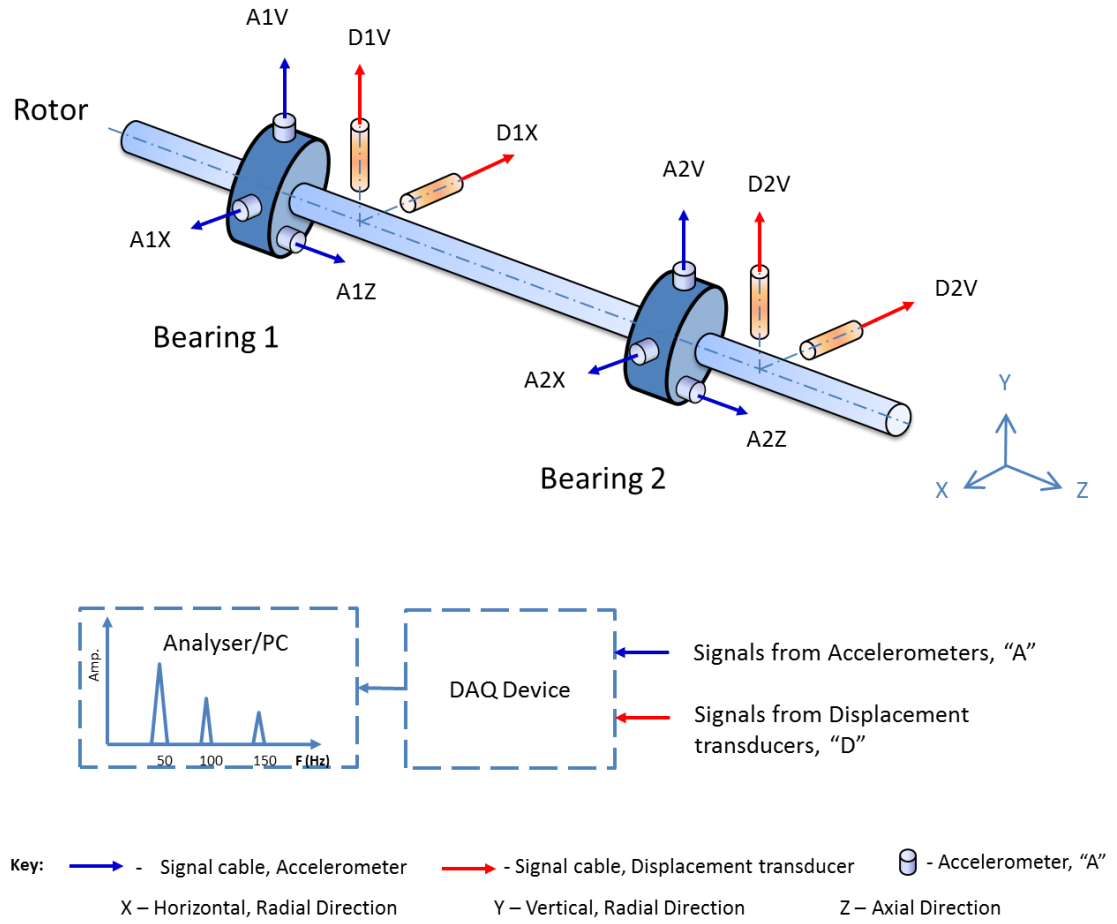


Figure 2.4 Typical set up for a vibration-based condition monitoring system

2.5.2 Data manipulation

After acquiring the vibration data, there exists the challenge of removing the unwanted contents such as noise in the signal in order to produce a signal with features that are most representative of the health (condition) of the machinery being monitored. The objective of signal processing is to extract and display, from the measured data, the maximum amount of useful information (descriptors/features) which best represent the health of the machinery in order to make diagnosis much easier for the user [53, 54]. Descriptors can either exist in the time or frequency domain [51]. Commonly applied descriptors (also referred to as features) include Root Mean Square (r.m.s.), Crest Factor (CF) and Kurtosis (K) from the time domain and Spectrum Energy (SE) from the frequency domain [33].

State detection is achieved by calculation of descriptors and comparing with some historical reference or baseline usually by trend analysis

2.5.3 Health assessment

After an anomaly is detected, an assessment of the health of the machinery requires expertise from a trained analyst or otherwise to diagnose the cause of the condition or state of the machinery being monitored. In standard practice, on acquiring data, trending of an established condition indicator is done to compare the measured parameter to a known baseline. If this parameter exceeds a predetermined safe limit, then fault diagnosis is performed. The ability to accurately discriminate machines states is the basis of confident fault diagnosis. If confident diagnosis is unattainable or if confidence is low, then additional diagnostic techniques may be required [31]. Further details of the diagnosis process are provided in following sections.

2.6 Standard practices in vibration-based rotor fault diagnosis

An outline of relevant and readily available literature on the simple spectrum analysis in the context of rotating machinery and more specifically, rotor fault diagnosis is given. This is followed by a short but comprehensive review of the application of the orbit analysis to rotor fault diagnosis.

2.6.1 Simple spectrum analysis

Of the vibration-based techniques currently in use in practical applications the simple amplitude spectrum derived from the Fast Fourier Transform (FFT) is well established and most commonly used for rotor fault diagnosis because of factors including its range of fault sensitivity, relative computational simplicity and flexibility for application to different types of machines. The output of the FFT is represented in the amplitude or Fourier spectrum for feature extraction and analysis. However, the effectiveness of a vibration-

based diagnostic programme is highly dependent on the capabilities of the technician or analysis that carries out data acquisition and analysis. It is requisite for such persons to be highly skilled, knowledgeable and well trained [2] as the diagnosis process can be relatively onerous. The challenges inherent to the diagnosis process are even more evident when considering FD of machines with multiple bearings, say a multi-stage turbo-generator; as a number of vibration measurements are required at each bearing location [1]. This results in the acquisition of large volumes of data which become a burden to extract useful information (features) that best represent machinery health [53, 54]. Even after successful extraction, fault features may be indistinguishable and misleading [3], which may resort in increased subjectivity in the interpretation of diagnostic information. Inherently, because of such difficulties, the FD process can be lengthy and erroneous. As such, various researches have been done in gaining a better understanding of the interpretation of the dynamic response of commonly encountered rotating machinery faults in the amplitude spectrum, such as: crack [3-6, 55], looseness [7, 8], misalignment [3, 6, 8, 9, 55], rub [10, 56] and unbalance [8, 11].

It is common knowledge that there still exists equivocality and general lack of confidence in the interpretation of the spectral features of common faults such as crack compared to misalignment [3, 55, 57], and bow compared to added unbalance. Interestingly, it was noted that experimental studies on misalignment [6] and rotor bow is lacking. There also still exist challenges with the diagnosis of rub. Consequently, it has been accepted that the simple spectra on its own may not be adequate for confident FD and might require insight from additional techniques, such as the orbit plot [12].

2.6.2 Orbit plot analysis

The orbit plot is a two dimensional representation of the dynamic motion of the centre of a rotating shaft at a measurement plane [53]. It presents a snapshot of the rotor actual motion at its centre [58]. Proper interpretation of the orbital paths or rotor lateral motion (rotor orbital and its direction) provides insight into the nature of the machinery fault [58] and the forcing functions acting on a shaft [53].

Since its introduction more than forty years ago [59] the orbit plot has been utilised in theoretical studies aimed at gathering insight to the nature of different rotor fault conditions such as: bow [60-62], crack [60, 63-71], looseness [72, 73], misalignment [74-76], rub [61, 62, 68, 72, 75, 77-80] and unbalance [61, 67, 69, 75]. Though these theoretical studies have been highly relevant to revealing the intricate nature of machinery faults, it was generally observed that they are often attempted with several assumptions and simplifications that may produce results or features that may not be observed in practice [3, 69].

It is therefore apparent that the validation of theoretical models with experimental or practical field acquired results is important [58, 59]. Both theoretical and experimental studies should co-exist in a continuously improving symbiotic relationship in order to advance the knowledge of the nature of failures and the understanding of diagnostic tools. Relatively lesser experimental works have been attempted than theoretical ones. Compared to the simple spectra, orbit plots have had fewer applications in literature, and as such a brief but comprehensive review of literature is provided on experiments relevant to the current study in which orbit plots were applied.

In an attempt to characterize the presence of a crack on an overhung rotor, Adewusi and Al-Bedoor [81] extracted different vibration features from different techniques including the orbit plot analysis. During crack propagation at a steady-state speed, the rotor tracked a smooth inner looped orbit which became distorted, due to wobbling, on increasing the bending moment acting on the overhung rotor. Both Darpe et al. [63] and Sinou [4] identified a similar inner looped orbit which changes size around half of the first critical speed for a transverse crack due to the presence of a dominant second harmonic [63]. While Darpe et al. [63] used experiments to validate results obtained from the analysis of a Jeffcott rotor passing through subcritical resonances with a transverse breathing crack, Sinou [4] presented a complete experimental study on slotted rotors that represented rotors with open cracks. Darpe et al. [63] concluded that the change of orientation of the inner looped orbit on passing through “subcritical resonances” could be a crack diagnostic indicator. Sinou [4] added that the inner loop size is proportional to slot depth.

Lee and Lee [74] validated a theoretical model for a misaligned rotor bearing system at different steady-state speeds near the first critical speed of a laboratory test rig supported

by ball bearings. It was shown that with increasing angular misalignment, the orbit tends to collapse from a circular shape to an ellipse; due to an increase in the anisotropic nature of the bearing stiffness. The major axis of this ellipse was perpendicular to the misalignment direction below the critical speed, but was aligned to the misalignment direction after passing through the critical speed (that is, a 90^0 rotating of the elliptical orbit). The orbits for parallel misalignment were, however, unperturbed relative to the healthy orbit due to the effect of a very flexible coupling element. Similarly, Pennacchi and Vania [82] also reported a collapsed $1\times$ filtered orbit for an angular coupling misalignment case on a real turbo-generator train. The fault symptoms were analysed on a real machine and then modelled and experimentally verified for identification. Both Lee and Lee [74] and Pennacchi and Vania [82] conducted experiments in the vicinity of the first critical speed of a small experimental rig. One fundamental difference was the type of bearings used - Lee and Lee [74] employed deep grooved ball bearings, whereas Pennacchi and Vania [82] used lemon shaped oil-film bearings. Interestingly, Pennacchi and Vania [82] concluded that their observations were even applicable to machines supported by ball bearings, but was exacerbated for machines on oil-film journal bearings.

Patel and Darpe [3] conducted experiments to study the whirl nature of higher frequency components of the vibration response due to coupling misalignment at or near different “sub-harmonic resonances”. It was noted that regardless of the type of misalignment, rotor orbits are stretched in the direction of the plane of the misalignment due to an increase in the effective stiffness, and consequent suppression of vibration response, in the direction perpendicular to the plane of the misalignment. It was further added that rotors with angular misalignment reveal outer loops, whereas those from parallel misalignment might exhibit inner looped orbits. Further to this, with the aim of identifying features which are better able to discriminate faults with similar spectral features; such as crack and misalignment, Patel and Darpe [55] presented experimental investigations on crack, misalignment and rub from steady-state vibration response at sub-critical rotational speeds. The results show that misalignment generates a backward whirling outer loop orbit which is stretched in the direction orthogonal to the misalignment direction as compared to forward whirling inner loop of a crack. The direction of the orbit stretch was consistent with earlier findings [3].

With the intent to ascertain which pattern of vibrations represents steady-state processes and to identify what are the most sensitive parameters affecting changes in said steady-state regions, Muszynska and Goldman [72] examined the dynamic behaviour of unbalanced rotor bearing systems with a loose bearing pedestal or rotor-stator rubs using different experimental rigs, respectively. Results from a local impact model were compared to results from experiments that were presented in the orbit plot, amongst others, to mainly provide insight to the dynamics of rotor-stator rub. It was observed that at higher machines speeds during partial rotor-stator rubbing, orbits contain distinct reverse-procession loops due to the rub-related tangential force which opposes the direction of rotation. It was also shown that the rotor support anisotropy resulted in a “butterfly” (sideways 8) effect for a rotor operating at twice its first balance resonance speed under the influence of a partial rub.

The nature of rotor/seal full annular rub was demonstrated with orbit plots by Yu et al. [77], which conducted experiments on a brass bushing “annular rub test rig”. The authors made a clear distinction between reverse precession full annular rub, which had a very smooth orbital pattern and “multicontact intermittent rub” which had a “bounce pattern”. The difference in the mentioned rub patterns depended on friction between contacting surfaces during the rub. Aided by tracking the evolution of the orbit around the first natural frequency, it was concluded that reverse precession (dry whip) can occur without external disturbances for small rotor/seal clearances.

Chu and Lu [10] explored the dynamic effects of partial and full rotor-stator rub on a small experimental rig in order to aid rub fault diagnosis. The authors were able to correlate the different types of rubs with the different rotor orbits from responses that contained $\frac{1}{2}$ and $\frac{1}{3}$ fractional harmonics as well as super harmonic components. Pennacchi et al. [79] analysed the effects of light rub between rotor and seal strips by comparing experimental results with simulations from a mathematical model. At both sub-critical and super-critical speeds, it was noted that the shape of the rotor orbit is strongly dependent on the interference between the seal and rotor. Cong et al. [83] validated an earlier proposed rub-impact model with experimental work on small rig that was instrumented with a pair of orthogonally mounted eddy current probes. Testing was done at four different rotating speeds; two subcritical and two supercritical and at different damping ratios. Orbit plots were employed to observe the damping ratio with the first critical speed and the severity of

rub with changing speed ratio. The key among several observations made is that the severity of rub impact fault becomes low with increasing speed ratio; where the orbit transforms from an irregular shape to an ellipse.

Evidently the orbit plot analysis has been well applied to rotor fault analysis especially for crack and rub fault investigations, however, it has been applied to only a few faults on machines. Indeed, the Bently Nevada Research Corporation provided highly relevant articles in which the orbit analysis was applied to a myriad of fault conditions, but these were based on observations from different industrial case studies and experiments on several different machines [12, 84, 85]. Additionally, Muszynska [58] comprehensively reviewed a variety of rotating machinery malfunctions that were illustrated by orbital patterns, but again these were based on different experiments and actual field data from different machines. Hou et al. [86] demonstrated a shaft orbit denoising technique with unbalance, coupling misalignment rubbing and crack data; as seen in previous studies, the former two were from a laboratory rig and the latter two were from industrial cases.

2.6.3 Overview of standard practices

Despite the usefulness in observing rotor orbits for revealing the dynamic responses of rotors when influenced by different conditions, it was generally noticed that, like the simple amplitude spectra, orbit plots can be equivocal in nature and might not provide additional insight [13]. Thus, attempts at diagnosis would require additional phase measurement [87, 88] and advanced techniques [31]. This is likely to cause costly delays to the diagnosis process. Hence, experimental research efforts aimed at methods focused on getting the data flow process complete in the shortest time possible while preserving or increasing the confidence in diagnosis and the affordability of the approach relative to standard practice are warranted.

2.7 Research on alternative methods to standard practices

Focus is given in the current section to experimental research aimed at improving condition monitoring techniques or proposing new techniques. The work done can generally be categorised into three focus groups which are aligned to the last three steps in the condition monitoring flow process (see Figure 2.3) [51], namely: data input (sensors and measurement) [15-18, 28], data manipulation (signal processing) [21-23, 89], and health assessment (diagnosis by expert) [24-26, 28, 29].

2.7.1 Data acquisition

2.7.1.1 *Wireless sensors*

Hashemian [16] demonstrated the usefulness of wireless vibration sensors for remote condition monitoring of rotating equipment on a research nuclear facility. The biggest benefit was of course remote access to equipment which would have otherwise been unsafe for manual data collection. Similarly, Arebi et al. [15] compared wireless sensors with three commonly used sensors; a laser vibrometer, an accelerometer and an encoder. These were used to measure and compare their respective responses in the time and frequency domain on a misalignment condition to test the performance a wireless measurement scheme. It was found, amongst other things, that “the wireless sensor produces a full separation of levels and shows a unique increasing trend with speed.” Though, useful for remote access of machinery with clear benefits for increased safety condition monitoring technicians, the use of wireless sensors does not mitigate the aforementioned difficulties associated with standard practice in vibration-based fault diagnosis.

2.7.1.2 *Micro Electro Mechanical Systems (MEMS)*

Elnady et al. [17] proposed the use of the on-shaft vibration (OSV) measurement technique using a Micro Electro Mechanical System (MEMS) accelerometer with a

wireless node for data transmission. The objective of the study was to bypass the need for a number of on-bearing vibration (OBV) sensors at each bearing location by using a single on-shaft sensor during vibration analysis. Experiments were conducted on a small laboratory rig considering added unbalance, looseness and misalignment fault cases with reference to a baseline healthy case. OBV measurements were also acquired for comparison. Various common machinery vibration health indicators were computed from both OSV and OBV data and input to a pattern recognition-based classifier. It was found that the OSV approach had improved classification accuracy to the OBV method, but it was noted that requires special arrangement of the measurement instrumentation that currently may not be applicable in a practical sense.

2.7.1.3 Multi-sensor fusion

Jiang et al. [18] suggested that for a complex system, a single sensor is incapable of collecting data requisite for accurate fault diagnosis, and as such, “multiple sensors are “needed in order to do a better job” and when applied simultaneously are better able to comprehensively describe a machine state.

Temperature was identified as a possible parameter to be combined with vibration because of studies confirming its sensitivity to common rotor faults. Sanderson cited by Sabnavis [90] outlined a large temperature change from rotor bore to surface amongst the symptoms observed for a propagating crack in a 935 MW turbo-generator. The heat generated from the crack was significant enough to cause bending of the shaft. Crack depth reached 25% of shaft diameter before its presence was confirmed and there existed a large temperature gradient within the rotor from bore to surface. Gaberson [91] contested claims from alignment instrumentation manufacturers that misalignment accounts for as much as 15% of the energy losses in rotating machinery. It was observed that with misalignment causing 2% energy losses, a significant temperature rise of the coupling was measured. It was also observed that energy losses were dependent on coupling type. Contrary to alignment instrumentation manufacturers claims, it was found that gross misalignment and unbalance cause less than 3% and 1% energy losses, respectively. Kelch and Grover [92] also looked into heat generation in couplings. Flexible couplings were assessed and it was found that coupling temperature was proportional to misalignment. The findings of both

studies have implications on the dynamic loading of rotating machinery shaft and bearings during misalignment. Considerable focus has been given to the thermal analysis of rotor to stator rub, particular due to its high incidence in turbo machinery. However, most of these have been model based where an attempt is made to simulate the rub incident and subsequent thermal bending of rotor [93-95].

Therefore, with studies confirming the sensitivity of temperature to rotating machinery faults and the wide availability of temperature monitoring systems on rotating machines in industries, an opportunity exists to integrate temperature and vibration data for effective FD. Nembhard [20] compared overall vibration r.m.s. amplitudes with bearing steady-state temperature for numerous rotor faults and was able to fuse vibration and temperature with encouraging results. However, it has been noted that the fusion method used was not robust and thus a fundamental challenge for fusion of different sensors has been to create a fusion technique that is simple but adequately robust for practical application. Notwithstanding, the results achieved by Nembhard [20] suggest an opportunity still exists for vibration-temperature sensor fusion for effective FD.

2.7.2 Data manipulation

2.7.2.1 Time-frequency analyses

Numerous studies have focused on developing relatively new data manipulation techniques such as time-frequency analyses [21-23]. Even with over 20 years of development and promising results thus far, there still exist various difficulties with the practical application of the widely studied time-frequency analysis methods to machine FD as noted by Feng et al. [21] in a fairly current review and comparison of twenty different time- frequency techniques who stated that a consistent limitation of these techniques is their “high computational complexity” amongst other significant things [21, 23]. Qin et al. [89] proposed a technique which focused on multicomponent vibration signal separation. The objective was to introduce a method that could accurately extract features that would be useful for FD. Though it was posited that the proposed method had better accuracy than

some established time frequency techniques, it was noted that the method is slow and in need of future development.

2.7.2.2 *Empirical Mode Decomposition (EMD) and Wavelet Analysis*

Lei et al. [22] compiled a comprehensive review of application of the advanced time-frequency analysis technique, Empirical Mode Decomposition (EMD). The review outlined the suitability of the method over the FFT for the diagnosis of rotating machinery faults when signals are non-stationary and especially for rotor-related faults when vibration data are acquired in displacement. The method, however, does not do well with signals obtained from accelerometers which are usually noisy, hence why it was suggested that wavelets could be more appropriate in that case. Then again, it was also cited that wavelets are susceptible to subjective judgement as the analysis results are dependent on the choice of wavelet base function. An ill-selected wavelet basis function that does not match the signal structure may yield misleading diagnosis [21]. For such reasons amongst others, Yan et al. [23] conceded in a review of common wavelet techniques that “there still exist some challenges in using wavelets for rotary machine diagnosis”. Conversely, EMD mitigates this limitation by being a self-adaptive processing technique. Notwithstanding, the EMD method has its share of limitations, including difficulty in accurately reproducing intermittent signals. As such various improved derivations of EMD or combinations of EMD with other processing techniques have been proposed to overcome such limitations. These improvements are, however, “time consuming” which limits its applicability in practical scenarios.

2.7.3 **Health assessment**

2.7.3.1 *Artificial Intelligence-based techniques*

Considerable research has been done on the application of artificial intelligence (AI) techniques such Neural Networks and Fuzzy Logic to circumvent the human dependence in traditional diagnosis by fully automating vibration-based FD in the health assessment

process [24]. Consequently, this would minimize VCM's dependence on human elements and improve its processing capabilities. However, AI-based methods can be somewhat digressed from current practical applications, because of their limited diagnosis capabilities when used as an "individual decision system with a single classifier" [26]. Attempts to overcome these limitations, namely the combination of multiple classifiers for fault diagnosis (FD) [26, 27], often times lead to methods with added complexity. Though, AI-based systems have shown promise for automating vibration signal analysis [25], its application is still in the nascent stages and needs further development. On an advanced level to automated diagnosis, there exist Prognostic and Health Management (PHM) techniques. These techniques can be treated as a future-based evolution of Condition-based Maintenance (CBM) that emphasizes a maintenance methodology of predict-and-prevent; as opposed to the traditional fail-and-fix (also referred to as diagnostics), while still relying on the said traditional diagnostic techniques for data input [30]. It is therefore implicit that given the current need for development in CBM practices, the reliable implementation of PHM techniques may be somewhat protracted. Thus, a more simple, but robust technique that would be well appreciated by the relevant industries for practical application is required.

2.7.3.2 *Data fusion*

Other researchers have directed efforts that address combined improvements in data input, data manipulation and health assessment with data fusion techniques. Sinha and Elbhbah [28] suggested fusion of data from all sensors in the frequency domain for the extraction of useful diagnostic features, while avoiding the difficulties associated with standard techniques. The Higher Order Spectra (HOS), namely bispectrum, which is derived from a composite spectrum, was demonstrated. It was postulated that the HOS would facilitate sensor reduction (as only one sensor per bearing was required) and utilisation of computational power in current signal processing to compensate for sensor reduction and data fusion. By exploring the relations of different harmonics of the same signal measured at a bearing pedestal, the authors were able to obtain unique features for the conditions tested. Elbhbah and Sinha [29] later explored the usefulness of the coherent and non-coherent composite spectra for data fusion of on-bearing vibration data for fault discrimination and observed that the coherent composite spectra were better able to

discriminate between the faults tested. In both studies, it was similarly concluded that the suggested methods had the potential for practical application, but the methods were computationally involved.

Jiang et al. [18] proposed a multi-sensor feature-level fusion methodology with subsequent Support Vector Machine (SVM) classification of time domain vibration features for the diagnosis of rotating machinery faults including rotor crack. The technique was demonstrated on a small laboratory rig with crack fault amongst others. Though promising, since there is no standard method for choosing the kernel function [30], which is the key process for SVM, the choice of the kernel function used here, and by extension the results obtained, is questionable.

2.7.3.3 *Pattern recognition*

Some researchers [96-99] have chosen to explore the use of pattern recognition techniques such as Principal Component Analysis (PCA) for FD. Of the non-model-based techniques available including knowledge-based systems, pattern recognition and artificial neural networks, to name a few, pattern recognition is desirable because it provides a relatively simple and systematic approach to acquiring knowledge from fault samples and fundamentally, mechanical fault diagnosis is a problem of pattern recognition [38, 39]. PCA's use in vibration-based fault diagnosis is based on the premise that it relaxes the computational load by condensing the number of inputs required for effective classification to a representative few, thereby removing any redundant or contradictory information. The extracted features are usually fed into a classification tool. Malhi and Gao [96] successfully used a Neural Network classifier, with features including those from the wavelet domain, which, however, made the results questionable. Researchers have even coupled PCA with multiple classifiers [26, 27]), on the basis that a single classifier is not suitable for real life applications [26]. However, this usually adds to the computational rigor of the method and may also be somewhat removed from practical application [26].

However, some studies have had success with its application. Baydar et al. [100] investigated the use of PCA on small localized helical gear fault detection in a two-stage industrial helical gearbox. It was noted that conventional gear fault detection techniques

did not provide adequate information about the fault, such as location and severity, and thus the objective of the study was to propose a technique that was sensitive to and descriptive of gear faults. Experiments were conducted using a small gearbox from which vibration measurements were acquired incrementally for conditions ranging from healthy to a single gear tooth with 50% wear. It was concluded that the PCA-based approach used was capable of detecting severe faults as well as early stage growing faults and as such, can be used as a “powerful tool for fault detection in rotating machinery”.

Li et al. [38] proposed a gear fault classification technique based on pattern recognition by PCA. On-bearing vibration acceleration measurements were taken from an automobile gearbox during three progressive states; from normal healthy, to cracked gear tooth to said cracked tooth propagating to broken tooth. Commonly used machine condition indicators or features were computed from the measured data for each state and input to the PCA tool for processing. The output of the PCA-based technique was a two dimensional (2D) diagrammatical representation, which had three isolated clusters representing the machine states, which formed the basis for a condition recognition method. Importantly, it was noted that the choice of PCA for the study was due to its straightforward interpretation and relatively moderate computational burden for real time machine condition monitoring. He et al. [97] proposed a method similar to Li et al. [38] for automobile transmission gearbox monitoring with a 2D representation of variables, but with different features applied. Experiments were done for three different wear stages. Both studies [38, 97] showed that on their own the features used were not capable of discriminating the different gearbox states, but when processed by PCA and combined as new variables called principal components (PCs), they would be capable of identifying the gearbox condition with high sensitivity and regularity. The studies equally concluded that the proposed method was capable of effectively diagnosing industrial gearbox defects. However, effectiveness is dependent on the set of features selected.

Pirra et al. [98] introduced a PCA-based monitoring technique for the diagnosis of rolling element bearing faults. The objective of the study was to couple PCA's damage detection prowess to its success in removing the influence of environmental conditions on vibration features for bearing FD. Testing was performed on different experimental rigs at different speeds with varying inner race and element faults referenced to a healthy

condition. Statistical parameters were computed from vibration data measured using tri-axial accelerometers and input to a PCA algorithm to produce a global index for trending in the proposed technique. It was observed that the proposed method was able to correctly detect, classify and localise different levels of the same fault. It was also cited that the method overcomes the problem of acquiring data under different environmental conditions without needing separate measurement and biasing the data, because environmental factors are accounted as embedded variables. Liying et al. [99] had similar observations to Pirra et al. [98].

Therefore, the encouraging observations made in the aforementioned studies [38, 97-100] testify to the opportunity which exist in using PCA as a simple but robust tool for the diagnosis of rotating machinery rotor or shaft-related faults, which is currently unprecedented. Pattern recognition techniques are classified as data driven, thereby requiring independent data history of “a relatively large number of identified fault and non-fault samples” [40]. As previously mentioned, standard FD with the simple spectrum on a multi-stage turbine already requires copious amounts of data. Therefore, attempts at FD with a pattern recognition approach would seemingly have, at best, an equally demanding data requirement. Needless to say, any attempt at a viable data driven technique requires a feasible method to mitigate the need for large vibration data history without compromising diagnosis confidence.

Current practices limit vibration data to a single machine because of the effect of machinery dynamics on system response. As represented in Figure 2.5, it is possible that the same design or model rotating machine when installed at different plant sites have different foundations with different natural frequencies and the vibration data history requisite for condition monitoring may exist at one site and be lacking in the other. Therefore, if sharing of vibration data between similar machines was possible, the need for different large data histories unique to a machine would be mitigated or eliminated. Based on observations made by Pirra et al. [98] in PCA’s ability to negate environmental effects on measured vibration data, an opportunity exists to make sharing of data possible. This has not been previously attempted.

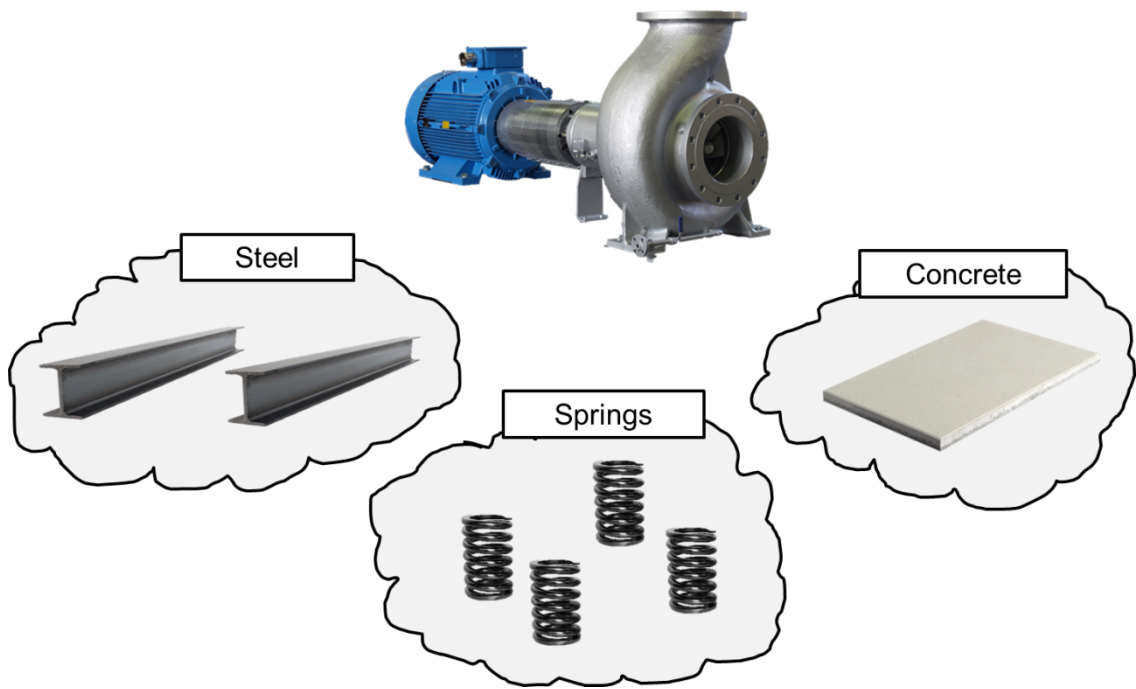


Figure 2.5 One machine with possibilities for different foundation set up which results in different dynamic characteristics including different natural frequencies.

2.8 Vibration-based fault diagnosis for transient operation

On complex rotating machines like aero-engines, where speeds constantly change under normal operating conditions, performing VCM during constant speed is a fundamental challenge. It is recommended that machine speed remain constant when conducting vibration-based condition monitoring (VCM) of rotating machinery. Typically, during the VCM process, diagnostic features are extracted at a particular speed and compared to a healthy (baseline) feature previously generated at the same speed. This is necessary because features may be sensitive to machine speeds and changes in these relative to the baseline could signify the presence of a fault. Thus, it is imperative to ascertain whether a change in the feature is due to a fault or speed fluctuations by mitigating the effects of any speed fluctuations [31].

Current practice shows the selection of data in the most steady state condition available; say during idle or cruising [34], but accurate fault diagnosis (FD) are not guaranteed, since fault signals are oftentimes fleeting and replete with noise [101]. Normalization of

diagnostic features with respect to speed is also often employed, but this can be complex and usually leads to less accurate or less robust fault detection [34]. In a review of aircraft engine health monitoring systems, Tumer and Bajwa [102] cited that tools which better discriminate engine healthy from faulty states using the wealth of data available from existing aero-engine management systems are lacking. More recently, to bridge this gap, numerous works have been done on improving aero-engine vibration-based FD [14, 35-37]. These, however, still remain somewhat digressed from the current needs of industry [14].

Of the readily accessible literature, few researchers have sought to develop methods that are applicable during transient operations. Barragan [32] proposed a vibration monitoring system (VMS) that processes data acquired during engine acceleration and deceleration for the diagnosis of unbalance and misalignment faults. Fault detection was achieved by comparing “vibration patterns” from several selected indicators generated in time waveform and waterfall diagrams to a library of known patterns of engine faults. The method relies on a Finite Element Model for FD. Thus, the method may not be robust; since it is widely held that generating a FE model which accurately reflects the true dynamics of a machine for confident FD is difficult. Modgil et al. [103] suggested an advanced vibration diagnostic system for engine test cells which sampled data from engine idle to full power.

Similar to Barragan [32], FD was achieved predominantly with Waterfall diagrams of a spectrum. VCM techniques based on transient operations are good during aircraft landing and takeoff, but efforts based on the waterfall diagrams group data generated in the amplitude spectra at different speeds with diagnosis being based at a single speed, which may not be useful in continuously changing speed conditions. On a slightly different note, Grabill et al. [33] developed an advanced airborne Turbine Engine Diagnostic System (aTEDS) for the C17/F117 aero engines. The system automatically triggered vibration data collection and processing during acceleration, deceleration and steady state speeds for the diagnosis of a comprehensive list of faults. Though the systems was intelligent, its FD capabilities were predominantly based on normalization of time domain features at a single speed and on features extracted from the amplitude spectra, both of which do not guarantee accurate fault detection [34]. Despite the promising developments of efforts based on transient operations, the fundamental techniques used for processing of data may

not be useful during continuous operations with varying speeds. Hence, a technique which is insensitive to changing speeds is warranted.

2.9 Simple mathematical modelling in vibration-based fault diagnosis

In the development of new techniques, it is useful to conduct theoretical simulations to test the utility of the approach and possibly to garner a greater appreciation of the dynamics of faults encountered. It has been noted that theoretical analyses are not trivial and require much time and diligence. However, in the pursuit of experimental development of a technique within a research context there has to be some balance between time devoted to experimental work and theoretical work. In the pursuit of adequate balance between the two, it often becomes necessary to select an appropriate modelling technique that allows sufficient time for the development of the experimental process. The Finite Element Method (FEM) is currently the staple method for the theoretical exploration of the dynamic effects of different faults on rotating machinery [14, 57, 65, 76, 104, 105]. However, FEM is undoubtedly intricate and there are instances, such as an initial theoretical investigation of a newly proposed FD technique, in which a simple mathematical model may be preferred. The Jeffcott rotor is the simplest mathematical for understanding the dynamic behaviour of rotating machines under different conditions [106]. One of the earliest accounts of the use of the Jeffcott rotor for rotor fault investigation was provided by Jeffcott [107] who investigated the dynamics of an unbalanced shaft. Since then, it has been applied in numerous vibration-related studies with literature accounting extensively for studies on cracks and rotor-stator rub and to a lesser extent other faults.

Jun et al. [108] applied a Jeffcott rotor to identify the characteristics of a breathing crack, which opens and closes. Using fracture mechanics it was concluded that the switching crack model with bi-level direct stiffness was mathematically simple, but physically sensible when the rotor operated well below the second bending critical speed. Gasch [66] studied the dynamic behaviour of a transverse crack on a Laval rotor that was modelled like a low pressure turbine with weight dominance. Time dependent stiffness variations were based on the hinge model. It was suggested that trend analysis from

permanent monitoring would prove helpful to early crack detection. In contrast, Cheng et al. [109] analysed the dynamic response of a Jeffcott rotor with a breathing crack sans the typical weight dominance assumption. Simulations were run near the system's critical speed and shaft breathing was expressed a function of the whirling of the rotor. It was observed that the response of a cracked rotor near its critical speed is similar to those of a healthy rotor. Patel and Darpe [68] cautioned the use of the switching crack model to predict the vibration response of a cracked rotor with deeper cracks. It was found that unbalance phase, unbalance level, crack depth and system damping have significant effect on the vibration response of the rotor with switching crack but have no influence on the rotor with breathing crack. However, Penny and Friswell [110] provided comparisons of the responses of a simple Jeffcott rotor with three different crack models (the hinge model, the Mayes model, and the model of Jun et al.) and suggested that the differences in the models would be negligible in a crack identification scheme.

Chu and Zhang [111] used a Jeffcott rotor to examine the nature of rotor-stator rub. Equations of motions of the system were developed and solved via Runge Kutta integration. It was observed that the rub feature transitioned to three different routes to chaos on increasing rotating speeds. Similarly, Lin et al. [112] was able to study the behaviour of rub-related vibrations with numerical simulations on a Jeffcott rotor model in order to "reveal the nonlinear mechanisms" underlying the chaotic phenomena previously observed in works such as Chu and Zhang [111]. Though simplified, the model was able to capture the rich dynamics of a rotor system rubbing its housing. It was found that there exist threshold values for rotor-stator clearance and friction coefficient above which the bouncing phenomena would not be experienced. It was also suggested that the results of the simulations from such a simple model can be useful for the development of sensitive machinery diagnostic techniques. Just over a decade ago, Redmond and Al-Hussain [113] and Al-Hussain and Redmond [114] bemoaned the lack of requisite theoretical studies with thorough treatment of the nature of misalignment using "suitably representative models". Consequently, a coupled twin Jeffcott rotor model was similarly offered by Redmond and Al-Hussain [113] and Al-Hussain and Redmond [114] to provide insight to the dynamic behaviour of machines with coupling misalignment and residual unbalance. The former [113] explored a flexible coupled rotor model, while the latter [114] investigated a rigidly coupled set up. Both studies considered only pure parallel misalignment and solved the system's equations with the Newmark-Beta method of integration. Redmond and Al-

Hussain [113] found that the presence of misalignment caused a radial preload in the rotor system which modified the system vibration amplitude and phase characteristics. More interestingly, Al-Hussain and Redmond [114] did observe the customary $2\times$ harmonic component in the rigidly coupled system response, therefore leading to the conclusion that other system properties including rotor asymmetry and in some cases coupling kinematics are the sources of higher harmonics in misalignment response.

Though it is indicated that the Jeffcott model is too simple and limited to a qualitative understanding of the machine state which does not concur to “real life conditions” [105], the literature reviewed here made observations somewhat contrary to such claims; as the Jeffcott rotor model enabled adequate representation of the fundamental dynamics of rotating machinery under different fault conditions.

2.10 Summary

Numerous studies have attempted to improve knowledge of FD with the simple spectra, but its interpretation remains equivocal. As such, the orbit plot analysis is used to aid diagnosis. Though useful for visualising machinery response with faults, orbit analysis can also be inconclusive. Consequently, several studies attempted alternatives to standard practices, but as promising as they may be, the resulting methods have been complex. Similarly, studies that have attempted methods applicable to transient operations have proven less than accurate or too intricate for real life application. Of the methods perused, pattern recognition methods appeared most promising. However, this has not been attempted for rotor or shaft-related FD. Any attempt at FD with pattern recognition requires a feasible method to mitigate the need for large vibration data history without compromising diagnosis confidence. Current practices limit vibration data to a single machine, but if sharing of data between similar machines were possible, this would mitigate the need for various relatively large sets of unique data history. From readily available literature, this has not been encountered. Hence, a study that proposes a simple but robust FD approach which addresses the aforementioned issues and gaps in standard practices is warranted.

3 EXPERIMENTAL APPROACH

3.1 Introduction

The experimental set up used and experiments conducted in the present study are briefly introduced in this chapter. Complete descriptions of the rig and experiments are provided in subsequent chapters.

3.2 Experimental set up

Three different rig configurations were used in the study; relatively rigid, relatively flexible with 10 mm diameter supports (FS1) and relatively flexible supports with 6 mm diameter (FS2). A brief description of the dynamic characteristics of each set up, rig layout and instrumentation used is presented in this section. The experimental rig used in the current study was previously used by Nembhard [20] and Elbhbah and Sinha [29].

3.2.1 Rigid support

3.2.1.1 Mechanical layout

The experimental rig with rigid supports and the rig's main dimensions are presented in Figures 3.1 and 3.2, respectively. The set up consists of two 20 mm nominal diameter dissimilar length (1000 mm and 500 mm) rigidly coupled (Coupling 2) shafts (or rotors) that are supported by four grease lubricated ball bearings. These are secured atop flexible steel pedestals that are bolted to a large lathe bed secured to the concrete flooring. Machined sections accommodating balancing discs are mounted on each rotor. System drive is provided by a 0.75kW, 3 phase, 3000 rev/min motor that is mated to the rotor-bearing system via a semi-flexible coupling (Coupling 1). The current rig set up with two rigidly coupled shafts was used to represent the real life case of a turbine, which has different stages that are rigidly coupled. Using the impulse-response method of modal testing, by appearance the first three natural frequencies of the rig are 68 Hz, 144 Hz and 352.5 Hz [29].

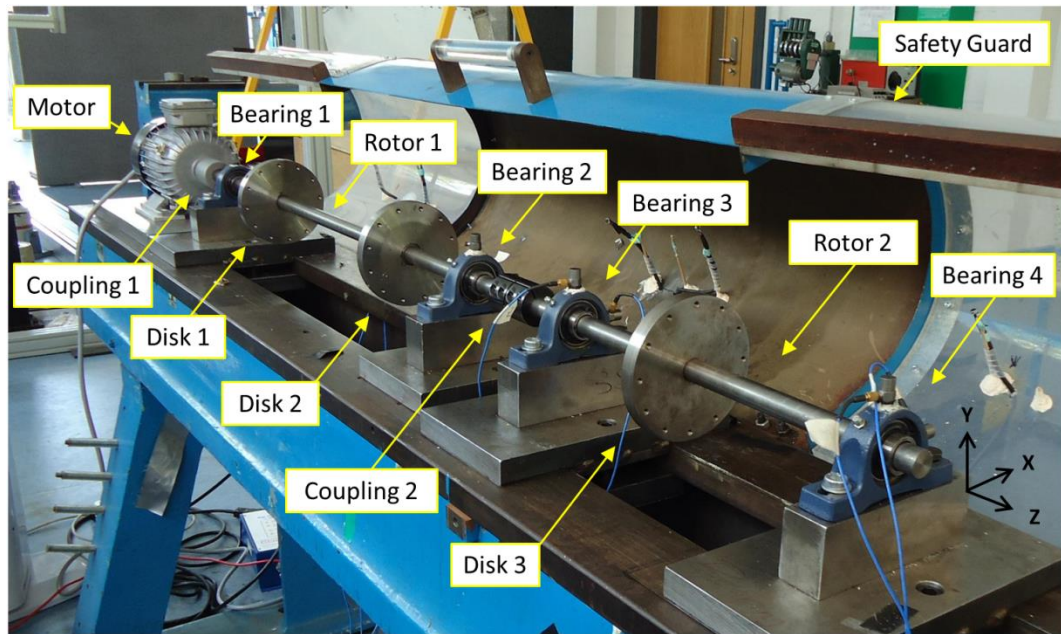


Figure 3.1 Experimental rig mechanical layout with relatively rigid supports [20]

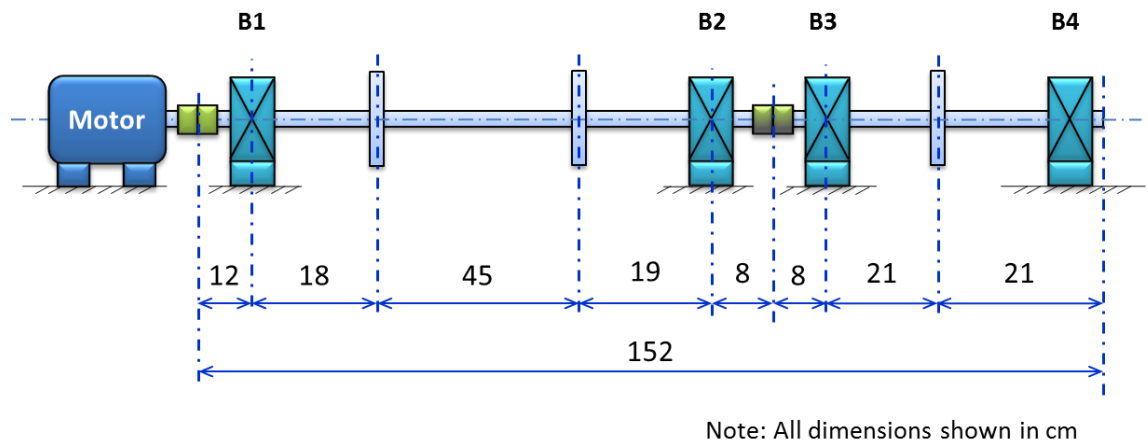


Figure 3.2 Experimental Rig with relatively rigid supports major dimensions

3.2.1.2 Instrumentation

The instrumentation and software schematic for the set-up is depicted in Figure 3.3. Rig speed is varied with a speed controller that is operated from a personal computer. The dynamic response of the system is then measured with 100 mV/g accelerometers. Each bearing location has two accelerometers that are mounted with adhesive in mutually perpendicular directions. The vibration data are transmitted through two four channel

signal conditioners to a 16 Bit Analogue to Digital (A/D) DAQ System. Data logging software then stores the digitized vibration data on the personal computer.

In order to measure the thermal response of the system, K-type Picotech (Model: SE030) thermocouples are attached, with Bluetaq, between the bearing casing and outside of outer bearing race to each bearing location. All four temperature readings were captured with Picotech (Model: TC-08) eight channel data logger and saved to the computer using PicoLog Recorder data logging software for subsequent analysis.

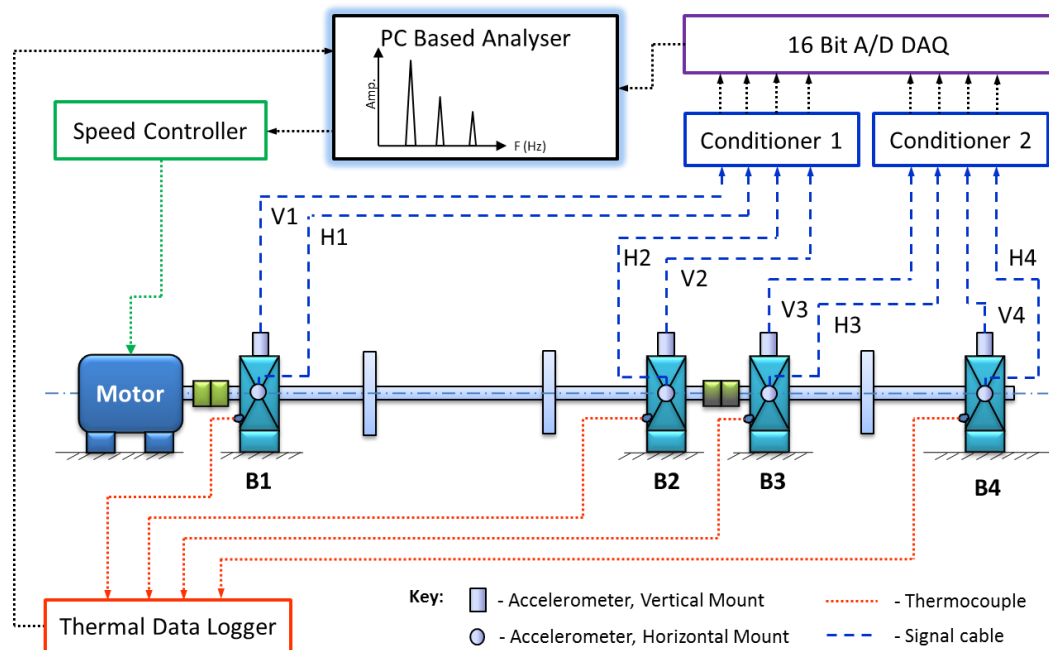


Figure 3.3 Schematic of software and instrumentation used in the experiment for the rigid support

3.2.2 Flexible support

3.2.2.1 Mechanical layout

Figure 3.4 shows the mechanical set up for the flexible supports in The Dynamics Laboratory at the University of Manchester, UK. Rig dimensions are provided in Figure 3.5. It can be seen that the general configuration of the rig is preserved from the rigid set up. The rig consists of the same 20 mm nominal diameter shafts dissimilar length shafts of

1000 mm (Rotor 1) and 500 mm (Rotor 2). Couplings (both semi-flexible and rigid) and balance discs are identical to those used in the rigid support described in the previous section.

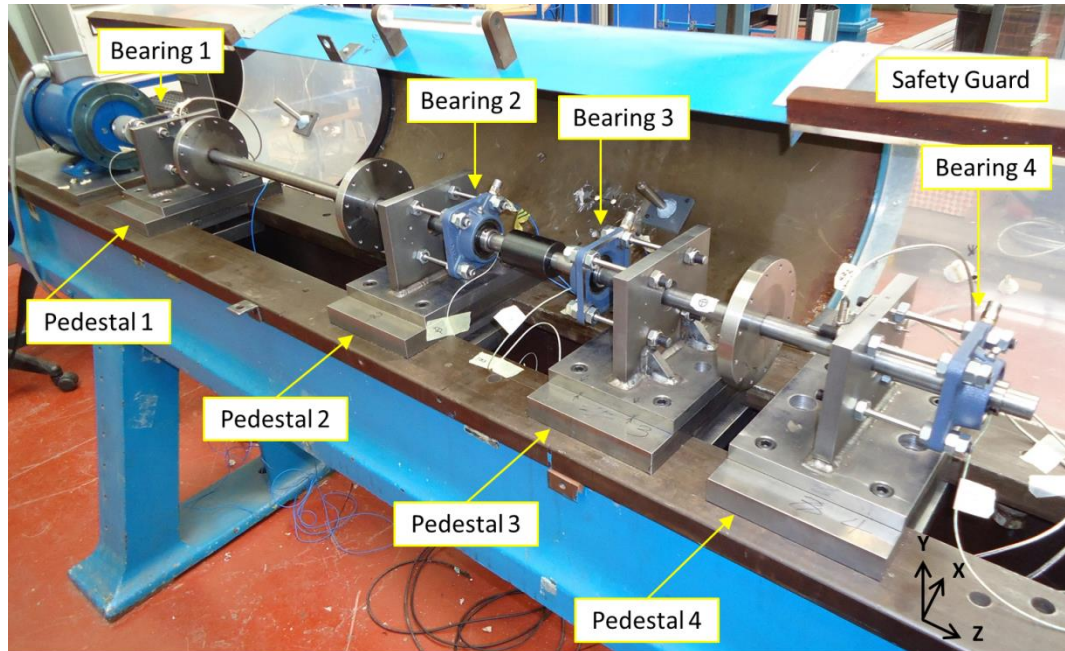


Figure 3.4 Mechanical layout of experimental rig with relatively flexible supports

However, the electrical motor and bearing pedestals were changed. System drive in this set up is provided by a 3 phase 3000 rev/min 0.70 kW (down from 0.75 kW in rigid assembly) AC motor. The frame of the motor used in the previous set up is almost identical to the current set up. The major change in the assembly is the reconfiguration of the bearings and bearing support type (see Figure 3.6). The bearings shown are grease lubricated SKF FY 20 TF flanged bearings. Details of the main components on the rig are summarized in Table 3.1.

Each bearing is mounted at its corners, in a “floating set up”, by four flexible machined steel rods that are secured to the flexible mild steel bearing pedestals. Like the rigid support, each bearing pedestal is bolted to the relatively high mass steel lathe bed that serves as the rig’s foundation. The flexible machined steel rods combined with the steel pedestals act as the overall bearing supports and are thus referred to in the present study as “Flexible Supports”. Two different sets of flexible supports, Flexible Support 1 (FS1) and

Flexible Support 2 (FS2), consisting of machined steel rods of 10 mm and 6 mm diameter, respectively were investigated. In most real machines, the foundations appear stiff, but due to the mass of the rotor the dynamic stiffness of the complete system becomes low and the complete machine generally has a number of critical speeds below its operating rpm [115, 116]. This is typically observed in heavy rotating machines like steam turbines. Hence, the flexible support rods used in the current study is representative of the foundation of a real machine. At any given time the experimental set up consisted of purely FS1 or FS2. Note that when changing between FS1 and FS2 set up, care was taken to ensure that rotating assembly and bolting between the bearing pedestals and the lathe bed were undisturbed. Thus, the rig configuration and main dimensions shown in Figure 3.5 were consistent between FS1 and FS2.

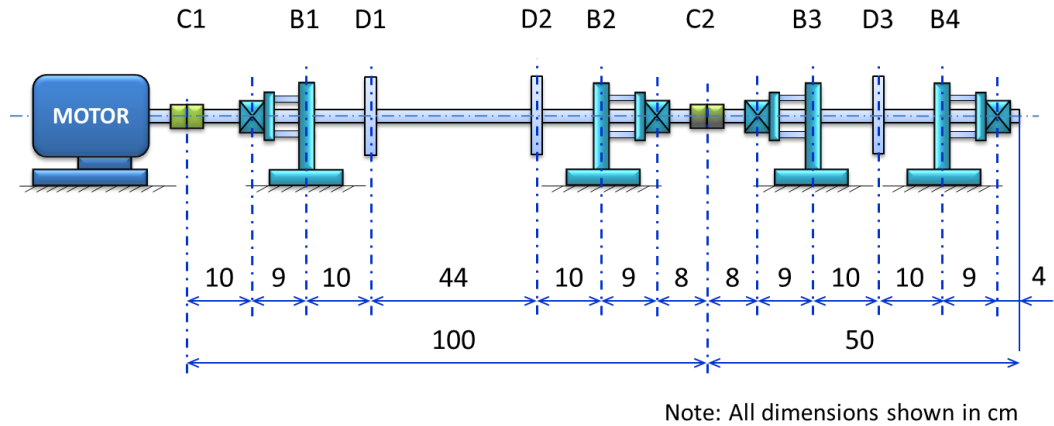


Figure 3.5 Dimensions of main components on rig with flexible supports

The impulse-response method of modal testing was carried out to define the dynamic characteristic of the relatively flexible supports. This was required to ascertain whether the objective of changing the dynamics of the rig by increasing the flexibility of the bearing support types. The first four natural frequencies for FS1 were found to be 50.66 Hz, 56.76 Hz, 59.2 Hz and 127 Hz. The same was done for FS2 and the first four natural frequencies were identified as; 47 Hz, 55.54 Hz, 57.97 Hz and 127 Hz.

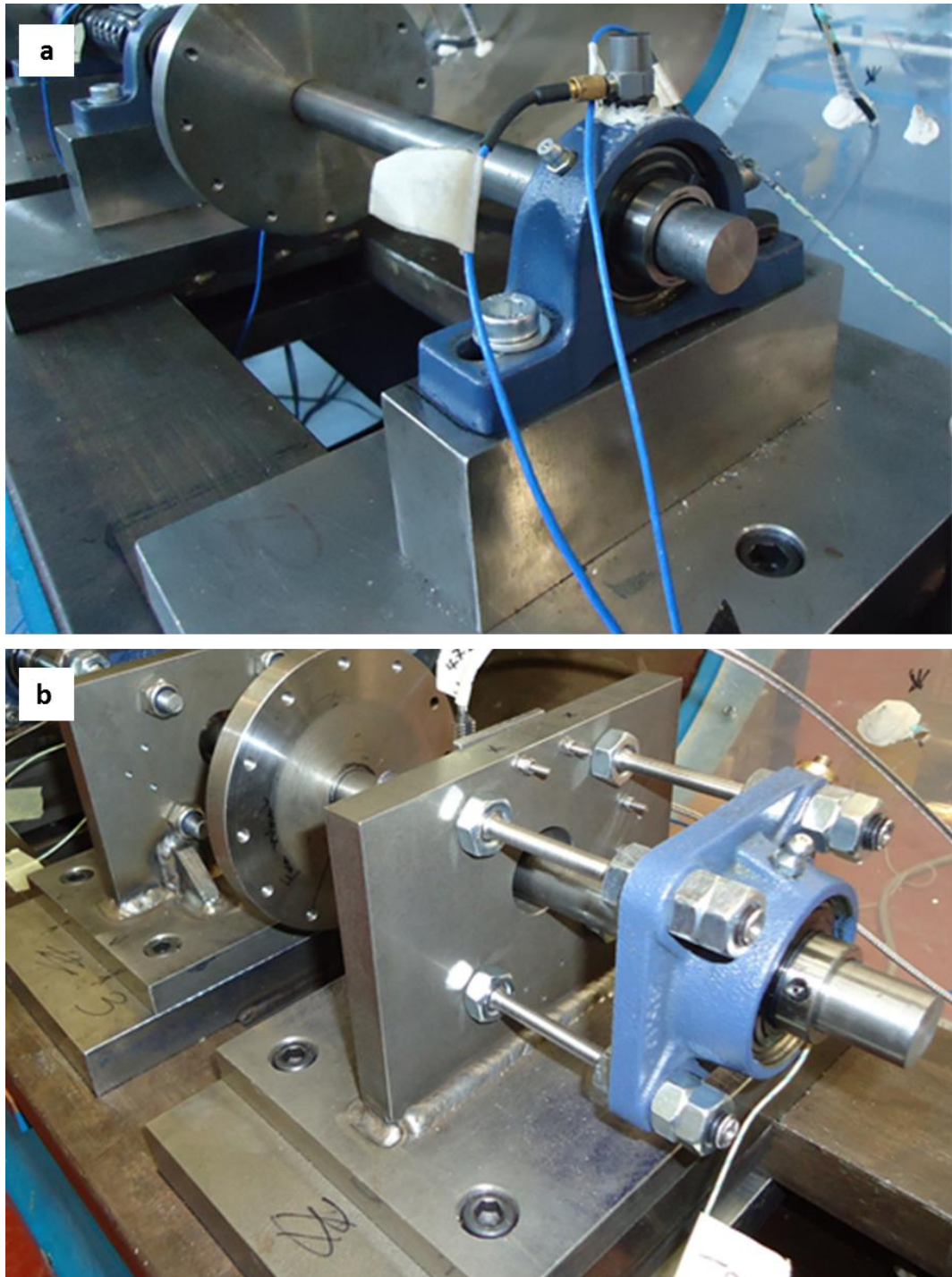


Figure 3.6 Close up of bearing pedestal from (a) rigid support and (b) flexible support

Table 3.1 Details of main components used on mechanical rig with flexible supports

#	Name	ID*	Make/Model	Description
1	Balancing disc	D1, D2, D3	None	125 mm diameter \times 14 mm thick sections
2	Bearing	B1, B2, B3, B4	SKF/ FY 20 TF	Flange mounted grease lubricated bearings with 20 mm nominal bore
3	Coupling 1	C1	Ruland/ FCMR38-16-16-A	Semi-flexible coupling, 16 mm \times 20 mm bore
4	Coupling 2	C2	n/a	Rigid coupling, 20 mm \times 20 mm bore
5	Motor	Motor	Crompton Greaves/ GF7965	3 phase, 0.70 kW, 3000 rev/min
6	Rotor 1	R1	None	20 mm nominal diameter \times 1000 mm long rod
7	Rotor 2	R2	None	20 mm nominal diameter \times 500 mm long rod

*Same nomenclature used throughout remainder of report

3.2.2.2 Instrumentation

Minor changes were also made to the instrumentation used for the flexible supports shown in Figure 3.7. One PCB 100 mv/g accelerometer was used at each bearing instead of two. This was mounted at a 45^0 orientation on the edge of the flanged bearing (see Figure 3.8b). Other noticeable changes in the instrumentation used were the addition of Monitran MTN/EP080 8mV/ μ m eddy current type displacement probes with MTN/ECPD driver (Driver) and a DFM 125 pulse tachometer. The eddy current probes were mounted in the horizontal (x-plane) and vertical positions (y-plane) at bearing 1 (B1) and bearing 4 (B4). Figure 3.9 shows the set up done at B1 location which was similar at B4 location. Thus a total of four drivers were used in this set up. Outputs of the driver were connected directly to the DAQ system for later storage on the personal computer. Hence a total of 14 different instruments were used for the experimental set up.

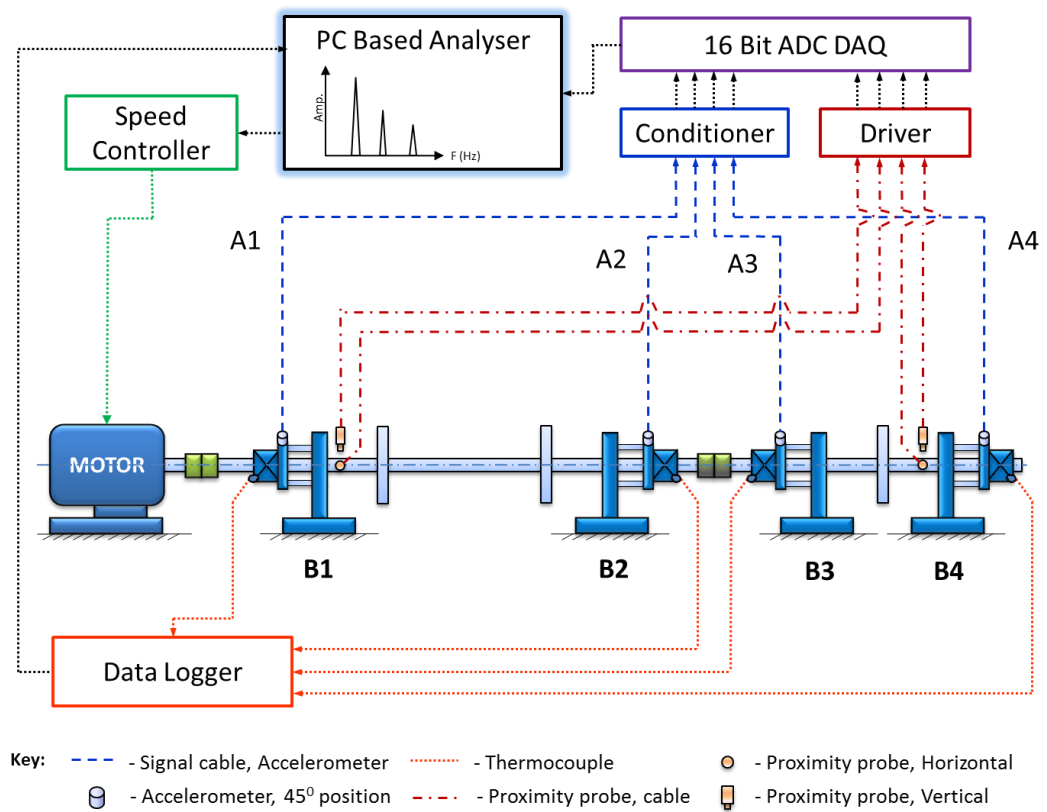


Figure 3.7 Schematic of instrumentation used for testing with flexible supports

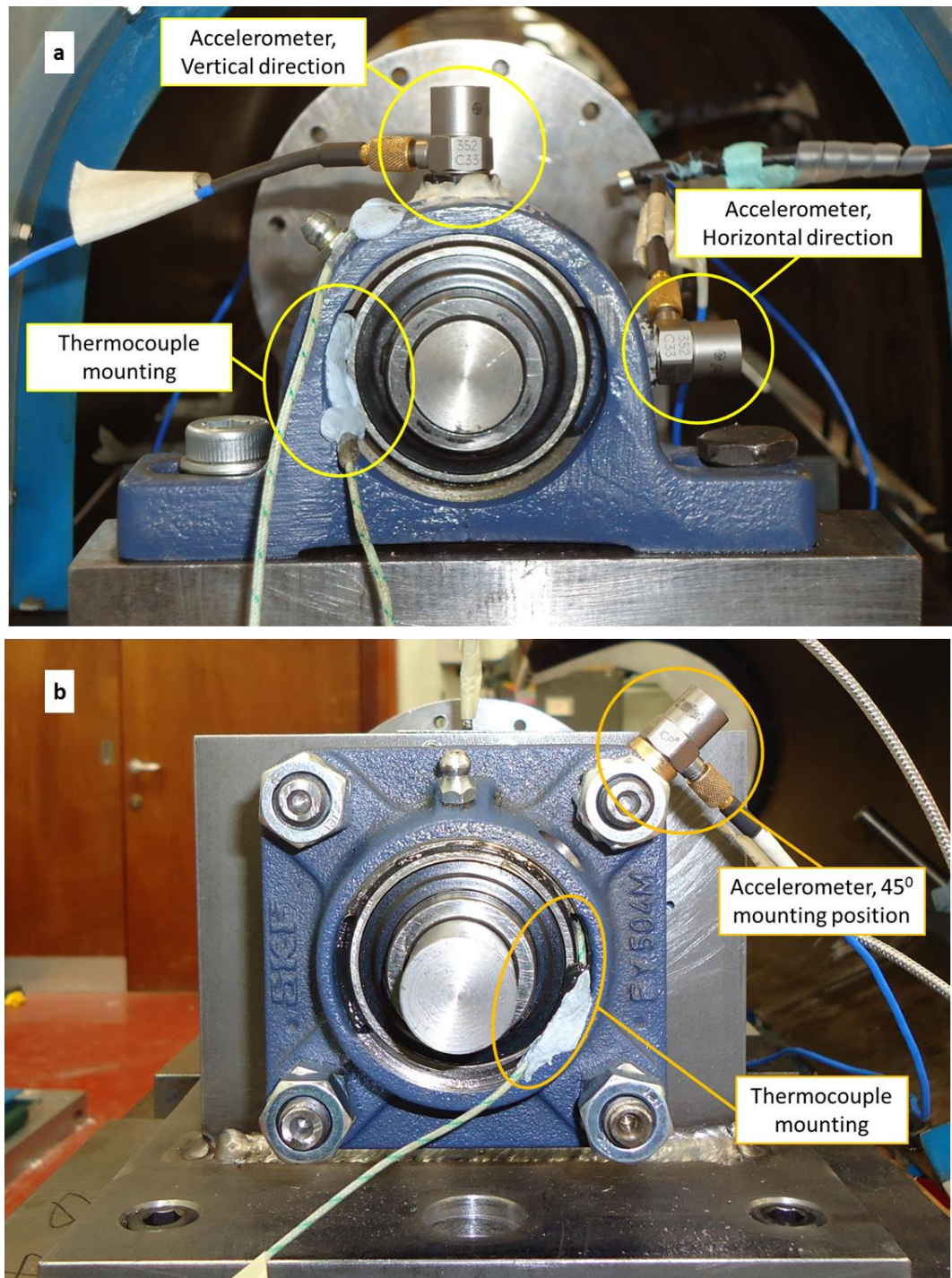


Figure 3.8 Details of accelerometer and thermocouple configuration for:
a) rigid supports and b) flexible supports

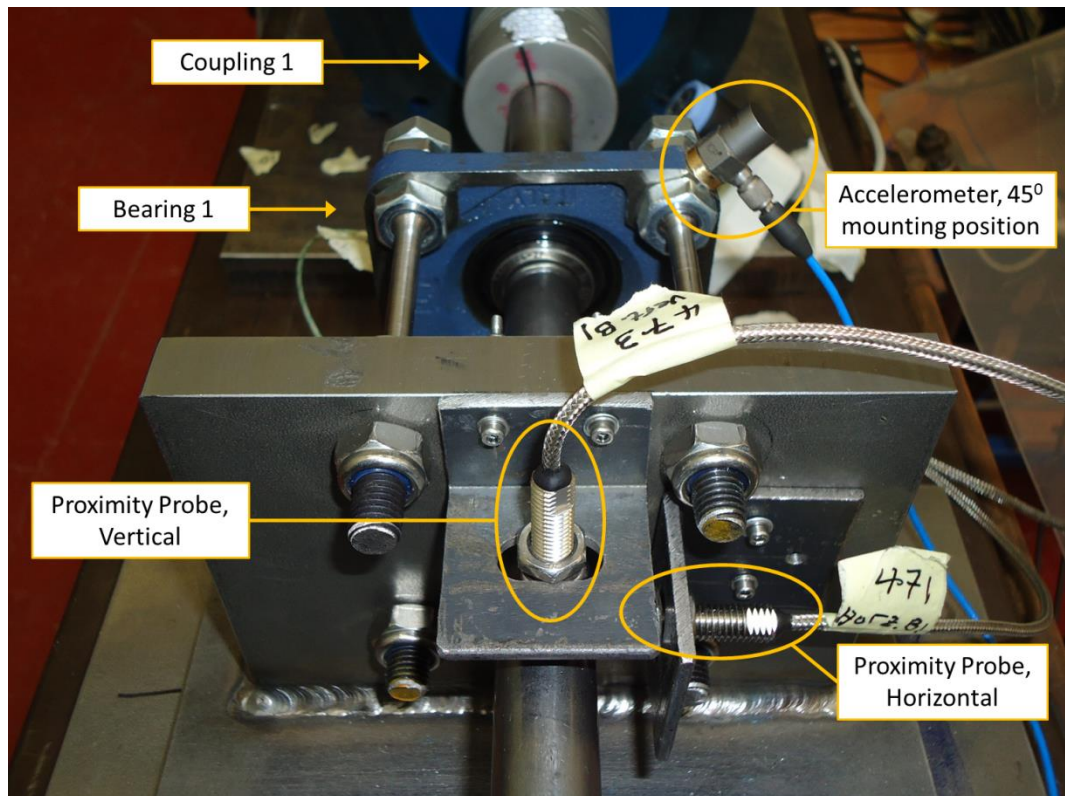


Figure 3.9 Details of instrumentation used at Bearing 1 (B1)

3.3 Experiments conducted

Two sets of experiments were conducted based on rig configuration. Experiments were done on the rigid set up first and then on FS1 followed by FS2. On-bearing temperature and vibration readings were collected at each bearing location for the different conditions tested at different speeds. For each experiment done, one condition was introduced to the rig at a time and all tests were conducted below the rigs' first natural frequency. Vibration measurements were acquired at a data sampling rate of 10,000 Hz.

3.3.1 Rigid set up

For each fault scenario, experiments were performed at rotational speeds of 600 rev/min, 1200 rev/min, 1800 rev/min, 2400 rev/min and 3000 rev/min. Data for the healthy machine condition were collected first in order to establish the baseline conditions for the rig. Vibration and temperature measurements were then taken for three fault conditions:

cracked rotor, rotor rub, and coupling misalignment. Cracked rotor condition was simulated in three different locations along the length of the rotor. On starting the system from rest, bearing temperatures were recorded for a period of ten minutes. The PicoLog data recorder was configured to capture bearing temperatures every 5 seconds for a total of 180 samples (total recording time of 15 minutes). Vibration measurements were then taken at the ten minute point for a total sample time of one minute. Therefore, a total of four conditions, including healthy, with six total scenarios at five different speeds were tested. A summary of experiments done with the rigid set up is provided in Table 3.2. Complete descriptions of experiments done with full details of each fault conditions tested are given in following chapters.

3.3.2 Flexible set up

The same experiments were conducted for FS1 and FS2 in which experiments were done with the rig configured with FS1 first and then it was reconfigured to FS2. As noted earlier, extreme care was taken to ensure the rig dimensions (see Figure 3.5) and the experimental procedure were consistent for the two flexible configurations. Therefore, the brief description given here for experiments done on the flexible set up applies to both FS1 and FS2.

In order to establish baseline operating conditions for the experimental rig, data were first collected for a residual misalignment with residual unbalance (RMRU) condition which was essentially the healthy case with some residual misalignment. Testing was afterwards done for six fault conditions: added unbalance, bow, cracked rotor, looseness, misalignment and rub. Four different misalignment conditions of varying magnitudes and three rub cases (two blade rub and one shaft seal rub) were seeded. Therefore, a total of 12 scenarios spanning 1 baseline condition and six fault conditions were simulated. For each scenario tested, experiments were performed at speeds of 600 rev/min, 1200 rev/min, 1800 rev/min and 2400 rev/min. Experiments were not conducted at 50 Hz as was the cases in the rigid setup, because of fear of damage from resonance given the first observed natural frequency for both FS1 and FS2 were in the vicinity of 50 Hz with 50.66 Hz and 47 Hz, respectively. Therefore, a total of seven conditions, spanning twelve scenarios at four

different speeds were tested. A summary of experiments conducted with the flexible set up is provided in Table 3.2. Complete descriptions of experiments done with full details of each fault conditions tested are presented in following chapters.

3.4 Summary

Experiments were first carried out on laboratory rig [20, 29] with relatively rigid bearing supports at different speeds with different fault conditions. The rig was afterwards modified to accommodate relatively flexible bearing supports. Two flexible support mountings were developed using 10 mm diameter and 6 mm diameter support rods, referred to here as FS1 and FS2, respectively. Experiments were conducted at different speeds with more fault conditions than what was tested with the rigid configuration. Prior to the start of experiments, modal testing was done on both relatively flexible supports in order to define the dynamic characteristics of the rig in comparison to the rigid support. Natural frequencies for the rigid support were obtained from Sinha and Elbhbah [29] who previously conducted modal testing on same. A summary of rig parameters, conditions tested and instrumentation described in this chapter is given in Table 3.2.

Table 3.2 Summary of experimental approach used in present study

Rig	Nat freq. (Hz)	Conditions (scenarios)	Speed (Hz)	Experiment Summary	Vibration measurement		Temperature measurement
					Displacement	Acceleration	
Rigid	68, 144 & 352	Healthy, Crack (3 locations), Misalignment & Rub	10, 20, 30, 40 & 50	4 conditions 6 scenarios 5 speeds (120 cases)	None		
FS1	50.66, 56.76, 59.2 & 127	RMRU, Added unbalance, Bow, Crack, Looseness, Misalignment (4 sizes) & Rub (3 scenario, two locations)	10, 20, 30 & 40	7 conditions, 12 scenarios 4 speeds, (336 cases)	Sensor: Eddy probe, 8mV/ μ m DAQ: A/D DAQ, USB	Sensor: Accelerometer, 100 mv/g DAQ: A/D DAQ, USB	Sensor: Thermocouple, K-type DAQ: Data Logger, Thermocouple
FS2	47, 55.54, 57.98 & 127	RMRU, Added unbalance, Bow, Crack, Looseness, Misalignment (4 sizes) & Rub (3 scenario, two locations)	10, 20, 30 & 40	7 conditions, 12 scenarios 4 speeds, (336 cases)	DAQ: A/D DAQ, USB Sampling: 10 kHz	Sampling: 10 kHz	Sampling: 1 sample/5 sec

Note: Additional experiment details are provided in subsequent chapters.

4 EXPERIMENTAL OBSERVATIONS IN THE SHAFT ORBITS OF RELATIVELY FLEXIBLE MACHINES WITH DIFFERENT ROTOR- RELATED FAULTS

Reformatted version of the following paper:

Title: Experimental Observations in the shaft orbits of relatively flexible machines with different rotor related faults

Authors: Adrian. D. Nembhard, Jyoti K. Sinha and A. Yunusa-Kaltungo

Status: Accepted to Measurement Journal and in press

Abstract: An experimental study on the shaft orbit response for different rotor-related faults is presented in this paper. Similar studies in readily available literature on this subject were previously done considering a few fault conditions on different machines. Therefore, an opportunity exists to provide further insight to changes in the behaviour of a single machine when affected by a wider range of different rotor-related faults. Experiments are done on a small laboratory ball bearing rig on which vibration displacement data are acquired for a baseline condition as well as six different fault conditions that are introduced separately at different subcritical steady-state speeds. For each condition tested, orbit plots are generated and critically analysed. These orbits are also compared to those observed on a similarly configured rig with different dynamic characteristics on which the same experiments are done. The present work provides useful results for practical rotor fault diagnosis as well as worthwhile qualitative information to analytical studies related to the rotor faults observed here.

Keywords Orbit plot analysis, Vibration analysis, Condition monitoring, Fault diagnosis, Rotating machinery, bow, crack, looseness, misalignment, rub, unbalance

4.1 Introduction

The orbit plot is a two dimensional representation of the dynamic motion of the centre of a rotating shaft at a measurement plane [53]. It presents a snapshot of the rotor actual motion at its centre [58]. Proper interpretation of the orbital paths or rotor lateral motion (rotor orbital and its direction) provides insight into the nature of the machinery fault [58] and the forcing functions acting on a shaft [53].

Unsurprisingly, since its introduction at least some forty years ago [59] the orbit plot is widely utilised in theoretical studies aimed at gathering insight to the nature of different rotor fault conditions such as: bow [60-62], crack [60, 63-71], looseness [72, 73], misalignment [74-76], rub [61, 62, 68, 72, 75, 77-80] and unbalance [61, 67, 69, 75]. Though these theoretical studies have been highly relevant to revealing the intricate nature of machinery faults, it was generally observed that they are often attempted with several assumptions and simplifications that may produce results or features that may not be observed in practice [3, 69].

It is therefore apparent that the validation of theoretical models with experimental or practical field acquired results is important [58, 59]. Needless to say, both theoretical and experimental studies should co-exist in a continuously improving symbiotic relationship in order to advance the knowledge of the nature of failures and the understanding of tools such as the orbit plot. That said, relatively lesser experimental works have been attempted than theoretical ones. A brief review of readily available literature on experimental works, whether for theoretical validation or standalone experimentation, in which the orbit analysis was utilised, is provided.

In an attempt to characterise the presence of a crack on an overhung rotor, Adewusi and Al-Bedoor [81] extracted different vibration features from different techniques including the orbit plot analysis. During crack propagation at a steady-state speed on an experimental rig with self-lubricated sleeve bearings, the rotor tracked a smooth inner looped orbit which became distorted, due to wobbling, on increasing the bending moment acting on the overhung rotor. Both Darpe et al. [63] and Sinou [4] identified a similar inner looped orbit which changes size around half of the first critical speed for a transverse crack due to the

presence of a dominant second harmonic [63]. Whilst Darpe et al. [63] used experiments on a self-aligning ball bearing rig to validate results obtained from the analysis of a Jeffcott rotor passing through subcritical resonances with a transverse breathing crack, Sinou [4] presented a comprehensive experimental study using a rig with bush bearings and slotted rotors that represented rotors with open cracks. Darpe et al. [63] concluded that the change of orientation of the inner looped orbit on passing through “subcritical resonances” could be a crack diagnostic indicator. Sinou [4] added that the inner loop size is proportional to slot depth. Interestingly, Bai et al. [117] also reported an inner looped orbit for a ball-bearing rotor system, but not for a cracked rotor condition. Instead, that orbit shape was “provoked” by subharmonic resonance which occurred when the rotating speed of a small ball bearing rig under an unbalance load was around twice its critical speed.

Lee and Lee [74] validated a theoretical model for a misaligned rotor bearing system at different steady-state speeds near the first critical speed of a laboratory test rig supported by deep groove ball-bearings. It was shown that with increasing angular misalignment, the orbit tends to collapse from a circular shape to an ellipse; due to an increase in the anisotropic nature of the bearing stiffness. The major axis of this ellipse was perpendicular to the misalignment direction below the critical speed, but was aligned to the misalignment direction after passing through the critical speed (that is, a 90° rotating of the elliptical orbit). The orbits for parallel misalignment were, however, unperturbed relative to the healthy orbit due to the effect of a very flexible coupling element. Similarly, Pennacchi and Vania [82] also reported a collapsed $1\times$ filtered orbit for an angular coupling misalignment case on a real turbo-generator train with lemon shaped oil-film bearings. The fault symptoms were analysed on a real machine and then modelled and experimentally verified for identification. Both Lee and Lee [74] and Pennacchi and Vania [82] conducted experiments in the vicinity of the first critical speed of the system explored. As earlier demonstrated by similar findings by Lee and Lee [74], Pennacchi and Vania [82] reiterated that their observations were applicable to machines supported by ball bearings, but was exacerbated for machines on oil-film journal bearings, because of lower bearing stiffness and hence possible higher rotor deflections in the latter case.

Patel and Darpe [3] studied the whirl nature of higher frequency components of the vibration response due to coupling misalignment at or near different “sub-harmonic resonances” on an experimental rig supported by single-row ball bearings. It was noted that

regardless of the type of misalignment, rotor orbits are stretched in the direction of the plane of the misalignment due to an increase in the effective stiffness, and consequent suppression of vibration response, in the direction perpendicular to the plane of the misalignment. It was further added that rotors with angular misalignment reveal outer loops, whereas those from parallel misalignment might exhibit inner looped orbits. Further to this, with the aim of identifying features which are better able to discriminate faults with similar spectral features, such as crack and misalignment, Patel and Darpe [55] presented experimental investigations on crack, misalignment and rub from steady-state vibration responses at sub-critical rotational speeds on two different laboratory rigs supported by ball bearings. The results show that misalignment generates a backward whirling outer loop orbit which is stretched in the direction orthogonal to the misalignment direction as compared to forward whirling inner loop of a crack. The inner looped orbit for crack fault was consistent with aforementioned findings [4, 63, 81].

With the intent to ascertain which pattern of vibrations represents steady-state processes and to identify what are the most sensitive parameters affecting changes in said steady-state regions, Muszynska and Goldman [72] examined the dynamic behaviour of unbalanced rotor rolling element bearing systems with a loose bearing pedestal or rotor-stator rubs using different experimental rigs, respectively. Results from a local impact model were compared to results from experiments that were presented in the orbit plot, amongst others, to mainly provide insight to the dynamics of rotor-stator rub. It was observed that at higher machines speeds during partial rotor-stator rubbing, orbits contain distinct reverse-procession loops due to the rub-related tangential force which opposes the direction of rotation. It was also shown that the rotor support anisotropy resulted in a “butterfly” (sideways 8) effect for a rotor operating at twice its first balance resonance speed under the influence of a partial rub.

The nature of rotor/seal full annular rub was demonstrated with orbit plots by Yu et al. [77], which conducted experiments on a brass bushing “annular rub test rig” supported by two brass bushing bearings. The authors made a clear distinction between reverse procession full annular rub, which had a very smooth orbital pattern and “multicontact intermittent rub” which had a “bounce pattern”. The difference in the mentioned rub patterns depended on friction between contacting surfaces during the rub. Aided by tracking the evolution of the orbit around the first natural frequency, it was concluded that

reverse procession (dry whip) can occur without external disturbances for small rotor/seal clearances. Chu and Lu [10] explored the dynamic effects of partial and full rotor-stator rub on a small experimental rig with rolling element bearings in order to aid rub fault diagnosis. The authors were able to correlate the different types of rubs with the different rotor orbits from responses that contained $\frac{1}{2}$ and $\frac{1}{3}$ fractional harmonics as well as super harmonic components. Pennacchi et al. [79] analysed the effects of light rub between rotor and seal strips by comparing experimental results from a rig supported by two lemon shaped oil-filmed bearings with simulations from a mathematical model. At both sub-critical and super-critical speeds, it was noted that the shape of the rotor orbit is strongly dependent on the interference between the seal and rotor. Cong et al. [83] validated an earlier proposed rub-impact model with experimental work on small rig supported by oil filled journal bearings that was instrumented with a pair of orthogonally mounted eddy current probes. Testing was done at four different rotating speeds; two subcritical and two supercritical and at different damping ratios. Orbit plots were employed to observe damping ratio with the first critical speed and the severity of rub with changing speed ratio. Key among several observations made is that the severity of rub impact fault becomes low with increasing speed ratio; where the orbit transforms from an irregular shape to an ellipse.

Evidently, orbit plot analysis has been well applied to rotor fault analysis, especially for crack and rub fault investigations, however, it has been applied to only a few faults on machines. Indeed, the Bently Nevada Research Corporation provided highly relevant articles in which the orbit analysis was applied to myriad fault conditions, but these were based on observations from different industrial case studies and experiments on several different machines [12, 84, 85]. Additionally, Muszynska [58] comprehensively reviewed a variety of rotating machinery malfunctions that were illustrated by orbital patterns, but again, these were based on different experiments and actual field data from different machines. Therefore, the objective of this study is to gain insight to the shaft orbit behaviour of a single machine under the influence of different fault conditions at different rotating speeds. Such a study could offer further useful information on how different faults alter the behaviour of rotating machinery, whilst complementing already available works.

From the literature perused, it has been noted that observations made in orbit analysis are applicable to machines irrespective of the bearing type used; for example whether anti-friction or journal. That being said, unlike studies with machines supported on journal bearings in which measurements are made at the bearing location, it was however, noted that for studies in which anti-friction bearings were employed care was taken to ensure measurements were made in locations in which shaft deflection was adequate to generate an accurate representation of the dynamic motion of the rotor. In the current study, experiments were conducted on a small laboratory rig with grease lubricated ball bearings that are mounted on relatively flexible supports. Six different commonly encountered rotor fault conditions were introduced separately and compared to a baseline “healthy” condition. With knowledge of the dynamic characteristics of the rig including its mode shape, vibration measurements are made with orthogonal XY eddy current probes at different steady-state subcritical speeds near bearings and not near the middle of the rotor span, as is often reported in previous studies [3]. Considering the sensor positioning in some cases may obscure or amplify the difference in the level of response in the two orthogonal directions [3, 79], placement near bearing and not near the mid span would be a better representation of practice. All observations made are presented here.

The paper hereafter is organised as follows. In Section 4.2, the experimental set up and instrumentation used are described. The procedure for the different experiments conducted are summarised in Section 4.3. Then, in Section 4.4, the data processing methodology is outlined. Section 4.5 holds the presentation of results obtained as well as discussions on said results. Finally, conclusions are drawn in Section 4.6.

4.2 Experimental Set Up

In this section the experimental rig is described in brief. Relevant details are provided for both mechanical components and the instrumentation employed. Afterwards, a synopsis of the procedure used to define the dynamic characteristics of the rig is also provided.

4.2.1 Mechanical Layout and Instrumentation

Figure 4.1 shows the experimental rig used for the present study, which is located in the The Dynamics Laboratory at the University of Manchester, UK. The rig consists of two dissimilar length, 1000 mm (long shaft) and 500 mm (short shaft), bright mild steel shafts of 20 mm diameter. The system is driven by a 3 phase 0.75 kW 3000 rev/min electric motor (Mod.: EGF 6382) which is connected to the long shaft via a semi flexible coupling (Coupling 1). The long shaft is rigidly coupled (Coupling 2) to the short shaft. Machined bright mild steel sections which act as balancing discs (125 mm in diameter and 14 mm thick) are mounted on each shaft; two discs (Disc 1 and Disc 2) for the long shaft and one disc (Disc 3) for the short shaft. The shafts are supported by four grease lubricated 4 bolt flanged ball bearings (Mod.: SKF FY 20 TF). Each bearing is secured to a pedestal by four flexible rods. Figure 4.2 provides close up views of the steel rods and bearing pedestal used. The bearing pedestals are bolted to a high mass lathe bed which forms the foundation of the system. The lathe bed sits on vibration isolators on the concrete floor. Two different diameter rods, 10 mm and 6mm, of same lengths were used on the rig to investigate whether changes in the flexibility of the bearing support affected the shaft orbit. Note that at any given time in the experiments the size of the rod used at all four bearings were homogenous.

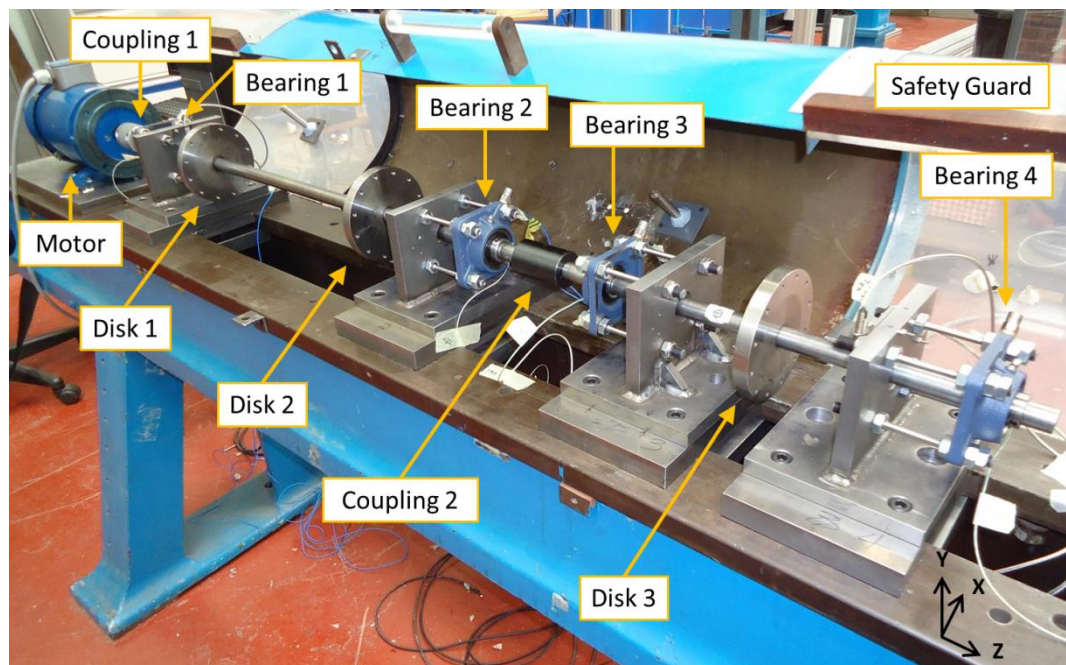


Figure 4.1 Mechanical layout of experimental rig

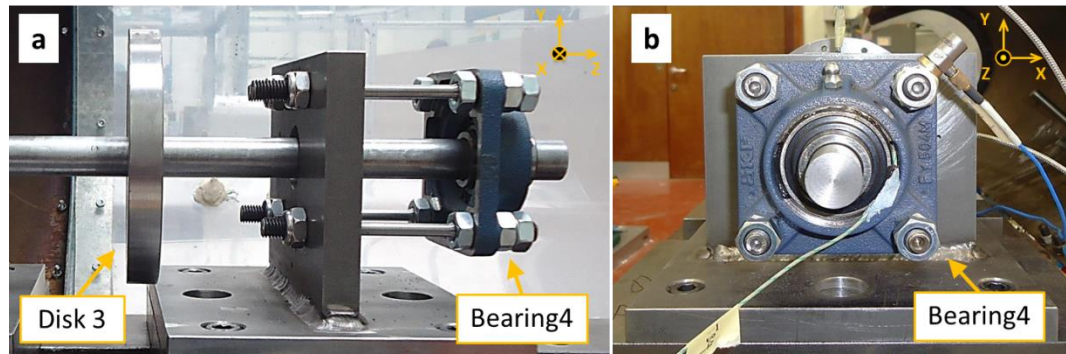


Figure 4.2 Close up of: a) Bearing 4 side view with Disk 3 and pedestal and b) Bearing 4 end view

A schematic of the instrumentation used is provided in Figure 4.3. The dynamic response of the system is measured by two sets of orthogonal XY Monitran 8mV/ μ m industrial type eddy current displacement probes (Mod.: MTN/EP080). One set of probes is mounted near Bearing 1 (B1) and the second set near Bearing 4 (B4) to obtain the responses for the long and short shafts, respectively. Details showing how the probes are mounted are given in Figure 4.4. Each eddy current probe transmits data to and is powered by dedicated Monitran (Mod.: MTN/ECPD+24) drivers. The drivers are powered by an external 24 VDC at 30 mA power supply (not shown in Figure 4.3). Vibration data from the drivers are acquired by a National Instrument 16-bit 16 channel A/D DAQ system (Mod.: NI USB-6229). The DAQ system also acquires rig rotating speed reference data from a tachometer comprising of a retro-reflective sensor and driver. The DAQ system is connected to a personal computer (PC), on which all data are recorded and stored for subsequent processing and analysis. The rig's speed is also controlled from the PC via a Newton Tesla (Mod.: CL750) speed controller.

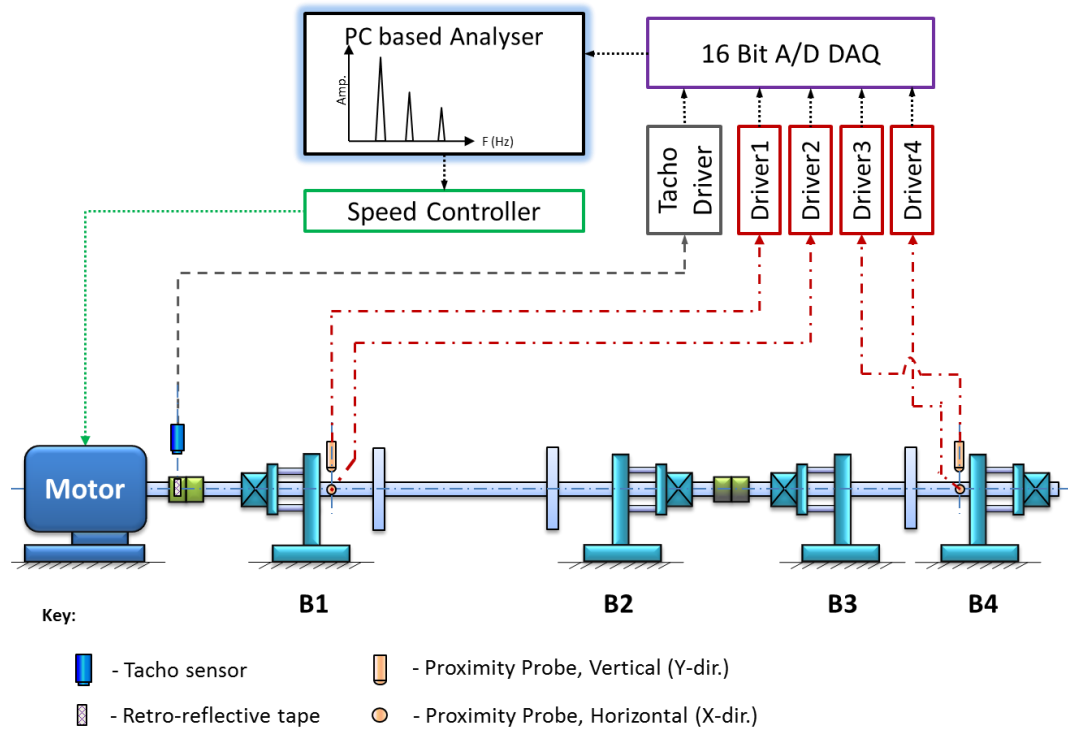


Figure 4.3 Schematic of experimental rig instrumentation

Main dimensions of the experimental rig and measurement locations are presented in Figure 4.5.

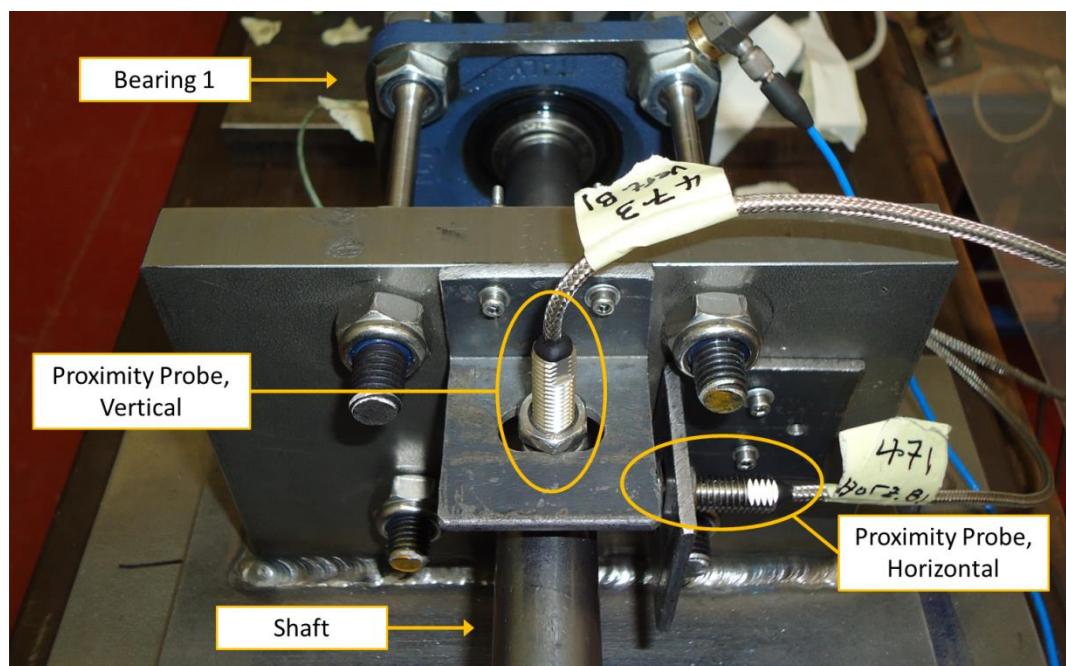


Figure 4.4 Details of eddy current probe mounting at Bearing 1 of experimental rig

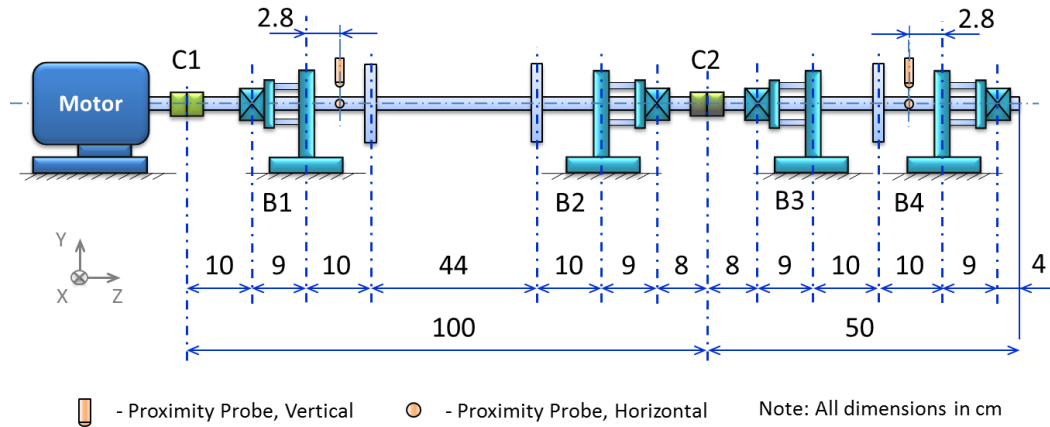


Figure 4.5 Schematic of rig dimensions and measurement location

4.2.2 Dynamic Characterization of Experimental Rig

In order to define the dynamic characteristics of the rig prior to experimenting with different faults, the impact response method of modal testing [50] was done. A schematic of the set up and instrumentation used for modal testing is shown in Figure 4.6. The rig was excited by a PCB 23 mV/g instrumented hammer (Mod.: PCB 0870C03). The system's response was measured by nine PCB 100 mV/g accelerometers (Mod.: PCB 352C33). As shown in the diagram the accelerometers were carefully spaced along the length of both long and short shafts so as to acquire a good approximation of the mode shapes of the system. The instrumented hammer and accelerometers were connected to the same DAQ system mentioned in the previous section (Section 4.2.1) via three PCB four channel signal conditioners (Mod.: 482C Series) with a 1:1 gain. Data storage and processing were done from the aforementioned PC.

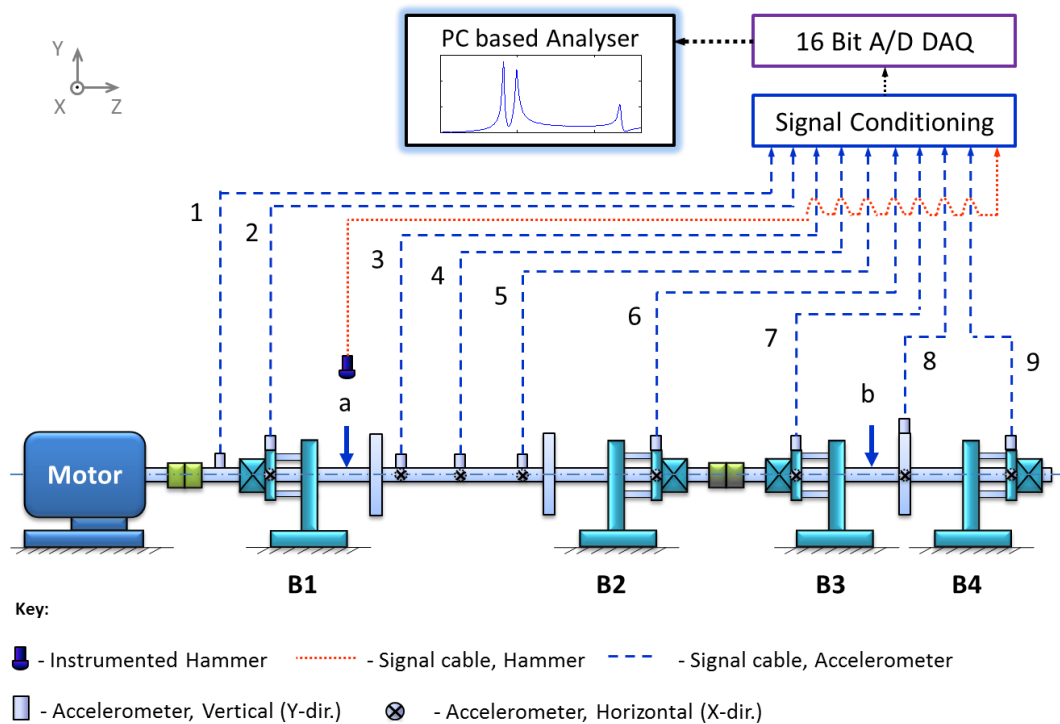


Figure 4.6 Schematic of experimental rig set up for modal testing

Modal testing was done at two impact locations, “a” and “b” as shown in Figure 4.6. For each impact location, the responses for ten impacts were acquired first in the vertical radial direction at all nine measurement locations. The shaft would then be rotated by 90° so as to align the accelerometers in the horizontal radial direction. Accelerometers at the bearing locations in positions 2, 6, 7 and 9 were also repositioned in the same horizontal radial direction. Similarly, the response from ten impacts would be acquired in the horizontal radial direction. The procedure would then be repeated for the “b” impact location. Modal testing was done for the rig configured with the 10 mm supports and then with the 6 mm supports. Impacting was done at evenly spaced time intervals and care was taken to allow the free response to fully decay before making another impact. Additionally, data acquisition was started just before the first impact and stopped after the free response decayed for the 10th and last hit. Care was also taken to ensure the same impact location was struck for all ten hits and that double hits were avoided.

The acquired data were processed to compute the Frequency Response Function (FRF) and generate mode shapes at the observed modes using an algorithm written in Matlab software. The FRF was computed at each measurement location by; applying a rectangular

window, averaging the ten responses acquired and using a frequency resolution of 0.61 Hz from data sampled at 5000 Hz. A typical FRF obtained is shown in Figure 4.7. The FRF in question is for position 4 in the vertical direction. It is extremely critical to note that the nine accelerometers shown in Figure 4.6 were needed to obtain mode shapes. Because of concern that the mass of the accelerometers might have biased the location of the natural frequencies, eight accelerometers were removed leaving a single accelerometer on Bearing 1 (Position 2 in Figure 4.6) with two different impact locations in both the vertical and horizontal radial directions. The FRF was recomputed and by appearance the first four natural frequencies for the 10 mm support were observed at 50.66 Hz, 56.76 Hz, 59.2 Hz and 127 Hz. Similarly, the first four natural frequencies for the 6 mm support were observed at 47 Hz, 55.54 Hz, 57.98 Hz and 127 Hz. The mode shapes for the first two natural frequencies observed are shown in Figure 4.8. The 50.66 Hz natural frequency was dominant in the vertical direction, while the 56.76 Hz natural frequency was dominant in the horizontal direction.

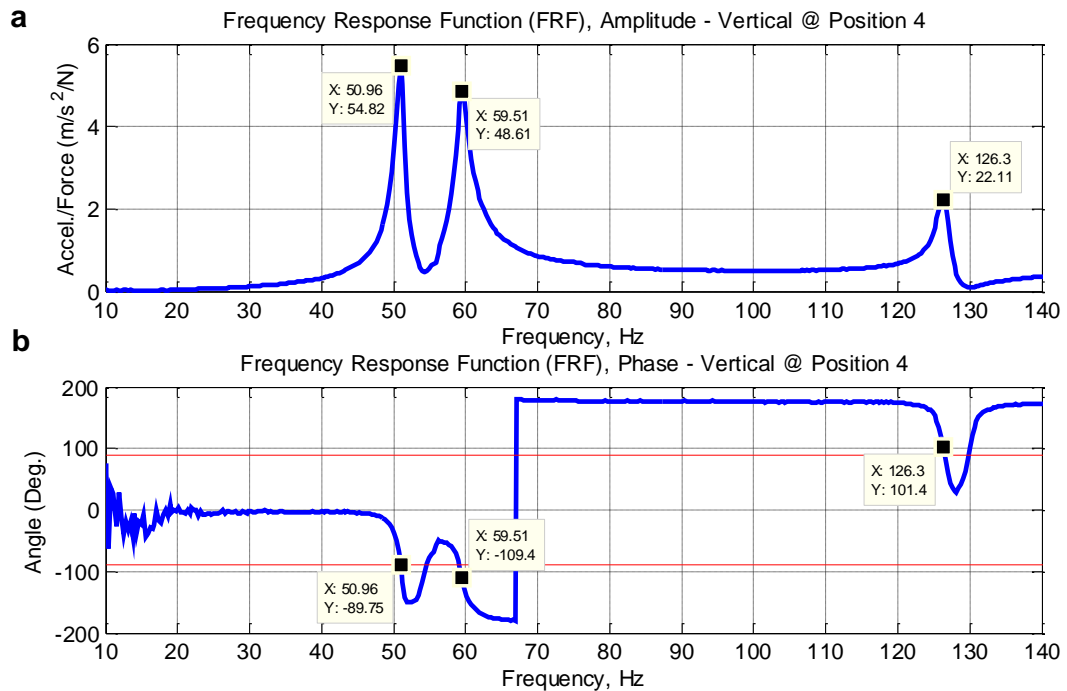


Figure 4.7 Frequency Response Function (FRF) in the vertical direction at position 4 obtained during modal testing

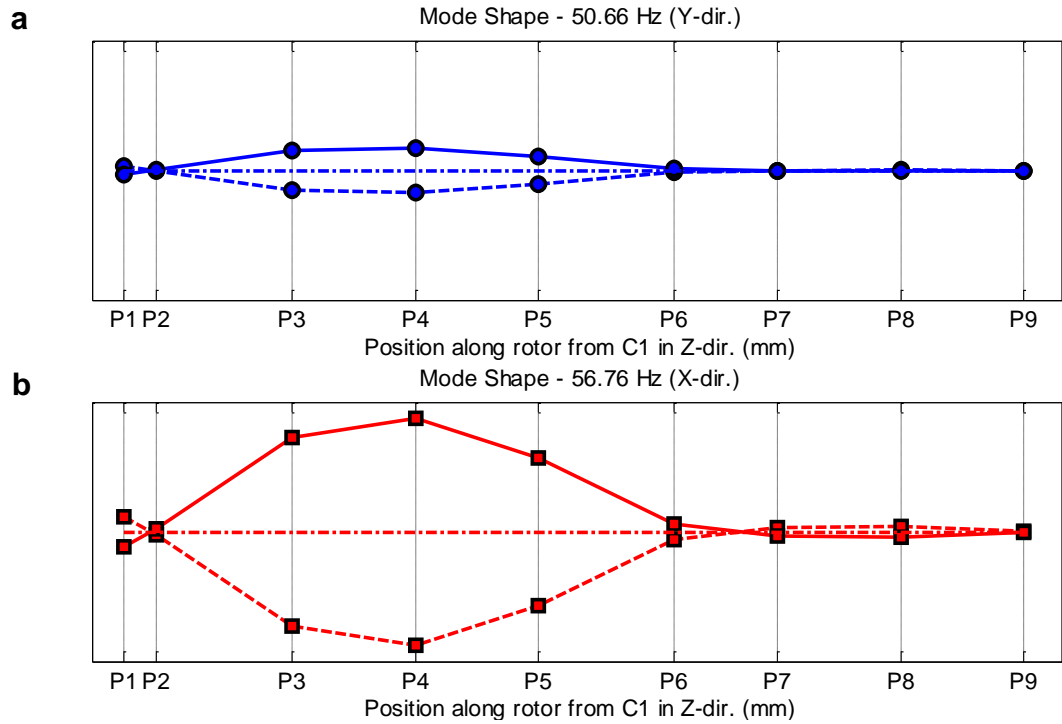


Figure 4.8 Mode shapes of experimental rig with 10 mm supports for first two observed natural frequencies in: a) vertical and b) horizontal direction

4.3 Experiments conducted

Six different fault conditions were observed as well as a baseline condition. Testing was done at four different subcritical steady-state speeds; 600 rev/min (10 Hz), 1200 rev/min (20 Hz), 1800 rev/min (30 Hz) and 2400 rev/min (40 Hz) in order to observe the impact of changing machine speeds on the rotor orbit. For each condition tested, vibration data were acquired at a sampling rate of 10 kHz for a total sample time of approximately 2 minutes.

For the baseline condition the rig had no seeded faults. This state represented the “healthy” state of the machine, however, as with a real machine; it was not possible to eliminate the residual misalignment and residual unbalance in the system. Thus this condition is hereafter referred to as the Residual Misalignment with Residual Unbalance (RMRU) case. The RMRU case was considered the baseline condition. The second condition tested was Added Unbalance. Unbalance is the most common fault in large rotating machinery. It is a condition of unequal mass distribution at each section of the rotor [58, 86]. To introduce this condition, a 2.6 g mass was added to Disc 2 at a radius of

55 mm; thereby creating 1.43×10^{-4} kgm unbalance. The aim was to create a mass eccentricity on the rotor. On completing testing for the Added Unbalance condition the 2.5 g mass was removed from Disc 2. Afterwards, a rub apparatus was installed 275 mm from Bearing 1. The set up used for Rub is shown in Figure 4.9. The apparatus consist of a pedestal in which a Perspex disc is secured. The rub would be simulated when the upper disc lightly rubs on the shaft. A light rub condition is generated when the residual unbalance in the rotor system is high enough to create a small interference between the rotor and stator. Therefore a 0.1 mm gap was initially set between the Perspex disc and the upper shaft surface.

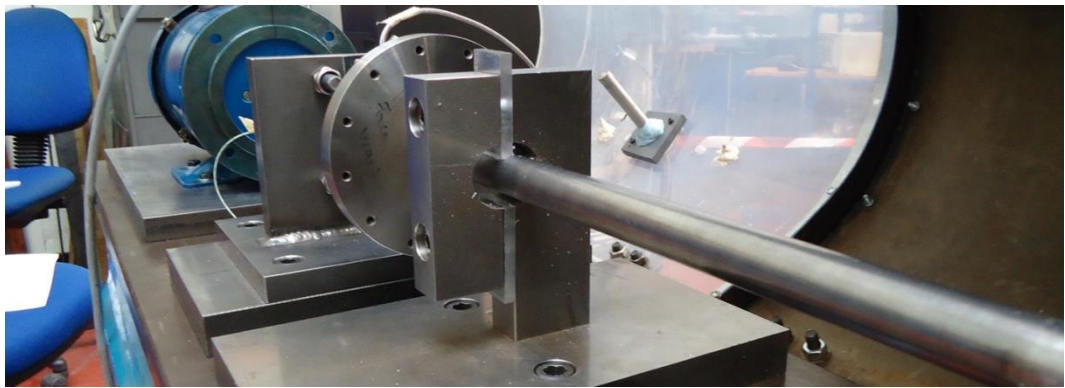


Figure 4.9 Rub fault apparatus mounted near Bearing 1

The rub apparatus was cleared from the rig after data acquisition at 40 Hz was completed. The fourth fault tested was shaft misalignment. As shown in Figure 4.10, Bearing 1 pedestal was displaced from its aligned condition in the vertical direction by placing 2×0.8 mm thick shims between the lathe bed and the underside of the pedestal. This therefore created a misalignment between the motor shaft and the long shaft across Coupling 1. After testing the shims were removed from the rig and the alignment restored to the baseline RMRU state.

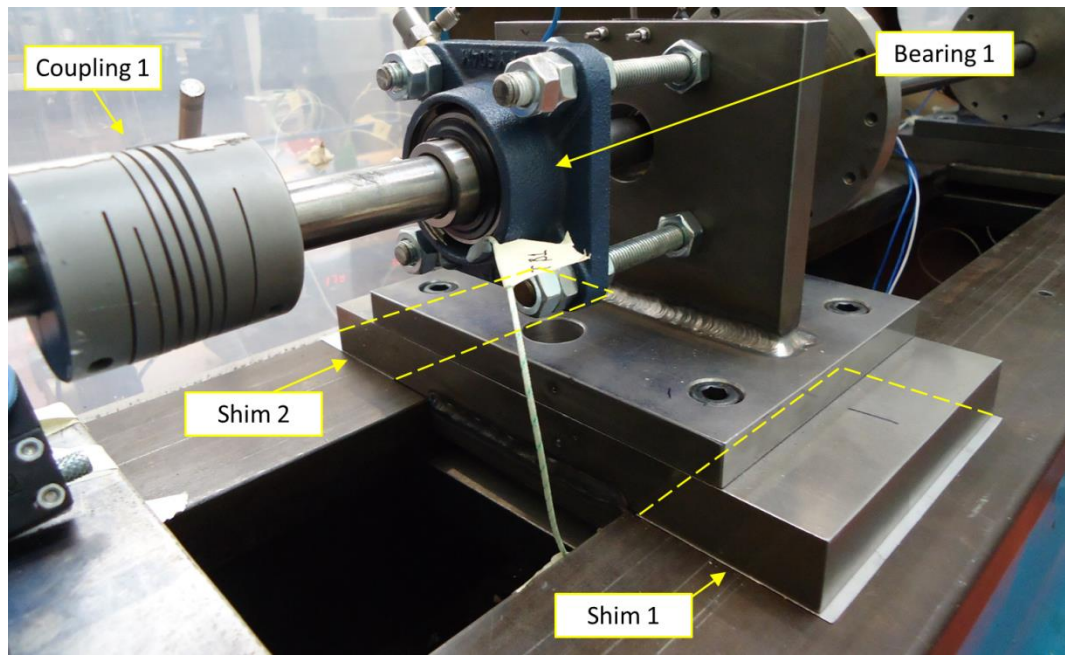


Figure 4.10 Seeding of misalignment in vertical direction at Bearing 1 by 2×0.8 mm shims under Bearing 1

The last three conditions seeded were looseness, cracked rotor and then bow (initial permanent deflection). Figure 4.11 pictorially describes how looseness was seeded. As shown, the flange nuts that secure Bearing 3 to its supports were slackened at all four corners. This therefore allowed restricted movement of the bearing about the axis of shaft. The unfastened nuts were also able to move along the securing support rods (10 mm or 6mm). In the vertical direction, Bearing 3 movement would be in concert with the shaft motion, but limited to the clearance between the flange mounting holes and the supporting rods. Bearing movement was restricted along the axis of the shaft as the securing grub screw locking the bearing to the shaft remained in place. On completing looseness, the nuts were fastened and shaft crack fault was seeded. With the aim to create a shallow breathing crack [69], the “healthy” long shaft was replaced by a shaft with a 0.34 mm wide 4 mm (20% shaft diameter) deep notch located 160 mm from Bearing 1. A 0.33 mm shim was inserted to the notch and glued to one side thus securing the shim to the inner wall of the notch while the other side was left free resulting in an effective crack width of 0.01 mm. The notch was cut by the Electro Discharge Machining (EDM) Wire Erosion process. The crack condition is shown in Figure 4.12.

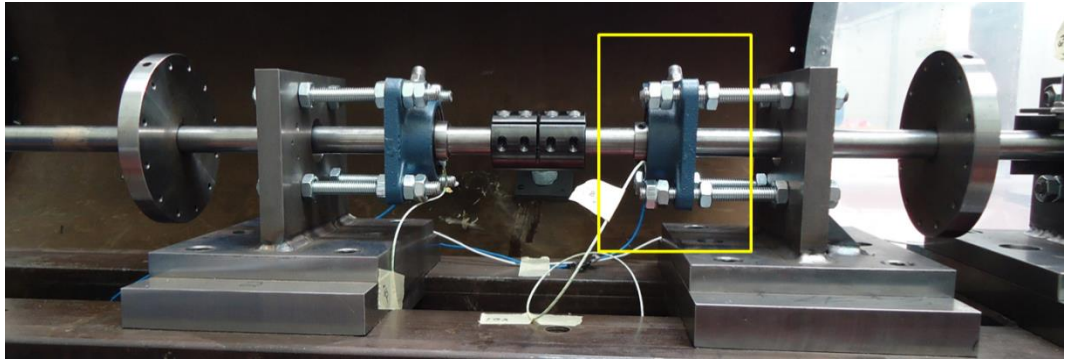


Figure 4.11 Details of looseness fault at Bearing 3



Figure 4.12 Details of crack showing close up of notch and shim

Finally, on completing crack testing the long cracked shaft was replaced with a long bowed shaft with a 3.2 mm maximum displacement from the axis of rotating (run out). The objective here was to create a scenario akin to an initial permanent deflection of a rotor. It is expected that this will create a mass unbalance in the system which may or may not increase rotor vibration. Though similar to the Added Unbalance case which is representative of a mass eccentricity, which also promotes mass unbalance, it has been shown previously that an initial permanent deflection and a mass eccentricity, though similar, can have different effects on the vibration of the rotor system [61]. The differences will be observed in following sections. On completing testing of all fault conditions the rig was reconfigured for the 6 mm bearing supports and the procedure was repeated. Care was taken to ensure that in cases where removal of the long shaft was necessary; the rig was so designed that the shaft could be removed without disturbing the alignment of bearing locations and consequently the alignment in the system.

A list of the experiments conducted is provided in Table 4.1.

Table 4.1 Summary of experiments conducted in present rotor orbit study

No	Code*	Scenario Name	Highlight
1	RMRU	Residual Misalignment with Residual Unbalance	No fault
2	Add_Unb	Added Unbalance	1.43×10^{-4} kgm eccentricity
3	Bow	Bow	3.2 mm run out
4	Crack	Crack near Bearing 1	0.34 mm wide \times 4 mm deep notch with 0.33 mm shim
5	Loose	Looseness on Bearing 3	Loosened flange nuts at Bearing 3
6	Mlign	Misalignment at B1 with 2 shims at 0.8 mm	Bearing 1 displaced 0.8 mm in vertical direction
7	Rub	Rub (blade) near Disc 1 (D1)	Perspex disc on shaft

*same nomenclature used throughout remainder of article

4.4 Data processing

The orbit shape was generated by pairing the time waveforms from the XY orthogonal eddy current probes so that the time element was removed [12]. At each speed tested, this was done by plotting the vertical eddy current probe response (Y-response) against the horizontal response (X-response) for one cycle of rotation. Before doing so, the measurements were converted to units of mm (since the readings would have been acquired as voltages), the DC offset in the responses were removed, and the responses were low pass filtered to include up to the $2\times$ harmonic components in the signal. For example at 40 Hz, a high pass filter was applied at 3 Hz to remove the DC offset in the signal and a low pass filter was applied at 92 Hz; thereby including the $1\times$ fundamental frequency at 40 Hz, the $2\times$ harmonic component occurring at 80 Hz and any fractional subsynchronous frequencies and its harmonics occurring between 3 Hz and 92 Hz. Deductively, the low pass filter cut-off frequency was adjusted to occur just after the $2\times$ harmonic component for the different rotating speeds tested, however, the high pass filter cut-off was unchanged. It was important to filter for the synchronous ($1\times$) vibration and its

2 \times harmonic component as these are the most significant features that describe the motion of the shaft [118].

The speed reference signal from the tachometer was used to track the start and end of the cycle over which the rotor orbit was plot. Samples of the vertical and horizontal responses with the corresponding tachometer signal are shown in Figure 4.13. The cycle was chosen from around midway the 2 minutes sample time to ensure a steady signal was used to generate the plot and also to avoid any noisy or unsettled data that might have been acquired at the start of sampling. The green circle on Figure 4.13c marks the start of a cycle while the red square marks the end of the cycle. The time waveform data between these start and end points were used to plot the shaft orbit. These said start and end markers were included on the orbit plots to illustrate the motion of vibration relative to the direction the shaft rotates; its procession or whirl direction [119].

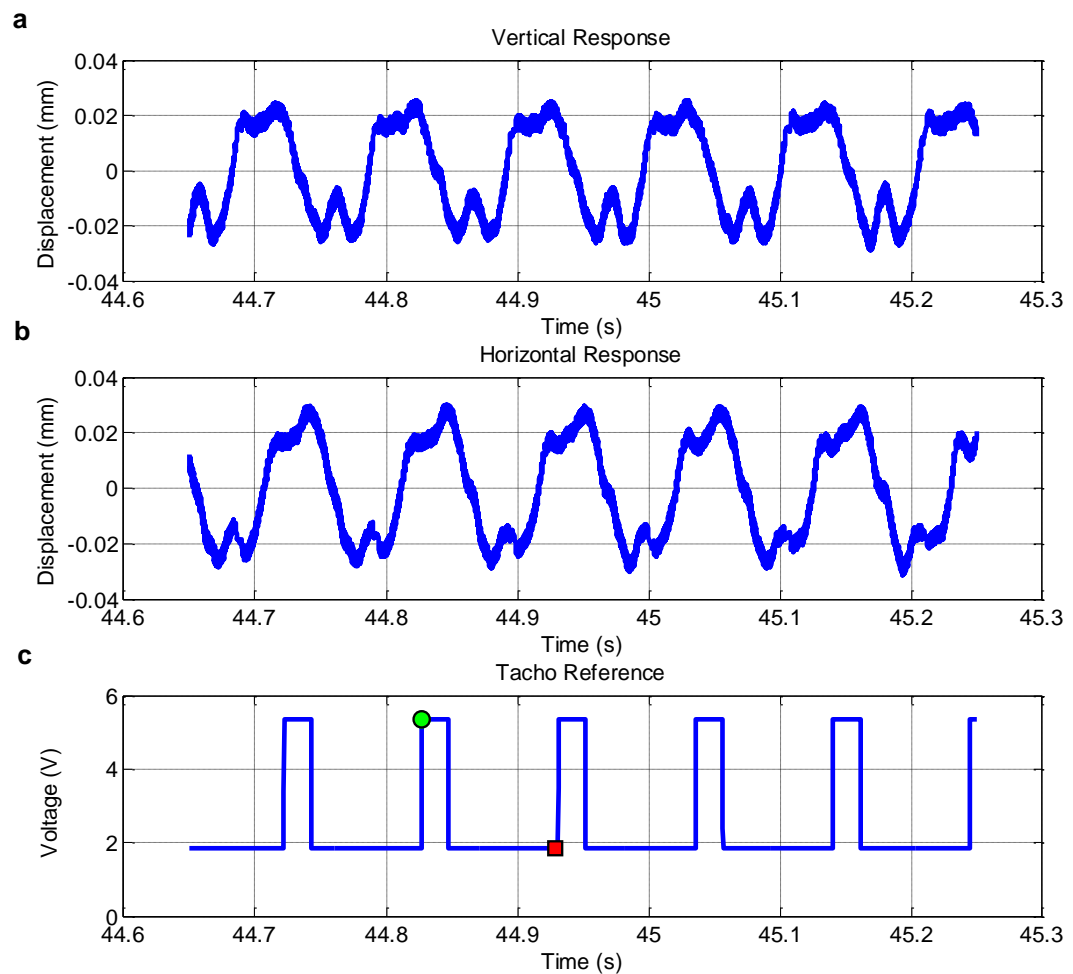


Figure 4.13 Sample of processing method for Rub showing: a) vertical response, b) horizontal response and c) tachometer reference signal with start and stop point for 1 cycle

4.5 Shaft orbit observations

In this section, the orbits produced at the four different subcritical speeds tested for each condition are presented for the 10 mm bearing support first. These are followed by general observations made with the experimental rig configured for the 6 mm bearing support.

4.5.1 Residual Misalignment with Residual Unbalance - Baseline

Orbit plots for the unfiltered RMRU response at Bearing 1, filtered RMRU response at Bearing 1 and the filtered RMRU response at Bearing 4 are shown in Figures 4.14, 4.15 and 4.16, respectively. The unfiltered response was included to show how different it is to the filtered response. It can be seen that the orbit shapes at the different speeds are not as clear as the filtered response. Also, the shapes seen at 10 Hz and 20 Hz are noticeable different from those seen in the filtered response due to the presence of higher harmonics which distort the shape. Therefore, as previously mentioned, all observations will focus on the filtered orbits.

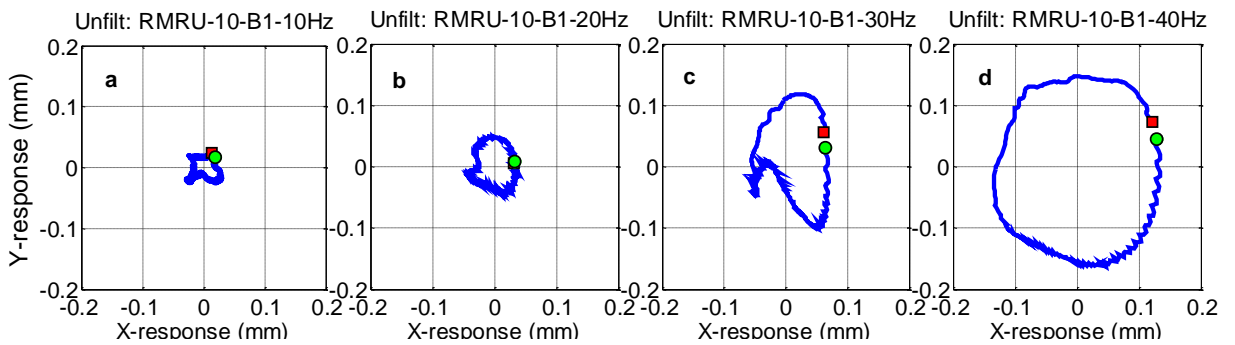


Figure 4.14 RMRU unfiltered orbits for 10 mm supports at B1 for: a) 600 rev/min (10 Hz), b) 1200 rev/min (20 Hz), c) 1800 rev/min (30 Hz) and d) 2400 rev/min (40 Hz)

The filtered response (Figure 4.15) produced forward whirling orbits at all speeds tested. The size of the orbits produced increased with increasing steady-state speed. Except for 30 Hz (Figure 4.15c), the shapes generated at all other speeds suggest the rotor $1\times$ forced response to the residual mass unbalance was the major vibration component. This was

further supported by the almost perfect circular orbit seen at 40 Hz (Figure 4.15d). The point in the lower left corner and elongation of the orbit shape created at 30 Hz suggests the $2\times$ component in the vibration response at this speed [118] was larger than at the other speeds. There exist several possibilities for the generation of a $2\times$ component in the vibration response. According to Muszynska [118], the most likely reasons are radial preload from misalignment and shaft or support stiffness asymmetry. Given that 30 Hz is approximately half of the first few natural frequencies observed for the rig, it was most likely due to the occurrence of 0.5 fractional resonance [66].

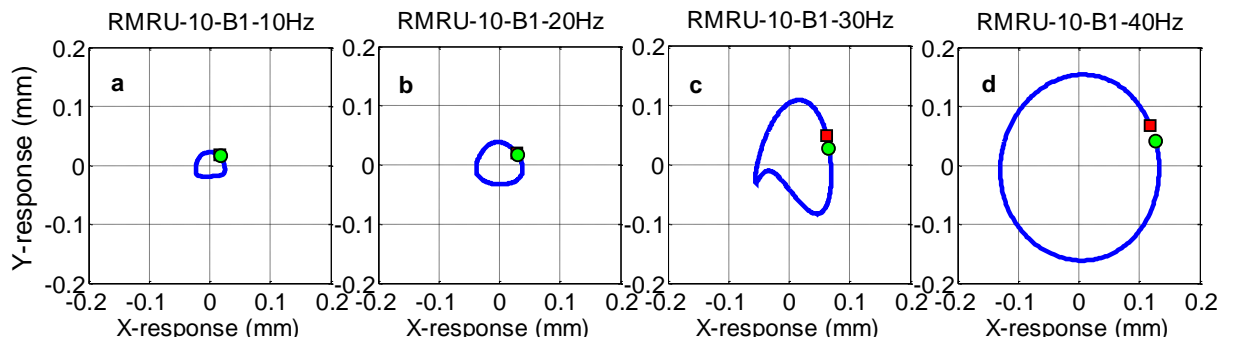


Figure 4.15 RMRU orbits for 10 mm supports at B1 for: a) 600 rev/min (10 Hz), b) 1200 rev/min (20 Hz), c) 1800 rev/min (30 Hz) and d) 2400 rev/min (40 Hz)

Forward whirling centred orbits were obtained at Bearing 4 (see Figure 4.16). Note that the shape and size of these orbits remained fairly unchanged over the speed range tested. The almost perfectly circular shapes suggest the dynamic behaviour of the shorter rotor was the shaft lateral synchronous vibration ($1\times$) due to unbalance with little or no influence of preload from the residual misalignment. Similar observations of circular orbits with negligible change in size with increasing speed were made at Bearing 4 for all fault conditions tested. The short shaft was too rigid at this measurement location to be affected by the fault conditions. It was also quite interesting to note that for all the conditions, the circular orbits meant that stiffness asymmetry for the short shaft was almost non-existent. There is also the possibility that the measurement location at Bearing 4 was too far removed from the actual fault locations (all of which were on the long shaft in close proximity to Bearing 1) to detect any changes in the system. Consequently, the observations hereafter will focus on the Bearing 1 location.

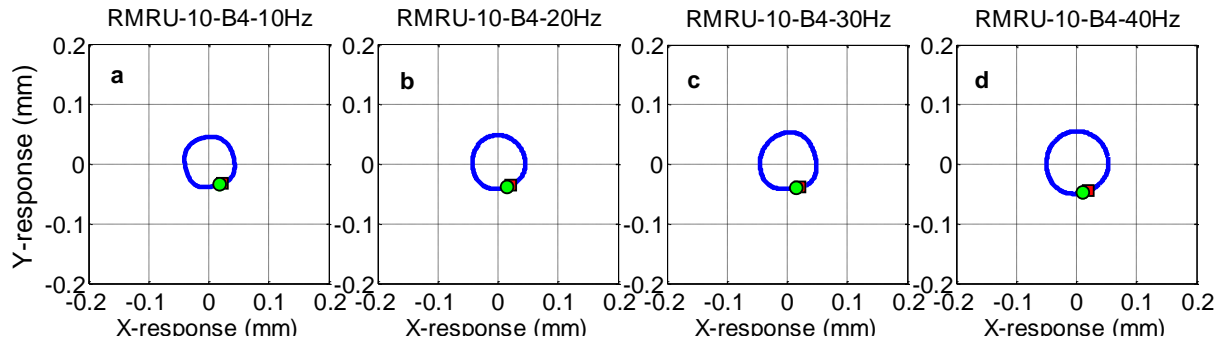


Figure 4.16 RMRU orbits for 10 mm supports at B4 for: a) 600 rev/min (10 Hz), b) 1200 rev/min (20 Hz), c) 1800 rev/min (30 Hz) and d) 2400 rev/min (40 Hz)

4.5.2 Added Unbalance

The effect of the Added Unbalance condition on the shaft behaviour is shown in Figure 4.17. Forward whirling orbits can be seen at all speeds tested. As seen previously in the baseline case, the size of the rotor orbit increased with increasing speed. During rotation, an unbalance condition causes the generation of an inertia centrifugal force which rotates at the rotor rotational frequency. Considering this, at low speeds the effect of the unbalance force would be negligible and this is evident for the Added Unbalance condition at 10 Hz and 20 Hz (Figures 4.17a and b, respectively); as the orbit shapes and magnitudes are almost identical to the orbit in the baseline condition at corresponding speeds. However, the Added Unbalance condition did affect the orbit shape at higher speeds.

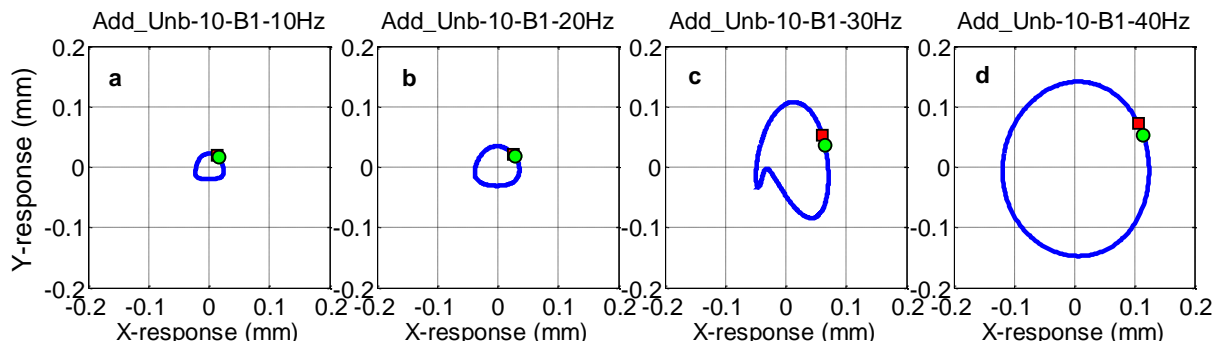


Figure 4.17 Added Unbalance orbits for 10 mm supports at B1 for: a) 600 rev/min (10 Hz), b) 1200 rev/min (20 Hz), c) 1800 rev/min (30 Hz) and d) 2400 rev/min (40 Hz)

At an initial glance the orbit produced for the current case at 30 Hz (Figure 4.17c) appeared similar to the RMRU case at the said speed (see Figure 4.15c), however, there was a slight change in the shape in the vicinity of the indentation to the bottom left corner of the orbit, which indicates a change in the relative amplitudes of the $1\times$ and $2\times$ components in the response [118]. There was either a reduction in the forced synchronous ($1X$) due to unbalance or an increase in the $2\times$ component. Given only an unbalance mass was added to the scenario, without any change in any other variable which might have altered the $2\times$ component in the measured signal, such as preload, support stiffness asymmetry etc., deductively, there was a reduction in the $1\times$ forced response amplitude on adding an unbalance mass to Disc 2.

One might instinctively think that the addition of an unbalance mass would increase the vibration response in the system [11], however, it is well accepted that the phase between the residual unbalance in a rotor-bearing system and any added unbalance determines the resultant effect on the system; when in phase the resultant effect is a net increase in the system's unbalance response and vice versa. This observation is consistent at 40 Hz (Figure 4.17d) as even though the shape is fully circular, and hence dominated by a synchronous unbalance $1\times$, there was a small but noticeable reduction in the vertical and horizontal responses when compared to the baseline RMRU condition at 40 Hz (Figure 4.15d).

4.5.3 Bow

Figures 4.18(a) and 4.18b show the orbit plots that were generated for the Bow condition at 10 Hz and 20 Hz, respectively. Forward whirling centred orbits are seen at both speeds. Vibration data were not acquired for 30 Hz and 40 Hz as near violent vibrations were experienced at 20 Hz thus leading to the decision to desist from testing at higher speeds to prevent any unsafe working conditions or damage to the rig.

For a rotor with an initial deflection or bow, the main force exerting on the rotor is the elastic restoring force from the flexible shaft deformation [62]. It can be seen that forces acting on the system are present from the lowest speeds tested, as the orbit generated at 10 Hz and 20 Hz had responses that were approximately three times as large as what was

observed for the RMRU (Figures 4.15a and 4.15b) and Added Unbalance (Figures 4.17a and 4.17b) conditions at the said speeds. The size of the shapes observed here suggests there was an increase in the synchronous ($1\times$) amplitude due to Bow.

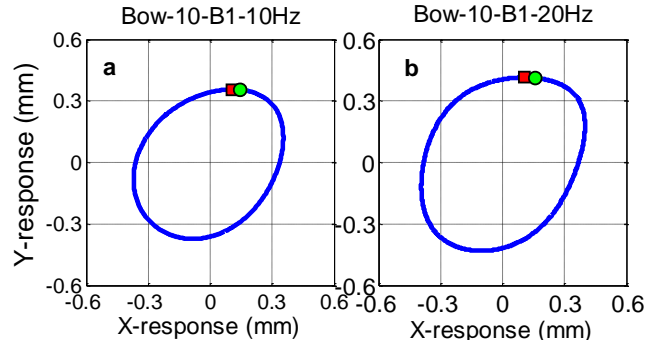


Figure 4.18 Bow orbits for 10 mm supports at B1 for: a) 600 rev/min (10 Hz) and b) 1200 rev/min (20 Hz)

Recall that the Added Unbalance case (see Section 4.5.2) was unchanged from the baseline RMRU condition at 10 Hz. It should therefore be noted that an increase in the orbit response due to changes in the synchronous ($1\times$) amplitude at low speeds could be a characteristic feature for distinguishing a rotor Bow from say a mass eccentricity (Added Unbalance) [84]. Notwithstanding, care should be taken when diagnosing a bow condition, as this might have been caused by a crack condition [84]. Even though the $1\times$ unbalance response was more dominant, the distorted ellipse seen at both speeds suggest the presence of $2\times$ harmonic components in the vibration response. This could possibly be due to the support stiffness asymmetry.

4.5.4 Crack

The rotor orbit shapes created by the Crack condition is presented in Figure 4.19. Forward precession orbits are observed at each speed. As seen with previous conditions, the size of the orbit increases with increasing speed and are stretched in the vertical direction at all speeds. At 10 Hz the stretched elliptical orbit suggest there is some $2\times$ component present in the vibration, but the synchronous ($1\times$) vibration, which might have been caused by bowing [58], was dominant. On increasing to 20 Hz the distorted orbit signals an increase in the $2\times$ component of the vibration response. The $2\times$ component

persists at 30 Hz, but interestingly not as dominant as what was observed for the RMRU and Added Unbalance conditions at the said speed. At 40 Hz the vibration response was dominated by the forced synchronous ($1\times$) response, but the distorted ellipse implies the presence of a smaller $2\times$ component. The consistency of the $2\times$ harmonic component at the different speeds suggests there was an increase in $2\times$ response because of an increase in the stiffness asymmetry of the rotor system due to the crack [58].

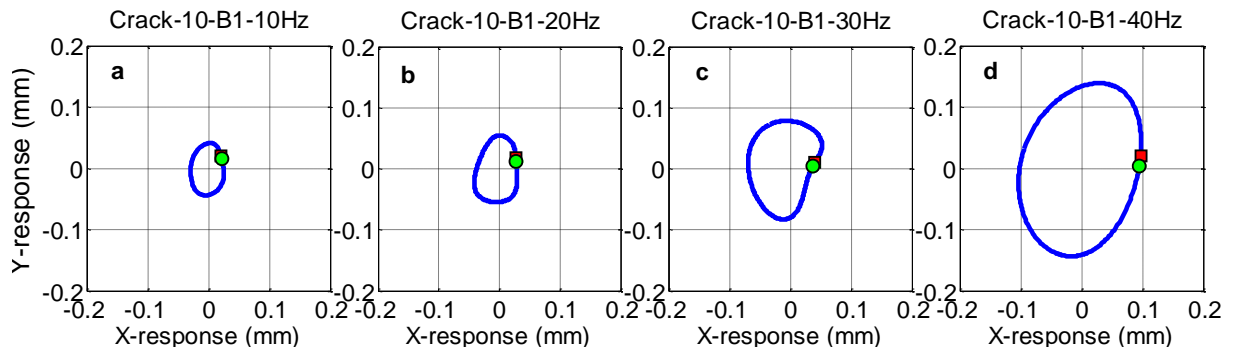


Figure 4.19 Crack orbits for 10 mm supports at B1 for : a) 600 rev/min (10 Hz), b) 1200 rev/min (20 Hz), c) 1800 rev/min (30 Hz) and d) 2400 rev/min (40 Hz)

The orbit shape at 30 Hz implies that a larger $1\times$ synchronous component exists for the crack case than with the RMRU and Added Unbalance cases. This could have been possible if the crack caused a shift in the natural frequency of the rotor [85] and thereby shifting the location of the $\frac{1}{2}$ fractional resonance that was observed earlier. The orbit was perused at different speeds between 25 and 30 Hz and, as shown in Figure 4.20, an orbit with an external loop (“figure 8”) was generated at 28.5 Hz. Needless to say that the customary inner loop that was presented in previous studies [63, 84, 85] was not observed here. Bently [84] reported that the “figure 8” or outside loop shape is a conventional example of a cracked shaft and resulting shaft bow combined with a steady-state preload, such as gravity. For reference, the RMRU conditions at half of the 1st and 2nd natural frequencies (by appearance) are presented in Figures 4.21a and b, respectively. The shape observed in Figure 4.21a indicates the $1\times$ frequency dominated the response, whereas in Figure 4.21b, at half the 2nd natural frequency ($56.76/2$ Hz), the shape has a small but noticeable outside loop which indicates the $2\times$ response at this speed excited the 56.76 Hz natural frequency. On comparing Figure 4.21b (RMRU at half of the 2nd natural frequency) to Figure 4.20 (crack at half of the 2nd natural frequency), it can be seen that

crack resulted in an increase in the $2\times$ response as the external loop is larger than observed for the RMRU case at the said speed. Patel and Darpe [55] presented a similar shape for the vibration response of a rotor with a slight angular misalignment at the $\frac{1}{2}$ bending critical speed.

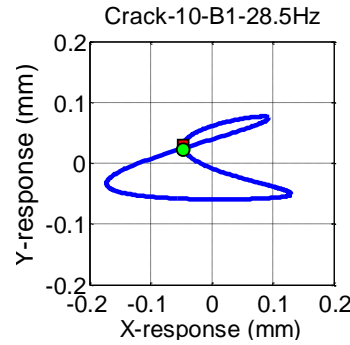


Figure 4.20 Crack orbit for 10 mm supports at B1 for: a) 1710 rev/min (28.5 Hz); approx. half of the second natural frequency (56.67 Hz)

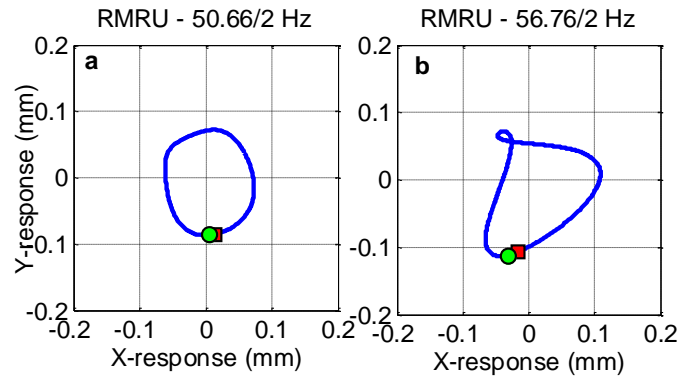


Figure 4.21 RMRU orbit at B1 for half of a) 50.66 Hz (1st) natural frequency and b) 56.76 Hz (2nd) natural frequency

Crack breathing, causes the shaft stiffness to vary twice; starting at open at 0^0 , the stiffness is lower when open, 180^0 afterwards the crack closes and the stiffness is higher and returns to the lower value on completion of the rotation. Due to this stiffness anisotropy crack breathing excites a $2\times$ frequency which usually generates a characteristic inner loop in the orbit plot. However, crack breathing is either aided or constrained by unbalance depending on the relative phase between the crack and shaft unbalance; the unbalance orientation [64, 67, 69]. The unbalance orientation can also be defined as the angular position of the unbalance mass relative to the weak crack direction [69]. This

unbalance effect increases with shaft rotation speed, because the centrifugal force due to unbalance is proportional to the square of angular speed (i.e. it increases rapidly with speed). Therefore, the unbalance effect can be sizeable enough to oppose crack opening when out of phase (180° relative phase difference) with the crack or promote crack opening when in phases (0° relative phase difference) with the crack.

A shaft unbalance which is in phase with the crack may even promote an open crack which remains open during shaft rotation, thus the usual $2\times$ harmonic response with an inner looped orbit shape would not be present. Muszynska [118] cited that the amplitude magnitudes between the $1\times$ caused by unbalance and the $2\times$ generated from the crack or the magnitude of the ratios of the $1\times$ and $2\times$ amplitudes predicts whether there will be a full internal loop or an indentation on the $1\times$ orbit. In cases where the magnitude of the $1\times$ or unbalance component is larger than the amplitude of the $2\times$, the internal loop does not exist. Therefore, it is apparent that the externally looped orbit generated for crack at half the 2nd natural frequency (see Figure 4.20) was due to breathing.

4.5.5 Looseness

Figure 4.22 shows the orbits obtained for the Looseness condition. As seen with previous conditions tested, centred forward procession orbit shapes were observed. As depicted by the increasing orbit sizes, the vibration response for Looseness increased with increasing speed. The shapes obtained suggest that forced synchronous ($1\times$) response due to unbalance dominated the vibration response at the different speeds tested. The distorted ellipse at 30 Hz is possibly due to the $2\times$ harmonic response mentioned earlier. The level of unbalance seen here because of Looseness was larger than what was observed in the RMRU (Figure 4.15) and Added Unbalance (Figure 4.17) conditions, especially at 40 Hz where the vibration amplitudes were significantly larger. Such large amplitudes are expected in cases where unbalance dominates given the unbalance force increases significantly with increasing speed.

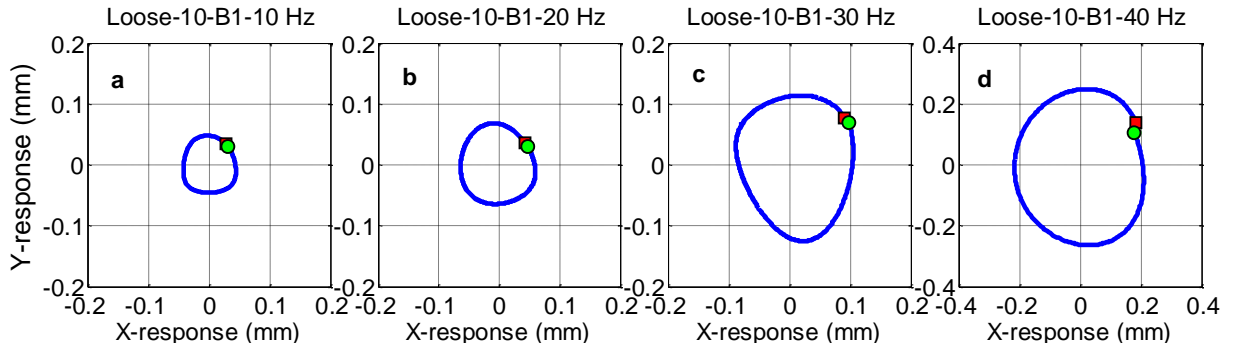


Figure 4.22 Looseness orbits at B1 for: a) 600 rev/min (10 Hz), b) 1200 rev/min (20 Hz), c) 1800 rev/min (30 Hz) and d) 2400 rev/min (40 Hz)

Conventionally, during a looseness case, the unbalance force carried by the rotor may occasionally exceed the gravity and/or other lateral forces applied to the rotor and pedestal. This causes a periodic lifting of the pedestal, resulting in system stiffness softening, its cyclic variability and impacting. These symptoms would result in changes in the synchronous responses and the appearances of fractional subsynchronous vibrations. Most notably, the occurrence of the $0.5\times$ vibration is most common in the field [58], however, this conventional observation was not noticed in the present study. This is not surprising given the bearing mounting used here is the flanged type and not, say a pillow block type, which sits on a pedestal.

4.5.6 Misalignment

Figure 4.23 presents the orbit plots generated by the Misalignment condition. Forward precession orbits can be seen for all speeds except at 30 Hz. The orbits observed at 10 Hz (Figure 4.23a) and 20 Hz (Figure 4.23b) appear slightly distorted, thus suggesting the presence of a $2\times$ component in the vibration response [63, 118]. The orbit seen at 30 Hz (Figure 4.23c) has a forward precession with a backward precession external loop. This indicates the presence of a strong preload due to the misalignment. Compared to the crack case previously observed in Figure 4.20, the orbit generated by the misalignment case at 30 Hz (see Figure 4.23c) has a smaller outside loop. This shows that the effect of the $1\times$ component in the Misalignment case is more dominant than in the crack case which, by extension, would be dominated by the $2\times$ component. Put differently, the $2\times$ component is secondary to the $1\times$ component, thus it possesses much smaller amplitude than that of the

$1 \times [118]$. It is popularly held that the difference in the classical orbit shapes generated by misalignment (outer loop/figure 8) and crack (inner loop) can be used to distinguish either fault conditions [63], however, as seen from the present study, care should be taken when using this as an unequivocal rule, since the outer loop can be generated for both fault conditions [84].

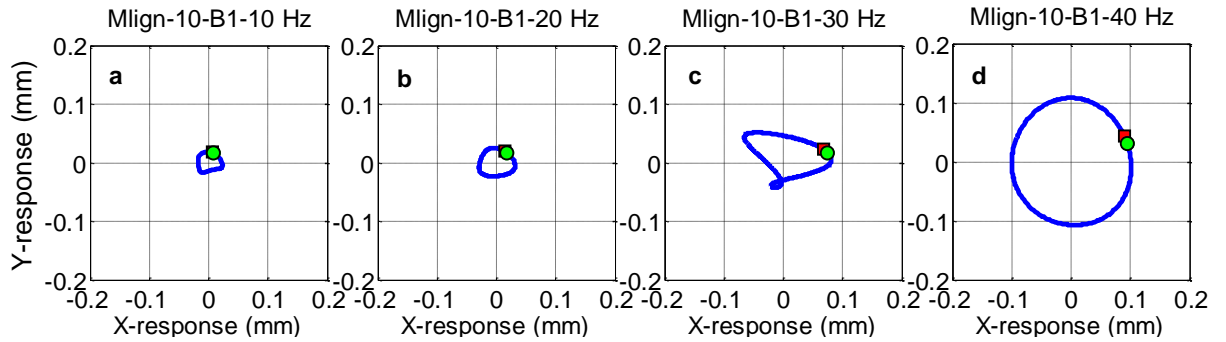


Figure 4.23 Misalignment orbits at B1 for: a) 600 rev/min (10 Hz), b) 1200 rev/min (20 Hz), c) 1800 rev/min (30 Hz) and d) 2400 rev/min (40 Hz)

The “figure 8” or outside loop for the misalignment case (Figure 4.23c) was generated in close proximity of half the 56.67 Hz critical speed. In the previously shown Crack case (Figure 4.20) the loop was generated at 28.5 Hz which is slightly less. It therefore seems that the presence of the crack on the rotor may have lowered the rotor natural frequency. Further experimentation would be required to confirm this.

At 40 Hz the orbit shape resorts to a perfectly centred circular orbit with only a hint of the vertical response being larger than the horizontal one. Clearly, the rotor $1 \times$ forced response to mass unbalance was the major component in the vibration. It seems that the addition of the shim under Bearing 1 pedestal for the present condition increased the rotor stiffness in the vertical direction, thus resulting in an almost 1:1 ratio of the X:Y deflection than what was observed in the baseline RMRU case at the said speed (see Figure 4.15d). This increased stiffness with misalignment is consistent with observations made by Patel and Darpe [3], which showed that the misalignment preload increases the effective stiffness of the rotor in the direction of the misalignment. This concludes that the slight stretching of orbits that were previously noticed at 40 Hz for the baseline RMRU (Figure 15d), Added Unbalance (Figure 4.17d) and Looseness (Figure 4.22d) cases were similarly caused by the rotor bearing support system stiffness asymmetry.

It was noticed that the amplitudes of the vibration response for the Misalignment condition at all speeds were smaller than those observed in the baseline RMRU condition. This could have been caused by the increase in the stiffness of the rotor system due to the misalignment.

4.5.7 Rub

The rotor orbital patterns observed for the Rub condition are shown in Figure 4.24. Unprecedented in the present study is the occurrence of backward whirling orbits at 10 Hz (Figure 4.24a) and 20 Hz (Figure 4.24b), whilst the orbital patterns for 30 Hz (Figure 4.24c) and 40 Hz (Figure 4.24d) are forward whirling. This is also the first case in which the size of the orbit did not progressively increase with increasing speed.

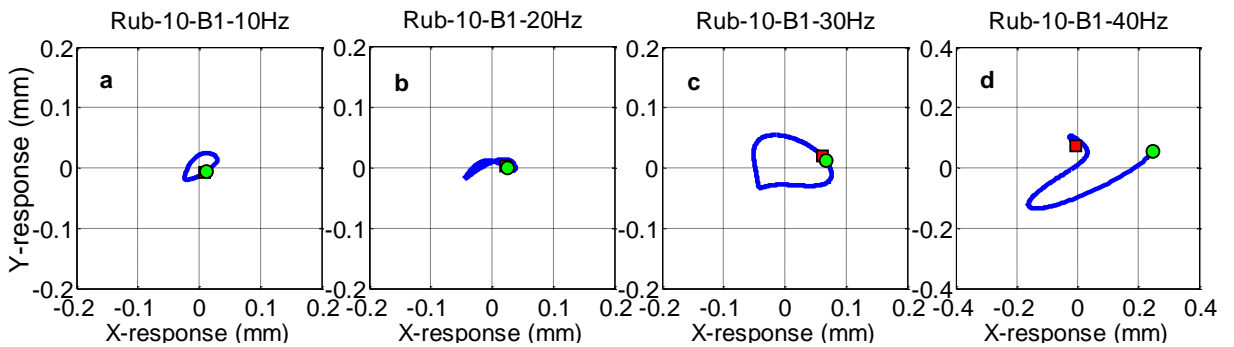


Figure 4.24 Rub orbits at B1 for: a) 600 rev/min (10 Hz), b) 1200 rev/min, (20 Hz), c) 1800 rev/min (30 Hz) and d) 2400 rev/min (40 Hz)

As seen in previous cases the slightly distorted elliptical shape with a point on the lower left hand corner suggest that there was a $2\times$ component in the response, but the forced synchronous ($1\times$) response due to unbalance was more dominant at 10 Hz. At 20 Hz the orbit, which is stretched in the horizontal direction, starts in a backward procession and then ends in forward whirling external loop. Therefore, on changing from 10 Hz to 20 Hz, the $2\times$ component clearly got larger. It seems at 20 Hz there was some increasing influence of a preload on the rotor and/or stiffness asymmetry or a combination of both. The shape of the looped orbit at this speed indicates that some loading acting downwards in the vertical direction was present [12]. Evidence of the strong vertical preload pervades

through all speeds tested, except at 40 Hz. This, of course, could be justified by the fact the rub apparatus made contact on the shaft surface in the vertical direction only. Since the radial force due to the rub apparatus was acting vertically downwards, the vertical amplitudes in the shapes shown are lower than the horizontal ones, as the rotor “freedom” is restricted in the vertical direction [72].

The shape seen at 30 Hz indicates the $2\times$ component was less dominant in the response than the $1\times$ component [118]. It was interesting to note that the strong presence of a $2\times$ harmonic component in the response possibly due to the $\frac{1}{2}$ fractional resonance that was suspected at the same speed for RMRU, Added Unbalance and Misalignment conditions was not seen here. It is quite possible that contact during the rub event increased the stiffness of the rotor thereby shifting its critical speed to some higher value [10, 77]. Again, the stretching of the orbit in the horizontal direction implies some increase in stiffness in the vertical direction.

The orbit pattern noticed at 40 Hz was quite incomplete. This was traced over one shaft rotation (cycle). To get a better indication of the complete orbit, the response was plot over two cycles. The result is presented with other speeds for comparison in Figure 4.25. Notice that the orbit is mostly forward whirling with a small backward whirling inner loop. The shape seen at 40 Hz for two cycles (Figure 4.25d) is similar to the orbit reported by Chu and Lu [10] for a single disc rotor-bearing rig operating at a rotating speed of 2857 rev/min (approximately 93.7 % of the first critical speed). The orbit observed by Chu and Lu [10] was dominated by multiples of the fractional $0.5\times$ harmonic component. To ascertain if this was the case in the present study, the displacement spectra for vertical and horizontal directions with reference to the RMRU baseline case were generated at 40 Hz as shown in Figure 4.26 and perused for signs of multiples of fractional subharmonics. It can be seen that in both horizontal and vertical directions (Figures 4.26c and d, respectively) subsynchronous frequencies and their integer multiple harmonics were generated by the rub fault when compared to corresponding vertical and horizontal RMRU spectra (Figures 4.26a and b, respectively). Therefore, this confirms that the orbit shape produced for rub at 40 Hz shown in Figure 4.24d was due to the presence of subsynchronous frequencies and their harmonics in the response.

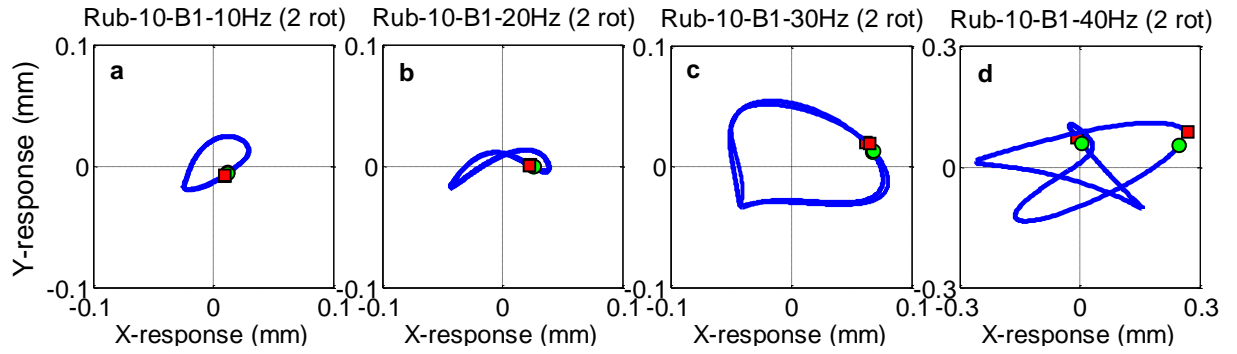


Figure 4.25 Rub orbits at B1 over 2 shaft rotations for: a) 600 rev/min (10 Hz), b) 1200 rev/min (20 Hz), c) 1800 rev/min (30 Hz) and d) 2400 rev/min (40 Hz)

The backward whirling orbit at 10 Hz and 20 Hz suggest the friction between the rub apparatus blade and the rotor was high enough to cause backward whirling [120]. This indicates there was a reduction in the friction at speeds above 20 Hz as the orbit evolved to forward whirling on reaching 30 Hz and remained as such at 40 Hz. As observed with the rub case in the present study, Muszynska [58] highlighted that the diagnosis of rotor rubbing from vibrational data is based on several factors including: the appearances of subsynchronous fractional components which when filtered most often exhibit backward orbiting. Most importantly, partial or full backward orbiting of the rotor is the most characteristic feature which distinguishes rub from other faults.

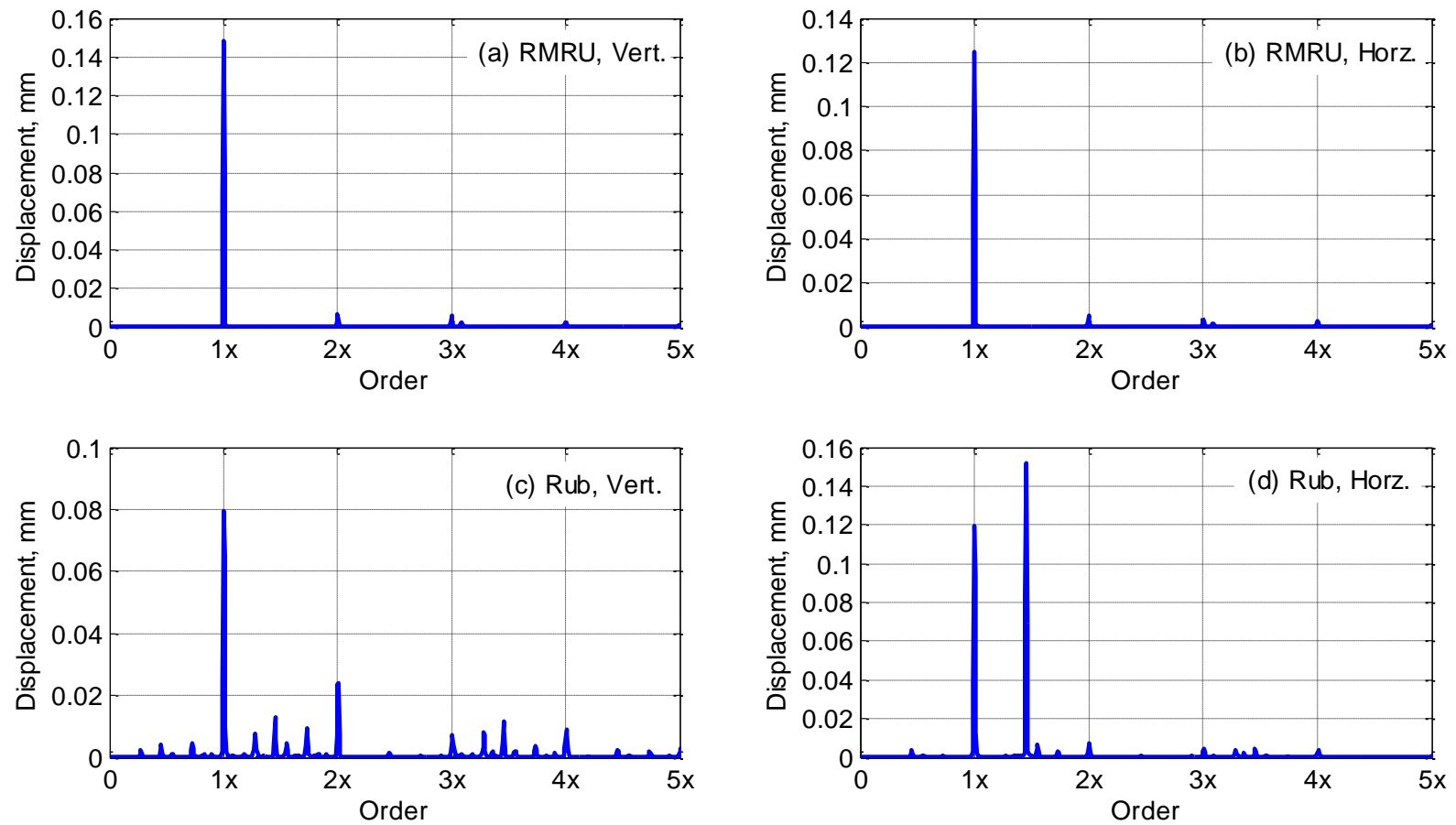


Figure 4.26 Simple amplitude spectra at 40 Hz from B1 of 10 mm supports for: (a) RMRU vertical, (b) RMRU horizontal, (c) Rub vertical and (d) Rub horizontal

4.5.8 General Observations of Orbit Shapes on a different Flexible Machine (with 6mm supports)

The orbit plots for the RMRU baseline condition with the 6 mm bearing supports are presented in Figure 4.27. For brevity a sample set of the orbits obtained at Bearing 1 measurement location for the conditions tested at 30 Hz is given in Figures 4.28. Note that Bow was included in Figure 4.28d at 10 Hz as oppose to 30 Hz because near violent vibrations with large deflections prevented testing at speeds higher than 10 Hz.

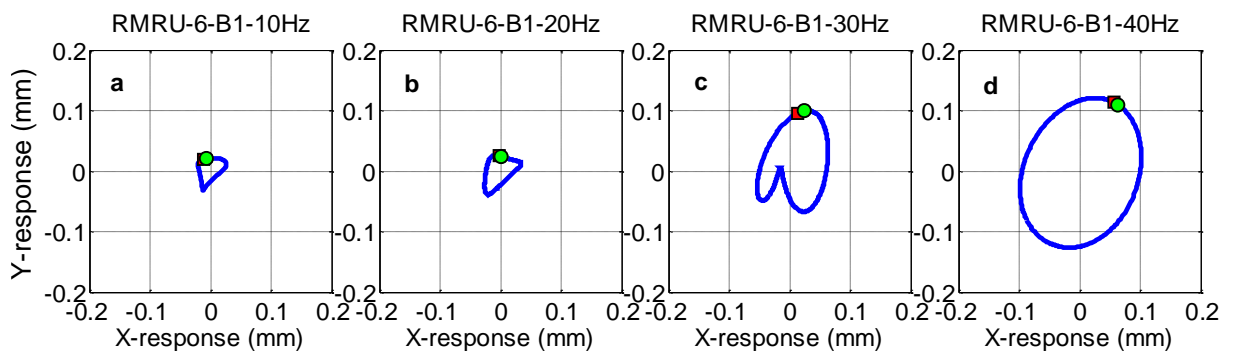


Figure 4.27 Residual Misalignment with Residual Unbalance orbits at B1 for: a) 600 rev/min (10 Hz), b) 1200 rev/min (20 Hz), c) 1800 rev/min (30 Hz) and d) 2400 rev/min (40 Hz);

The orbits for the baseline RMRU condition with 6 mm supports shows that the system's response is now dominated by a larger $2\times$ harmonic component that what was observed with the 10 mm support (Figure 4.15) [76, 118]. It therefore seems the more flexible supports were susceptible to increased levels of shaft misalignment. Despite this change in the response, and changes in the shapes of the orbits for the different conditions, it was noted that the relative behaviour of the shaft for a given condition at the different speeds was preserved. That is, the analysis given in the previous section still applies for the 6 mm supports. The only exception to this observation was the Rub condition which had different behaviour between 20 Hz and 30 Hz. Rub at 40 Hz (Figure 25f) for the 6 mm supports, however, showed the same behaviour as seen with the 10 mm supports.

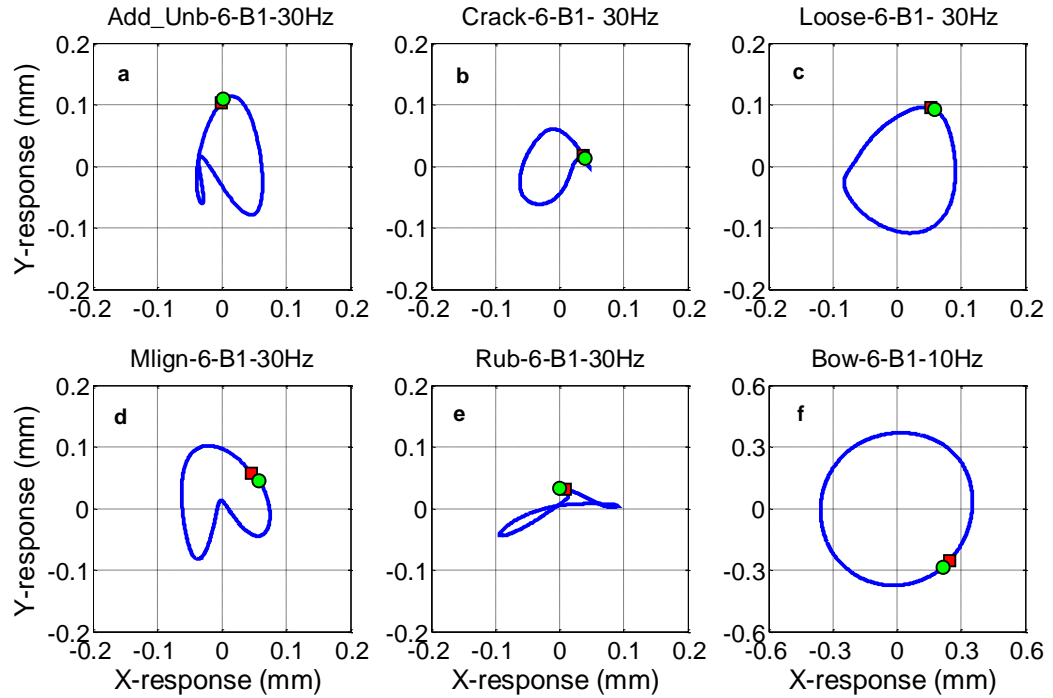


Figure 4.28 Orbit for 6 mm supports at B1 for : a) Added Unbalance, b) Crack, c) Looseness, d) Misalignment, e) Rub at 1800 rev/min (30 Hz) and f) Bow at 600 rev/min (10 Hz);

4.6 Summary

An experimental study on the shaft orbit response for a range of commonly encountered rotor-related faults was presented. Testing was done on a small laboratory rig on which shaft absolute vibration data, measured by orthogonal XY displacement probes, were acquired for a baseline condition as well as; added unbalance, bow, crack, looseness, misalignment and rub fault conditions that are introduced separately at four different subcritical steady-state rotating speeds. One fault was introduced to the rig at any given time. Orbit plots were generated and critically analysed to gain insight to changes in the behaviour of a single machine when influenced by different fault conditions at different speeds. The orbit plots generated were also compared to those observed on a similarly configured experimental rig with different dynamic characteristics on which the same experiments were done. The study presented here provides useful information for practical rotor fault diagnosis and also offers some worthwhile qualitative experimental insight to analytical studies related to the rotor faults observed.

5 COMBINED VIBRATION AND THERMAL ANALYSIS FOR THE CONDITION MONITORING OF ROTATING MACHINERY

Reformatted version of the following papers:

1. **Title:** Combined vibration and thermal analysis for the condition monitoring of rotating machinery

Authors: Adrian. D. Nembhard, Jyoti K. Sinha, A. J. Pinkerton and K. Elbhah

Status: Published in Structural Health Monitoring journal
2. **Title:** Fault diagnosis of rotating machines using vibration and bearing temperature measurements

Authors: Adrian. D. Nembhard, Jyoti K. Sinha, A. J. Pinkerton and K. Elbhah

Status: Published in Diagnostyka Science Journal
3. **Title:** Condition monitoring of rotating machines using vibration and bearing temperature measurements

Authors: Adrian. D. Nembhard, Jyoti K. Sinha, A. J. Pinkerton and K. Elbhah

Status: Published in Advances in Condition Monitoring of Machinery in Non-Stationary Operations

Abstract: Traditional practice in vibration-based condition monitoring of rotating machines with a multiple bearing system, such as turbo-generator sets, is data intensive. Since a number of sensors are required at each bearing location, the task of diagnosing faults on these systems may be daunting for even an experienced analyst. Hence, this study seeks to develop a simplified fault diagnosis method that uses just a single vibration and a single temperature sensor on each bearing. Experiments were done on a laboratory rig with two dissimilar length rotors supported through four ball bearings. Commonly encountered

rotor-related faults were independently simulated and compared to a baseline condition. For reference, conventional vibration spectrum analysis was done first. Overall vibration analysis was then conducted and combined with temperature data in two diagnosis approaches. Learning from the first combined approach, which had some limitations, was used to propose a principal component analysis–based approach that was demonstrated with and without temperature data. Results of the proposed principal component analysis–based method suggest that supplementing vibration data with temperature measurements gives improved fault diagnosis when compared to fault diagnosis using vibration data alone. The experimental rig, measurements done, description of both combined approaches and results obtained are presented in this article.

Keywords Vibration analysis, temperature monitoring, condition monitoring, rotating machinery, fault diagnosis, principal component analysis

5.1 Introduction

Traditional practice in vibration-based condition monitoring (VCM) is a mature technique for fault diagnosis (FD) of rotating machines, however, it is a relatively involved process that mandates judgment and expertise from a trained analyst. The limitations of the method are further compounded when considering VCM of a rotating machine with multiple bearings, such as a multi-stage Turbo-generator set. In that case, a number of vibration sensors and measurements are required at each bearing location [1], which results in the acquisition of large volumes of data. The method then becomes a computational burden to process and the task of diagnosing faults on these systems may be daunting, if not impossible, for even an experienced analyst.

After acquiring vibration data, there exists the challenge of removing unwanted contents in the signal in order to produce a signal with features that best represent the health (condition) of the machinery being monitored. The objective of signal processing is to extract and display from the measured data the maximum amount of useful information (descriptors/features) which best represent the health of the machinery in order to make

diagnosis much easier for the user [53, 54]. In standard practice, the Fast Fourier Transform (FFT) is the most widely applied signal processing technique for converting a signal from the time domain to the frequency domain. The output of the FFT is represented in the amplitude or Fourier spectrum for feature extraction and analysis. Popular features generated from the frequency domain include Spectrum Energy (SE) [33] and amplitudes of the $1\times$, $2\times$ and $3\times$ spectral harmonic components.

Even though it is a mature signal processing technique, the FFT derived amplitude spectrum has some limitations. It is widely accepted that different machinery faults generate similar features in a spectrum. Thus, various studies have been done on gaining a better understanding on interpreting the dynamic responses of commonly encountered rotating machinery faults such as; crack [3-6], looseness [7, 8], misalignment [3, 6, 8, 9], rub [10] and unbalance [8, 11]. Notwithstanding, there still exists ambiguity in the interpretation of information from faults which generate similar features such as crack and misalignment [3]. Hence, recent efforts in vibration-based condition have focused on proposing new techniques that simplifies the FD process for the vibration analyst.

Elnady et al. [17] proposed the use of the on-shaft vibration (OSV) measurement technique that requires special arrangement of the measurement instrumentation. Sinha and Elbhah [28] used just a single vibration sensor on each bearing and then data fusion in the composite spectrum for diagnosis, but this was slightly computationally involved. Lei et al. [22] compiled a comprehensive review of application of the advanced time-frequency analysis technique, Empirical Mode Decomposition (EMD). The review outlined the suitability of the method over the traditional FFT for the diagnosis of rotating machinery faults when signals are non-stationary and especially for rotor-related faults when vibration data are acquired in displacement. The method, however, does not do well with signals obtained from accelerometers which are usually noisy, hence why it was suggested that wavelets could be more appropriate in that case. Then again, it was also cited that wavelets are susceptible to subjective judgement as the analysis results are dependent on the choice of wavelet base function while EMD mitigates this limitation by being a self-adaptive processing technique. Notwithstanding, the EMD method has its share of limitations, including difficulty in accurately reproducing intermittent signals. As such various improved derivations of EMD or combinations of EMD with other processing techniques

have been proposed to overcome such limitations. These improvements are, however, complex and time consuming which limits its applicability in practical scenarios.

Considerable research has been done on the application of artificial intelligence (AI) techniques; including Neural Networks and Fuzzy Logic, to automate the vibration-based FD process [24]. Consequently, this would minimize VCM's dependence on human elements and improve its processing capabilities. However, AI-based methods can be somewhat digressed from current practical applications, because of their limited diagnosis capabilities when used as an "individual decision system with a single classifier" [26]. Attempts to overcome these limitations, namely the combination of multiple classifiers for FD [26, 27], often times lead to methods with added complexity. Though, AI-based systems have shown promise for automating vibration signal analysis [25], its application is still in the nascent stages and needs further development. Thus, a more simple, but robust technique that would be well appreciated by the relevant industries for practical application is required.

Some researchers [96-99] have chosen to explore the use of pattern recognition techniques such as Principal Component Analysis (PCA) to simplify the FD process. PCA's use in vibration-based fault diagnosis has been predominantly as a feature extraction tool. This is based on the premise that PCA relaxes the computational load by condensing the number of inputs required for classification to a representative few. PCA's usefulness is also based on the premise that a large number of input features does not necessarily contribute to improving the effectiveness of defect classification. The extracted features are usually fed into a classification tool, based on say Neural Network [96]. Researchers have even coupled PCA with multiple classifiers [26, 27] on the basis that a single classifier is not suitable for real life applications [26]. Even though multiple classifiers with PCA are less computationally involved than classification without PCA, these still remain somewhat complex for practical application [26]. The successful classification of gear [38, 97, 100] and bearing [96-99] faults in previous studies done, testify to the opportunity that exists in applying PCA-based technique for the classification of rotating machinery faults. However, from readily available literature, this capacity has not been tried on the FD of commonly encountered rotor-related faults.

The present study aims to develop a diagnosis technique that uses fewer sensors while preserving moderate computational load. The objective is to keep both data acquisition and processing simple. With the wide availability of temperature monitoring systems on rotating machines in industries and studies confirming the sensitivity of temperature measurement to rotating machinery faults [19, 20, 90, 91, 95], an opportunity exists to integrate temperature and vibration data for effective FD. Hence, a simplified FD method that uses a single vibration sensor and a single temperature sensor on each bearing is proposed. Temperature measurements are expected to compensate for the reduction in vibration sensors while replacing the need for advanced and complex signal processing of the vibration data.

Experiments were done on a small laboratory rig with two dissimilar length rotors supported through four ball bearings. Vibration and temperature data were collected for cracked rotor, coupling misalignment and rotor rub faults and compared to a healthy condition. Conventional vibration spectrum analysis was conducted first for reference. Overall vibration analysis was then carried out and combined with temperature data in two diagnosis approaches. The first approach, which uses a simple linear model, was found to have some limitations. Learning from the first approach was then used to propose a Principal Component Analysis (PCA) based approach that was attempted with and without temperature data. Results from the proposed PCA-based method suggested the addition of temperature to vibration data negates the need for complex signal processing and consequently improves the FD process when compared to FD with vibration data alone.

The paper hereafter is organised as follows. In Section 5.2 an illustrated description of the experimental set up and data collection instrumentation is given. The method used to simulate the different fault conditions are then summarized in Section 5.3. Afterwards, conventional vibration spectrum analysis is carried out and discussed in Section 5.4. In Section 5.5, the linear combined approach and the proposed PCA-based combined approach are presented and discussed. Finally, concluding remarks are made in Section 5.6.

5.2 Experimental set up and data collection

Figure 5.1 shows a photograph of the experimental rig used for the experiment [20]. The set up consists of two 20 mm nominal diameter dissimilar length (100 mm and 50 mm) rigidly coupled (Coupling 2) rotors that are supported by four grease lubricated ball bearings. These are secured atop flexible steel pedestals that are bolted to a large lathe bed secured to the concrete flooring. Machined sections accommodating balancing discs are mounted on each rotor. System drive is provided by a 0.75kW, 3 phase, 3000 rev/min motor that is mated to the rotor-bearing system via a semi-flexible coupling (Coupling 1).

The instrumentation and software schematic for the set-up is depicted in Figure 5.2. Rig speed is varied with a speed controller that is operated from a personal computer. The dynamic response of the system is then measured with 100 mV/g accelerometers. Each bearing location has two accelerometers that are mounted with adhesive in mutually perpendicular directions. The vibration data are transmitted through two four channel signal conditioners to a 16 Bit Analogue to Digital (A/D) Data Acquisition System. A data logging software then stores the digitized vibration data on the personal computer. To measure the thermal response of the system, K-type thermocouples are attached between the bearing casing and outside of the outer race of each bearing. This mounting position was used to get the most immediate and accurate temperature measurements possible. All four temperature readings were captured with an eight channel data logger and saved to the personal computer for later analysis.

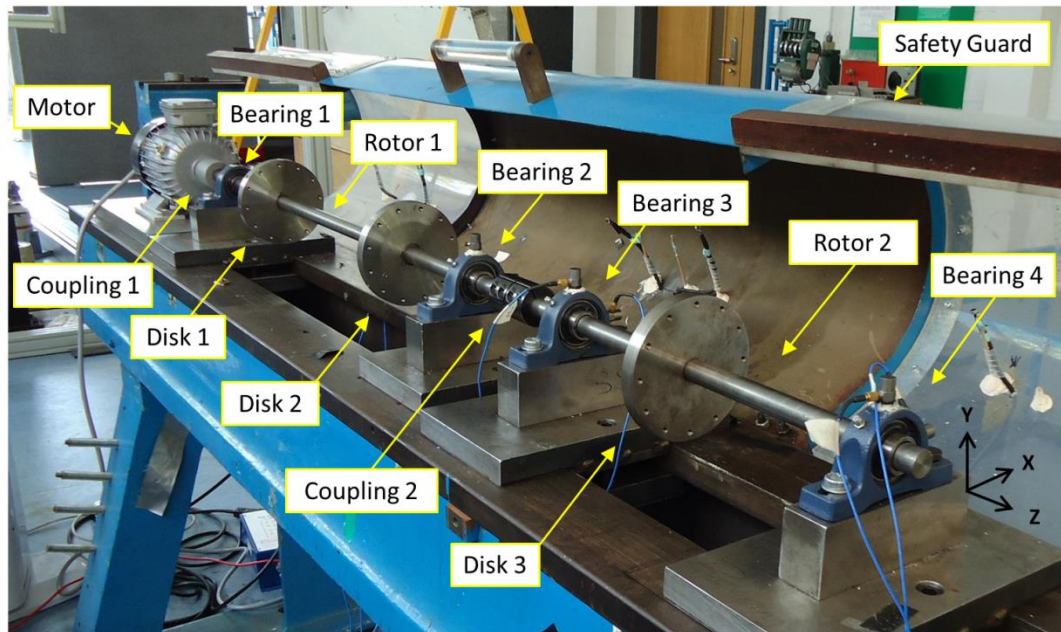


Figure 5.1 Experimental rig mechanical layout

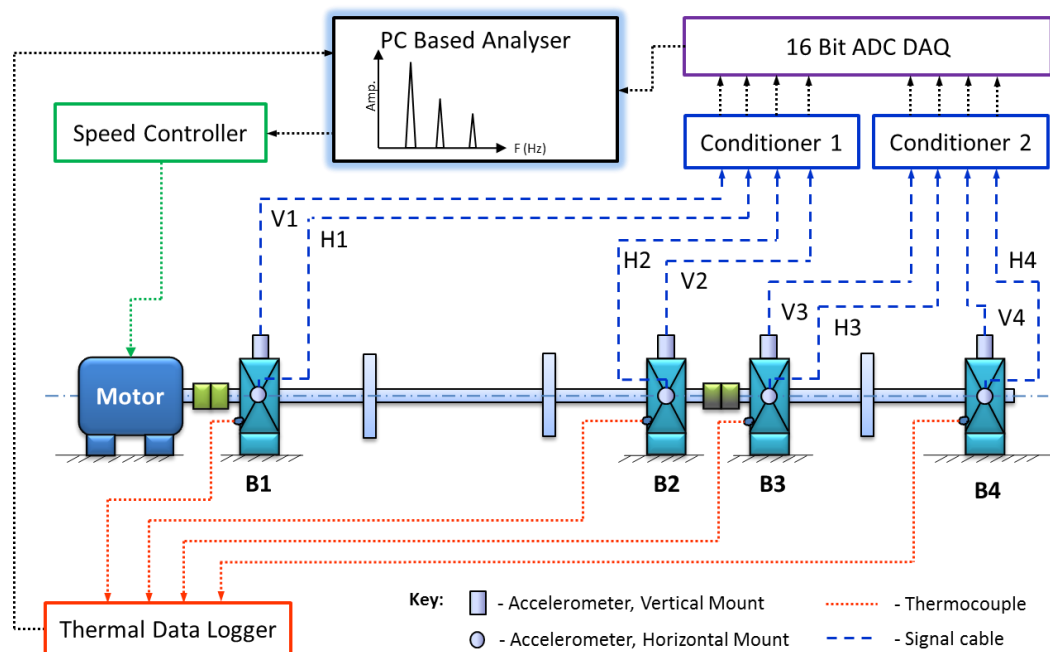


Figure 5.2 Schematic of software and instrumentation

5.3 Simulated faults and experiments

Experiments were done at 40 Hz and 50 Hz to evaluate the impact of speed changes on the different analyses done. Data for the healthy machine condition was collected first in order to establish the baseline conditions for the rig. Vibration and temperature measurements were then taken for three fault conditions; cracked rotor, rotor rub and coupling misalignment. Cracked rotor condition was simulated in three different locations along the length of the rotor as shown in Figure 5.3a. To produce the rotor crack, a 0.25 mm \times 4 mm deep notch (see Figure 5.3b) was cut in the shaft using the Wire Erosion Electro Discharge machining process. In each case a “breathing crack” [90], with a depth of 20% shaft diameter was desired, however, the 0.25 mm notch was too large to give this desired condition. Thus a thin metal sheet of 0.24 mm was inserted down to the base of the notch and glued to one side (see Figure 5.3c) to essentially produce a thin 0.01 mm crack that would breathe (open and close) as the shaft rotates (see Figures 5.3b and 5.3c).

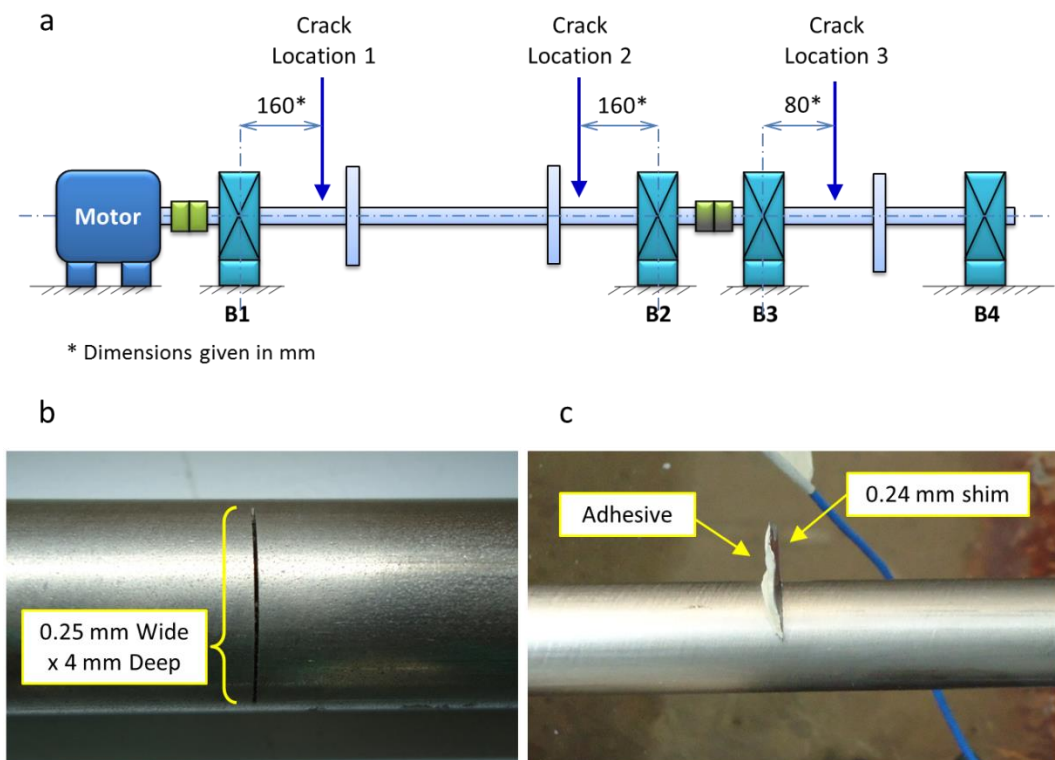


Figure 5.3 Details of crack simulation: (a) locations tested, (b) crack dimensions and (c) shim details

Rub was simulated by a Perspex apparatus consisting of a base bolted to the lathe bed (at 115 mm from bearing 4) and a stand as shown in Figure 5.4. The rub apparatus was installed so that the contact zone of the inner bore on the rub apparatus just touched the rotor shaft. Therefore a full annular rub scenario was created. Misalignment was the final scenario tested in order to minimise the effect of any residual misalignment that could be retained in the system after testing. A steel shim was installed under bearing 3 housing to induce angular misalignment in the y-z plane across the rigid coupling (Coupling 2) located between bearing 2 and bearing 3 (see Figure 5.5). Table 5.1 summarizes the experiments and data collection procedure employed.

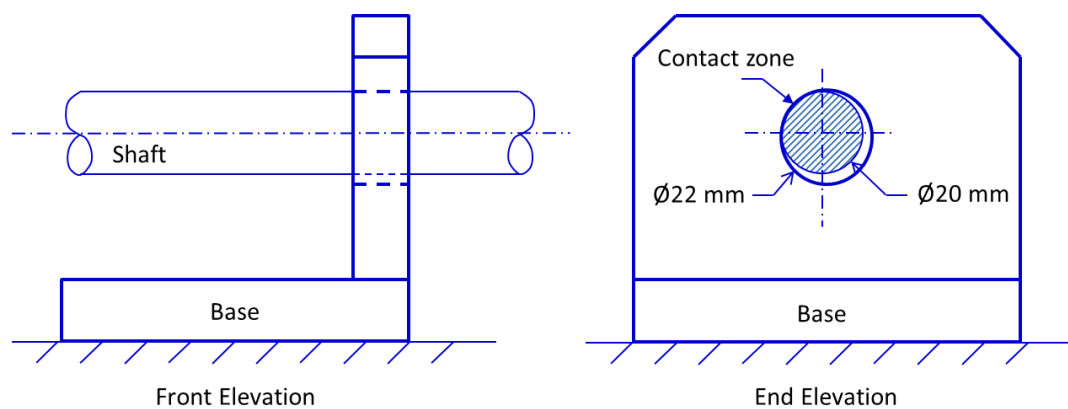


Figure 5.4 Details of apparatus used for rub simulation

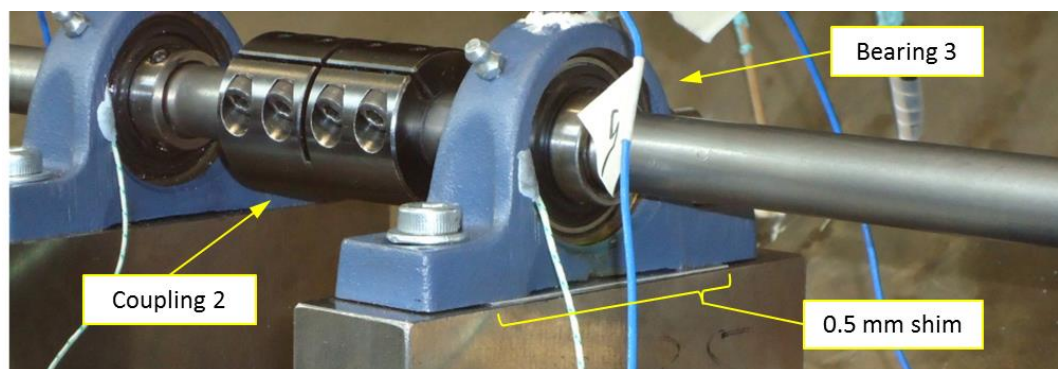


Figure 5.5 Details of Misalignment simulation at Bearing 3

Table 5.1 Summary of experimental procedure used.

No	Code*	Scenario Name	Data collection method
1	Healthy	Healthy	On starting system from rest, bearing
2	Cr Nr1	Crack near bearing 1	temperatures were recorded for a period of ten
3	Cr Nr2	Crack near bearing 2	minutes at 5 second intervals. Vibration data were
4	Cr Nr3	Crack near bearing 3	collected at the ten minute point for a total sample
5	Mlign	Misalignment	time of one minute. After each experiment the
6	Rb Nr4	Rub near bearing 4	system was allowed to cool to ambient
			temperature before configuring the rig to a
			different scenario.

One fault scenario was simulated at a time.

*Same nomenclature used in figures throughout remainder of paper

5.4 Vibration spectrum analysis

For each scenario tested, the acceleration spectrum was generated from data measured in the horizontal radial direction with a sampling frequency of 10 kHz. The stiffness of the experimental rig was higher in the vertical radial direction; thus the amplitudes of vibration measurements taken in this direction were found to be highly suppressed and less useful than those measured in the horizontal radial direction. A sample of the measured vibration signal is shown in Figure 5.6. High pass and low pass filters at 5 Hz and 800 Hz, respectively, were applied to remove unwanted frequencies including noise. An 800 Hz upper frequency limit was adequate for analysing rotor-related faults; as it is usually sufficient to observe the first few spectral components ($1\times$, $2\times$, $3\times$ and $4\times$) for rotor fault analysis, as was the case in this study. Since the 800 Hz frequency limit would have excluded bearing faults and lubrication issues, which would appear as a mound between 1 kHz and 5 kHz, from the spectra, a prior bearing analysis was done to confirm the health of bearings used.

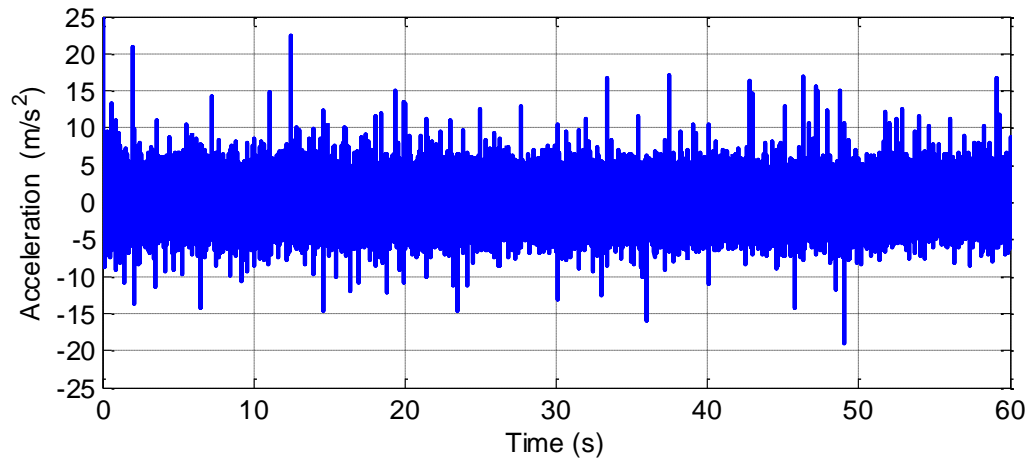


Figure 5.6 Time waveform sample of the measured vibration data

The Fast Fourier spectrum was generated using 16,384 spectral lines which maintained a frequency resolution of 0.610 Hz. For increased clarity, 75% overlap was used to average the spectrum and a Hanning window was also applied. Each spectrum was analysed, starting with the Healthy condition, to gain insight into the different scenarios tested and to identify any possible diagnostic pattern. For the purposes of condition monitoring the amplitudes of the spectral components in the healthy spectrum would be used to establish alarm limits for each bearing location. Violation of these limits in any subsequent spectrum, for the said bearing would signal the presence of a fault. This would trigger the need for fault diagnosis, in which the fault spectrum would then be interrogated in order to note the spectral components present which could indicate the type of fault present. Since the objective of the current study is the development of an FD technique with reference to FD with the amplitude spectra, attention is given to observing and comparing the generation of different spectral components for different fault conditions relative to the healthy condition.

This was done by first looking for a peak in the spectrum that corresponded to shaft rotational speed ($1\times$ component). The said spectrum was then perused for all spectral components present; namely fractional and multiple harmonics of the $1\times$ frequency. The spectrum for each fault scenario was similarly interrogated and compared to the healthy spectrum. Any changes in spectral components between a particular fault and the healthy spectrum was noted and attributed to the presence of the fault. Afterwards, the results

obtained for each fault scenario was compared to identify any possible unique discriminative feature. The analysis was then repeated for each bearing location.

In an attempt to further assess diagnosis with the amplitude spectrum the amplitudes of the $2\times$, $3\times$ and $4\times$ harmonic components at each bearing location for all conditions tested at a particular speed were normalized with their respective $1\times$ component and used to generate plots of the normalized $3\times$ harmonic component against the normalized $2\times$ harmonic component and the normalized $4\times$ harmonic component against the normalized $2\times$ harmonic component. The $2\times$, $3\times$ and $4\times$ harmonic components were normalized with the shaft fundamental frequency ($1\times$) to remove the effect of unbalance across the spectrum, which would be present in all conditions tested, thus making the amplitudes of these spectral features fully indicative of the condition present at each bearing location. Therefore the comparison of spectral features would provide further insight to the results obtained at all bearing location in a single plot.

5.4.1 Results: Spectrum analysis - 40 Hz (2400 rev/min)

Figure 5.7 shows the amplitude spectra obtained at bearing 2 from data acquired at 40 Hz (2400 rev/min). This was typical of results obtained at all four bearing locations. For healthy condition, a dominant peak which corresponds to shaft rotational speed ($1\times$ harmonic component) in addition to a $2\times$ harmonic component was observed. Based on the size of the $2\times$ component in comparison to the $1\times$ component, it is evident that some residual misalignment was present in the rig when testing at the Healthy condition was done [3]. Despite this, the healthy condition still possessed the lowest amplitude of all the conditions observed; thus making it useful for this analysis. Crack near bearing 3 and Rub near bearing 4 conditions generated spectral components similar to those obtained in the Healthy spectrum. However, in both cases the amplitude of the $1\times$ harmonic component was larger than that observed in the Healthy spectrum. This, therefore, meant breathing was not observed for the crack case and the effect of the rub condition was an increase in the rotor unbalance. It was evident that the traditional fractional harmonic component that would be observed with rotor-stator interactions [10] was not seen in this rub case.

Crack near bearing 1 had a spectrum which was expected of Healthy condition; possessing a sole $1\times$ harmonic component. Results obtained for Crack near bearing 1 represented a purely unbalance case. Even though the amplitude of the $1\times$ component was larger than that observed in the healthy spectrum, it seems breathing did not occur.

It was interesting to note that Crack near bearing 2 possessed $1\times$, $2\times$ and a small $4\times$ harmonic component. This behaviour contradicts the widely held view that coupling misalignment faults dominate the spectrum with the $2\times$ component and its harmonics [3]. Interestingly, the Misalignment fault spectrum indicated $2\times$ and $3\times$ harmonic components; much like what is conventionally expected of a cracked rotor condition [3, 4]. Notwithstanding, the presence of the $3\times$ harmonic component was somewhat concurrent to results obtained by Patel and Darpe [3], where $1\times$ and $3\times$ harmonic components dominated the spectrum for misalignment fault. Then again, they also suggested that cracked rotor conditions are known to exhibit dominant $2\times$ and $3\times$ spectral components also.

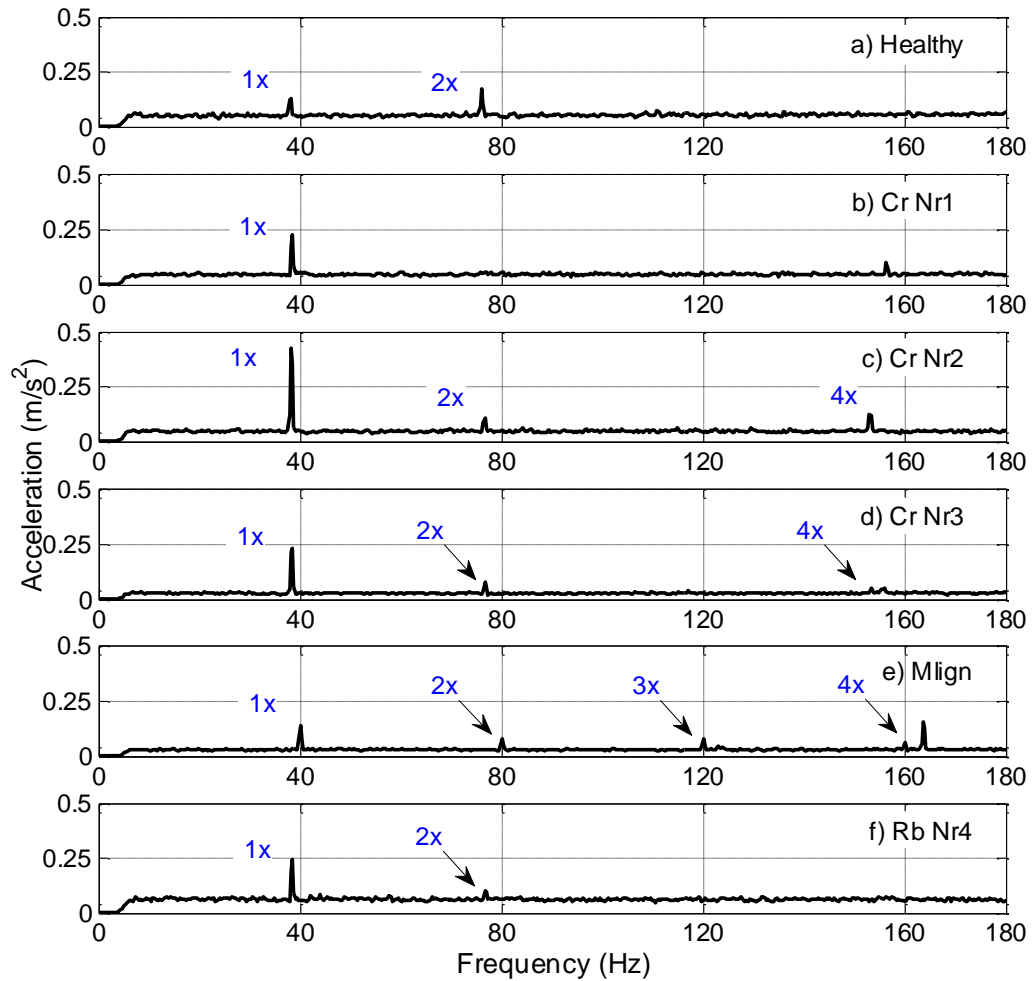


Figure 5.7 Acceleration spectra at bearing 2 for all faults at 40 Hz

Overall, it can be seen that the method did give an indication of the presence of fault conditions, as there were noticeable increases in the $1\times$ component amplitude for all fault conditions relative to the healthy spectrum. However, FD was not possible as different faults excited similar spectral features. Was this trend noticeable at other bearing locations? Figure 5.8 shows the comparison of spectral features done at 40 Hz (2400 rev/min). If different faults generated unique features that were consistent across all four bearing locations then the results would have separate clusters of each fault conditions in the plot. However, though some clustering and separation was observed with the Healthy data, the results shows that different faults generated similar features across all four bearing locations and also that features for a particular fault changed for each bearing location.

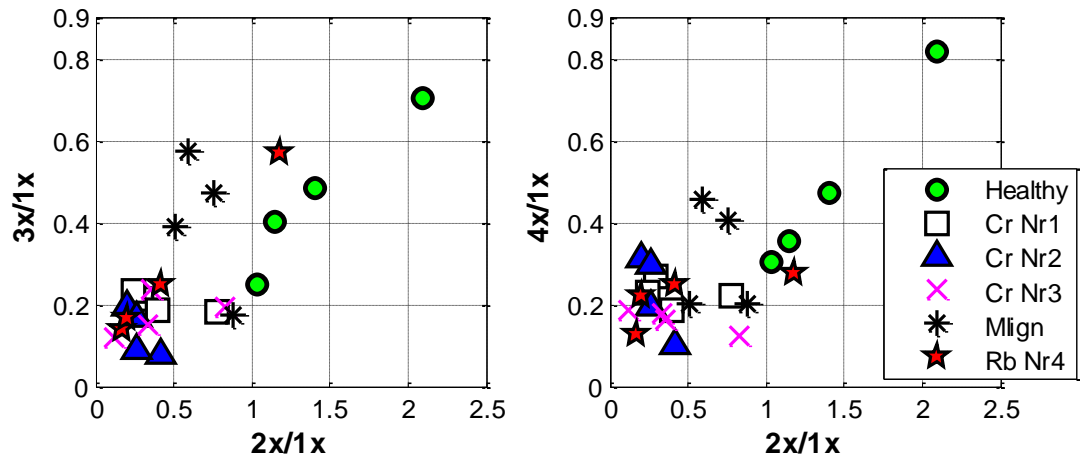


Figure 5.8 Comparison of spectral features for all conditions tested at 40 Hz

5.4.2 Results: Spectrum analysis - 50 Hz (3000 rev/min)

Figure 5.9 shows the amplitude spectra obtained at Bearing 2 from data acquired at 50 Hz (3000 rev/min). This was typical of results obtained at all four bearing locations. For the Healthy condition, the presence of $1\times$ and $2\times$ harmonic components was consistent to observations made at 40 Hz. Similarly the presence of the $2\times$ harmonic component meant that some residual misalignment remained in the system during testing at this speed. However, given the Healthy condition excited harmonic components with the lowest amplitudes of all scenarios tested for the $1\times$ harmonic component, it was adequate for the present analysis.

As previously observed, the solitary $1\times$ harmonic component observed in Crack near bearing 1 was indicative of a purely unbalance case, thereby indicating that breathing was not experienced. The small peak that was noticed in the vicinity of 150 Hz was digressed from a multiple of the fundamental frequency (50 Hz or $1\times$ harmonic component) to be considered a harmonic component.

Crack near bearing 2, Crack near bearing 3 and Misalignment generated similar spectral features; distinct $1\times$ component with almost inconspicuous $2\times$ and $3\times$ harmonic components. These results concurred with traditional deduction that both crack and misalignment fault conditions generate similar spectral features and are usually

indistinguishable with amplitude spectrum analysis without the use of phase information [3].

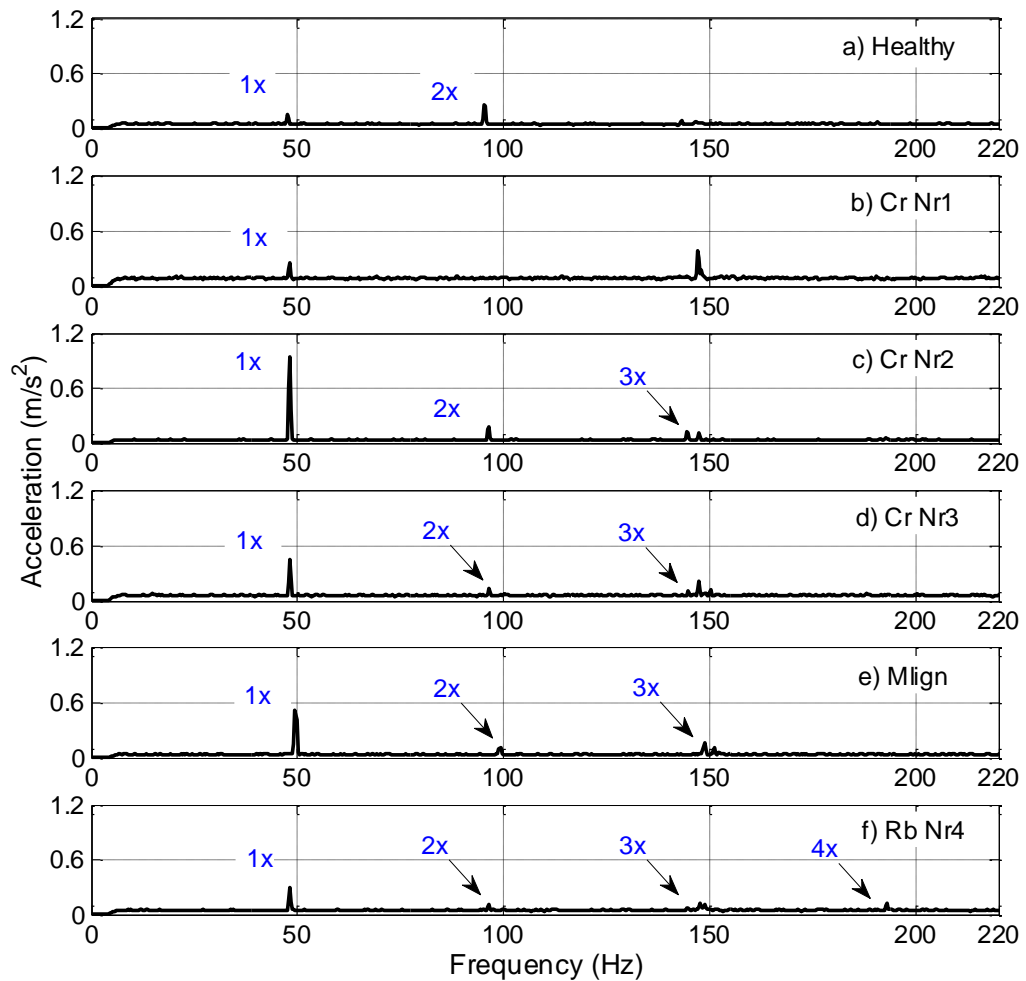


Figure 5.9 Acceleration spectra at bearing 2 for all faults at 50 Hz

The rub condition generated multiple harmonics of the fundamental frequency ($1\times$, $2\times$, $3\times$ and $4\times$). Though devoid of fractional harmonics, the feature observed in the Rub spectrum was consistent with previous work done [10].

Similar to the results garnered at 40 Hz (see Section 5.4.1), all fault conditions tested at 50 Hz appeared detectable; as the amplitude of the $1\times$ harmonic component in each faulty case was larger than that observed in the Healthy case. However, the features observed in the simple spectra did not appear useful for FD. The comparison of spectral features, shown in Figure 5.10, seems to be analogous to its equivalent generated at 40 Hz. The haphazard bundling of the different fault conditions signifies that the observations made

from Figure 5.10 which was generated at bearing 2 location was consistent across all four bearings. That is, for a particular bearing location, different faults generated similar spectral features and also that the features were not consistent across the different bearing locations.

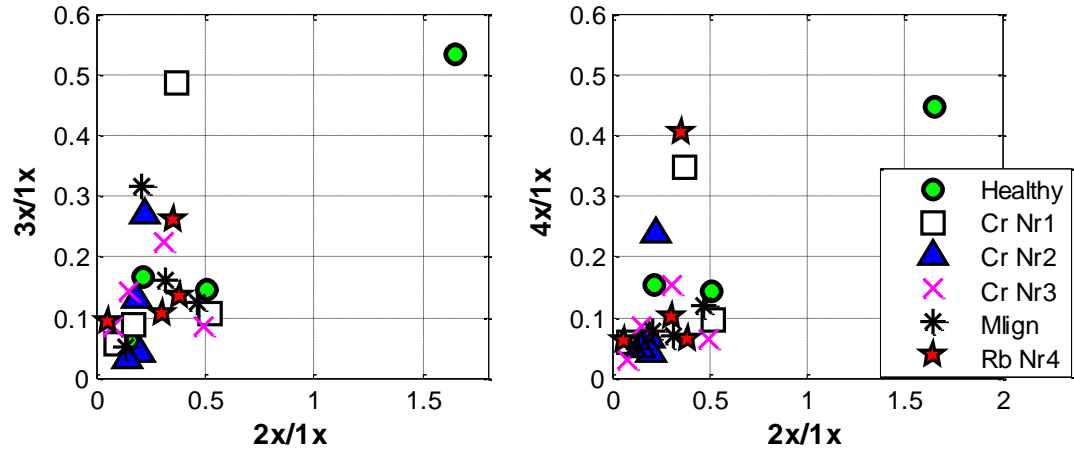


Figure 5.10 Comparison of spectral features for all conditions tested at 50 Hz

5.5 Combined vibration and thermal analysis

In Section 5.4, as expected, spectrum analysis alone did not give any discriminative feature for diagnosis. However, combining temperature with vibration data may produce results that are useful for diagnosis. Therefore, two combined vibration and temperature analysis approaches have been attempted in this section.

5.5.1 Theory: Computation of steady-state temperatures

Assuming the majority of heat loss from the bearing was via conduction to the steel pedestals, which could have acted as a large heat sink, Figure 5.11 represents a heat transfer model of the experimental rig bearings. This model became the basis of deriving the simple equation of the thermodynamics of the bearing which was used to approximate steady-state temperatures attained [20]. The derivation is given hereafter.

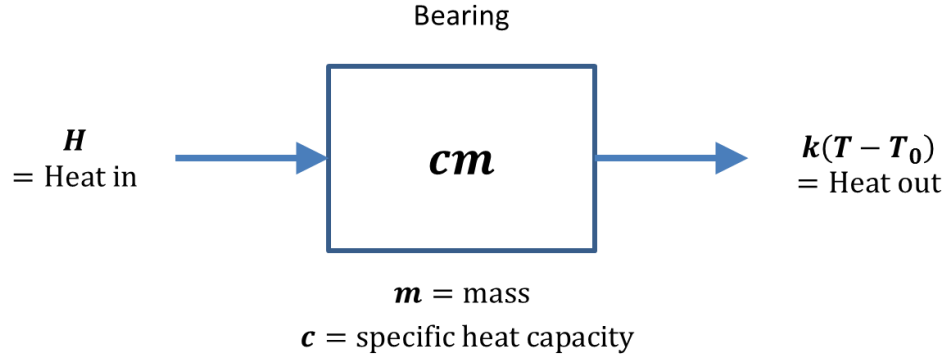


Figure 5.11 Bearing heat transfer model

Consider equation (5.1), the fundamental equation of heat transfer, where ambient temperature = T_0 , Bearing mass = m , Specific Heat Capacity = c , heat input = H and bearing heat loss coefficient = k

$$cm \frac{dT}{dt} = H - k(T - T_0) \quad (5.1)$$

At steady-state conditions, $t \rightarrow \infty$, bearing temperatures tend to maximum value = T_{max} , therefore;

$$H = k(T_{max} - T_0) \quad (5.2)$$

Combining equations (5.1) and (5.2) produces:

$$cm \frac{dT}{dt} = k(T_{max} - T)$$

$$cm \int_{T_0}^T \frac{dT}{T_{max} - T} = k \int_0^t dt$$

$$[-cm \ln[T_{max} - T]]_{T_0}^T = [kt]_0^t$$

$$\ln[T_{max} - T] - \ln[T_{max} - T_0] = \frac{-k}{cm} t$$

$$\frac{T_{max} - T}{T_{max} - T_0} = e^{\frac{-k}{cm}t}$$

$$T = T_{max} - (T_{max} - T_0)e^{\frac{-k}{cm}t} \quad (5.3)$$

If $\frac{k}{cm} = A$;

$$\Delta T = (T_{max} - T_0)e^{-At} \quad (5.4)$$

where ΔT is temperature increase, T_{max} is steady-state temperature, T_0 is ambient temperature, A is an arbitrary variable and t is time.

5.5.2 Simple linear analysis

Thermal and overall vibration data were combined in a single analysis using a linear model. This was done in an attempt to ascertain whether any correlation exists between temperature and vibration data and also to possibly produce discriminative features for all scenarios tested. Overall r.m.s. acceleration values used in this approach were computed from the measured horizontal vibration data.

For the thermal data, since temperatures were recorded during machine run up, it was necessary to extrapolate it to obtain steady-state bearing temperatures and for this the simple thermodynamic model of the bearing (see Section 5.1) plus curve fitting process based on equation (5.4) were used. Figure 5.12 depicts a sample of the results of the curve fitting process. Unknown variables in the equation for each condition were adjusted until the model (dashed lines) matched the warm up curves (solid lines) (see Figure 5.12a). These variables were then used to generate full steady-state curves (see Figure 5.12b) for each fault condition. Since bearing faults and lubrication issues would have affected temperature measurements, the need for full interrogation of the acceleration spectra for such faults in Section 5.4, becomes manifest.

After computing the requisite variables, a scatter plot of bearing steady-state temperature (dependent variable) against overall r.m.s. acceleration amplitude (independent variable) was generated. Both 40 Hz and 50 Hz data were plotted on a single chart and observed. Linear regression lines (lines of best fit) were then applied to the data points for each

condition tested and its equation noted. Afterwards, these equations were extracted from the scatter plot and used to transfer the said trend lines to a single separate chart for observation without the scatter plot. This was done to see how each condition behaved relative to each other as well as to the healthy (baseline) condition.

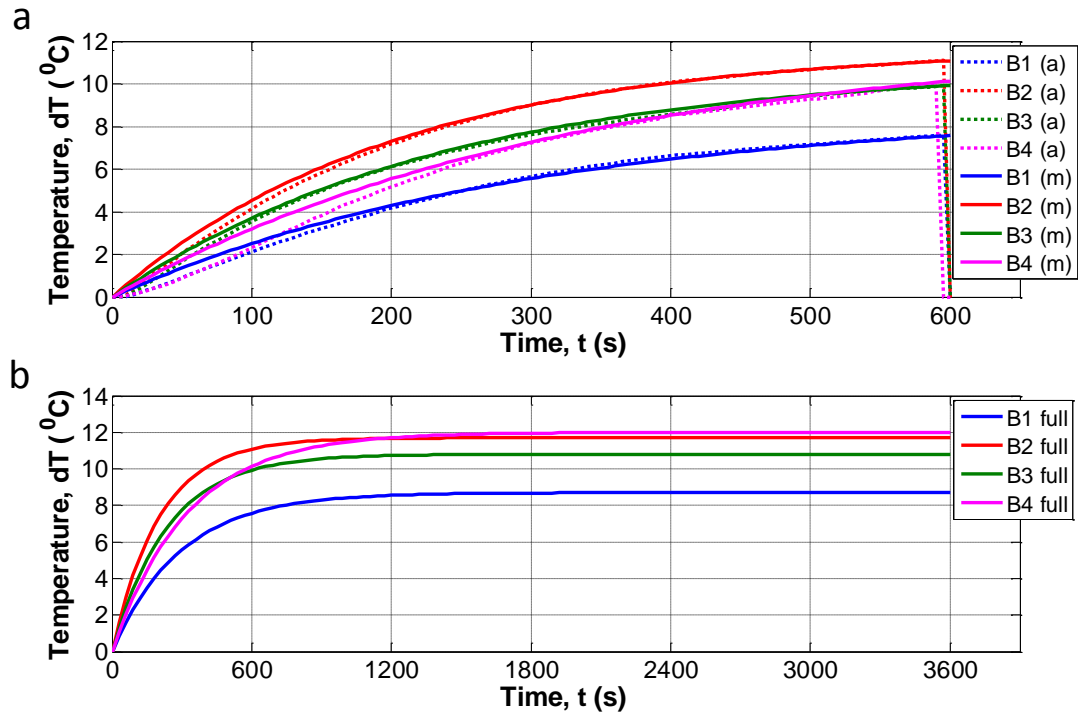


Figure 5.12 Sample showing progression of temperature trends in curve fitting process:
a) transient curve fitting and b) generation of steady-state curves

5.5.2.1 Results: Simple linear analysis

Results of the first combined approach attempted are shown in Figure 5.13a. The data points presented appeared haphazard and devoid of any useful pattern, but it was encouraging to note that different fault conditions appeared to occupy separate sections of the plot.

Figure 5.13b shows the results of the extraction of linear regression lines from the first linear approach (see Figure 5.13a). The diagram shows clearly that there was some deviation of different faults from healthy condition. It appears that the direction of deviation from healthy condition was of no consequence to the diagnosis process. That is,

whether the best fit line deviated above or below healthy condition did not matter. The important aspect was that different fault conditions produced uniquely different deviations (gradients) from the healthy condition. Crack near bearing 1 and Crack near bearing 2 had very similar gradients. Crack near bearing 3 was slightly different to the previous two conditions. Breathing was not as prominent on the shorter less flexible shaft as seen on long shaft. It was also encouraging to note that misalignment and cracked rotor condition deviated in different directions relative to Healthy. This suggested that the proposed method could be useful for distinguishing both conditions.

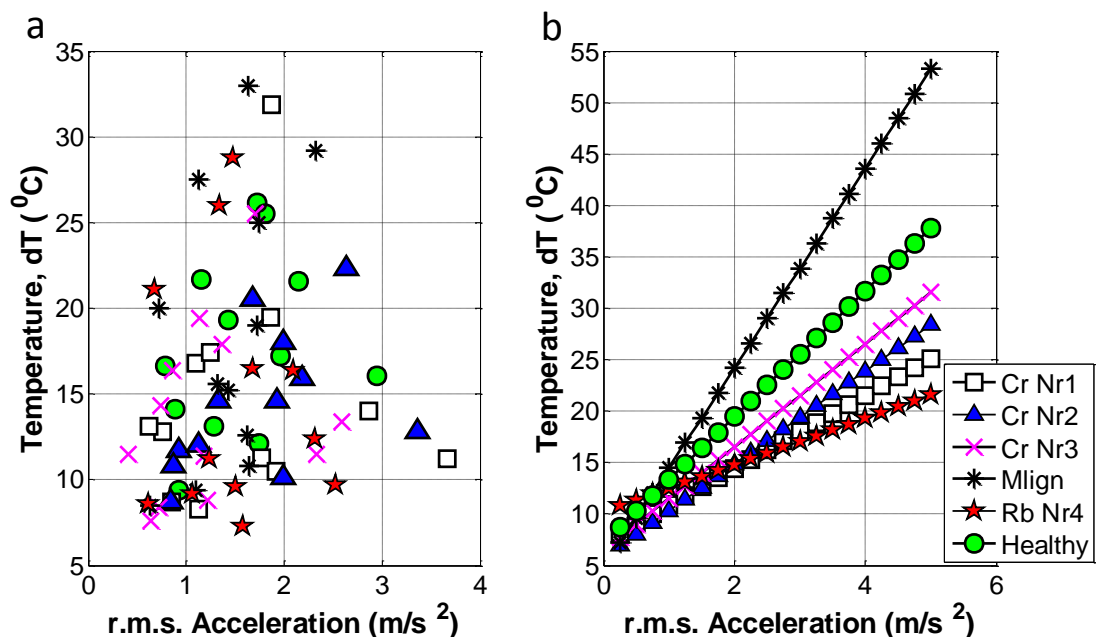


Figure 5.13 Linear combined approach: a) Temperature and vibration scatter and b) Proposed linear combined diagnostic trend

However, the method did have a noticeable limitation; the scatter produced for each fault condition did not produce an ideal fit with the linear trend line applied. From further analysis of the data, it was found that a second order polynomial line would have had a better fit than a linear one. Therefore, any diagnosis done with the above method would have questionable accuracy as the linear model utilised was not robust. While noting that bearing steady-state temperature increased with increasing vibration levels, a more robust approach to combining and analysing these two correlated variables would be required.

5.5.3 PCA-based analysis

In the previous section, it was observed that a correlation exists between temperature and overall vibration data. To quantify this correlation, Principal Component Analysis [121] was applied in the final attempt to develop a simplified combined vibration and temperature FD method. Analysis was done first with vibration data alone and then with vibration and temperature data to compare the effect of temperature addition.

PCA is a widely established and applied multivariate statistical analysis technique that can reduce a large number of interrelated data set to a small number of variables, while retaining the variance in the original data set. This is accomplished by computing uncorrelated ordered variables known as Principal Components (PCs); the first few of which best represent the variability in the original correlated dataset. Graphical representation of these PCs can reveal simplified structures which are oftentimes hidden in the complex datasets [121].

First, for each scenario tested, the measured vibration data were segmented into 20 observations. Each observation was used to compute one time domain feature (root mean square [r.m.s.]) and three frequency domain features (amplitudes of $1\times$, $2\times$ and $3\times$ harmonic components). Each bearing location was treated as a separate set of features [122]. Hence a total of 16 features ($4 \text{ bearings} \times 4 \text{ features}$) were computed each for 20 different observations. These were used to populate a feature matrix, \mathbf{X}_v , for loading to the PCA algorithm. Each scenario simulated was treated as a different set of observations. Hence, matrix \mathbf{X}_v would have 16 rows (features) and 120 columns ($6 \text{ scenarios} \times 20 \text{ observations}$). Before computing of Principal Components (PCs), each element in \mathbf{X}_v was converted to zero mean and unit variance [17, 121].

Second, the steady-state temperature, T which was calculated for each bearing in Section 5.1, was included as an additional feature at each bearing location. This resulted in a total of 5 features per bearing location. Thus a 20×120 feature matrix, \mathbf{X}_{t+v} was input to the PCA algorithm. The process of normalizing elements in \mathbf{X}_{t+v} was repeated and PCs were calculated.

To provide an additional perspective to the compilation of the PCA feature matrix, consider a random feature say, \mathbf{F} obtained during a random fault \mathbf{Q} , at all four bearing locations. Mathematically this can be expressed as

$$\mathbf{F}_Q = \begin{bmatrix} F_{Q1,1\cdots 20} \\ F_{Q2,1\cdots 20} \\ F_{Q3,1\cdots 20} \\ F_{Q4,1\cdots 20} \end{bmatrix} \quad (5.5)$$

where $F_{Q1,1\cdots 20}$, $F_{Q2,1\cdots 20}$, $F_{Q3,1\cdots 20}$ and $F_{Q4,1\cdots 20}$ are row vectors of all 20 observations of \mathbf{F} at bearings 1, 2, 3 and 4, respectively. Thus, for both the previously mentioned temperature and vibration features used in the current study, the feature matrix for say the Healthy condition can be expressed mathematically as

$$\mathbf{X}_{(t+v)H} = \begin{bmatrix} T_{H1,1\cdots 20} \\ rms_{H1,1\cdots 20} \\ 1x_{H1,1\cdots 20} \\ 2x_{H1,1\cdots 20} \\ 3x_{H1,1\cdots 20} \\ T_{H2,1\cdots 20} \\ rms_{H2,1\cdots 20} \\ 1x_{H2,1\cdots 20} \\ 2x_{H2,1\cdots 20} \\ 3x_{H2,1\cdots 20} \\ T_{H3,1\cdots 20} \\ rms_{H3,1\cdots 20} \\ 1x_{H3,1\cdots 20} \\ 2x_{H3,1\cdots 20} \\ 3x_{H3,1\cdots 20} \\ T_{H4,1\cdots 20} \\ rms_{H4,1\cdots 20} \\ 1x_{H4,1\cdots 20} \\ 2x_{H4,1\cdots 20} \\ 3x_{H4,1\cdots 20} \end{bmatrix} \quad (5.6)$$

Using the same basis shown in equation (5.6) for the compilation of the feature matrix for the remaining five conditions tested, the complete feature matrix for input to the PCA algorithm can be expressed as

$$\mathbf{X}_{t+v} = \begin{bmatrix} \mathbf{X}_{(t+v)H} \\ \mathbf{X}_{(t+v)C1} \\ \mathbf{X}_{(t+v)C2} \\ \mathbf{X}_{(t+v)C3} \\ \mathbf{X}_{(t+v)M} \\ \mathbf{X}_{(t+v)R} \end{bmatrix}^T \quad (5.7)$$

where H , $C1$, $C2$, $C3$, M and R denote Healthy, Crack near bearing 1, Crack near bearing 2, Crack near bearing 3, Misalignment and Rub near bearing 4, respectively. Note that the sole difference between matrix \mathbf{X}_v and \mathbf{X}_{t+v} is the removal of all four temperature rows from the feature matrix for each condition tested. A flow chart summarising the PCA data analysis process is given in Figure 5.14.

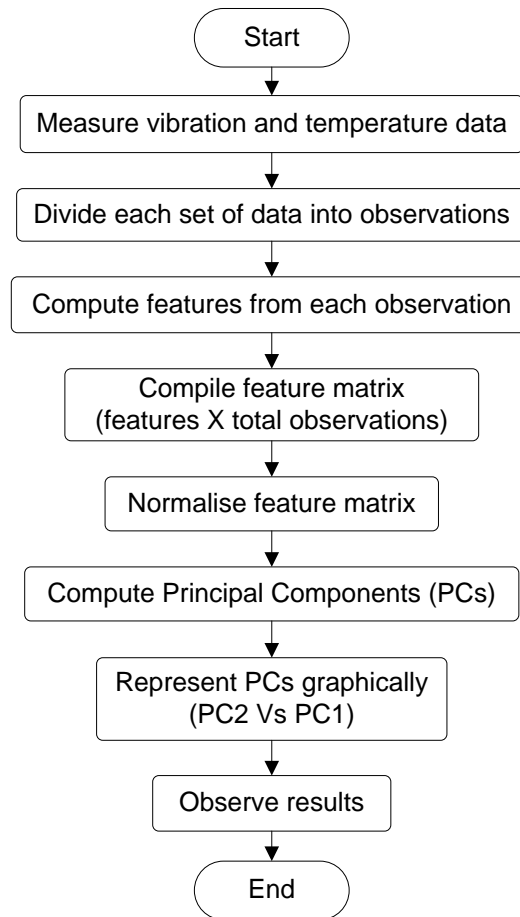


Figure 5.14 PCA flow process

5.5.3.1 Results: PCA-based analysis - 40 Hz (2400 rev/min)

Results of the proposed combined analysis at 40 Hz without temperature data are shown in Figure 5.15. Representation of the results was made by a two dimensional plot of the 2nd PC (PC2) against the 1st PC (PC1) [121]. It can be seen that Healthy condition did not occupy a distinct space on the plot; as there was some overlap between it and the Rub near bearing 4 data points. As indicated, there was also overlap between Misalignment and Crack near bearing 1 and Crack near bearing 3 data. This was analogous to results obtained in the spectrum analysis (see Figure 5.7) where it was not possible to distinguish cracked rotor conditions from Misalignment. It therefore appears that PCA with vibration data alone was no more useful than spectrum analysis in this case.

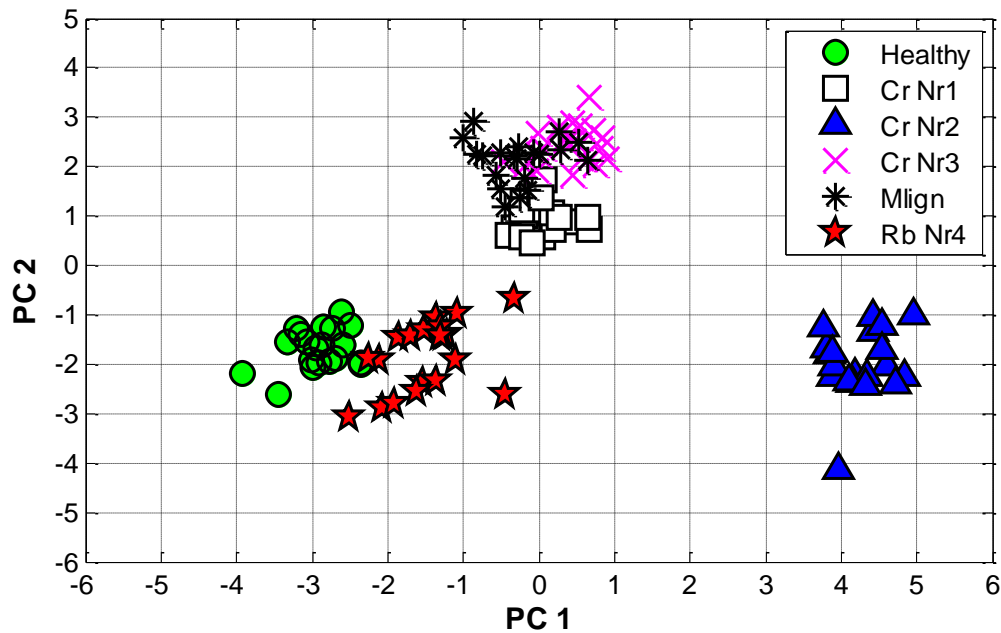


Figure 5.15 PCA-based approach **without Temperature** - 40 Hz

Conversely, as shown in Figure 5.16, the addition of temperature fully separated Healthy from all fault data points. The overlap between Misalignment and Crack near bearing 1 and Crack near bearing 3 conditions that was previously noticed (in Figure 5.15), does not exist in this plot. The addition of temperature grouped each fault condition into clearly defined clusters on the plot. Given its ability to simultaneously separate Healthy from faulty data and distinguish different fault conditions, it seems the proposed PCA-based approach with

temperature may be useful for rotor-related fault detection and classification. It also appears that the proposed method may be able to determine the severity of a fault condition, because Crack near bearing 2 conditions had the largest separation from the Healthy condition. This was analogous to results obtained in the simple spectrum analysis at 40 Hz (Figure 5.7), where Crack near bearing 2 was identified as the most severe fault condition. Further experimentation would be required to verify this.

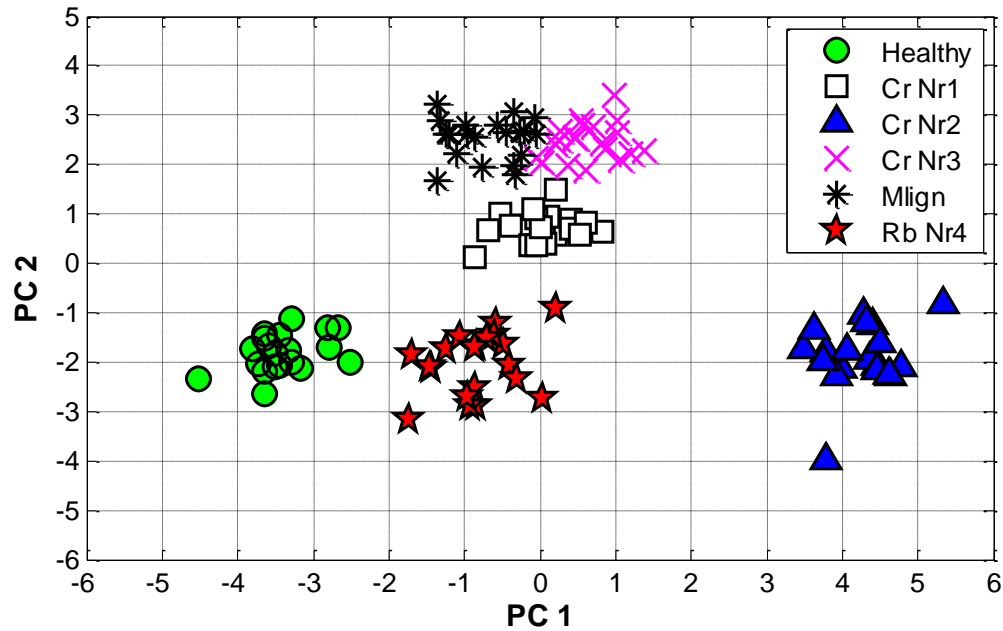


Figure 5.16 PCA-based approach **with Temperature** - 40 Hz

5.5.3.2 Results: PCA-based combined analysis - 50 Hz (3000 rev/min)

Results of the proposed combined approach at 50 Hz without bearing temperature data are shown in Figure 5.17. With exception of a slight overlap between Crack near bearing 3 and Misalignment condition, there was improved separation of the different conditions when compared to observations made without temperature at 40 Hz. Unlike the results obtained at 40 Hz, the Healthy condition in this case is fully separated from the fault condition data.

The effects of temperature addition to the analysis can be observed in Figure 5.18. Though not as significant as the results produced at 40 Hz, there was improvement in the

level of separation between the Healthy and faulty conditions when compared to the results without temperature. Further separation was also seen along the PC1 axis between Crack near bearing 1 and Misalignment fault. There was little change between remaining conditions. As also seen at 40 Hz, Crack near bearing 2 condition remained the farthest separated from the Healthy data. This therefore suggests that the level of separation between a fault condition and the Healthy condition may be an indication of the severity of the fault [96].

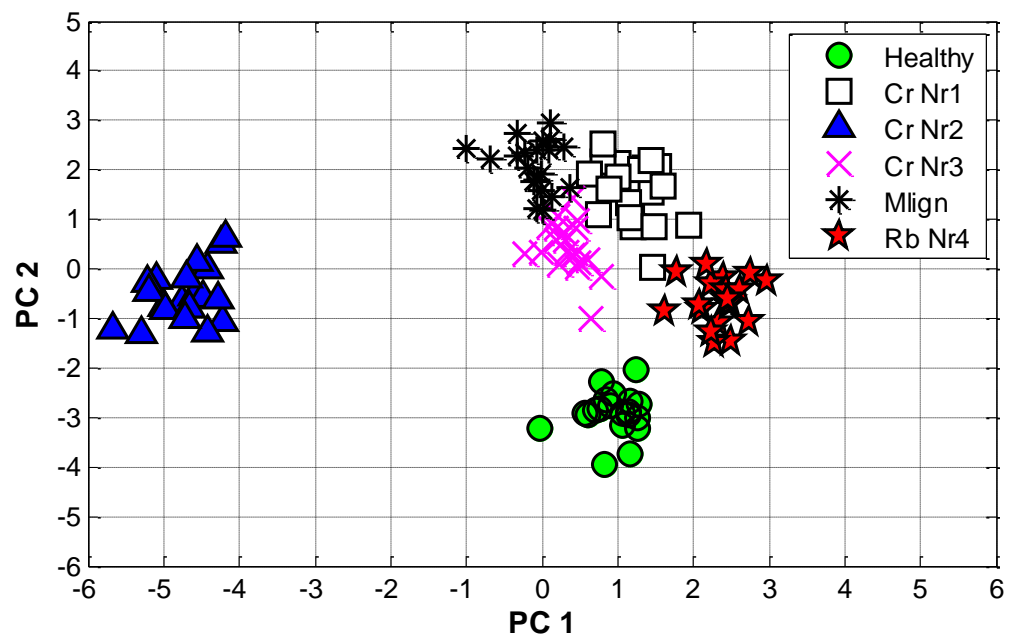


Figure 5.17 PCA-based approach **without Temperature** - 50 Hz

Although, the analysis at 50 Hz was not as improved with the addition of temperature data, as observed at 40 Hz, it was important to note that; consistent fault detection was done without the equivocality associated with conventional spectrum analysis and consistent isolation of misalignment from crack rotor condition was observed. It also seems that the interpretation of results in the proposed method is not sensitive to changes in the speed of machine. The recognition of particular pattern was insignificant to this analysis, what mattered was the formation of different clusters for different fault conditions and the separation of these clusters from each other and the Healthy condition.

Thus, the addition of bearing steady-state temperature data to the PCA-based analysis improved the efficacy of the method. The PCA-based combined vibration and temperature

analysis appears more simplified than conventional vibration-based diagnosis techniques that usually require phase information or advanced techniques, such as the polar and orbit plots [3, 4, 9, 10] for diagnosis of faults.

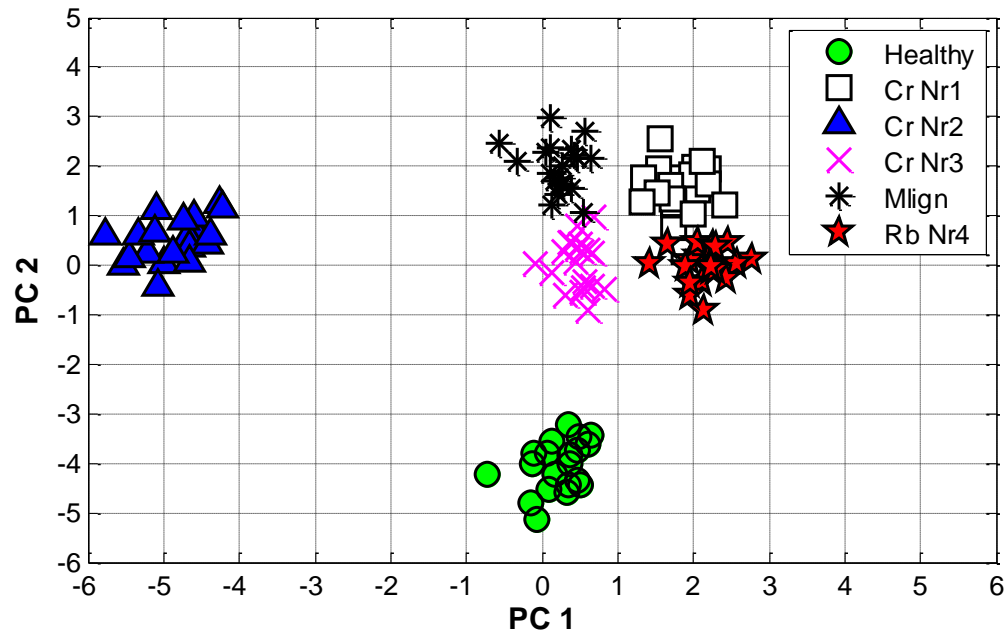


Figure 5.18 PCA-based approach **with Temperature** - 50 Hz

5.6 Summary

A FD technique for rotating machinery, rotor-related faults was proposed using a single vibration and temperature sensor on each bearing. Experiments were done on a small laboratory rig with rigidly coupled dissimilar length shafts mounted on four ball bearings. It was shown that supplementing vibration data with temperature measurements gave better discrimination of the state of the machine when compared with vibration data alone. The use of temperature with vibration data produced good results without the expense of complex signal processing. Simple signal processing was used to compute r.m.s. and spectral components which were then used to generate a simple diagrammatical representation that represents the different states of the machine. Interpretation of results from the proposed method does not require the expertise of a seasoned analyst to deduce the state of the machinery. Hence, the subjectivity which is associated with the amplitude spectra and other commonly applied techniques is avoided here.

In practice, the proposed combined vibration and temperature technique would require historical data; from say a database of actual fault occurrences. As new data become available, this would be fed into the database from which the algorithm mines and generates the input matrix. Continuous classification would be done. Therefore, if a fault does not exist with data that is fed into the algorithm, it would be grouped into the healthy cluster. This would continue until, say data with a fault occurrence is supplied to the tool, which would classify and group the fault into its respective cluster. Therefore the efficacy of the proposed technique is limited to the quality of data available for processing. Despite this limitation, the proposed unified method is beneficial in being a computationally efficient data driven learning system that is easily updated to include new features or faults.

6 UNIFIED MULTI-SPEED ANALYSIS (UMA) FOR THE CONDITION MONITORING OF AERO-ENGINES

Reformatted version of the following papers:

- 1.** **Title:** Unified Multi-speed Analysis (UMA) for the condition monitoring of aero-engines

 Authors: Adrian D. Nembhard and Jyoti K. Sinha

 Status: Published in Mechanical Systems and Signal Processing journal
- 2.** **Title:** Combined vibration and temperature analysis for condition monitoring of aero-engines (GT2014-25726)

 Authors: Adrian D. Nembhard and Jyoti K. Sinha

 Status: Published in Proceedings of ASME Turbo Expo 2014: Turbine Technical Conference and Exposition GT2014

Abstract: For rotating machinery in which speeds and dynamics constantly change, performing vibration-based condition monitoring can be challenging. Thus, an effort is made here to develop a Unified Multi-speed fault diagnosis technique that can exploit useful vibration information available at various speeds from a rotating machine in a single analysis. Commonly applied indicators are computed from data collected from a rig at different speeds for a baseline case and different faults. Four separate analyses are performed: single speed at a single bearing, integrated features from multiple speeds at a single bearing, single speed for integrated features from multiple bearings and the proposed Unified Multi-speed analysis. The Unified Multi-speed approach produces the most conspicuous separation and isolation among the conditions tested. Observations made here suggest integration of more dynamic features available at different speeds improves the learning process of the tool which could prove useful for aero-engine condition monitoring.

Keywords: Rotating machinery, vibration-based condition monitoring, fault diagnosis, aero-engine, Principal Component Analysis

6.1 Introduction

It is recommended that machine speed remains constant when conducting vibration-based condition monitoring (VCM) of rotating machinery. Typically, during the VCM process, diagnostic features are extracted at a particular speed and compared to a healthy (baseline) feature previously generated at the same speed. This is necessary because features may be sensitive to machine speeds and changes in these relative to the baseline could signify the presence of a fault. Thus, it is imperative to ascertain whether a change in the feature is due to a fault or speed fluctuations by mitigating the effects of any speed fluctuations [31]. However, on complex machines like aero-engines where speeds constantly change under normal operating conditions, performing VCM during constant speed is a fundamental challenge.

Current practice shows the selection of data in the most steady-state condition available, say during idle or cruising [34]. However, accurate fault diagnosis (FD) is not guaranteed, since fault signals are oftentimes fleeting and replete with noise [101]. Normalization of diagnostic features with respect to speed is also often employed, but this can be complex and usually leads to less accurate or less robust fault detection [34]. In a review of aircraft engine health monitoring systems, Tumer and Bajwa [102] cited that tools which better discriminate engine healthy from faulty states using the wealth of data available from existing aero-engine management systems are lacking. More recently, to bridge this gap, numerous works have been done on improving aero-engine vibration-based FD [14, 35-37]. These, however, still remain somewhat digressed from the current needs of industry [14].

Of the readily accessible literature, few researchers have sought to develop methods that are applicable during transient operations. Barragan [32] proposed a vibration monitoring system (VMS) that processes data acquired during engine acceleration and deceleration for the diagnosis of unbalance and misalignment faults. Fault detection was achieved by

comparing “vibration patterns” from several selected indicators generated in time waveform and waterfall diagrams to a library of known patterns of engine faults. The method relies on a Finite Element Model for FD. Thus, the method may not be robust; since it is widely held that generating a FE model which accurately reflects the true dynamics of a machine for confident FD is difficult. Modgil et al. [103] suggested an advanced vibration diagnostic system for engine test cells which sampled data from engine idle to full power. Similar to Barragan [32], FD was achieved predominantly with Waterfall diagrams of the spectrum. VCM techniques based on transient operations are good during aircraft landing and takeoff, but efforts based on the waterfall diagrams are grouping data generated in the amplitude spectra at different speeds with diagnosis being based at a single speed, which may not be useful in continuously changing speed conditions. On a slightly different note, Grabill et al. [33] developed an advanced airborne Turbine Engine Diagnostic System (aTEDS) for the C17/F117 aero engines. The system automatically triggered vibration data collection and processing during acceleration, deceleration and steady-state speeds for the diagnosis of a comprehensive list of faults. Though the system was intelligent, its FD capabilities were predominantly based on normalization of time domain features at a single speed and on features extracted from the amplitude spectra, both of which do not guarantee accurate fault detection [34].

Despite the promising developments of efforts based on transient operations, the fundamental techniques used for processing of data may not be useful during continuous operations with varying speeds. Hence, a technique which is insensitive to changing speeds is warranted. Therefore, an effort is made in the current study to develop a simple but confidence inspiring approach that fuses data acquired at different steady-state speeds in a single analysis step.

Experiments were done on a small ball bearing laboratory rig [20, 29, 123] with rigidly coupled dissimilar length shafts. A healthy (baseline) condition was first tested followed by the separate introduction of crack, misalignment and rotor rub faults. On-bearing vibration data were collected at different subcritical steady-state speeds. Recent developments [28, 29, 123] used fewer sensors than standard practice for vibration fault diagnosis at a single speed. Similarly, for all conditions tested, only one vibration measurement per bearing is employed in the current study. These vibration signals were processed to compute commonly applied condition indicators (features) for each bearing

location. Fusion of these indicators and subsequent classification of the different faults, with respect to a healthy state, was achieved with a Principal Component Analysis (PCA) based algorithm. Brotherton et al. [39] and Nembhard et al. [123] demonstrated the potential for rotating machinery fault classification with PCA, and as such it is employed in this study. To demonstrate the robustness of the multispeed technique it was compared to other analyses done at a single speed and multi-speed. It was observed that the Unified Multi-speed approach produced improved separation and isolation of the conditions tested than other analyses done.

A brief description of the experimental set up and data collection method is given in Section 6.2. This is followed by an overview of the effects of speed change on the simple amplitude spectra in Section 6.3. The theoretical basis for the method introduced in the present study is highlighted in Section 6.4. Section 6.5 provides a synopsis of the data processing done. In section 6.6, the results of proposed Unified Multispeed method is given in addition to its comparison with other analyses done at a single speed and multi-speed. Lastly, a brief discussion of results is given and concluding remarks are made in Sections 6.7 and 6.8, respectively.

6.2 Experimental set up

Figure 6.1 shows a photograph of the small experimental rig, located in the University of Manchester (UK) Dynamics Laboratory. The rig consists of two 20 mm nominal diameter rigidly coupled (Coupling 2) dissimilar length shafts of 1010 mm (Rotor 1) and 500 mm (Rotor 2) that are secured to a steel lathe bed by four pillow block ball bearings (Model: SKF SY504M). Machined sections that accommodate balancing discs (125 mm in diameter and 14 mm thick) are mounted on each shaft. System drive is produced by a 3000 rev/min 0.70 kW 3 phase motor that is coupled to the rotating assembly via a semi-flexible coupling (Coupling 1). The impulse response method of modal testing [50] was done to identify the dynamic characteristics of the test rig. The first two natural frequencies were identified at 67.14 Hz and 142.2 Hz. The mode shapes corresponding to these natural frequencies are provided in Figure 6.2. A sample of the measured Frequency Response Function (FRF) obtained from the modal analysis is shown in Figure 6.3.

Experiments were conducted at steady-state rotating speeds of 600 rev/min (10Hz), 1200 rev/min (20 Hz), 1800 rev/min (30 Hz), 2400 rev/min (40 Hz) and 3000 rev/min (50 Hz), to evaluate the impact of steady-state speed changes on the results obtained. Note that all experiments were conducted below the first critical speed of 4028.4 rev/min (67.14 Hz). With one condition tested at a time, a total of three different fault conditions were introduced to the rig; crack, misalignment (M) and rotor rub. Rub condition was simulated near Bearing 4 (R4). Cracked rotor was tested in three different locations; near Bearing 1 (C1), near Bearing 2 (C2) and near Bearing 3 (C3). Additional details of the experimental set up, including instrumentation can be found in [123].

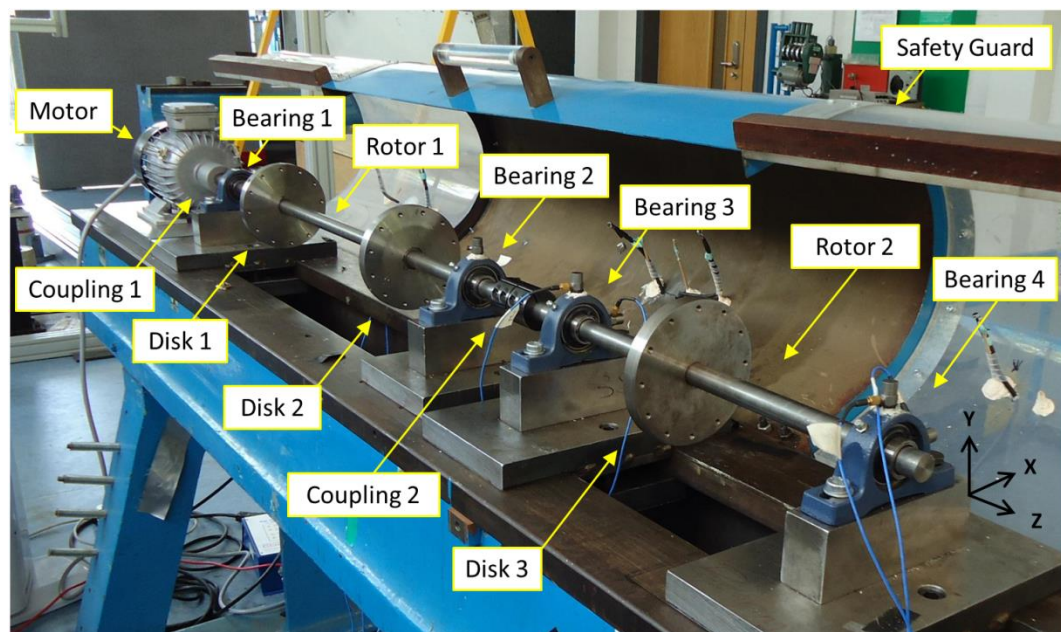


Figure 6.1 Layout of rotating machinery experimental rig

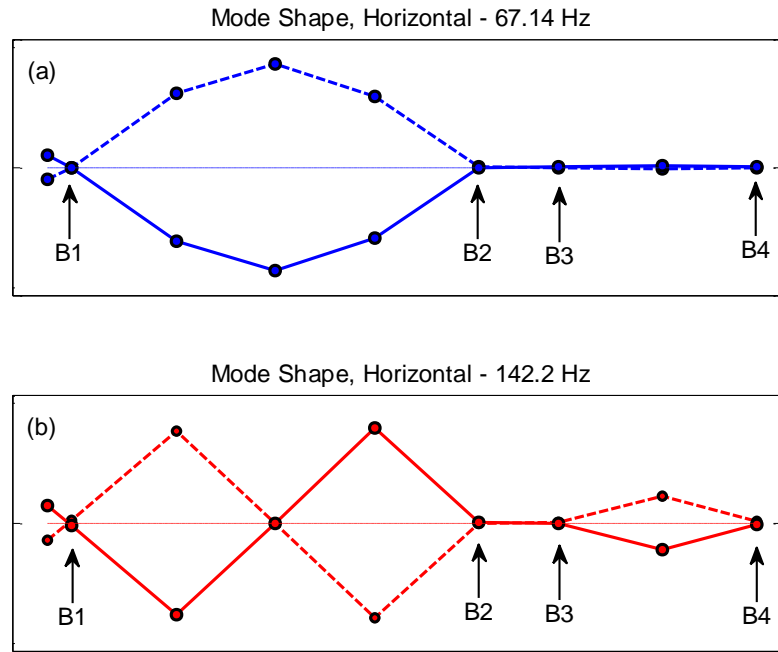


Figure 6.2 Measured mode shapes (dots represent measurement locations) of experimental rig: (a) mode 1: 67.14 Hz and (b) mode 2: 142.2

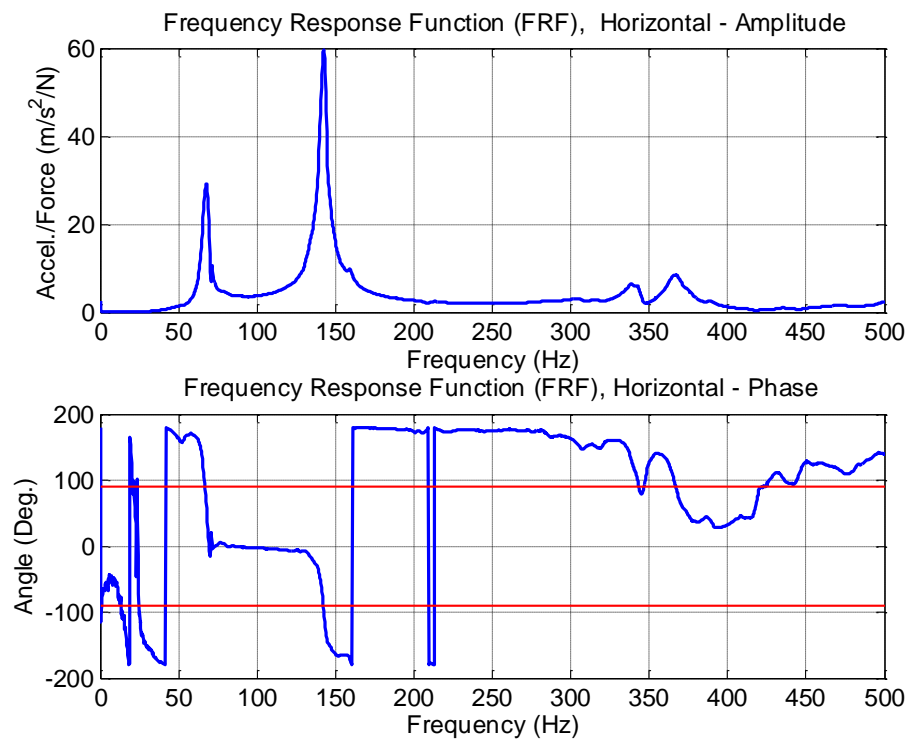


Figure 6.3 Sample of Frequency Response Function (FRF) in the horizontal direction; measured on long shaft near bearing 2 during modal testing

6.3 Spectrum analysis

Vibration responses were measured at a rate of 10 KHz in both the vertical and horizontal directions. During processing the data were filtered between 5 Hz and 1 kHz. After which, the averaged amplitude spectra (with 85% overlap) were generated to have a frequency resolution of 0.61 Hz. A Hanning window was also applied. Given the 1000 Hz upper band limit would have excluded bearing faults and lubrication issues from the spectrum, a prior bearing analysis was done to confirm the health of bearings used. Only vibrations measurements acquired in the horizontal direction were used for the present study. The stiffness of the experimental rig was higher in the vertical direction, which resulted in the collection of highly suppressed and less useful readings in this direction compared to the horizontal direction.

6.3.1 Effect of speed change on spectral features

Figures 6.4 and 6.5 provide samples of the spectra obtained from Bearing 2 for all conditions tested at 2400 rev/min (40 Hz) and 3000 rev/min (50 Hz), respectively. For each scenario tested, interrogation of the spectrum was done for the first few harmonic components as this is the region in which rotor-related faults are usually identified [124]. Except for the Misalignment (M) condition, the speeds tested for all other conditions were slightly deviated from 40 Hz and 50 Hz. This occurred because the rotating speed of the rig was set manually and therefore brought about some difficulty in attaining the desired speed set point. It was expected that these speed offsets would not have any significant bearing on the observations.

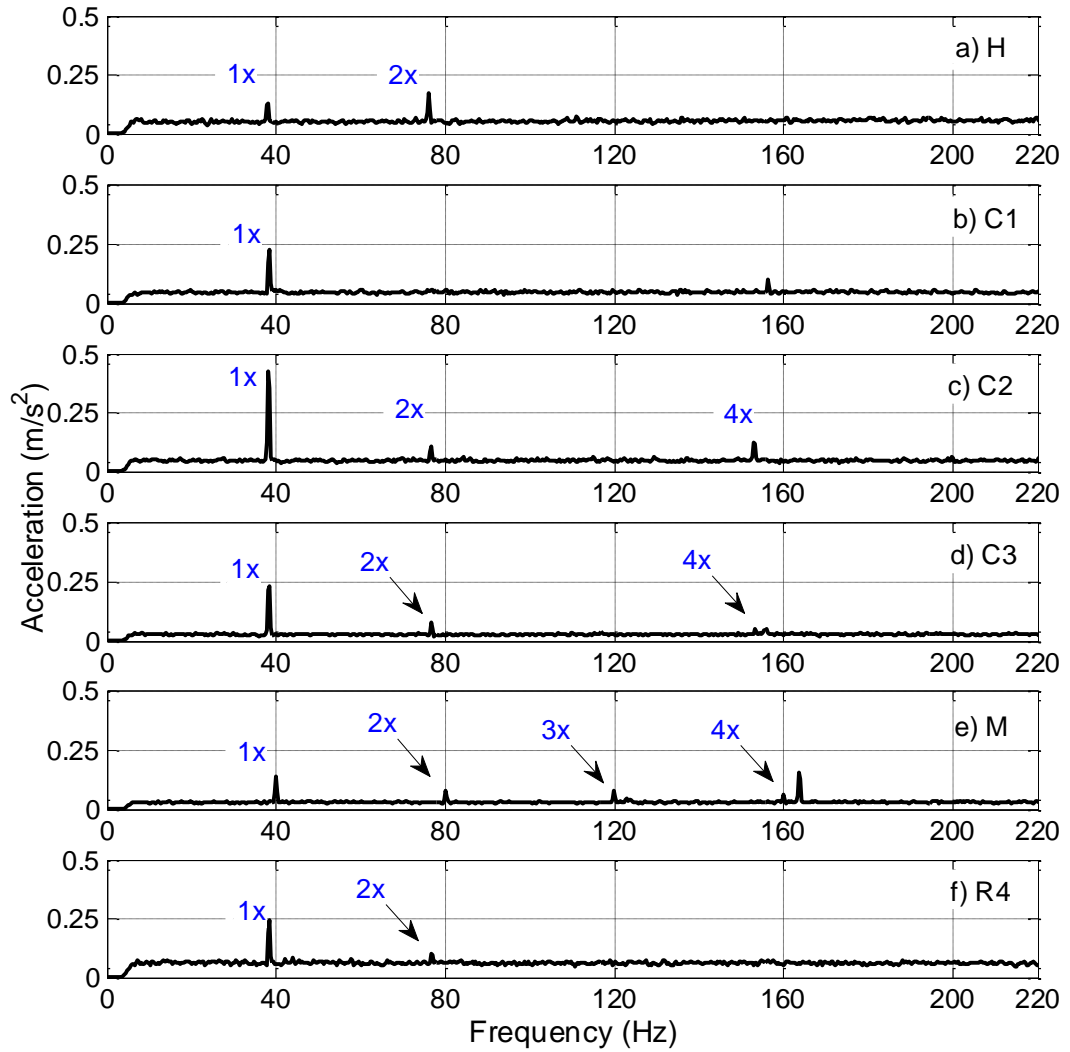


Figure 6.4 Amplitude Spectra from Bearing 2 at 2400 rev/min (40 Hz) for: a) healthy, b) crack near Bearing 1, c) crack near Bearing 2, d) crack near Bearing 3, e) misalignment and f) rub near Bearing 4

At 40 Hz, the healthy (H) case appeared indicative of some residual misalignment, as the spectrum possessed a small $1\times$ with a larger $2\times$ harmonic component. Introduction of the C1 condition to the rig resulted in an increase in the shaft unbalance as evidenced by the increase in the $1\times$ amplitude. It was interesting to see that a $2\times$ harmonic component did not exist for this case. At an initial glance, the peak in close proximity to the 160 Hz frequency location seemed to be a $3\times$ harmonic component, but closer inspection revealed this frequency was somewhat removed from an integer multiple of the $1\times$ vibration and therefore was not deemed a harmonic component. The peak seen was also not an excited mode. Consequently, the C1 spectrum was representative of a pure unbalance case. When a crack was introduced to the shaft near bearing 2 (C2), there was a sizeable increase in the

synchronous vibration ($1\times$), reduction in the $2\times$ harmonic component and generation of a $4\times$ harmonic component. Crack near bearing 3 (C3) generated a similar response to C2. The system's response to the M condition had $3\times$ and $4\times$ harmonic components in addition to the $1\times$ and $2\times$ components seen in the baseline (H) case. Similar to the unidentified peak observed close to 160 Hz in the C1 spectrum, the peak seen just above 160 Hz in the M case was neither a harmonic component nor an excitation of any of the rig's identified natural frequencies. Lastly, the rub scenario (R4) had both $1\times$ and $2\times$ harmonic components similar to the H case, however, the amplitude of the $1\times$ response was doubled.

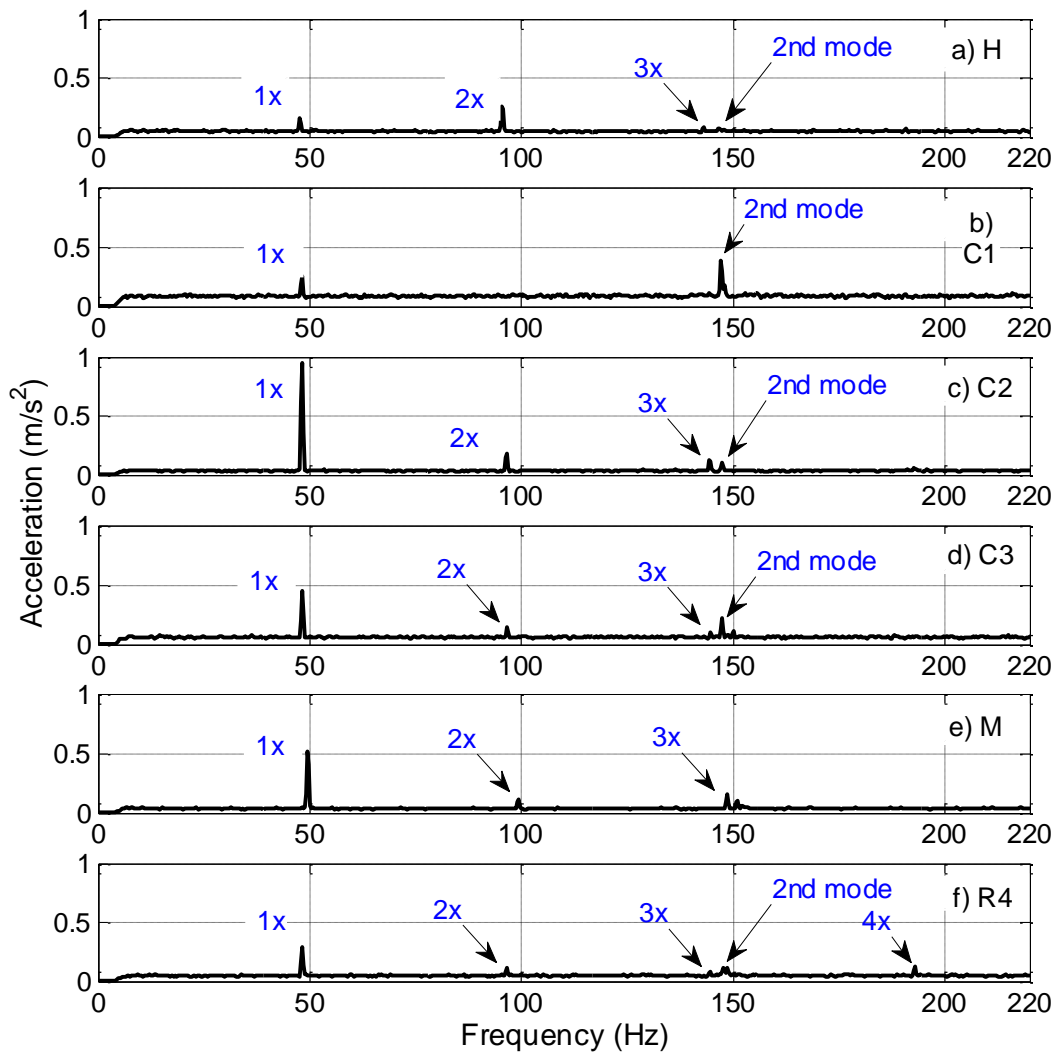


Figure 6.5 Amplitude Spectra from Bearing 2 at 3000 rev/min (50 Hz) for: a) healthy, b) crack near Bearing 1, c) crack near Bearing 2, d) crack near Bearing 3, e) misalignment and f) rub near Bearing 4

Except for the C1 condition, the harmonic composition of the spectra was noticeably modified on increasing rig speed from 40 Hz to 50 Hz. An additional $3\times$ component was generated in the H condition. C2 and C3 cases similarly generated $1\times$, $2\times$ and $3\times$ harmonic components instead of the $1\times$, $2\times$ and $4\times$ components seen at 40 Hz. For the M condition, the $4\times$ harmonic component seen previously was non-existent, thereby resulting in a spectrum identical to the C2 and C3 cases at 50 Hz. R4 condition generated two additional harmonic components; $3\times$ and $4\times$. The C1 spectrum appeared to have $1\times$ and $3\times$ components, but the peak located close to the 150 Hz frequency location was not a harmonic component. In fact, the peak shown was located at 147.1 Hz and was due to an excitation of the rig's 2nd mode. Note that this was possible, because the 2nd natural frequency (142.2 Hz) had a broad base in the FRF (Figure 6.3) which encompassed the 147.1 Hz frequency location. That being said it can be seen that at 50 Hz operation, all cases with a $3\times$ harmonic component (≈ 150 Hz) excited the rig's second mode (see Figure 6.2b).

It is well established that diagnosis of faults using the amplitude spectrum generated from steady-state vibration data is challenging. As observed in Figures 6.4 and 6.5, which were generated from bearing 2, different faults generate similar harmonic components. This observation, however, was not limited to bearing 2, and to demonstrate this, a comparison of spectral features was done at 2400 rev/min. The amplitudes of the $4\times$, $3\times$ and $2\times$ harmonic components at each bearing location for all conditions tested at this speed were normalized with their respective $1\times$ components. This was used to generate plots of the normalized $3\times$ harmonic component against the normalized $2\times$ harmonic component and the normalised $4\times$ harmonic component against the normalized $2\times$ harmonic component. The $2\times$, $3\times$ and $4\times$ harmonic components were normalized with the shaft fundamental frequency ($1\times$) to remove the effect of unbalance across the spectrum, which would be present in all components, thus making the amplitudes of these harmonic components fully indicative of the condition present at each bearing location.

The spectral comparison plot at 2400 rev/min is presented in Figure 6.6. For a single scenario, say R4, the haphazard scatter shown in the plot indicates that each bearing location generated different spectral components (with different amplitudes). Depending on where the frequency location of a particular harmonic component is situated in the FRF,

the amplitudes of said harmonic component simultaneously at the four different bearing measurement locations would be governed by one or a combination of two of the rig's mode shapes [124]. For example, at 50 Hz operation the amplitudes of the $1\times$ component (at all bearings), which is located below the 67.14 Hz first natural frequency (Figure 6.3), would be characterized by the first mode shape (Figure 6.2a). The $2\times$ harmonic component, located at 100 Hz, would be found in the FRF between the 1st and 2nd natural frequencies and therefore characterized by a combination of the 1st and 2nd mode shape. The response at the $3\times$ harmonic component would be characterized by the 2nd mode, because it has a frequency location at 150 Hz which falls within the broad base of the 2nd natural frequency location in the FRF (Figure 6.3).

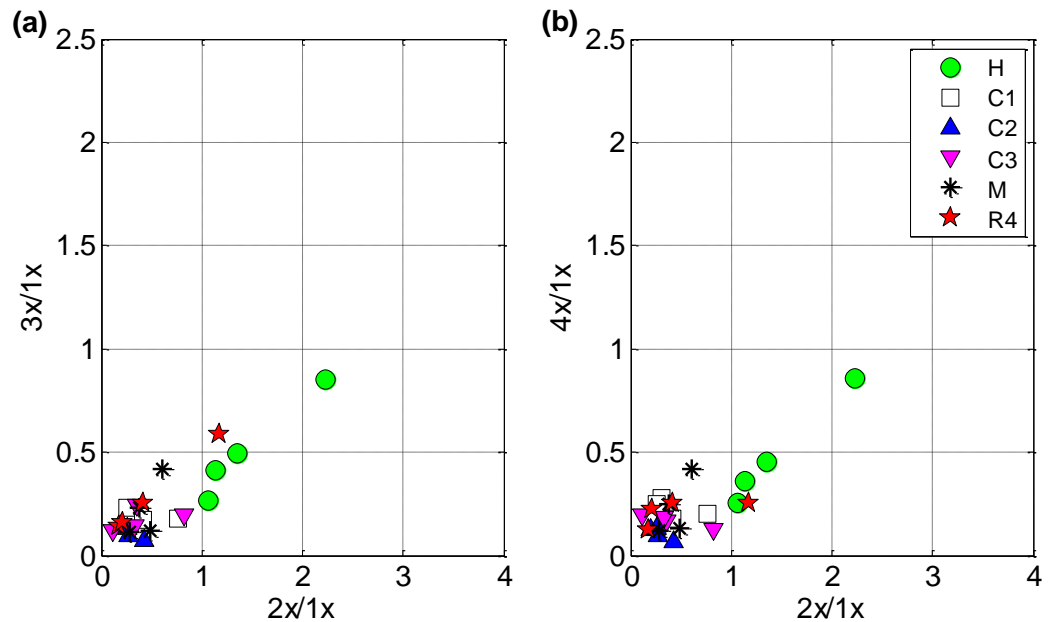


Figure 6.6 Comparison of spectral features at 2400 rev/min (40 Hz) for all conditions tested

The overlap of different fault conditions (say Rub with Cracked rotor) indicated that different faults generated similar spectral features. Bearing this in mind, to demonstrate the changes in spectral components across all speeds tested, a spectral comparison plot was similarly produced for all fault conditions at all speeds tested at all four bearings. The resulting plots are shown in Figure 6.7. It can be seen that the random nature of the plot was further exacerbated by the inclusion of data from different speeds. In this case, even features generated from the H condition overlapped with different fault conditions, thus

indicating there were instances in which fault conditions, even though physically present on the rig, did not generate harmonic components different from what was present in the healthy spectrum.

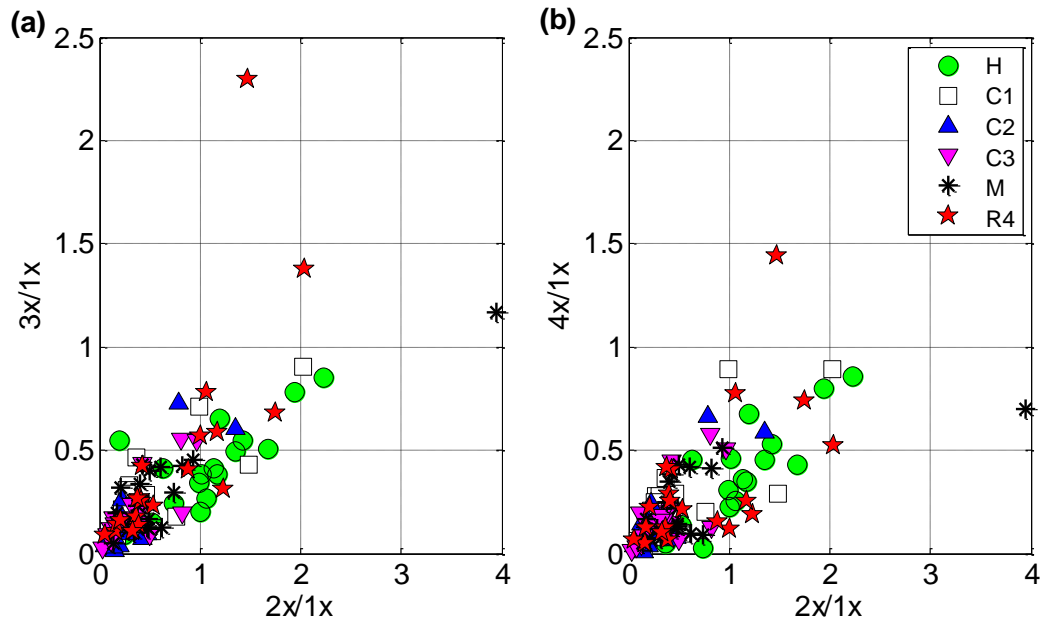


Figure 6.7 Comparison of spectral features at all speeds for all conditions tested

In summary, several key observations were made with the amplitude spectra. On changing rotating speed, the response spectrum was modified by both fault condition (excitation) and the FRF, as the excitation frequency location was dependent on speed. It was also seen that for a given steady-state speed, different spectral features may be observed for a particular fault at different bearings locations. At the same time, different faults may generate similar spectral features at a particular bearing location. Added to this, even when physically present, faults may not generate features dissimilar to a healthy or baseline case, therefore making the fault undetectable. With so many variables to consider, the process of analysing vibration data available from different steady-state speeds for the purpose of fault diagnosis is intricate, to say the least.

6.4 Application of principal component analysis (PCA)

Principal Component Analysis (PCA) can be defined mathematically as an orthogonal linear transformation that converts a data set to a new coordinate system where the greatest

variance by any projection of the data comes to lie on the first coordinate and the second greatest variance on the second coordinate [98]. This is accomplished by computing uncorrelated ordered variables, Principal Components (PCs); the first few of which best represent the variability in the original dataset [121]. Graphical representation of these PCs can reveal simplified structures that are oftentimes hidden in complex datasets or give an early indication of abnormality in these datasets [38, 121].

To supplement the definition of PCA, this section will provide an abridged overview of the computation of PCs. Consider p number of independent samples (observations) of m random variables (features), v , which can be represented by a $m \times p$ matrix, \mathbf{X} , such that;

$$\mathbf{X} = [\mathbf{x}_1 \quad \dots \quad \mathbf{x}_p] = \begin{bmatrix} \mathbf{v}_{11} & \dots & \mathbf{v}_{1p} \\ \vdots & \ddots & \vdots \\ \mathbf{v}_{m1} & \dots & \mathbf{v}_{mp} \end{bmatrix} \quad (6.1)$$

It is very useful to look for a few ($\ll m$) variables, Principal Components (PCs) which preserve variances of \mathbf{X} . PCs can be extracted by performing Singular Value Decomposition (SVD) of the covariance matrix of \mathbf{X} , C_x . Thus solving

$$\mathbf{X}\mathbf{X}^T = \mathbf{U}\mathbf{S}\mathbf{U}^T \quad (6.2)$$

where \mathbf{U} is an orthonormal matrix whose columns define the principal components and \mathbf{S} is diagonal matrix containing the corresponding singular values [98].

Figure 6.8 provides a simple graphical representation of the physical meaning of principle components when comparing two correlated variables X and Y . As shown, the first PC (PC1) is essentially the gradient between the two variables. Statistically, the gradient indicates that variables X and Y both contain some “redundant” information [125]. The position of PC1 minimizes the square of the distance of each point to that line, but simultaneously passes through the maximum variation in the said dataset [126]. PC2 must

be perpendicular (orthogonal) to PC1 and pass through the 2nd largest variation in the data set. If we rotate the PC1 axis to the X-axis and the PC2 axis to the Y-axis then we get a representation of the data in the Principal Component (PC) Space. As shown, interpretation of the data is rather simple with two correlated variables however, for large data sets with multiple variables interpretation of the data would be an arduous task. Thus, it is convenient to transform large intricate data sets with multiple variables to the PC space for ease of representation and processing without losing useful information contained in the data set [127].

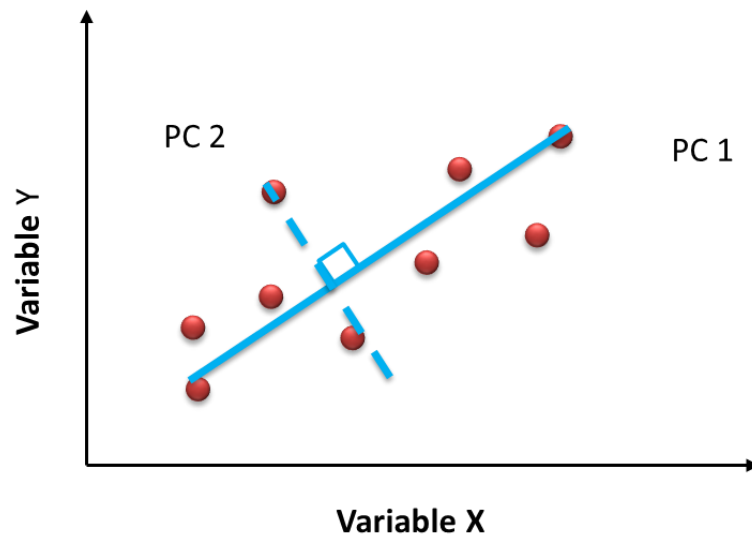


Figure 6.8 Basic example of a Principal Component representation of two correlated variables X and Y

6.5 Feature selection

Four widely employed condition indicators were selected for the current study; root mean square amplitude (r.m.s.), Crest Factor (C.F.), Kurtosis (K) and Spectrum Energy (SE). These four, commonly used features [33] were selected so as to develop a simple but robust technique which did not require spectrum interrogation and at the same time produced diagnostic features which best represented the state of a complex machine. A brief definition of each feature follows.

6.5.1 Root mean square (r.m.s.) vibration amplitude

The root mean square (r.m.s.) amplitude of a waveform (or signal) is widely accepted as a measure of the effective energy content in the signal. To further aid an appreciation of this index, consider the measured vibration signal $y(t)$ shown in Figure 6.9. The r.m.s. amplitude of the signal $y(t)$ is defined as

$$r.m.s.y(t) = \sqrt{\frac{\sum_{k=1}^p (y_k)^2}{p}} \quad (6.3)$$

where p is the number of samples taken.

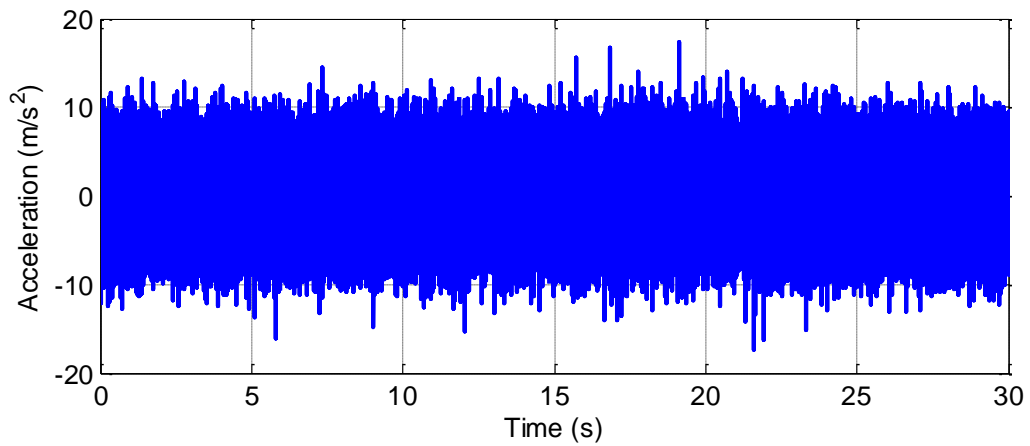


Figure 6.9 Time waveform sample of a measured vibration signal $y(t)$, where t is time in seconds

6.5.2 Crest factor

The Crest Factor (C.F.) of a vibration waveform is an index which is dependent on the shape of the waveform. It is defined as the ratio of its peak value to r.m.s. value [128]. Therefore, the C.F. of signal $y(t)$ is

$$C.F.y(t) = \frac{Peak_{y(t)}}{r.m.s.y(t)}$$

(6.4)

The crest factor contains information from both the peak and the r.m.s. level of the vibration signal.

6.5.3 Kurtosis

Kurtosis (K) provides a time domain measure of the impulsiveness of a signal. For signal $y(t)$, this can be defined as [129, 130]

$$Kurtosis, K_{y(t)} = \frac{\frac{1}{p} \sum_{k=1}^p (y_k - \bar{y})^4}{\left(\frac{1}{p} \sum_{k=1}^p (y_k - \bar{y})^2 \right)^2} \quad (6.5)$$

where p is the number of samples taken and \bar{y} is the mean of $y(t)$.

6.5.4 Spectrum energy (SE)

Spectrum Energy (SE) provides a measure of the energy content of the signal in the amplitude spectrum. Let $Y(f_k)$ be the Fast Fourier Transform (FFT) of signal $y(t)$ at frequency f_k , where $f_k = (k - 1)df$, $k = 0 \dots (N/2 - 1)$, N is the number of data points used for FFT computation and df is the frequency resolution. Therefore, with reference to Figure 6.10, the SE of $Y(f)$ between frequencies f_1 and f_w at intervals of df can be defined as

$$SE_{y(t)} = \sum_{k=f_1}^{f_w} Y(f_k) \times df \quad (6.6)$$

For the current study, SE was computed from spectra generated using a Hanning window, 95% overlap, 0.61 Hz frequency resolution and vibration data filtered between 5

Hz and 800 Hz. 5 Hz and 800 Hz frequency limits were used to exclude the effects of any DC offset and to focus solely on shaft related faults, respectively [124].

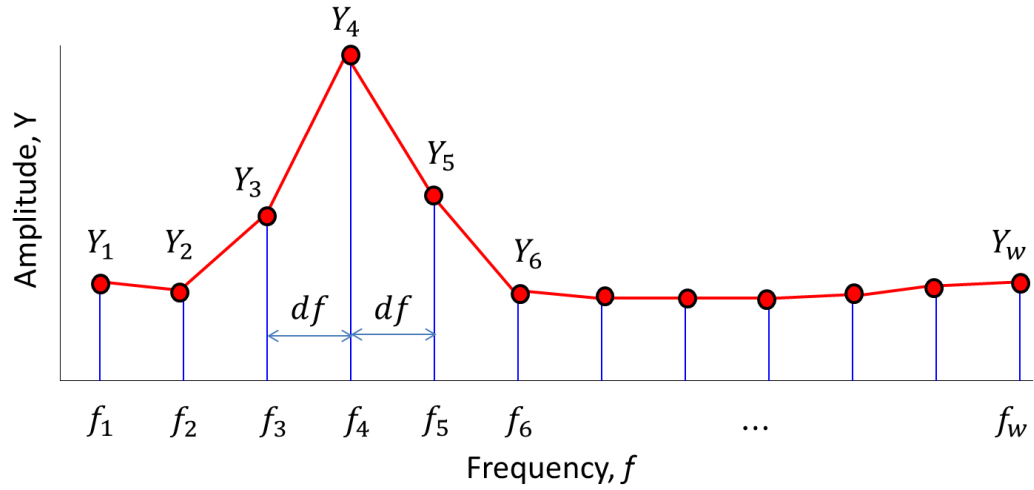


Figure 6.10 Actual sample of the amplitude spectrum $Y(f)$ of function $y(t)$ between frequencies f_1 and f_w

6.5.5 Feature selection summary

Three time domain features, r.m.s., C.F. and K, and one frequency domain feature, SE were selected for the current study. r.m.s. and SE similarly represent energy states and both characterize the overall state of the machinery. However, these two indicators are different. r.m.s. represents the energy content of the signal in the time waveform (time domain), while SE represents the energy content of signals in the amplitude spectrum (frequency domain). Since a single spectrum can represent several waves in the time domain, the difference between the two becomes apparent. Additionally, SE is a global indicator that accounts for all changes in the spectrum whether due to fault or FRF. Fault signals from aero-engines, including those associated with rotor crack [90, 101] and rub [131] are often times transient and impulsive. Since CF and K are generally indicative of the presence of transient and impulsive signals, they are appropriate inclusions in the list of features.

6.6 Data processing

For the different scenarios tested, 20 samples (observations) of vibration data were collected at a sampling rate of 10 kHz. For measurements obtained at Bearing 1 for Healthy condition at 600 rev/min, each observation was used to compute the three time domain features (r.m.s., C.F. and K) and the solitary frequency domain feature, SE.

For a single bearing analysis, these features were used to populate a 4×20 data matrix, \mathbf{X} for input to the PCA algorithm in Matlab software. Each row in the matrix represented one of the four features computed. For the integrated bearing analysis at a single speed, computation of the four features was repeated for each successive bearing location at that said speed, thus expanding \mathbf{X} , to a 16×20 matrix. After completing computations for 600 rev/min, the procedure was repeated for each successive speed, where the set of 16 features acquired at all 5 speeds tested was used to expand the rows of the data matrix. This further expanded \mathbf{X} , to an 80×20 matrix. On completing computations for all speeds in the Healthy scenario, the procedure was repeated for the next scenario, C1 and used to populate the next 20 columns of the input matrix \mathbf{X} , until all 6 scenarios tested were represented in the data Matrix as different sets of observations. When fully populated, matrix \mathbf{X} had 80 rows and 120 columns. Hence, for the single bearing analysis for all conditions tested the input matrix would be 4×120 . For the integrated bearing analysis with data for all four bearings at one speed, the input matrix would be 16×120 . Prior to loading to the PCA algorithm, each variable in \mathbf{X} was converted to zero mean and unit variance [121, 123].

To provide further insight to the features used in this analysis, Figure 6.11 shows a sample of the distribution of the normalized (zero mean and unit variance) features for all fault conditions measured at 2400 rev/min (40 Hz) at bearing 3. Note that the trend observed in Figure 6.11 is representative of that seen for all bearing locations at the other speeds tested. Except for the R4 condition, it can be seen that the selected features were either unable to reliably indicate the presence of the fault or did not vary consistently with the fault. Consequently, the observations made here suggest the selected features, when applied individually may not be sufficient for fault detection or diagnosis [129].

Notwithstanding, the current study seeks to combine the worth of these features at different speeds for fault detection and classification in a single analysis step.

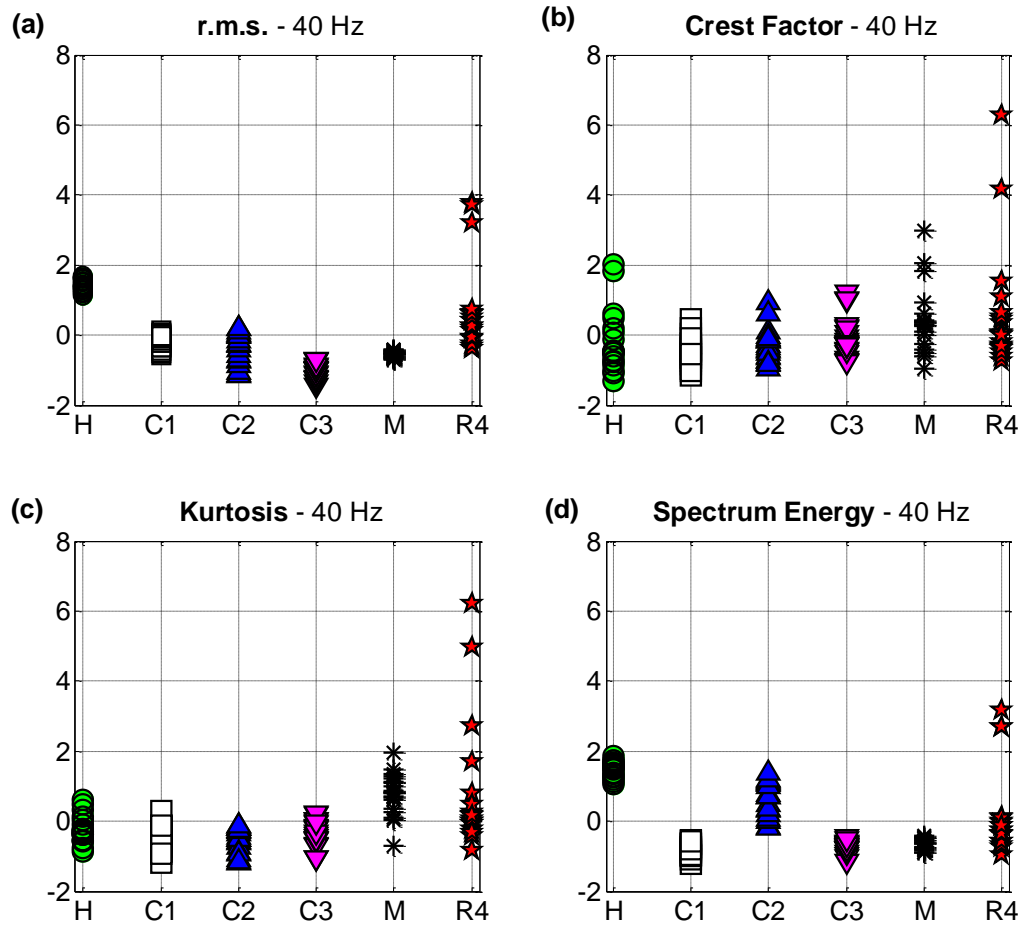


Figure 6.11 Sample showing variation of normalized PCA features for Bearing 3 at 2400 rev/min (40 Hz)

6.7 Results and discussion

In order to demonstrate the robustness of the technique being introduced, results from the analysis of features computed at a single speed and single bearing location are presented first. This is then compared to the results of the analysis of features integrated from multiple speeds at a single bearing. Thereafter, observations are made from the results of the analysis at a single speed for integrated features from multiple bearings. Finally, the results of the proposed Unified Multi-speed analysis is presented and compared to the aforementioned analyses. The results of all analyses done are shown in a

graphical two dimensional representation (plot) of the 2nd Principal Component (PC2) against the 1st Principal Component (PC1). The desired results which would be useful for diagnosis should have a plot with clearly visible separation and isolation among data clusters representing the different conditions tested.

6.7.1 Analysis of features from a single speed at a single bearing

Representative plots of the results of the analysis of features for a single speed at a single bearing are given in Figures 6.12-6.15 for Bearings 1-4, respectively. For each bearing the analysis was done at 600 rev/min (10 Hz), 1800 rev/min (30 Hz), 2400 rev/min (40 Hz) and 3000 rev/min (50 Hz) as denoted by sub-Figures (a), (b), (c) and (d), respectively. For conciseness, results were not presented for 1200 rev/min (20 Hz) but for completeness speeds selected demonstrated the entire speed range tested.

The plots shown were mostly overlapping with little or no separation between the healthy and faulty conditions. Isolation of the different conditions is virtually absent. Even in plots where some separation of the healthy condition was observed (Figures 6.12(c), 6.14(b) and 6.15(b)), the close proximity of the different conditions was not confidence inspiring. These observations imply that the information gleaned from analysing a single bearing at a single speed might not be adequate for consistent and confidence inspiring FD and therefore suggests more data would be required. It was postulated that two possible sources for obtaining the additional information needed for confidence inspiring diagnosis are either from using additional speeds in a single analysis and/or all bearing measurement locations in a single analysis. These possibilities are explored in subsequent sections.

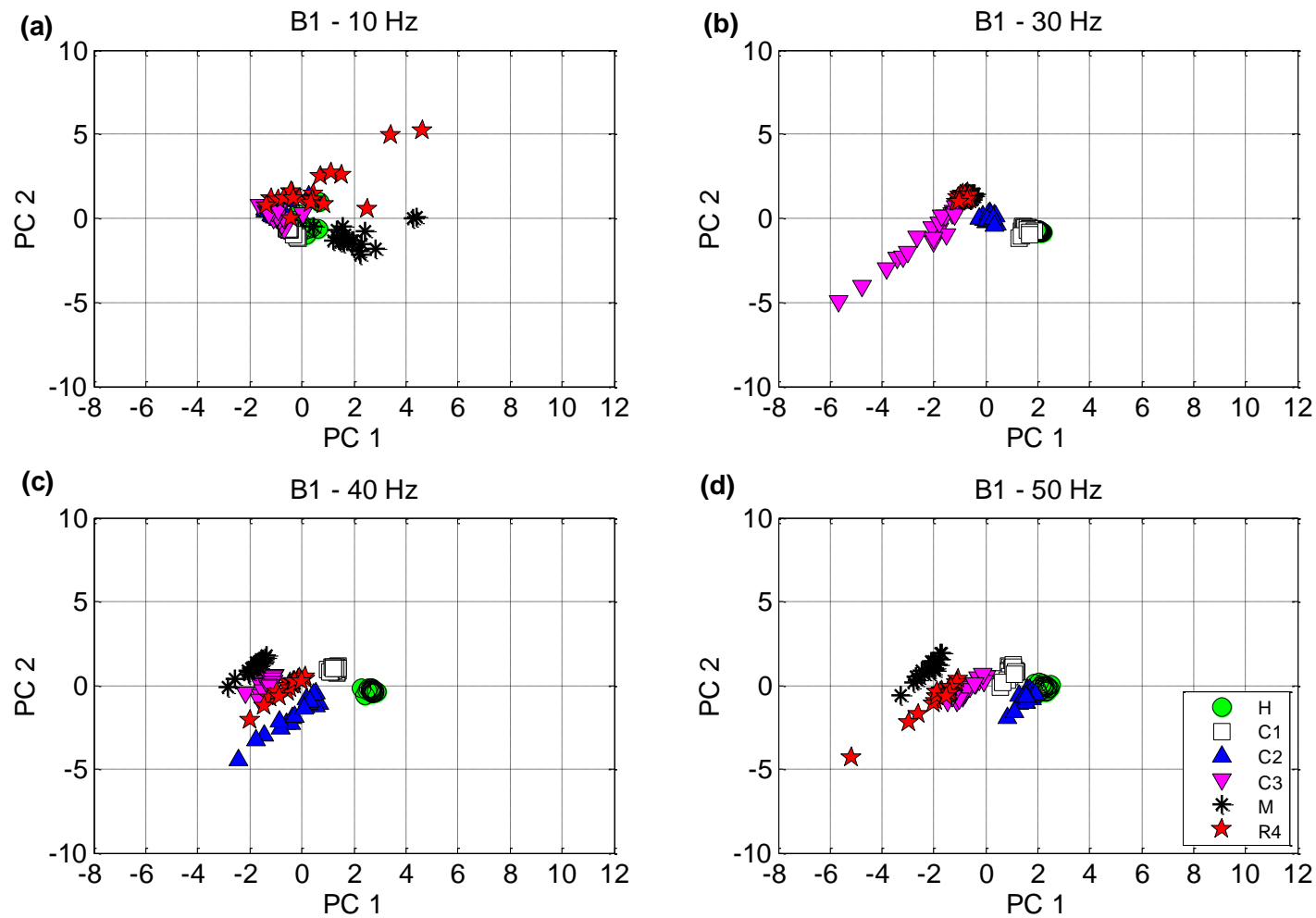


Figure 6.12 Single speed analysis using only **Bearing 1** features at: (a) 600 rev/min, (b) 1800 rev/min, (c) 2400 rev/min and (d) 3000 rev/min

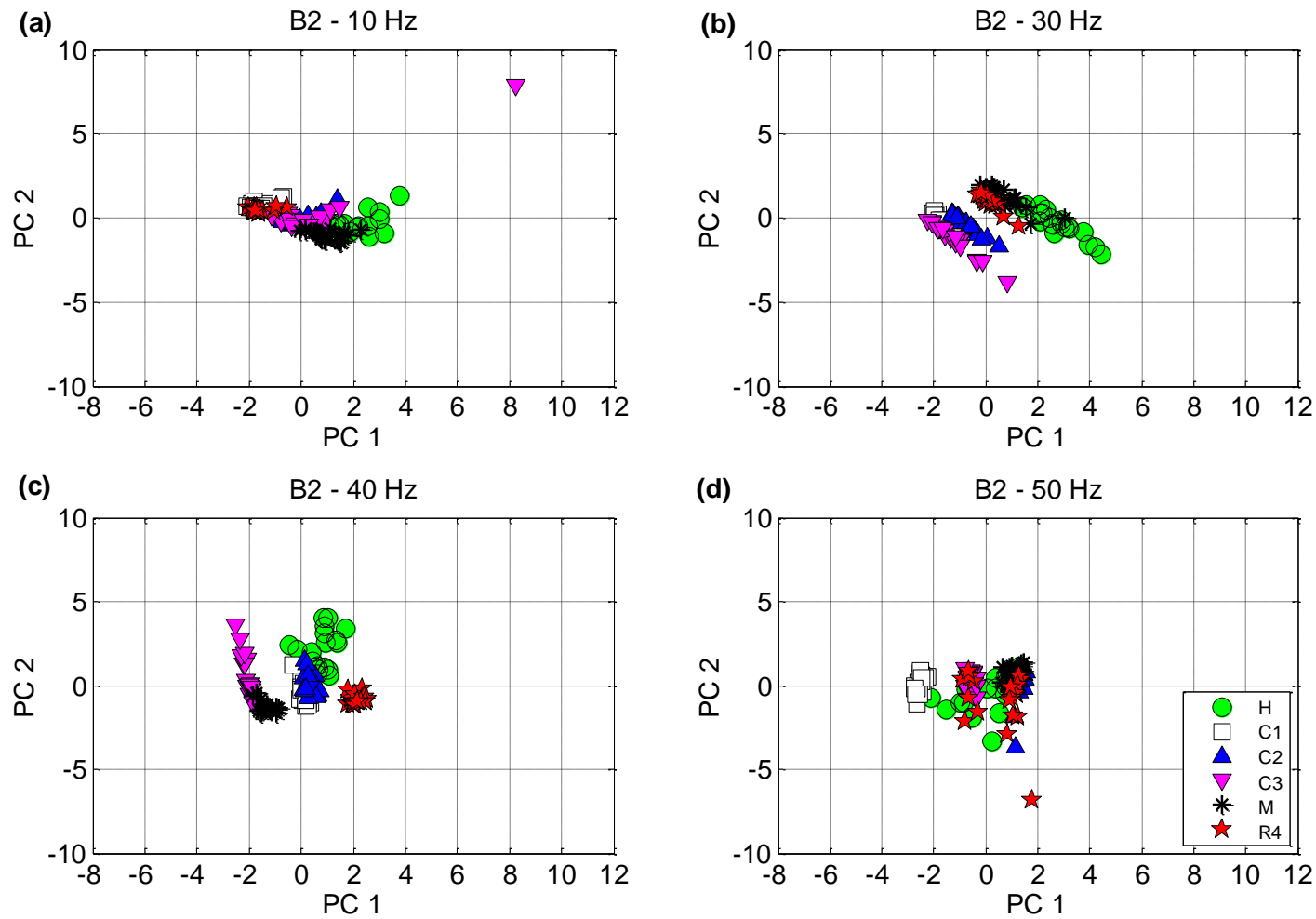


Figure 6.13 Single speed analysis using only **Bearing 2** features at: (a) 600 rev/min, (b) 1800 rev/min, (c) 2400 rev/min and (d) 3000 rev/min

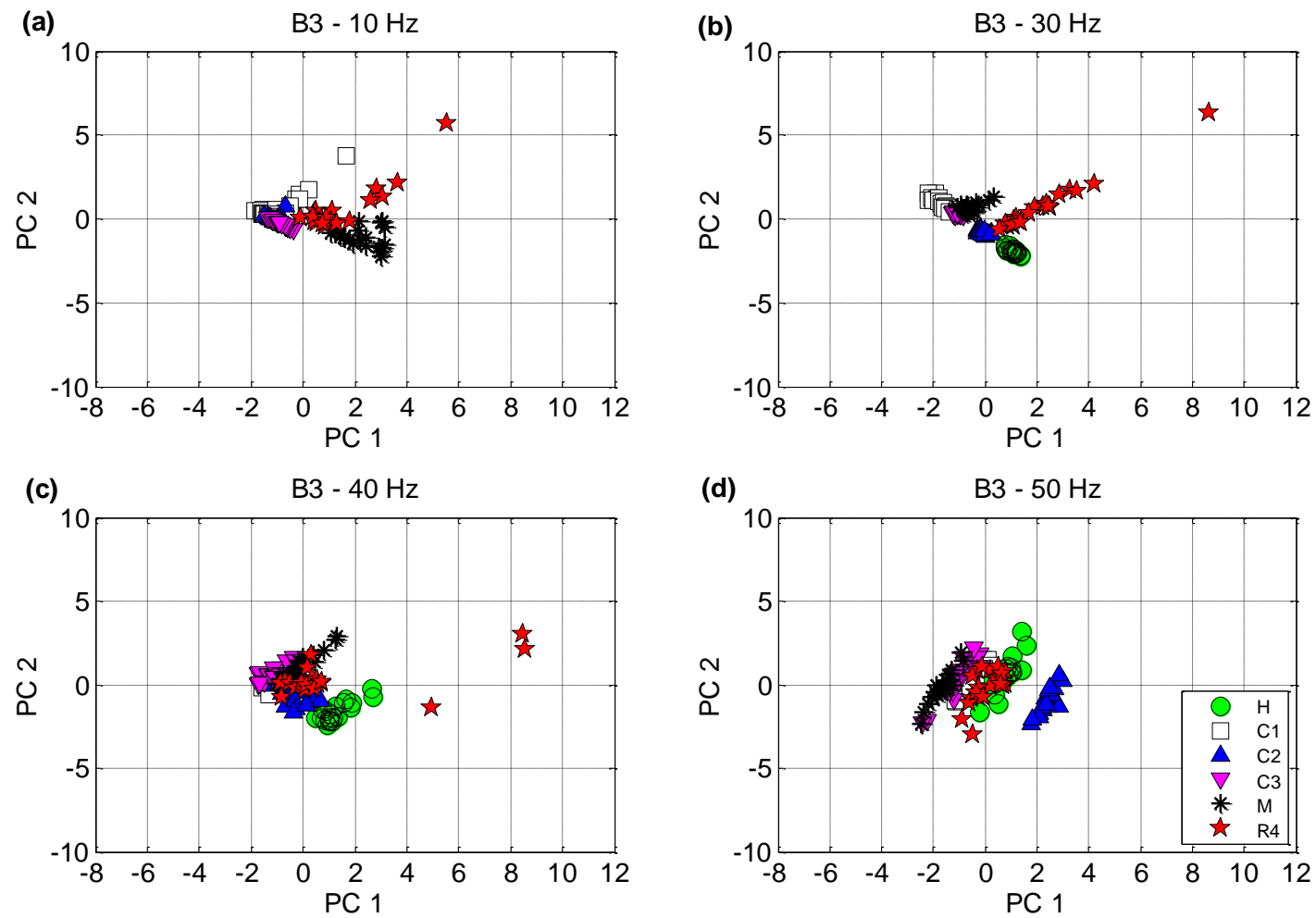


Figure 6.14 Single speed analysis using only **Bearing 3** features at: (a) 600 rev/min, (b) 1800 rev/min, (c) 2400 rev/min and (d) 3000 rev/min

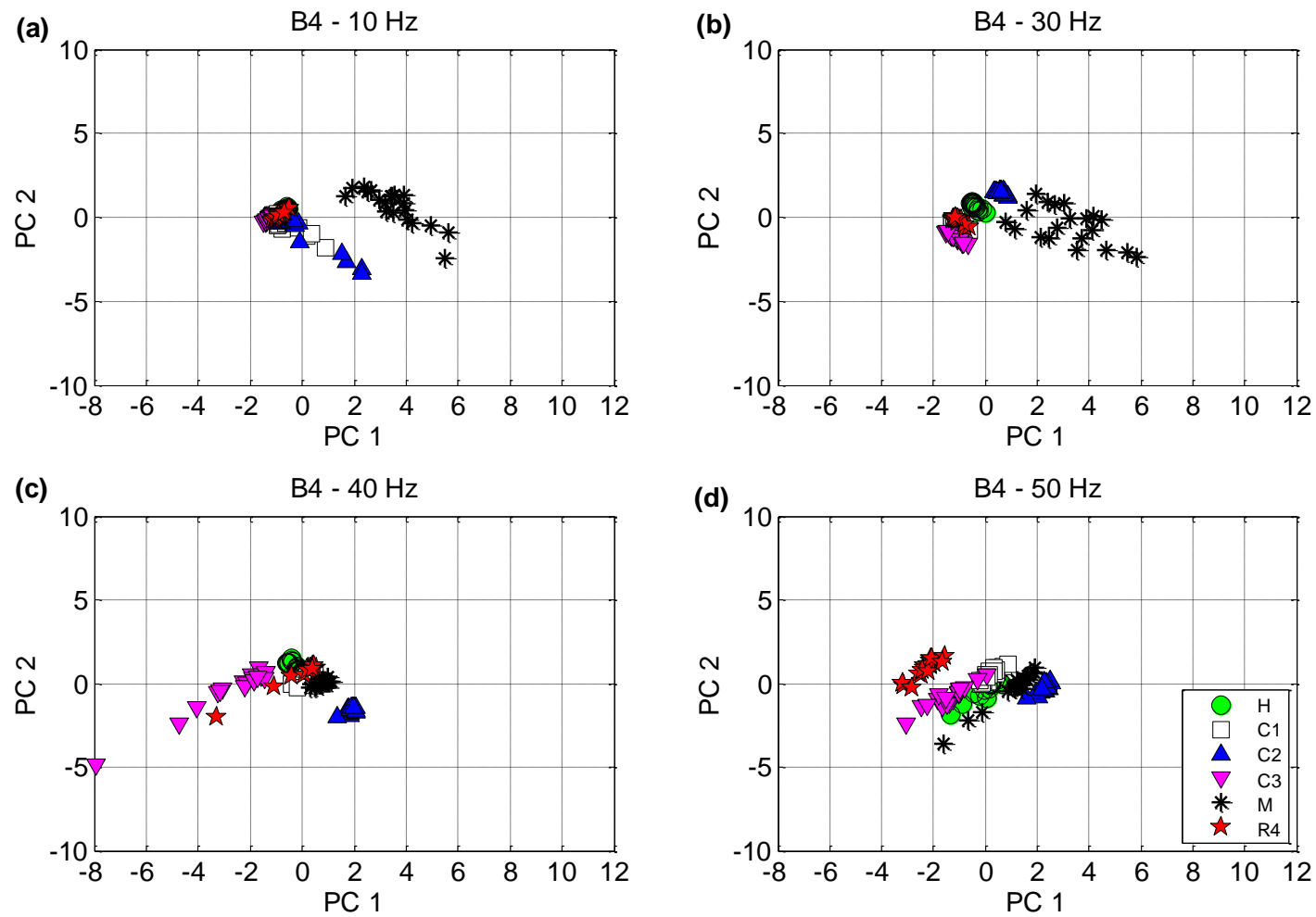


Figure 6.15 Single speed analysis using only **Bearing 4** features at: (a) 600 rev/min, (b) 1800 rev/min, (c) 2400 rev/min and (d) 3000 rev/min

6.7.2 Analysis of integrated features from multiple speeds at a single bearing

In light of the observations made in the analysis of features from a single speed at single bearing (see Section 6.7.1), consideration was given to analysing data obtained at different speeds at a single bearing location to ascertain whether any improvements could be achieved by combining any useful data available at a single measurement location at different speeds. Plots of the results of integrating features from multiple speeds acquired at a single bearing measurement location are shown in Figures 6.16(a)-(d) for Bearings 1-4, respectively. Note that features were combined for data acquired at all five speeds tested (600 rev/min, 1200 rev/min, 1800 rev/min, 2400 rev/min and 3000 Hz).

Improved separation of some fault conditions are observed compared to the previously seen single speed and single bearing analysis, however, the plots shown lack the isolation of the healthy condition and complete separation of different fault conditions that is desirable. Overall, it was encouraging to see some improvement over the previous analysis, but it seems more information is still required to accurately classify the state of the machine.

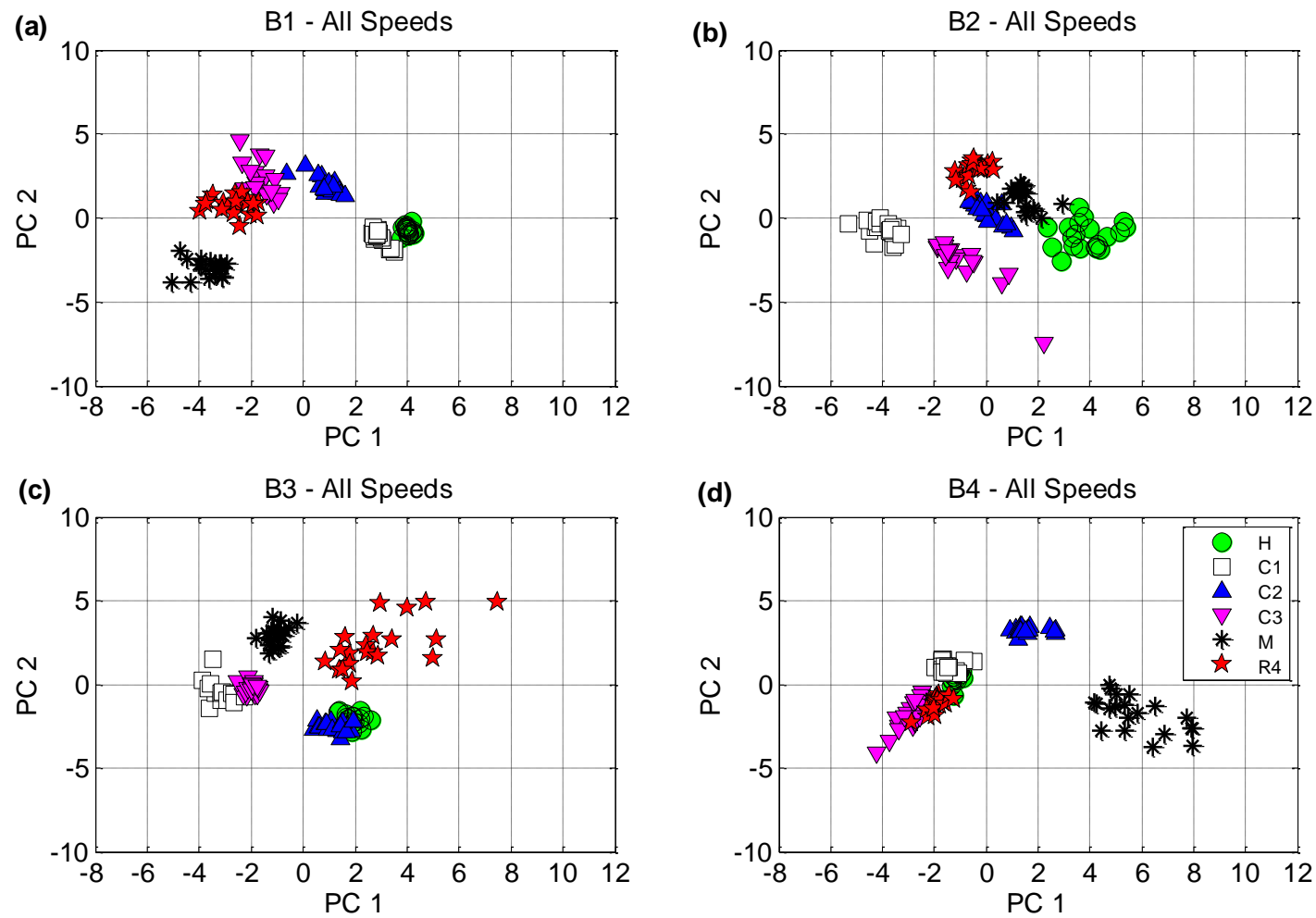


Figure 6.16 Results of integrating features from **all speeds** from **one bearing** for (a) B1, (b) B2, (c) B3 and (d) B4

6.7.3 Analysis at a single speed for integrated features from multiple bearings

Figure 6.17 shows representative samples of the results that were obtained for the integrated bearing analysis at a single speed. Results are presented for 600 rev/min (10 Hz), 1800 rev/min (30 Hz), 2400 rev/min (40 Hz) and 3000 rev/min (50 Hz) in Figures 6.17(a), (b), (c) and (d), respectively. Immediately, it was noticed that the isolation of the healthy data set is the best seen yet. Additionally, separation among the different faults tested was better than the single speed single bearing analysis (see Section 6.7.1) but comparable the multi-speed single bearing analysis (see Section 6.7.2). Consequently, the separation of the healthy condition seen here would most certainly be useful for confidence inspiring FD. From all analyses done so far it seems inclusion of data from different bearings increases separation among the fault conditions while integration of different speeds improves the isolation of the healthy condition. It therefore seemed an opportunity to further improve the efficacy of the tool if the benefits of integrating data from different bearing locations and different speeds are is performed in a single analysis. The utility of this concept is explored in the following section.

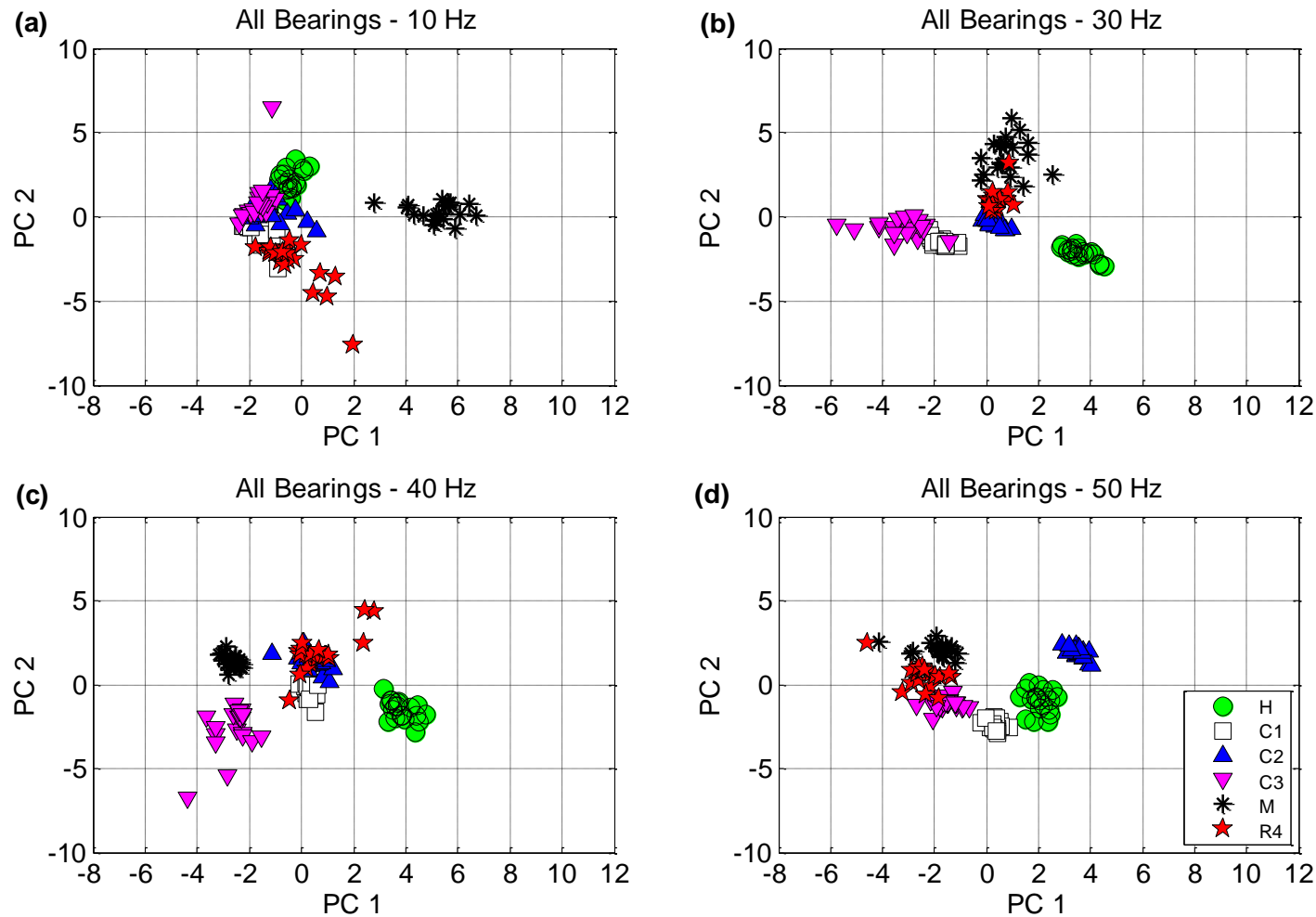


Figure 6.17 Samples of results from analysis at **one speed** for integrated features from **all bearings** for:
 (a) 600 rev/min, (b) 1800 rev/min, (c) 2400 rev/min and (d) 3000 rev/min

6.7.4 Unified Multi-speed analysis (integrated features from multiple speeds and multiple Bearings)

The results of the Unified Multi-speed Analysis which combines data from multiple speeds; 600 rev/min, 1200 rev/min, 1800 rev/min, 2400 rev/min and 3000 rev/min, and multiple bearing measurement locations in a single analysis is presented Figure 6.18. It can be seen that different well defined isolated clusters corresponding to each condition (observation) input to the analysis was generated on the plot. Each fault condition was visibly separated from the healthy condition with misalignment showing the greatest separation distance. At this point in the current study it is now known whether the distance of separation is an indication of the severity of the fault. Further experimentation would be required to ascertain this. It was also interesting to note that the Crack near Bearing 1 (C1) and the Crack near Bearing 3 (C3) conditions occupied the same region on the plot. On the other hand, the close proximity of the Crack near Bearing 2 (C2) case to the Healthy data set indicates that, over the speed range tested, this condition was most similar to the Healthy condition. It was also encouraging to note that Crack and Misalignment faults, which are oftentimes indistinguishable with traditional techniques, are separated in this instance. It was also duly noted that the clustering, isolation and separation of the different conditions tested were much improved for the Unified Multi-speed Analysis than for all other analyses previously done.

Overall, the observations made here further suggest analysis of a single bearing or single speed may not provide sufficient information to accurately discriminate the state of the machine. It was, therefore, worthwhile to collectively analyse the responses across the entire machine at the different steady-state speeds tested; in order to overcome the intricate challenges that exist when attempting analysis of data from different steady-state speeds with the amplitude spectrum. As noted earlier, PCA as a tool exposes relationships or patterns between large data sets, which otherwise would have been difficult to identify. Thus, when sufficient relevant information is input to the tool, it is accurately able to classify or identify the state of the machine. Therefore, the integration of more dynamic features that are available across different measurement locations and at the different steady-state speeds improved the learning process of the tool. Most importantly, the

desired result of conspicuous fault classification was obtained with the Unified Multi-speed approach without the expense of complicating the analysis process.

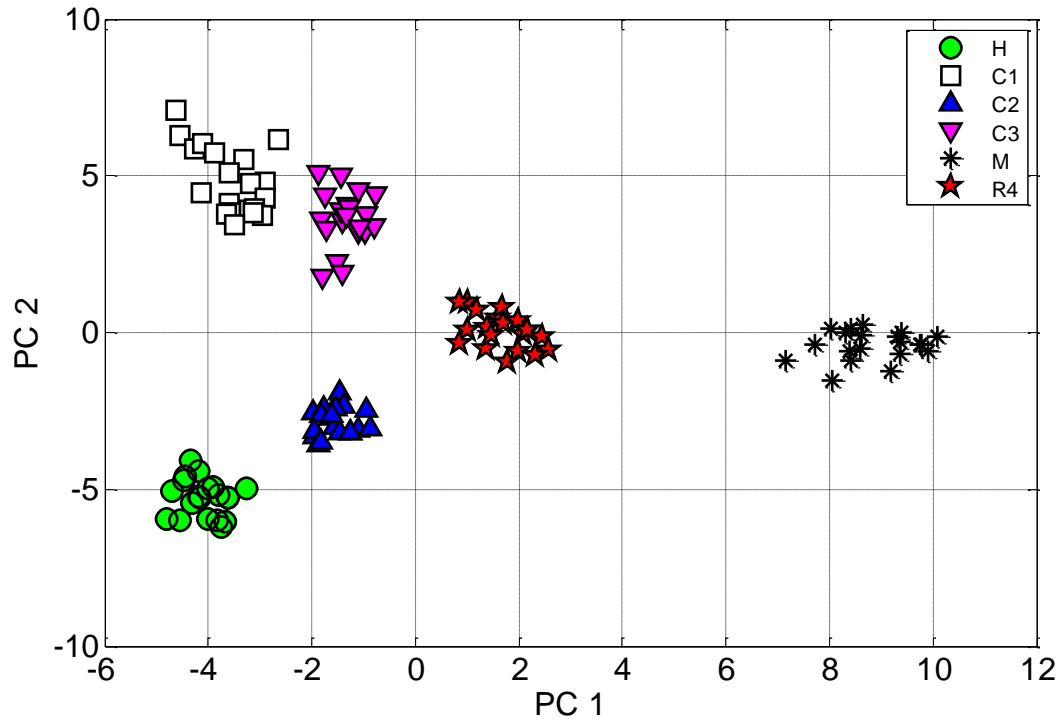


Figure 6.18 Results of proposed Unified Multi-speed Analysis comprised of features integrated from all speeds (600, 1200, 1800, 2400 and 3000 rev/min) and all bearings (B1–B4)

In practice, access to useful data can be a bane to vibration-based condition monitoring, thus the technique presented here offers a simple but, robust alternative for exploiting readily accessible data. The proposed technique would require historical data, from say a database of actual fault occurrences. As new data become available, this would be fed into the database from which the algorithm mines and generates the input matrix. Continuous classification would be done. Therefore, if a fault does not exist with data that is fed into the algorithm, it would be grouped into the healthy cluster. This would continue until, say data with a fault occurrence is supplied to the tool, which would classify and group the fault into its respective cluster. Indeed, the efficacy of the proposed technique is limited to the quality of data available for processing. Nevertheless, it would be a simple but robust data driven learning system that is easily updated to include new features or faults [39].

6.8 Summary

A unified fault diagnosis method was proposed for rotating machines operating at different steady-state speeds. Commonly applied condition indicators were computed from on-bearing vibration data collected from an experimental rig at different speeds for a healthy (baseline) condition, as well as crack, misalignment and rub fault conditions. Prior to applying these condition indicators, the amplitude spectra of the measured data were generated to demonstrate the difficulty encountered when analysing data from different steady-state speeds. Thereafter, using the condition indicators, four different sets of analyses were performed: single speed at a single bearing, integrated features from multiple speeds at a single bearing, single speed for integrated features from multiple bearings and then the proposed Unified Multi-speed analysis.

Single speed at a single bearing analysis had little or no separation between conditions, therefore suggesting not enough useful diagnostic information is available at a single bearing location when operating at a steady-state speed. Multi-speed single bearing and single speed multi-bearing analyses had good separation, with the latter having better isolation of the healthy case. However, the most promising results were obtained from the proposed Unified Multi-speed analysis approach which had well defined isolated clusters of data points corresponding to each condition input to the analysis. Each fault condition was also visibly separated from the healthy condition. Thus, integration of more dynamic features available at different speeds and different bearing locations improved the learning process of the tool. As with any data driven technique, the accuracy of the proposed method is confined to the quality of data available for processing. Notwithstanding, it is a simple, but robust data driven learning system that can be easily updated to include new faults. These attributes make the proposed method a potential tool that could effectively discriminate fault conditions using the wealth of data available from existing aero-engine management systems. Testing on different rigs with different bearing set up and validation of experimental results with numerical simulations are required to further explore the utility of this approach.

7 DEVELOPMENT OF A GENERIC ROTATING MACHINERY FAULT DIAGNOSIS APPROACH INSENSITIVE TO MACHINE SPEED AND SUPPORT TYPE

Reformatted version of the following papers:

- 1.** **Title:** Development of a generic rotating machinery fault diagnosis approach which is insensitive to machine speed and support type

Authors: Adrian. D. Nembhard, Jyoti K. Sinha and A. Yunusa-Kaltungo

Status: Published in Journal of Sound and Vibration
- 2.** **Title:** Vibration-based Condition Monitoring for Rotating Machinery with Different Flexible Supports

Authors: Adrian D. Nembhard, Jyoti K. Sinha and A. Yunusa-Kaltungo

Status: Submitted to 10th International Conference on Vibration Engineering and Technology of Machinery VETOMACX 2014. Manchester, UK, 9-11 Sept 2014. Paper ref: VCX2014_1003

Abstract: Despite numerous difficulties that can be encountered when using trend monitoring of harmonic components from the simple amplitude spectra to aid diagnosis of rotor-related faults on large multi-stage multi-bearing rotating machines, the technique continues to be the mainstay in industry. This is due in part to factors including a lack of adequate experimental validation of newly proposed techniques aimed at improving or replacing this traditional practice. Nevertheless, in recent studies, simple but robust Individual Speed Individual Foundation (ISIF) and Multi-speed Individual Foundation (MSIF) fault diagnosis (FD) methods that both used a single vibration sensor per bearing without the use of phase information was applied with good results to fixed and variable speed machines, respectively. A similar Individual Speed Multi-foundation (ISMF)

technique later enabled FD by direct comparison of vibration data between similarly configured machines with different dynamic characteristics operating at the same steady-state speed. However, the efficacy of these techniques was questioned as they were all applied to experimental rigs with the same few rotor-related faults. Thus, the objective of this study is to test the transferability of these said techniques on a wider range of rotor-related faults on different machines. A new Multi-speed Multi-foundation (MSMF) method which facilitates FD by the direct comparison of vibration data from similarly configured machines with different dynamic characteristics operating at different steady-state speeds is also proposed. It is observed that the previously proposed methods are indeed able to separate the range of conditions tested on machines with different dynamic characteristics. Analysis done with newly proposed MSMF approach gives improved isolation of fault conditions tested compared to the previously proposed techniques.

Keywords Condition monitoring; vibration analysis; rotating machinery; fault diagnosis; rotor-related faults; data fusion

7.1 Introduction

Vibration-based diagnosis of rotor-related faults using the simple amplitude spectra is widely used in practice; owing to factors including its range of fault sensitivity, relative computational simplicity and flexibility for application to different types of machines. Despite its versatility, challenges can be encountered when considering fault diagnosis (FD) of a large rotating machine with multiple bearings say, a multi-stage steam turbine. A number of vibration sensors and measurements (including phase information) are required at each bearing location [1]; which results in the acquisition of large volumes of data. The measured data then becomes a computational burden to process and extract useful information (features) which best represent the health (condition) of the machine [53, 54]. Even after successful extraction, fault features may be indistinguishable and misleading. Consequently, in traditional practice, it has been accepted that the simple spectra on its own may not be adequate for confident FD and might require support from additional techniques; such as the Orbit plot [12]. Because of such difficulties in processing and

interpretation of the data, the FD process can be lengthy, subjective and inconsistent; all of which could prove costly and hazardous to life.

Consequently, ongoing research has focused on improving vibration-based FD. Such efforts can be divided into two broad categories: the improvement or development of traditional techniques and alternatively the development of new techniques [14]. The works done can be further divided into different or a combination of different focus groups [51]: data input, data manipulation, health assessment and prognostic assessment. Data input deals with sensors, transducers and methods of data entry, while data manipulation addresses signal processing and feature (descriptor) extraction. The British Standards Institution [51] states that health assessment “utilizes expertise from human or automated agent to determine the current health of the equipment and to diagnose existing fault conditions”. Prognostics deal with predicting the future state of monitored equipment using various models and their algorithms. Some recent experimental works aimed at developing new approaches in the mentioned focus groups have been succinctly reviewed.

Hashemian [16] demonstrated the usefulness of wireless vibration sensors for remote condition monitoring of rotating equipment on a research nuclear facility. The biggest benefit was of course remote access to equipment which would have otherwise been unsafe for manual data collection. Similarly, Arebi et al. [15] compared wireless sensors with three commonly used sensors; a laser vibrometer, an accelerometer and an encoder. These were used to measure and compare their respective responses in the time and frequency domain on a misalignment condition to test the performance a wireless measurement scheme. It was found, amongst other things, that “the wireless sensor produces a full separation of levels and shows a unique increasing trend with speed.” Though, useful for remote access of machinery with clear benefits for increased safety condition monitoring technicians, the use of wireless sensors does not mitigate the aforementioned difficulties associated with the traditional practice in vibration-based fault diagnosis. That being said, Elnady et al. [17] proposed the use of the on-shaft vibration (OSV) measurement technique using a MEMS wireless accelerometer and found that it requires special arrangement of the measurement instrumentation that currently may not be applicable in a practical sense.

Numerous studies have focused on developing relatively new data manipulation techniques such as time-frequency analyses [21-23]. Even with over 20 years of

development and promising results thus far, there still exist various complexities, with the practical application of the widely studied time-frequency analysis methods to machine FD [21, 23]. Qin et al. [89] proposed a technique which focused on multicomponent vibration signal separation. The objective was to introduce a method that could accurately extract features that would be useful for FD. Though it was opined that the proposed method had better accuracy than some established time frequency techniques, it was noted that the method is slow and in need of future development.

Other researchers have directed efforts that address combined improvements in data input, data manipulation and health assessment. That said, Sinha and Elbhah [28] suggested fusion of data from all sensors in the frequency domain for the extraction of useful diagnostic features, while avoiding the complexity of traditional techniques. The Higher Order Spectra (HOS), namely bispectrum, which is derived from a composite spectrum, was demonstrated. It was postulated that the HOS would facilitate: sensor reduction (as only one sensor per bearing was required), utilisation of computational power in current signal processing to compensate for sensor reduction and data fusion. By exploring the relations of different harmonics of the same signal measured at a bearing pedestal, the authors were able to obtain unique features for the conditions tested. Elbhah and Sinha [29] later explored the usefulness of the coherent and non-coherent composite spectra for data fusion of on-bearing vibration data for fault discrimination and observed that the coherent composite spectra were better able to discriminate between the faults tested. In both studies, it was similarly concluded that the suggested methods had the potential for practical application, but the methods were complex.

Jiang et al. [18] proposed a multi-sensor feature-level fusion methodology with subsequent Support Vector Machine (SVM) classification of time domain vibration features for the diagnosis of rotating machinery faults including rotor crack. The authors opined that for a complex system, a single sensor is incapable of collecting data requisite for accurate fault diagnosis, and as such multiple sensors, when applied simultaneously are better able to comprehensively describe a machine state. The technique was demonstrated on a small laboratory rig with crack fault amongst others. Though promising, since there is no standard method for choosing the kernel function [30], which is the key process for SVM, the choice of the kernel function used here, and by extension the results obtained, is questionable.

Nembhard et al. [123] introduced a novel processing method for the diagnosis of rotor-related faults on a machine operating at an individual steady-state speed, while Nembhard and Sinha [132] later developed this technique for the diagnosis of faults on machines that can operate at different steady-state speeds called a “Unified Multi-speed Analysis”. The salient common objectives in both studies were the development of a simple but robust diagnostic method that could process data from a reduced number of sensors per bearing. The former technique was based on recognition of patterns in temperature and vibration-based features extracted from each bearing for a given condition, while the latter was based on feature-level fusion of purely vibration features extracted at different steady-state speeds from a given machine with a given rotor fault. Both studies similarly produced easily interpreted graphical representations that negated the need for a skilled and highly experienced vibration analyst. Although the results presented in both studies were seemingly practicable, both techniques were tested on the same experimental with the same three rotor-related faults, which brought to question their feasibility on different machines with a wider range of faults.

Further to this, Nembhard and Sinha [133] conducted a study with the aim of investigating the transferability of the method previously proposed by Nembhard et al. [123] on machines with different flexible supports and to apply a derivative of the said technique as a proposal of a “combined foundation” approach which enabled the direct comparison of vibration data between two rotating machines of the same type for the purpose of fault diagnosis. Experiments were done at a single steady-state rotating speed on two similarly configured laboratory rigs with different flexible supports, which were modified versions of the previously used rig. By computing different features from the measured vibration data, it was concluded that the previously proposed method was indeed transferable to machines with different dynamic characteristics for the diagnosis of crack, misalignment and rub. The newly introduced technique allowed comparison of vibration data between two different machines operating at the same steady-state speeds for the purpose of fault diagnosis. Though this study mitigated the question of the transferability of the previously proposed techniques, transferability is yet to be seen on the method proposed by Nembhard and Sinha [132]. Additionally, the question on whether the

techniques are useful for the diagnosis of a wider range of common rotor-related faults lingers, because the same there rotor-related faults were again tested.

Considerable research has been done on the application of artificial intelligence (AI) techniques including Neural Networks and Fuzzy Logic, to circumvent the human dependence in traditional diagnosis by fully automating vibration-based FD in the health assessment process [24]. However, though the subject of ongoing research, AI-based methods remain somewhat digressed from current practical applications [26]. On an advanced level to automated diagnosis, there exist Prognostic and Health Management (PHM) techniques. These techniques can be treated as a future-based evolution of Condition-based Maintenance (CBM) that emphasizes a maintenance methodology of predict-and-prevent; as opposed to the traditional fail-and-fix (also referred to as diagnostics), while still relying on the said traditional diagnostic techniques for data input [30]. It is therefore implicit that given the current need for development in CBM practices, the reliable implementation of PHM techniques may be somewhat protracted.

In light of the practicable opportunity for sensor reduction, simplicity and ease of interpretation offered by the techniques suggested by Nembhard et al. [123] and Nembhard and Sinha [132], the objective of this study is to test the feasibility of the said methods on a wider range of common rotor faults and at the same time investigate their transferability, with these said faults, to machines with relatively flexible supports. It is possible that the same rotating machine when installed at different plant sites exhibit different dynamic characteristics with different natural frequencies. However, the vibration data history requisite for condition monitoring and subsequent FD may exist at one site and be lacking in the other. Therefore, the current study also serves to test the efficacy of the method introduced by Nembhard and Sinha [133] on a wider range of commonly encountered rotor-related faults. A new method which is applicable to similarly configured rotating machines with different dynamic characteristics that can operate at different steady-state speeds is also proposed. To demonstrate the robustness of the proposed method, it has been tested for different conditions. As noted in the previous studies, the simplicity of data collection from a single sensor per bearing, processing and easy results interpretation would be preserved.

The experimental rig previously by Nembhard et al. [123] was modified to separately accommodate two different sets of relatively flexible bearing supports; Flexible Support 1 and Flexible Support 2 (FS2). Several samples of on-bearing vibration data were collected at different steady-state sub-critical speeds for a baseline condition as well as different fault conditions. For reference, comparisons are made to traditional diagnosis using Orbit Plots [12] and the simple amplitude spectra. The previous individual [123] and “Multispeed” [132] techniques were tested firstly on FS1 and then on FS2. Afterwards, the combined foundation approach [133] using FS1 and FS2 operating at the same steady-state speed is explored with a wider range of fault conditions. Lastly, the proposed method for comparison of similar machines with different foundations operating at different steady speeds is presented. The results of the individual speed, “Multi-speed” and combined foundation at individual speed analyses showed good separation between the different conditions tested, thus suggesting the methods are transferable to machines with different dynamic characteristics for the conditions tested. More encouragingly, the newly proposed multispeed combined foundation technique gave improved clustering and isolation of the conditions tested.

The paper hereafter is organised as follows. In Section 7.2, descriptions of the experimental set up and different conditions tested are given. Observations made using the orbit plot and simple amplitude spectra on the conditions tested here are discussed in Section 7.3. Afterwards, the basis for data processing and analyses employed in the current study are outlined in Section 7.4. FD with the previously proposed techniques on the experimental rig is offered in Section 7.5. Observations on the same rig with a different foundation are provided in Section 7.6. In section 7.7, FD with the newly proposed combined foundation approach is presented. Finally, concluding remarks are made in Section 7.8.

7.2 Experimental set up and experiments conducted

In this section, the experimental set up used in the current study is described in detail. This includes a detailed description of the mechanical layout and instrumentation used. Lastly, the different methods used to create the different conditions tested are outlined.

7.2.1 Mechanical layout and instrumentation

A diagram of the experimental rig used in this study is shown in Figure 7.1. The rig is a fundamental model of a multi-stage rotating machine. The previously used rig [123, 132] had relatively rigid supports and was modified to accommodate relatively flexible supports. The rig's rotating assembly consists of two 20 mm diameter rigidly coupled (C2) mild steel shafts of lengths 1000 mm and 500 mm. Machined steel sections which act as balancing discs (125 mm in diameter and 14 mm thick) are mounted to each rotor; two discs (D1 and D2) for the long shaft (Rotor 1) and one disc (D1) for the short shaft (Rotor 2). Rotor 1 is connected to a three phase 0.75 kW 3000 rev/min electric motor by a semi-flexible coupling (C1). The rotating assembly is supported by four grease lubricated 20 mm internal diameter SKF (FY 20TF) flanged ball bearings (B1–B4).

Each bearing is mounted at its corners by four flexible machined steel rods that are secured to a flexible mild steel bearing pedestals. Each bearing pedestal is bolted to a relatively high mass steel lathe bed that serves as the rig's foundation. The flexible machined steel rods combined with the steel pedestals act as the overall bearing supports and are thus referred to in the present study as "Flexible Supports". Two different sets of flexible supports, Flexible Support 1 (FS1) and Flexible Support 2 (FS2), consisting of machined steel rods of 10 mm and 6 mm diameter, respectively, were investigated. In most real machines, the foundations appear stiff, but due to the mass of the rotor the dynamic stiffness of the complete system becomes low and the complete machine generally has a number of critical speeds below its operating rev/min [115, 116]. This is typically observed in heavy rotating machines like steam turbines. Hence, the flexible support rods used in the current study is representative of the foundation of a real machine. At any given time the experimental set up consisted of purely FS1 or FS2. Note that when changing between FS1 and FS2 set up, care was taken to ensure that rotating assembly and bolting between the bearing pedestals and the lathe bed were undisturbed. Thus, the rig configuration and main dimensions shown in Figure 7.2 were consistent between FS1 and FS2.

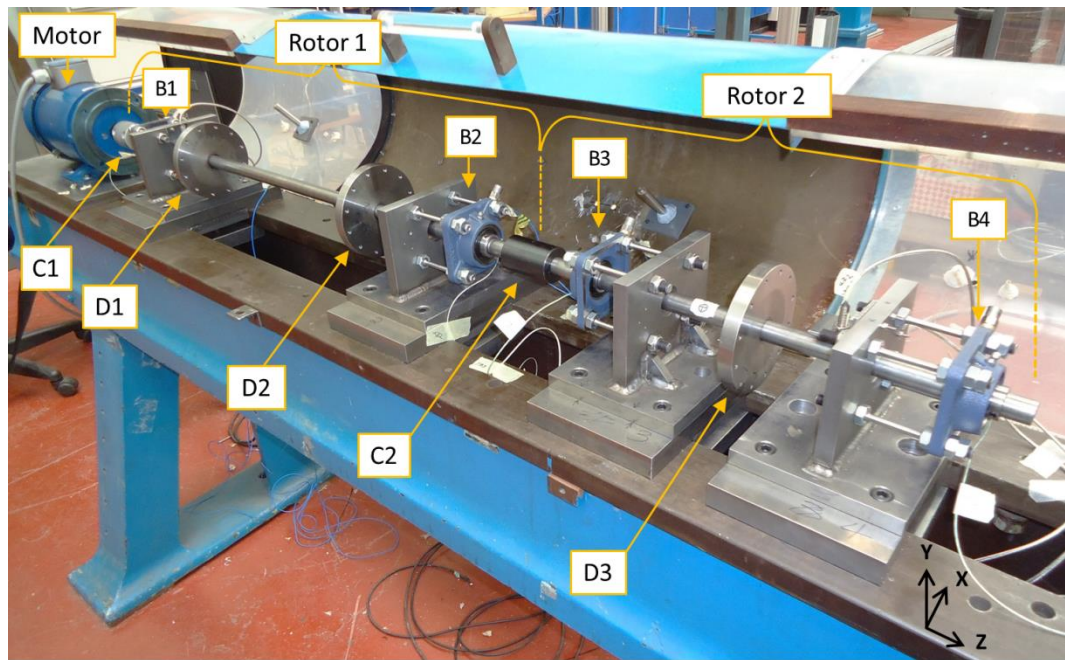


Figure 7.1 Mechanical layout of experimental Rig

The impact-response method of modal testing [50] was employed to confirm FS1 and FS2 dynamically different from each other and also from the supports used in the aforementioned previous studies. By appearance, the natural frequencies, of the previous rig were identified by Elbhbah and Sinha [29] at 68 Hz, 144 Hz and 352.5 Hz. By appearance, the first four natural frequencies for FS1 are 50.66 Hz, 56.76 Hz, 59.2 Hz and 127 Hz. Similarly, the first four natural frequencies for FS2 are 47 Hz, 55.54 Hz, 57.98 Hz and 127 Hz.

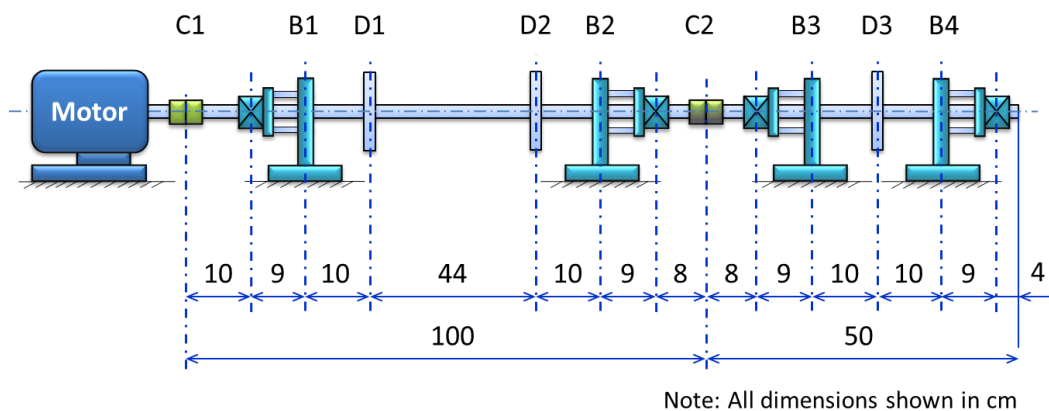


Figure 7.2 Schematic of experimental rig with main dimensions

A schematic of the instrumentation used is provided in Figure 7.3. As shown, the dynamic response of the rig is measured by four displacement probes and four accelerometers. Two Monitran (Mod.: MTN/EP080) 8mV/ μm industrial eddy current displacement probes are each mounted in mutually perpendicular (X-Y) directions (see Figure 7.4a) at B1 and B4. Each eddy current probe transmits data to and is powered by its dedicated Monitran (Mod.: MTNECPD) driver. The drivers are in turn powered by an external 24 VDC at 30 mA power supply (not shown in Figure 7.3). The accelerometers used are PCB (Mod.: 352C33) ICP type 100 mV/g accelerometers; one each mounted at a 45° position in the X-Y plane on the flange of each bearing (see Figure 7.4b). This accelerometer mounting position was adopted to simultaneously account for the measurement of both the vertical and horizontal responses from the sole accelerometer used at each bearing. The accelerometers are mounted on studs that are attached to the bearings with super glue.

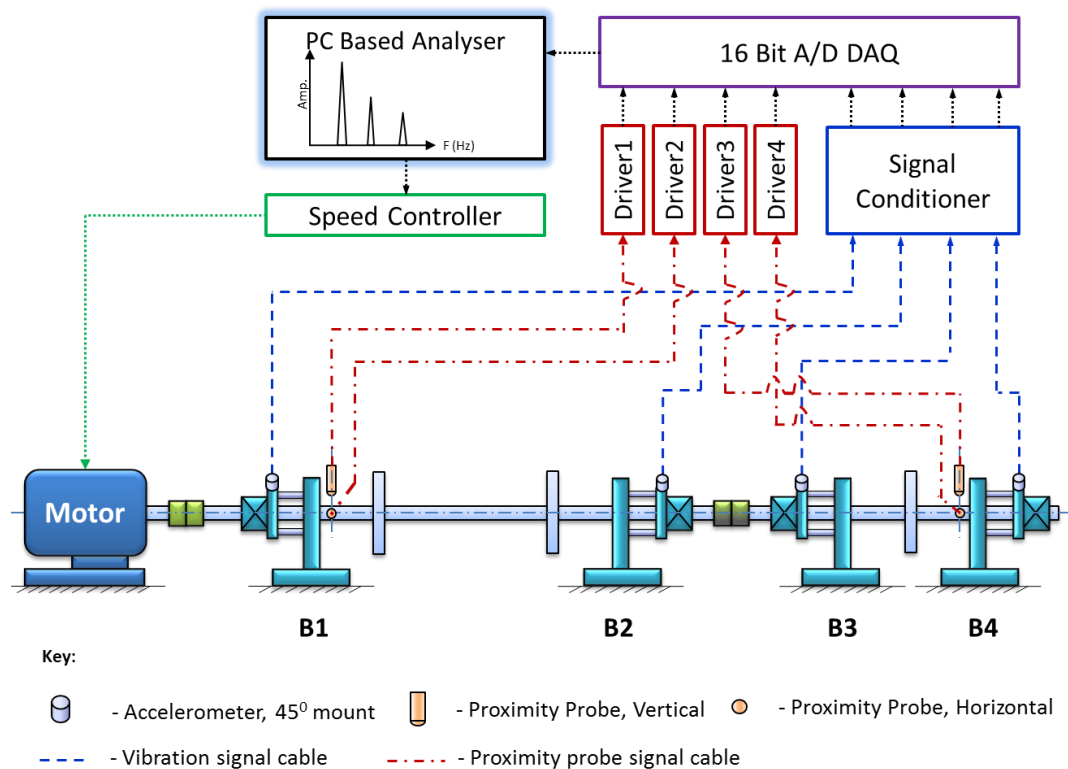


Figure 7.3 Schematic of experimental rig instrumentation and data acquisition (DAQ) system

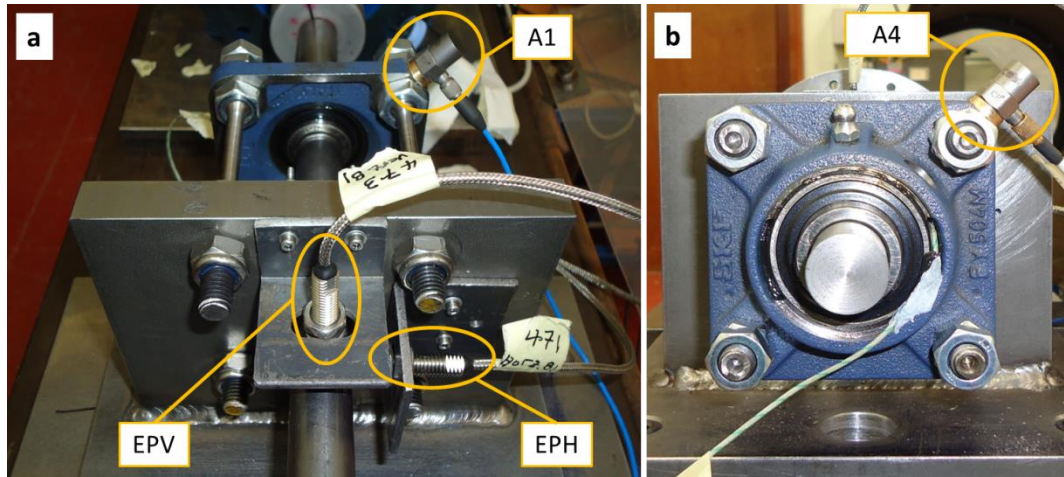


Figure 7.4 Details of mounting for: (a) proximity probes and (b) accelerometer

The vibration data are transmitted from the accelerometers to a PCB (Mod.: 482C Series) four channel signal conditioner with a 1:1 gain. The signal conditioner also powers the accelerometers. Both the eddy current probe drivers and the signal conditioner transmit data to a National Instrument (Mod.: NI USB-6229) 16 bit 16 channel analogue to digital (A/D) data acquisition (DAQ) system which is in turn connected to a personal computer via a USB cable. The vibration data are then recorded and stored on the personal computer for later processing and analysis. The rotational speed of the rig is varied with a Newton Tesla (Model: CL750) speed controller that is operated from the personal computer with a Melsoft FR Configurator software.

7.2.2 Experiments conducted

Data were first collected for a baseline condition which served as a reference state for the experimental rig. It is desirable for the baseline condition to be as “healthy” as possible to be used as a reference however, there were some difficulty in getting the rig sufficiently aligned to be deemed fully healthy. This, however, is typical of what would be observed in a practical case [28] and as such was suitable for the current study. The baseline condition was therefore characterised by some residual misalignment with residual unbalance, and thus referred to here as the Residual Misalignment with Residual Unbalance (RMRU) case. Six commonly encountered rotor fault conditions were tested; added unbalance, shaft bow, shaft crack, mechanical looseness, coupling misalignment and shaft rub. Three different

misalignment conditions of varying magnitudes and three rub cases (two blade rub and one shaft seal rub) were seeded. Therefore, a total of 12 scenarios spanning 1 baseline condition and six fault conditions were simulated. The faults investigated in the previous studies done [123, 132] were crack, misalignment and seal rub.

During testing, the initial set up of the experimental rig was FS1. Experiments were performed at steady-state rotational speeds of 1200 rev/min (20 Hz), 1800 rev/min (30 Hz) and 2400 rev/min (40 Hz). With one condition existing, testing started at 1200 rev/min (20 Hz). Vibration measurements were acquired at a rate of 10,000 Hz for a total of 20 different samples in a combined sample time of two minutes. With the condition unchanged, data acquisition was repeated for 1800 rev/min (30 Hz) and lastly for 2400 rev/min (40 Hz). A different condition was then introduced to the rig and the aforementioned procedure repeated until data were collected for all 12 scenarios. Afterwards, the rig was reconfigured to FS2 and the experimental procedure repeated. Testing was deliberately not done at 3000 rev/min (50 Hz) for either FS1 or FS2 so as to avoid dangerously high vibration amplitudes from resonance that could damage the rig or compromise the safety of the experiments. Resonance could occur due to excitation of the first natural frequencies in each set up; 50.66 and 47 for FS1 and FS2, respectively. Details of the different conditions seeded are provided hereafter.

As shown in Figure 7.5(a), a 2.6 g M5 × 25 mm screw was installed on D2, at 55 mm from the centre of the shaft; to create a 1.43×10^{-4} kgm unbalance for the Added Unbalance (Add_Unb) case. For the cracked shaft scenario (Crk_B1), the healthy shaft was replaced with a cracked shaft. The Wire erosion Electro Discharge Machining (EDM) process was used to create a 0.34 mm wide by 4 mm (20 per cent of shaft diameter) deep transverse notch (see Figure 7.5(b)). The crack was positioned so that when installed on the rig, it would lie 160 mm from B1 along the length of Rotor 1. A breathing crack was desired, however, the 0.34 mm notch was too large to give the desired effect. Thus, a thin 0.33 mm steel shim was inserted down to the base of the notch and glued to one side effectively producing a thin 0.01 mm crack that might breathe (open and close) as the shaft rotates.

Similar to cracked shaft, the healthy Rotor 1 was replaced with a bowed shaft with a 3.2 mm run out in the middle for the Bow condition (Bow). Looseness (Lse_B3) was introduced at B3 as shown in Figure 7.5(c). All nuts securing the bearing flange to the four machine steel support rods were slackened. Note that a grub screw locking the bearing collar to Rotor 2 prevented the bearing from moving along the length of Rotor 2 in Z-direction (see Figure 7.1). Thus, movement and consequently vibrations would be confined to the X-Y plane (see Figure 7.1). With reference to Figure 7.5(d), Misalignment fault was introduced at C1 in four scenarios with the placement of the following shims between the underside of B1 pedestal and the lathe bed: one 0.4 mm thick shim under “Right” side (Mlign104), one 0.8 mm thick shim under the “Right” side (Mlign108), two 0.4 mm thick shim one each on “Right” and “Left” side (Mlign204) and two 0.8 mm thick shims one each on “Right” and “Left” side (Mlign208).

The Rub cases tested were; blade rub and seal rub. Rub was introduced using the apparatus shown in Figures 7.5(e) and 7.5(f). The rub apparatus consists of a base and pedestal with clamp all made of steel. Blade rub was introduced by placing a Perspex rectangular disc between the clamps. The Perspex blade was positioned in the rub apparatus so that a 0.1 mm gap existed between the Perspex blade simulator and the shaft. Therefore, there was no initial contact between the blade and the shaft and a partial rub case would be created. Two blade rub scenarios were tested, Blade rub near D1(Rb_BD1) and Blade rub near Disc 2 (Rb_BD2), which positioned 275 mm from B1 (85 mm from D1) and 275 from B2 (85 mm from D2), respectively. To get the seal rub scenario (Rb_Seal), the Perspex blades were removed from the apparatus and a brass split bushing was introduced (see Figure 7.5(f)). Thus, a full annular rub case similar to that of a shaft seal rubbing against the shaft was introduced. For this condition, the apparatus was position 275 mm from B2. Note that that the rub apparatus was securely bolted to the lathe bed for each rub scenario. In all cases, the faults were introduced in a controlled manner, with minimal disturbance to the rig. In particular, the rig was designed to ensure that during set up for the crack and bow conditions, Rotor 1 could be removed from the rotating assembly with no disturbance to the bearing supports (FS1 or FS2).

Table 1 provides a summary of the current section, while a schematic outlining the locations of the different fault conditions tested on the experimental rig is given in Figure 7.6.

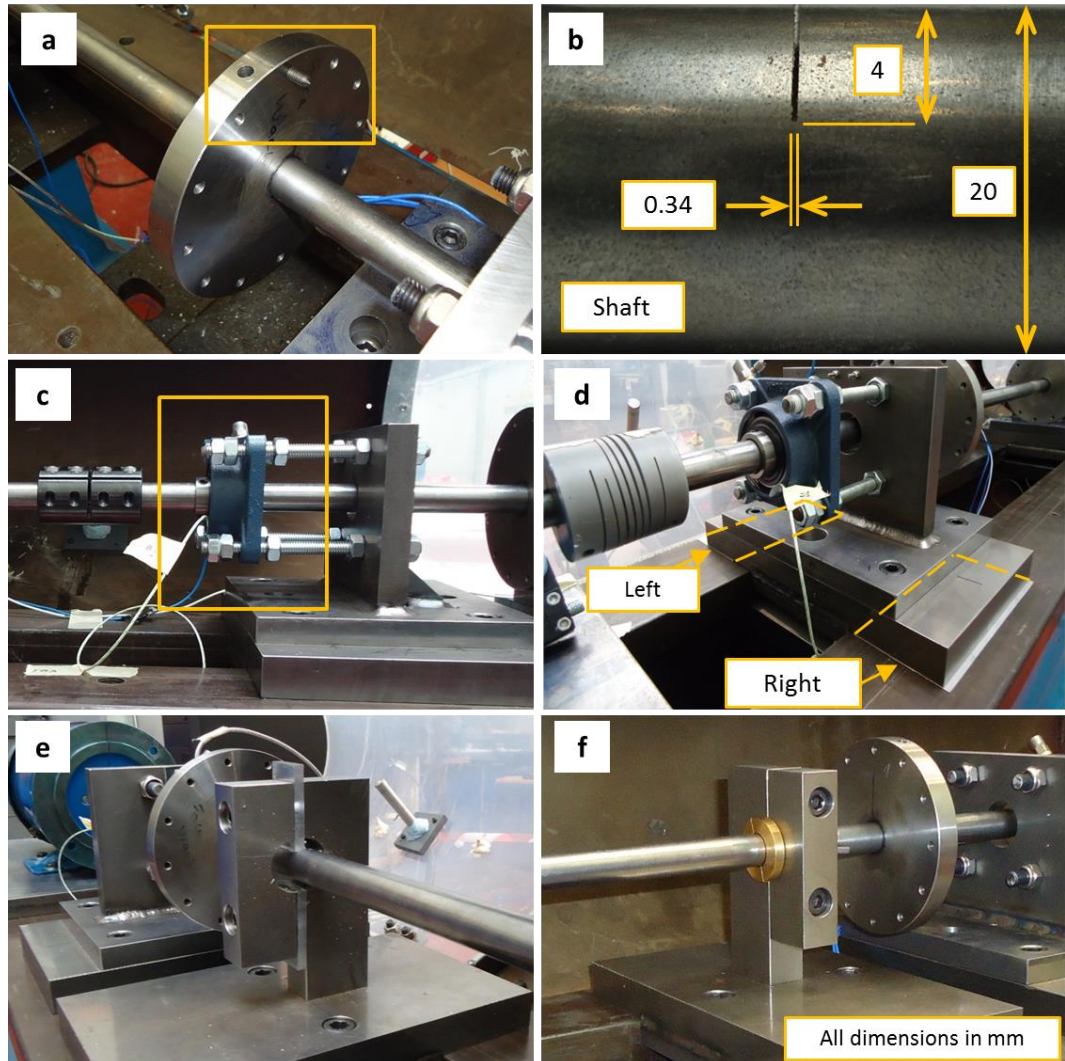


Figure 7.5 Details of all faults seeded: (a) Crack, (b) Added unbalance, (c) Looseness at B3, (d) Misalignment at B1, (e) Blade rub near D1 and (f) Seal rub near D2

Table 7.1 Summary of experiments conducted

No	Code*	Scenario name	Highlights
1	RMRU	Residual Misalignment and Residual Unbalance	No added fault: Baseline
2	Add_Unb	Added Unbalance	1.43×10^{-4} kgm
3	Bow	Bow	3.2 mm run out
4	Cr_Nr1	Crack near B1	20% of shaft diameter
5	Lse_B3	Looseness on B3	Motion in X-Y Plane
6	Mlign104	Misalignment at B1; 1 shim at 0.4 mm	“Right” underside
7	Mlign108	Misalignment at B1; 1 shim at 0.8 mm	“Right” underside
8	Mlign204	Misalignment at B1; 2 shim at 0.4 mm	“Right” and “Left” underside
9	Mlign208	Misalignment at B1; 2 shim at 0.8 mm	“Right” and “Left” underside
10	Rb_BD1	Rub (blade) near Disc 1 (D1)	Apparatus with Perspex blade
11	Rb_BD2	Rub (blade) near Disc 2 (D2)	Apparatus with Perspex blade
12	Rb_Seal	Rub (seal) near Bearing 2 (B2)	Apparatus with brass bushing

*Same nomenclature is used in figures throughout remainder of paper

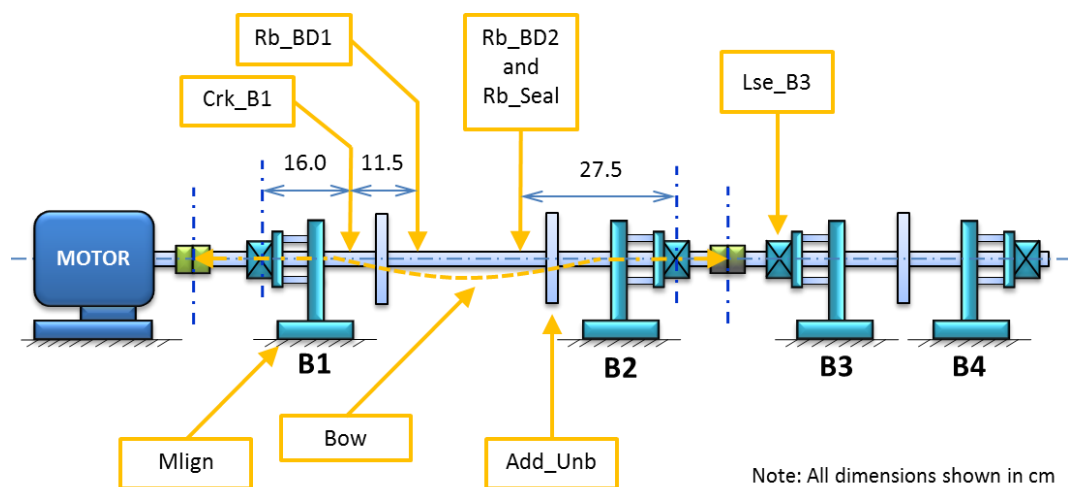


Figure 7.6 Schematic of experimental rig showing location of different fault conditions tested

7.3 Observations on orbit analysis and spectrum analysis

Observations made from the conventional practice of using the orbit plot for a time domain analysis and then the simple amplitude spectra for the frequency domain are discussed in this section.

7.3.1 Orbit plots – time domain analysis

The orbit plot presents the dynamic motion of the centre of the rotating shaft at the measurement plan [53]. It is widely accepted that relevant information on rapidly changing machine conditions can be had by observing Orbit shapes. Theoretically, the orbit shape should be circular if the dynamic stiffness at the measurement plane is equal in all radial directions and the only force acting on the rotor is its residual imbalance. Other forces or unequal restraints, such as those caused by faults (such as; bow, crack, misalignment, rub etc.) cause the rotor to respond with non-circular shapes [12].

Samples of the orbit plots generated at the B1 location, when the rig is operated at a steady-state rotational speed of 2400 rev/min (40 Hz) for FS1, are provided in Figure 7.7. Note that a signal was not acquired for the Bow condition as the proximity probes were removed for fear of damage due to the very high vibration amplitudes experienced with that condition. Each figure was generated by plotting the vertical proximity probe response (Y response) against the horizontal proximity probe response (X response). Both horizontal and vertical responses were filtered to allow only the $1\times$ and $2\times$ signal components.

With exception of the blade rub cases (RBD1, RBD2 and Rb_Seal), the shapes observed were not unique to a particular fault, but were in fact similarly elliptical (being slightly stretched in the vertical direction) with different magnitudes. The shapes produced could be due to the dominance of the $1\times$ component at 2400 rev/min due to the high flexibility of the rig, thus making the results look similar to what is customarily seen in a rig with an unbalance case [12, 86]. Similar observations of faulty cases producing shapes similar to the stretched ellipse seen here were made by Patel and Darpe [57] for misaligned rotors and Al-Shudeifat et al. [70] for a machine with a transverse crack operating near its first

critical speed. Justifications for the shapes shown in Figure 7.7 were beyond the scope to this study. The plots shown are presented to demonstrate that the Orbit plot was not indicative of the state of the machine at the speed tested and thus may not always be useful for rotor fault diagnosis. Similar observations were made for FS2 at 2400 rev/min (40 Hz).

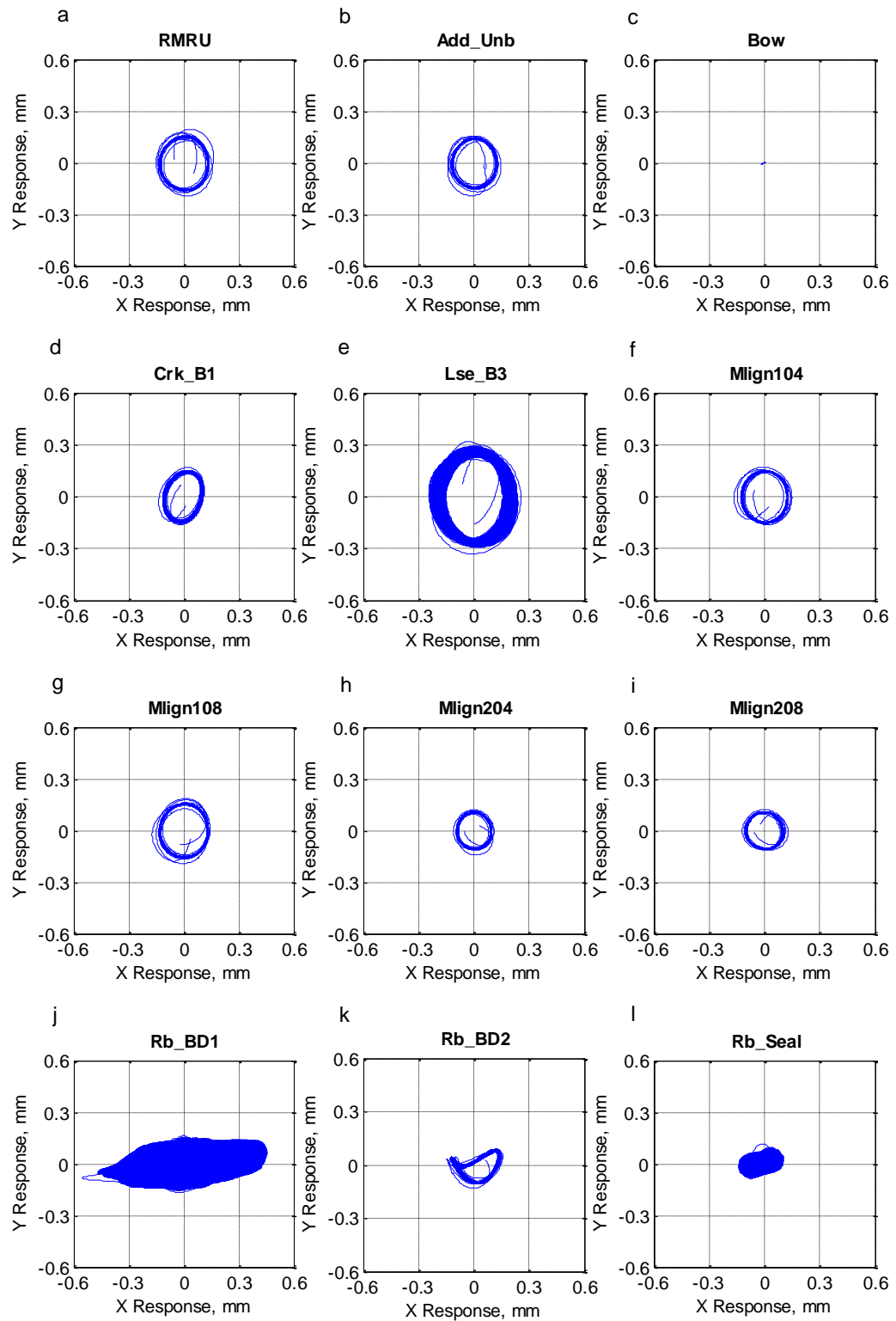


Figure 7.7 Orbit plots of FS1 at Bearing 1 for all faults at 2400 rev/min (40 Hz)

7.3.2 Amplitude spectra analysis – frequency domain analysis

Samples of the averaged simple amplitude spectra computed at B1 of FS1 for the different conditions tested are presented in Figure 7.8. Each spectrum was computed using on-bearing vibration data acquired from the accelerometer that was High Pass filtered at 5 Hz to remove any DC offset, if any was present, in the measured signal. The averaged spectra were generated using a Hanning window, a frequency resolution of 0.31 Hz and 95 per cent overlap. As previously noted in Section 7.2.2, and now shown in Figure 7.8(a), the RMRU baseline case used in the present study generated higher harmonics, thus confirming it was not “purely healthy”. Consequently, all spectra computed had multiple harmonics of $1\times$. The Add_Unb case (see Figure 7.8(b)) was identical to RMRU. The appearance of harmonics in a rotor bearing system, where unbalance is the only applied rotor fault, can be due to residual misalignment and other inherent forces in the system [6].

Though Bow (see Figure 7.8(c)) generated significantly larger amplitudes than Crk_B1 (see Figure 7.8(d)), both faults had almost exact same features. Except for Lse_B3 and RbD1 all other spectra did not have any noticeable unique feature. Lse_B3 did not change relative to the RMRU spectrum. There was, however, a noticeable mound at the $3.5\times$ frequency range. Rb_BD1 case had the only spectrum with higher fractional harmonics of the synchronous speed ($1\times$) [10]. Therefore, for FS1 at B1 at 2400 rev/min Looseness and RBD1 seem to have generated some discriminatory feature, but further analysis of spectra generated in both the horizontal, vertical and axial directions [53] for all four bearings present on the rig would have to be done to make that conclusion

A sample of the responses generated at a different bearing, B2, when operated at the same speed (2400 rev/min) for the same support, FS1, is given in Figure 7.9. It is immediately clear the reference condition previously seen at B1 (in Figure 7.8) does not apply at B2 (in Figure 7.9). Thus, as is noticeable in Figure 7.9, the features generated at B2 are considerably different from those observed at B1. That said, it was interesting to note that the mound previously observed for the looseness case remains at B2 and the higher fractional harmonics generated by RbD1 is also present at B2. The feature generated by blade was not consistent as these fractional higher harmonics are not present in the RbD2 at either B1 or B2. It therefore seems that the spectrum might be able, for the

experimental rig in this study, provide some insight to the diagnosis of Looseness and blade rub at the location tested, but further analysis in the horizontal, vertical and axial directions at all bearing locations would be required to ascertain this conclusion.

As observed in Figures 7.8 and 7.9, it is very difficult to conduct fault diagnosis using the simple spectrum as extensive analyses may be required in the three mutually exclusive directions at each bearing location. It is implicit that when considering a multi-stage rotating machinery, say a power generating steam turbine with 14 bearings, which is not atypical, the spectrum (such as those shown in Figures 7.8 and 7.9) would have to be generated at all bearing locations from measurements taken in the recommended two orthogonal directions [1]. Measurements may also be required at each bearing in the axial direction. Therefore, diagnosis becomes difficult, to say the least in such a case. This is why it is highly recommended that phase measurements [87, 88] and other techniques, such as the orbit plot analysis [12, 134], are used to compliment the simple amplitude spectrum to gain insight to the state of a faulty machine. But, as demonstrated in Section 7.3.1, the orbit plot may not provide the additional insight requisite for diagnosis. Consequently, more techniques would be required apart from the Orbit, which lends to the increased complexity of the diagnosis process.

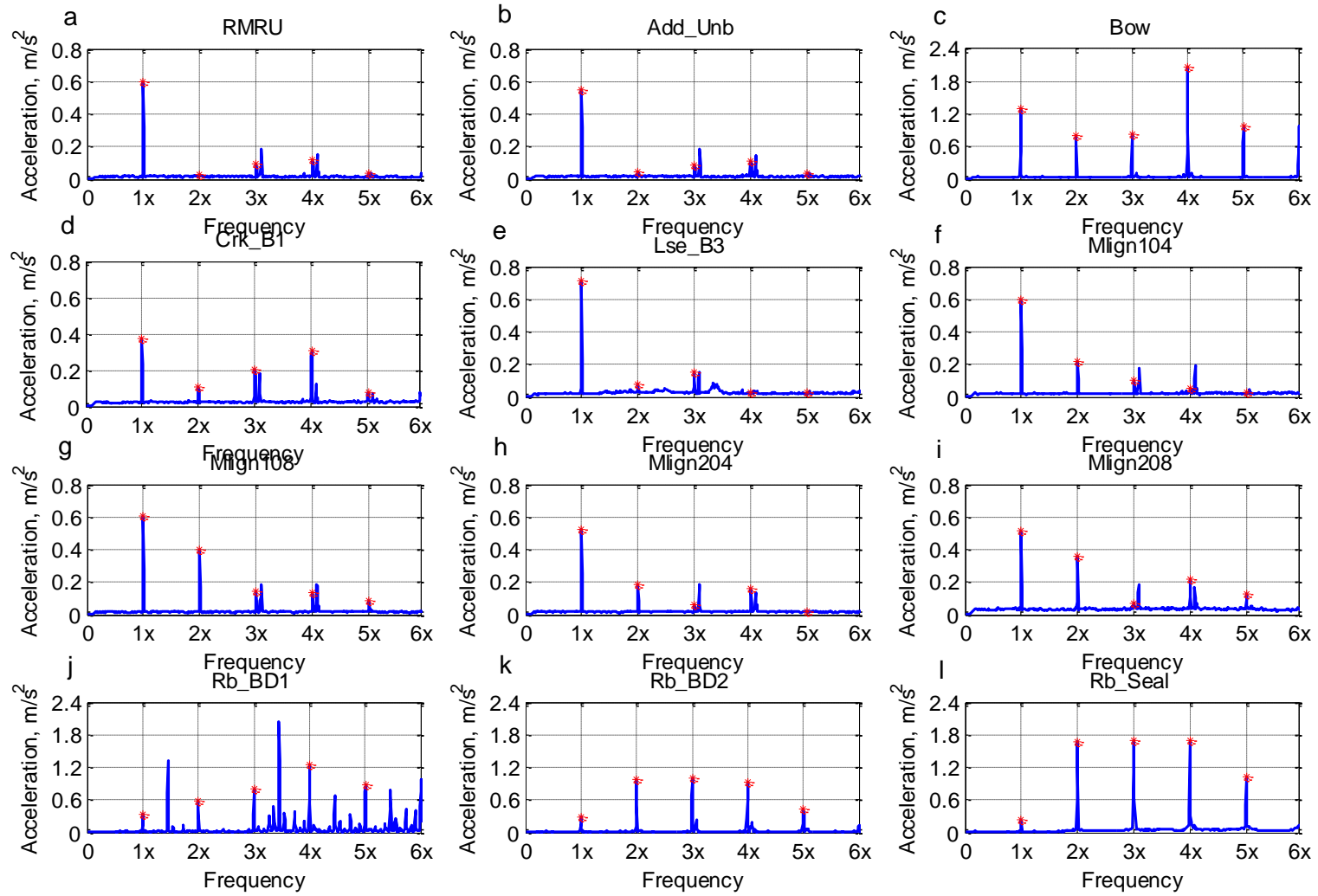


Figure 7.8 Sample of amplitude spectra for all faults of FS1 at B1 for 2400 rev/min (40 Hz)

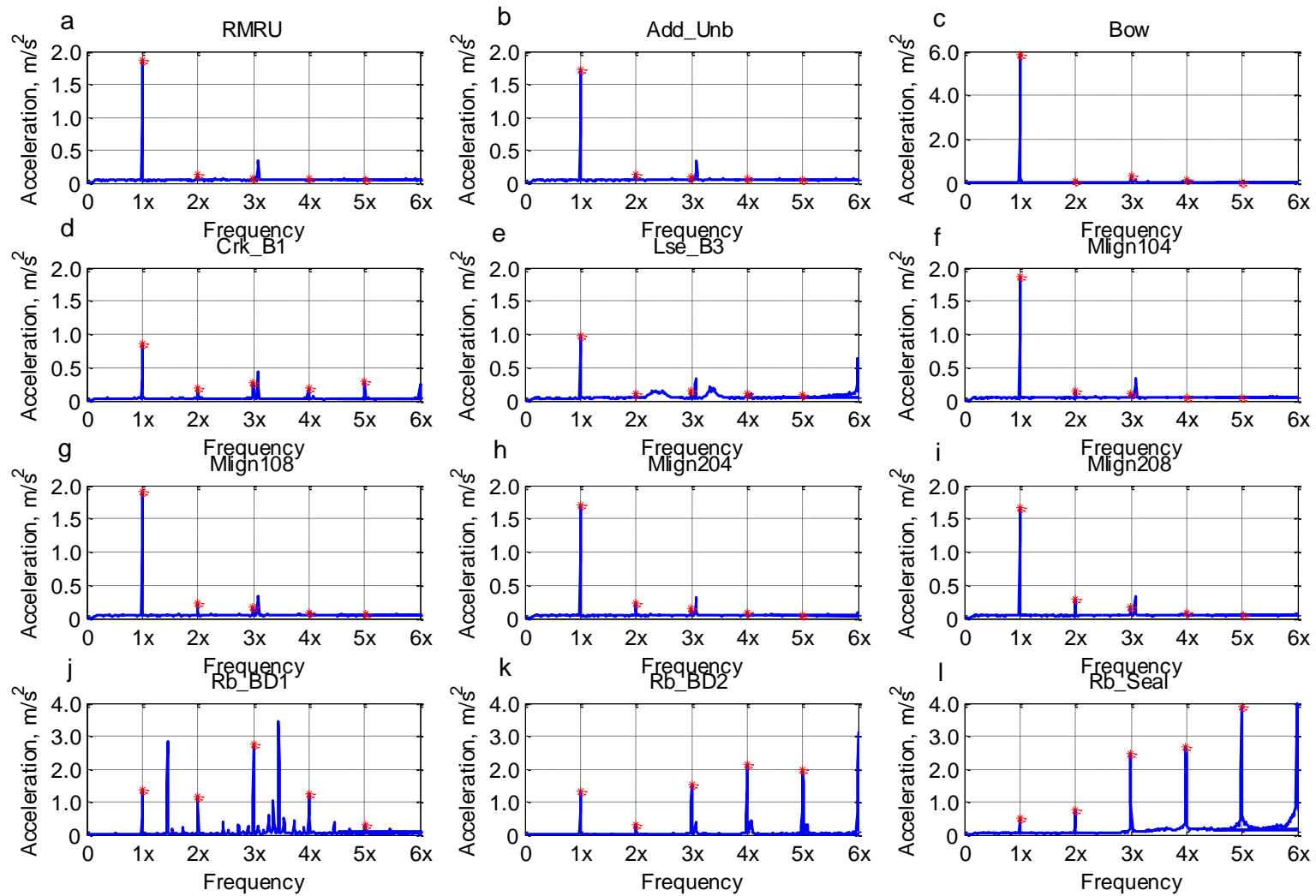


Figure 7.9 Sample of amplitude spectra for all faults of FS1 at B2 for 2400 rev/min (40 Hz)

7.4 Proposed approach - data processing and analyses

In light of the observations with the traditional practice in vibration-based fault diagnosis, it is evident why a different and relatively simple but robust method was considered in the previous studies [123, 132]. The application of these techniques to the processing of data acquired in this study is described in this section.

7.4.1 Application of principal component analysis

In general, PCA is used to reduce the dimensionality of a data set in which there are a large number of interrelated variables by transforming to a new set of ordered and uncorrelated variables which retain as much variations present in all the original data set, called principal components PCs [38, 121]. Consider p number of independent samples or observations of m random variables or features which can be represented by a $m \times p$ matrix, \mathbf{G} . The computation of PCs of \mathbf{G} reduces to the solution of an eigenvalue-eigenvector problem [121],

$$\mathbf{C}_G \mathbf{A} = \mathbf{A} \mathbf{\Lambda} \quad (7.1)$$

where \mathbf{C}_G is the covariance matrix of \mathbf{G} , \mathbf{A} is the orthogonal matrix whose k^{th} column is the k^{th} eigenvector of \mathbf{C}_G corresponding to the k^{th} largest eigenvalue, λ_k of \mathbf{C}_G . $\mathbf{\Lambda}$ is a diagonal matrix, whose k^{th} diagonal element is λ_k , the k^{th} largest eigenvalue of \mathbf{C}_G . Up to m PCs can be computed. However, in PCA it is hoped, in general, that most of the variation in \mathbf{G} will be accounted for by q PCs, where $q \ll m$.

In the present study, PCA is used to explore the structure of the relationship between the different conditions tested. The features used are comprised of computed vibration condition indicators for each bearing location at all conditions (scenarios) tested. Graphical representation of these PCs, can provide insight to the internal structures of the datasets, which otherwise might remain hidden in the original large, noisy, highly correlated and consequently complex dataset [38, 121].

7.4.2 Feature selection

Transformation of the features to the Principal Component space is done using a Matlab algorithm in which an array of features (health indicators), \mathbf{G} is input for processing. The processing done depends on the approach being considered. Four different approaches are used here; two from previous studies [123, 132] and two newly proposed. The first approach [123] applies to a single machine operating at a steady-state rotating speed. The second approach [132] applies to an individual machine that can operate at different steady-state speeds. The technique being proposed in this study applies to two similarly configured machines with different supports (say two multistage turbines of similar make and model located in different power plant locations). The technique being proposed can be applied to either two machines that operate at the same steady-state speed or two machines that can similarly operate at different steady-state speeds (i.e. variable speed machines). Table 2 outlines the different approaches considered.

Table 7.2 Summary of different approaches considered in the present study

No	Name	Code*	Application	Source
1	Individual Speed Individual Foundation	ISIF	Lone machine at steady-state speed	[123]
2	Multi-speed Individual Foundation	MSIF	Lone variable speed machines	[132]
3	Individual Speed Multi- foundation	ISMF	Comparison of two machines at steady-state speed	[133]
4	Multi-speed Multi- foundation	MSMF	Comparison of two variable speed machines	Current study

*Short code is used throughout remainder of paper

As shown in Table 7.3, different features were applied in the previous studies done. In order to select features for the current study, a review of the features used in the previous study was done. The basis for selection of features in the previous studies were the same; use of machine health indicators commonly applied in traditional practice that would yield results that best represent the state of the machine; thereby keeping the analysis simple. While retaining that ethos of familiarity and simplicity, the objective of the review was to

determine a set of features that could be consistently employed to all techniques considered here; thus standardizing the features utilised. It was found that the features employed by Nembhard and Sinha [133]; r.m.s. (R), amplitudes of 1×, 2×, 3×, 4×, and 5× and Spectrum Energy (S.E.), produced the most consistent results and was therefore applied here. Therefore, one time domain and six frequency domain features computed for each bearing location were applied.

Table 7.3 Features used in previous studies done

No	Source	Features used*	Technique applied
1	[123]	T, R, 1×, 2×, 3×	ISIF
2	[132]	R, C.F., K, S.E.	MSIF
3	[133]	R, 1×, 2×, 3×, 4×, 5×, S.E.	ISMF

*Key – T: Temperature, R: r.m.s., C.F.: Crest Factor, K: Kurtosis and S.E.: Spectrum Energy

7.4.3 Data processing

Firstly, for each scenario tested, the vibration data samples acquired were treated as 20 different observations. The features considered in the study (r.m.s., 1×, 2×, 3×, 4×, 5× and S.E.) were computed from each observation. Each bearing location was treated as a separate set of features [98]. Hence a total of 28 features (4 bearings × 7 features) were computed each for 20 different observations. These were used to populate the feature matrix, **G**, for loading to the PCA algorithm. Each scenario tested was treated as a different set of observations; hence matrix **G** would have 28 rows (features) and 240 columns (12 scenarios × 20 observations).

The flow process for the Individual Speed Individual Foundation (ISIF) analysis is presented in Figure 7.10. The process shown details how to compile the feature matrix, **G**. The processing done for the remaining techniques is largely similar to that given in Figure 7.10, with the difference being the compilation of matrix **G** being unique for each approach. An overview of the compilation of the different input feature matrix follows.

Consider machine a , from which data were acquired at n different steady-state speeds. Then

$$\mathbf{Y}_{MSIF,a} = [(\mathbf{G}_{a1})^T \quad \cdots \quad (\mathbf{G}_{an})^T]^T \quad (7.2)$$

where $\mathbf{Y}_{MSIF,a}$ is the input feature matrix for the MSIF analysis of a , \mathbf{G}_{an} is the input feature matrix for the ISIF analysis of a when operating at the n^{th} steady-state speed and T is transpose matrix operator. After completing computations for the 1st speed, the procedure was repeated for each successive speed, where each speed was treated as a separate set of features and thus increased the number of rows of \mathbf{G} . The MSIF analysis fuses the data available at the different steady-state speeds tested to provide a single plot representing the state of the machinery. Consider another machine, b , that is similar (say same make and model) to a , but have different dynamic characteristics to a (due to dynamic differences in supports or different physical locations). a and b operate at the same steady-state speed; the n^{th} steady state speed previously mentioned. On-bearing vibration data were acquired from both a and b . Then

$$\mathbf{Z}_{ISMF,a/b} = [(\mathbf{G}_{an})^T, (\mathbf{G}_{bn})^T]^T = [(\mathbf{G}_{bn})^T, (\mathbf{G}_{an})^T]^T \quad (7.3)$$

where $\mathbf{Z}_{ISMF,a/b}$ is the input feature matrix for a ISMF analysis of a relative to b (or b relative to a), \mathbf{G}_{an} and \mathbf{G}_{bn} are the input feature matrix for the ISIF analysis of a and b when operating at the n^{th} steady-state speed, respectively and T is transpose matrix operator.

Finally, for two similar variable speed machines a and b that can operate at different steady-state speeds, from which vibration data were acquired at the same n different steady-state speeds, then

$$\mathbf{Z}_{MSMF,a/b} = [(\mathbf{Y}_{MSIF,a})^T, (\mathbf{Y}_{MSIF,b})^T]^T = [(\mathbf{Y}_{MSIF,b})^T, (\mathbf{Y}_{MSIF,a})^T]^T \quad (7.4)$$

where $\mathbf{Z}_{MSMF,a/b}$ is the input feature matrix for a MSMF analysis of a relative to b , $\mathbf{Y}_{MSIF,a}$ is the input feature matrix for the MSIF analysis of a , $\mathbf{Y}_{MSIF,b}$ is the input feature matrix for the MSIF analysis of b and T is transpose matrix operator.

For the different approaches, prior to loading to the PCA algorithm, each variable in the input feature matrix was normalized by calculating the mean and standard deviation of each row, subtracting the mean of the row from each element within the row and then dividing by the aforementioned standard deviation of the row [123]. Normalization of the variables was done as a treatment to handle the variations of the different units which comprised \mathbf{G} . Therefore, after normalization each element became a comparable dimensionless quantity [121].

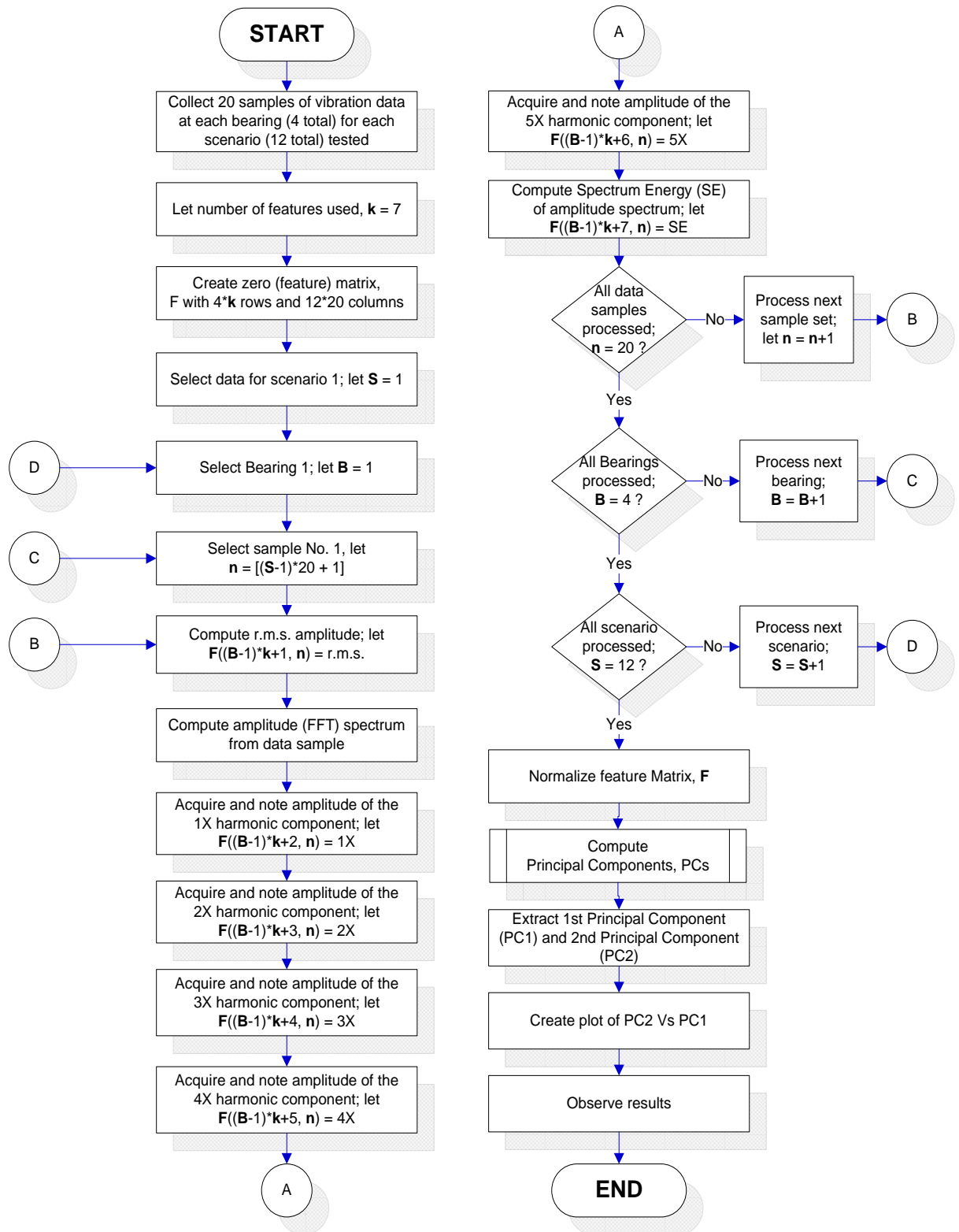


Figure 7.10 PCA flow process for vibration data acquired at a single steady-speed

7.5 Fault diagnosis - flexible support 1 (FS1)

In this section results of the different analyses done are presented in Principal Component (PC) plots of the 2nd PC against the 1st PC as shown in Figures 7.11-7.20. The plots developed are given in two part figures; “a” and “b”, which provides a full view of the plot which encompasses all scenarios tested and a zoomed view of sections of the plot around the baseline RMRU condition, respectively. These were examined for; separation between the different scenarios and the baseline RMRU condition, separation among the different faults tested and grouping of the different scenarios into clearly defined clusters. Note that, separation between the different scenarios tested represents differences between them. In contrast, a lack of separation or overlap between scenarios signals similarities in them based on the features used. Therefore, it was hoped that the different scenarios tested occupied separate isolated clusters on the PC plots.

7.5.1 Individual speed individual foundation (ISIF) analysis on FS1

Results of the ISIF analysis at 1200 rev/min (20 Hz), 1800 rev/min (30 Hz) and 2400 rev/min (40 Hz) are shown in Figures 7.11, 7.12 and 7.13, respectively. At 1200 rev/min good separation was observed for Looseness, Bow and seal rub. All other cases lacked separation with the baseline condition in full view (see Figure 7.11(a)). The lack separation between a fault and the baseline condition could be due to the ISIF technique not being sensitive enough to the fault, therefore being unable to distinguish between the baseline state and a faulty state. The possibility also exists that the magnitude of the fault conditions were too small to be noticeable at that speed. However, it was clear that the bow, looseness and rub seal conditions were large enough to occupy isolated areas on the PC plot. It was interesting to note that distinction between the two different rub scenarios tested, seal rub and blade rub, was observed at 1200 rev/min.

Compared to 1200 rev/min the results at 1800 rev/min, shown in Figure 7.12, were much improved. In full view (see Figure 7.12(a)) Bow, Looseness and Seal rub remained clearly separated around a cluster of RMRU, Added Unbalance, Crack near Bearing 1, all four misalignment cases and Rub near Disc 2 condition. Rub near Disc 1 condition did not

appear in the cluster of scenarios but was instead clearly separated. The differences in behaviour observed for the Rub near Disc 1 and the Rub near Disc 2 faults were interesting. There are several possible justifications for the contrasting observations seen with Rub near Disc 1 and Rub near Disc 2 relative to RMRU. There could have existed inconsistencies in the method of simulating the blade rub faults in the two locations tested (see Figure 7.6). It could also be that there were differences in the dynamic behaviour of the rig for the different locations tested at 30 Hz for the blade rub case. Further testing including a full modal analysis with perusal of mode shapes would be required to confirm this. As shown in Figure 7.12(b), the apparent cluster that was observed in Figure 7.12(a) was in fact misleading. With exception of the Misalignment at B1; 1 shim at 0.4 mm case, the fault conditions had good separation. It was interesting to note that the Crack near Bearing 1 was fully separated from all misalignment cases. This suggests that the technique is able to discriminate between crack and misalignment which are usually difficult to differentiate with traditional practices [55, 57]. Clustering of all four misalignment cases was also observed.

At 2400 rev/min, clear isolation was observed for Bow, crack, looseness and all rub cases. It was interesting to note that the three rub cases (Rb_D1, Rb_D2 and Rb_Seal) occupied the same region of the plot, even though there were noticeable distinctions in their locations without overlap. The clustering observed in full view (see Figure 7.13(a)) for the baseline condition, Added Unbalance and all four misalignment cases was unchanged in the zoomed view (see Figure 7.13(b)). Although the baseline condition occupied a different area in the cluster with misalignment and Added Unbalance, it seems that the approach used was not able to distinguish these scenarios at 2400 rev/min. The lack of separation between misalignment and the baseline condition was not be surprising as the baseline condition (RMRU) is characterised by some residual misalignment which, depending on its magnitude, could represent itself as a full misalignment case. Notwithstanding, except for Crack near Bearing 1, observations of the cluster in Figure 7.13(b) contrast what was noticed in the zoomed view at 1800 rev/min (30 Hz) (see Figure 7.12(b)). Since 30 Hz is approximately a half of the first natural frequency for FS1, this could suggest misalignment cases are best diagnosed at $\frac{1}{2}$ the critical speed for the ISIF analysis. Observation of improved diagnosis of misalignment at $\frac{1}{2}$ the critical speed was also reported by Patel and Darpe [6].

Overall good separation was observed for the faults tested relative to the healthy condition. In most cases, especially for bow, seal rub and looseness to a lesser extent, the approach was also able to distinguish between the faults tested. However, it appears the method is less effective at lower speeds as noticed from results obtained at 1200 rev/min (see Figure 7.11). The almost complete overlap between the baseline condition and the added unbalance case across all three speeds (see Figures 7.11(b), 7.12(b) and 7.13(b)) when compared to the overlap between the baseline and misalignment cases suggests that the baseline case was more characterised by a strong unbalance than misalignment. This observation concurs to what was observed in the orbit plots for the different fault conditions tested at 2400 rev/min shown in Figure 7.7; where the plots appeared similar to what is expected of a pure unbalance case. However, where the orbit plot was not able to distinguish between the different faults, the ISIF analysis has. This therefore suggests the ISIF analysis may be useful in cases where a machine is characterised by a strong unbalance that could mask other fault signals.

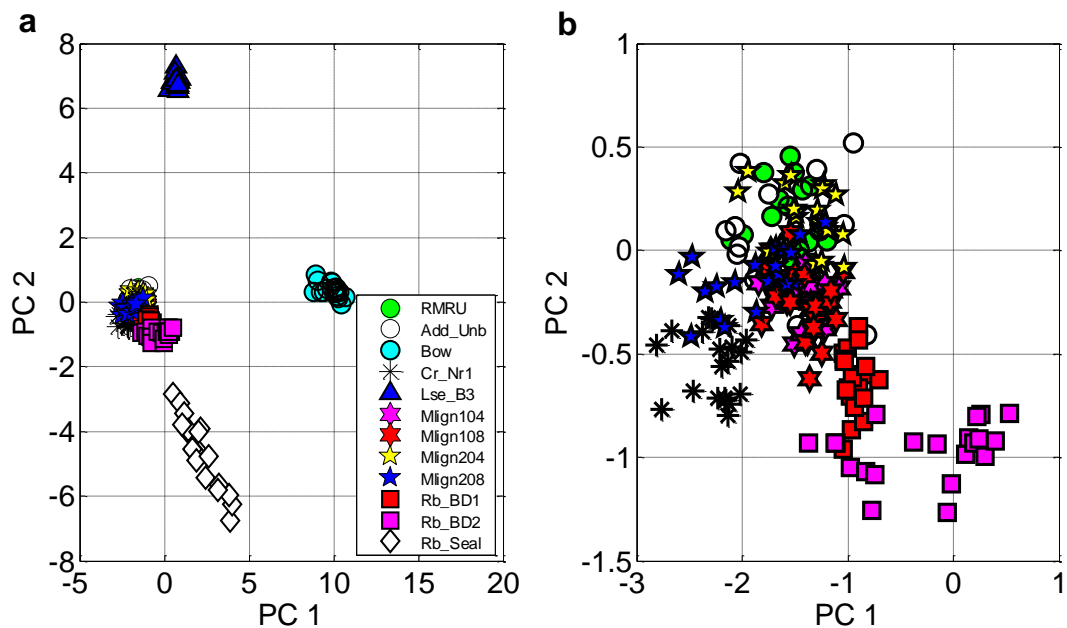


Figure 7.11 Fault diagnosis with ISIF analysis for FS1 at 1200 rev/min (20 Hz) in (a) full view and (b) zoomed view of clustered section with baseline case

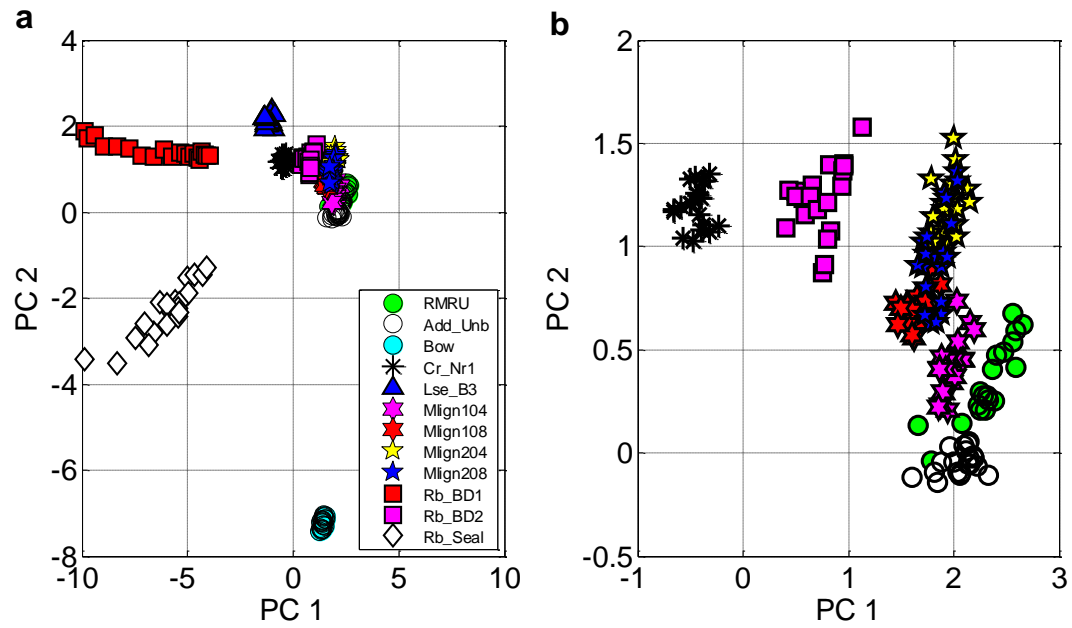


Figure 7.12 Fault diagnosis with ISIF analysis for FS1 at 1800 rev/min (30 Hz) in (a) full view and (b) zoomed view of clustered section with baseline case

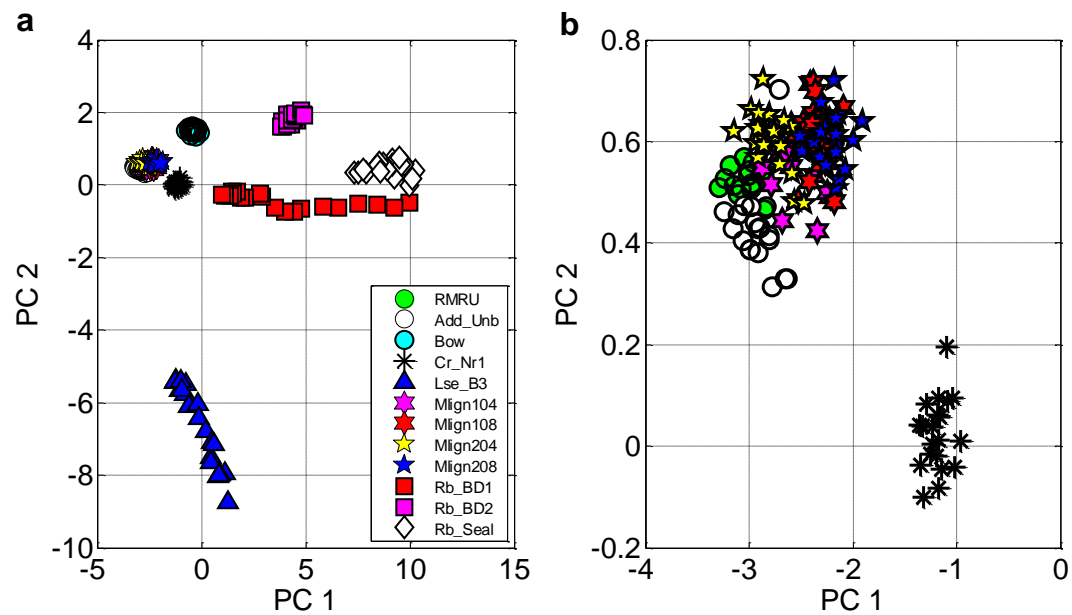


Figure 7.13 Fault diagnosis with ISIF analysis for FS1 at 2400 rev/min (40 Hz) in (a) full view and (b) zoomed view of clustered section with baseline case

7.5.2 Multi-speed individual foundation (MSIF) analysis on FS1

The results of the Multi-speed Individual Foundation (MSIF) analysis on FS1 from fusion of data acquired at steady-state speeds of 1200 rev/min (20 Hz), 1800 rev/min (30 Hz) and 2400 rev/min (40 Hz) are shown in Figure 7.14. Bow was a clear standout in the full view plot shown in Figure 7.14(a). To a lesser extent, Crack and Seal Rub occupied clearly distinct regions of the plot away from the baseline condition and from other faults tested. There appeared to be two different sets of clusters, but on closer inspection in the zoomed view (see Figure 7.14(b)), it was observed that the apparent overlap between Looseness on Bearing 3 and Rub near Disc 2 did not exist. The isolation of several conditions relative to the baseline case were improved in the current analysis compared to the ISIF analysis (see previous section), these were: Bow, Crack and Seal Rub.

As observed in the ISIF analysis presented in the previous section (see Section 7.5.1), the Added Unbalance case and baseline conditions were inseparable. However, the MSIF analysis was better able to separate Added Unbalance and the baseline condition from the cluster of four misalignment cases. The separation between the misalignment cases and the Crack condition is also improved over the individual speed analysis. Despite the noted improvements, there were downsides to the MSIF analysis, less separation was seen between the scenarios tested, especially for Looseness. With the exception of the bow scenario, all fault conditions tested did not occupy definite isolated regions on the plot. Nevertheless, in general it appears the MSIF analysis yields improved diagnosis over the ISIF analyses.

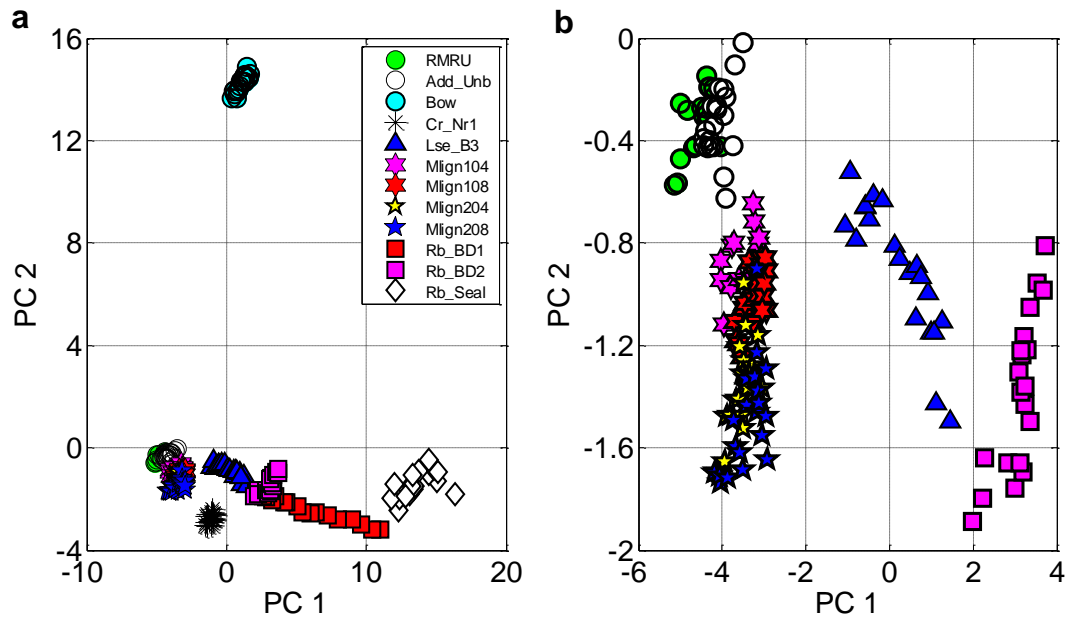


Figure 7.14 Fault Diagnosis with MSIF analysis (fusing data acquired at steady speeds of 20 Hz, 30Hz and 40 Hz combined) for FS1 in (a) full view and (b) zoomed view of clustered section with baseline case

7.6 Fault diagnosis – flexible support 2 (FS2)

Observations made with FS2 were similar to those noted for FS1. A sample of the findings of the ISIF analysis at 1800 and the MSIF analysis on FS2 are provided in Figures 7.15 and 7.16, respectively. As previously mentioned in Section 7.2.1, FS2 is more flexible than FS1, but even with increased flexibility the technique was able to clearly isolate Bow, Looseness and all three rub cases as shown in Figure 7.15(a). As seen in Figure 7.15(b), across all speeds tested, increased overlap (decreasing separation) was noted relative to FS1 for the baseline Residual Misalignment with Residual Unbalance case, Added Unbalance and misalignment cases. This suggested with increased flexibility, the rig's baseline case is somewhat characterised by equally dominant unbalance and misalignment forces (as opposed to the dominant unbalance characteristics noticed with FS1). Evidently, this suggests the level of misalignment preload on the rig was higher for FS2 than for FS1. Consequently, it was consistently observed with all speeds tested for FS2 that the ISIF analysis was less able to discriminate misalignment from Crack.

The lack of distinction between misalignment and the Residual Misalignment with Residual unbalance case was also noticeable in the MSIF analysis on FS2. Notwithstanding, the results observed were improved over the analysis done at an individual speed for the discrimination of Bow, Looseness and all three rub cases. It was interesting to note that, relative to the ISIF analysis on FS2, there was noticeably less separation between Crack near Bearing 1 and the baseline case and consequently Crack near Bearing 1 and misalignment.

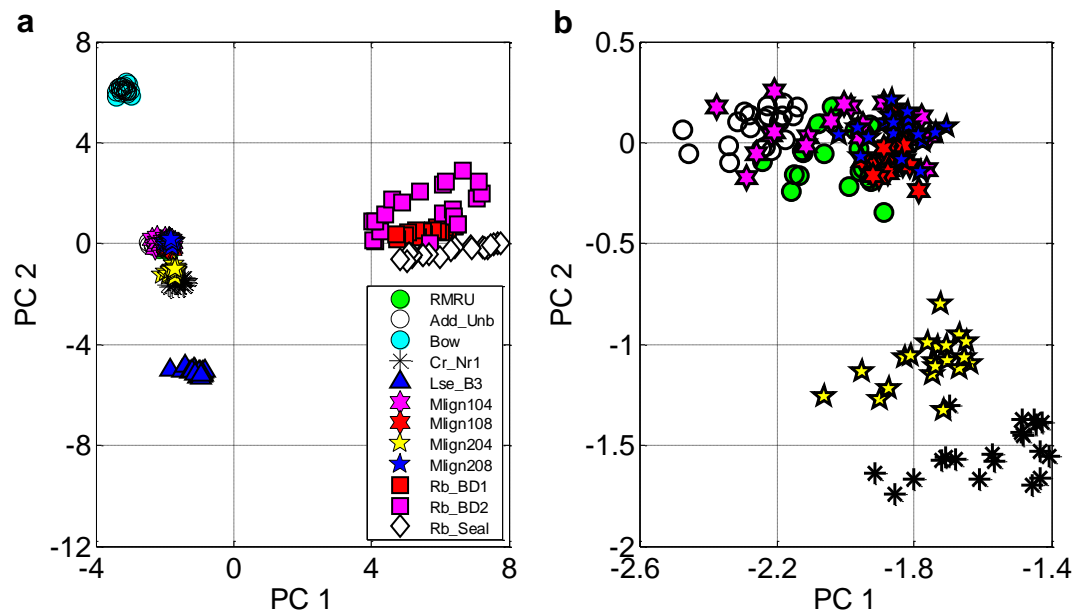


Figure 7.15 Fault diagnosis with ISIF analysis for FS2 at 1800 rev/min (30 Hz) in (a) full view and (b) zoomed view of clustered section with baseline case

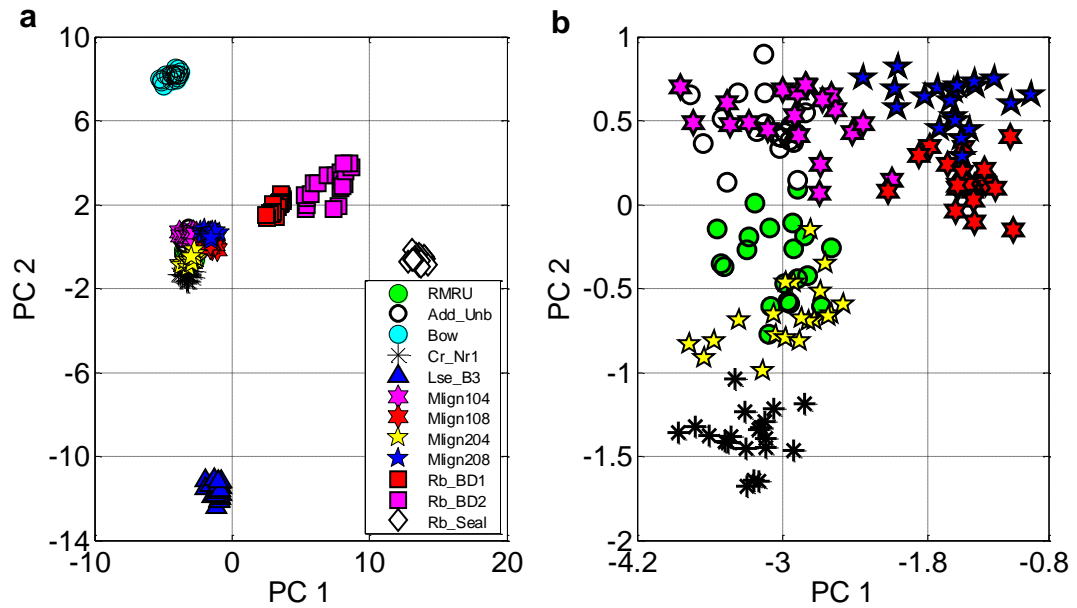


Figure 7.16 Fault Diagnosis with MSIF analysis (20 Hz, 30 Hz and 40 Hz combined) for FS2 in (a) full view and (b) zoomed view of clustered section with baseline case

7.7 Fault Diagnosis - combined foundations; FS1 and FS2

Analyses done with an individual foundation (ISIF and MSIF) require historical data from say a database from which data could be used to compare data measured from the machine in a suspected faulty state. If the machine is “healthy” then the measured data would be grouped with the baseline case, if not it would be classified into one of the fault clusters [123]. In the event the technique is not able to recognise the state of the machine, the vibration data would be simultaneously separated from the baseline condition and from any of the fault conditions. In that event, further investigation would have to be done to ascertain the cause of the fault.

However, there exists the possibility that fault diagnosis is required on a suspect machine which does not have any vibration data history (for example a newly installed machine). Therefore, the methods presented in previous sections (ISIF and MSIF analyses) would not be applicable. It would then be useful if data history from a similar machine at another location or site could be used to conduct the diagnosis. In practice, when conducting FD on rotating machines, it is normal to compare the vibration from a suspect machine to another “healthy” machine of the same type in an attempt to understand or gain

insight to the state of the faulty machine. In this case, separate analyses would be conducted and the different results compared. However, the data from another machine is generally not used for diagnosis of another machine, because the dynamics characteristics of the two machines may be different. Thus, an attempt was made to develop an approach that would enable “sharing” of vibration data between two similar machines that are dynamically different (referred to in the present study as “Multi-foundation”). This is perhaps the first account of a technique that compare vibration for different fault conditions in a single analysis step using reduced number of sensors on each bearing and no phase information. The observations made follow.

7.7.1 Individual speed multi-foundation (ISMF) analysis on FS1 and FS2

Results of the Individual Speed Multi-foundation (ISMF) analysis combining FS1 and FS2 data at a steady-state speed of 1200 rev/min (20 Hz), 1800 rev/min (30 Hz) and 2400 rev/min (40 Hz) are shown in Figures 7.17, 7.18 and 7.19, respectively. Observations of the ISMF analysis at the speeds tested are comparable to the ISIF analyses at the said speeds for both FS1 and FS2. However, the ISMF analysis had the added benefit of showing better discrimination and isolation for crack fault across all speeds tested. Therefore, even with mixing of on-bearing vibration data acquired from similar machines with different dynamic characteristics, the current technique was able identify the similarities and differences between the data sets.

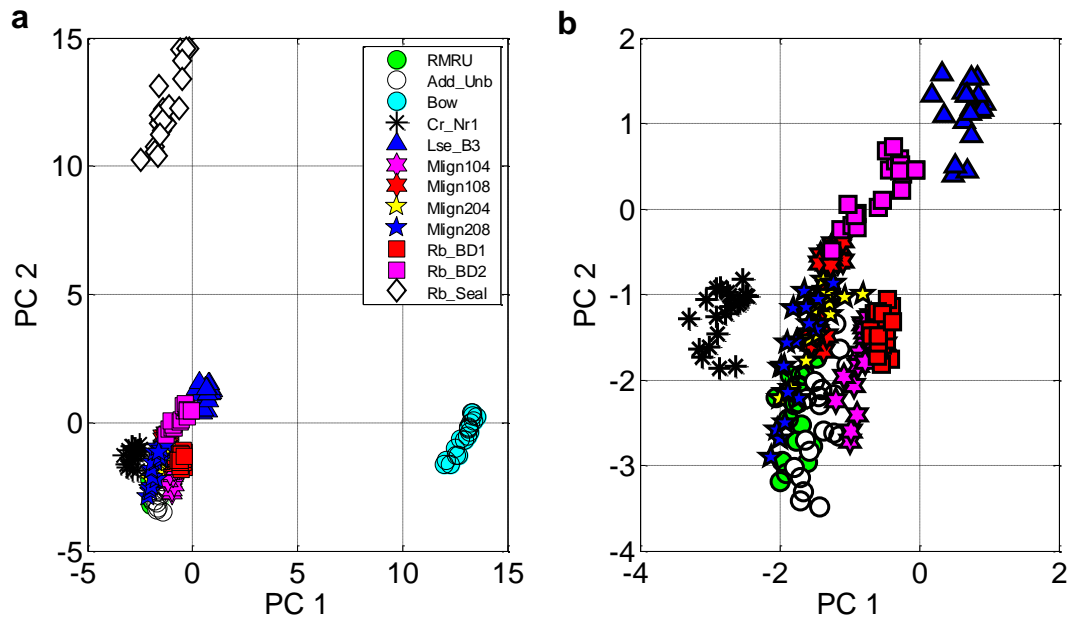


Figure 7.17 Fault diagnosis with ISMF analysis combining FS1 and FS2 at 1200 rev/min (20 Hz) in (a) full view and (b) zoomed view of clustered section with baseline case

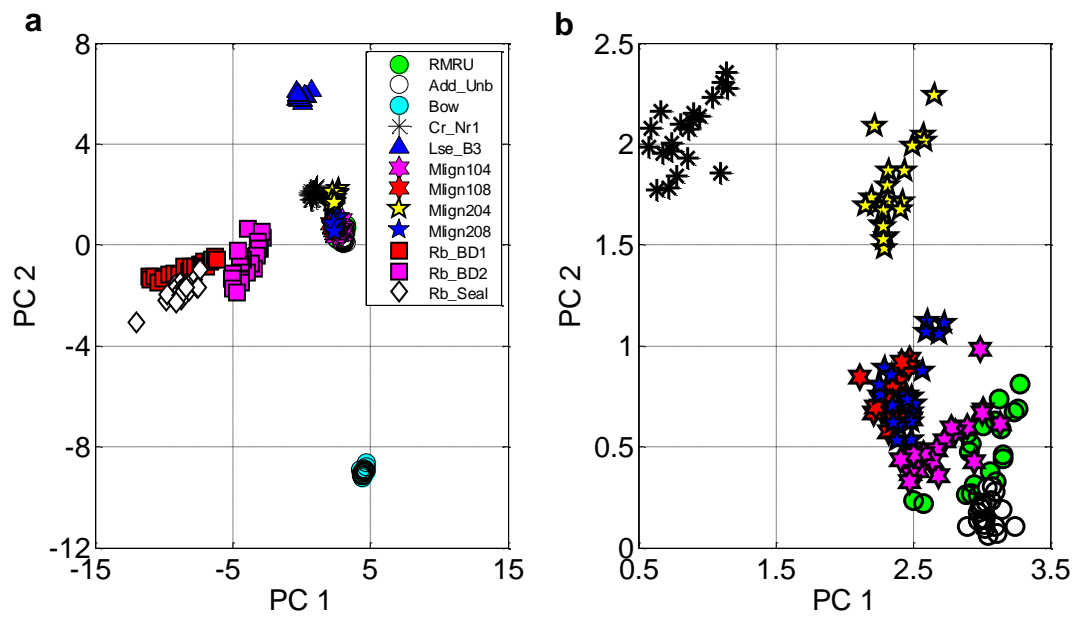


Figure 7.18 Fault diagnosis with ISMF analysis combining FS1 and FS2 at 1800 rev/min (30 Hz) in (a) full view and (b) zoomed view of clustered section with baseline case

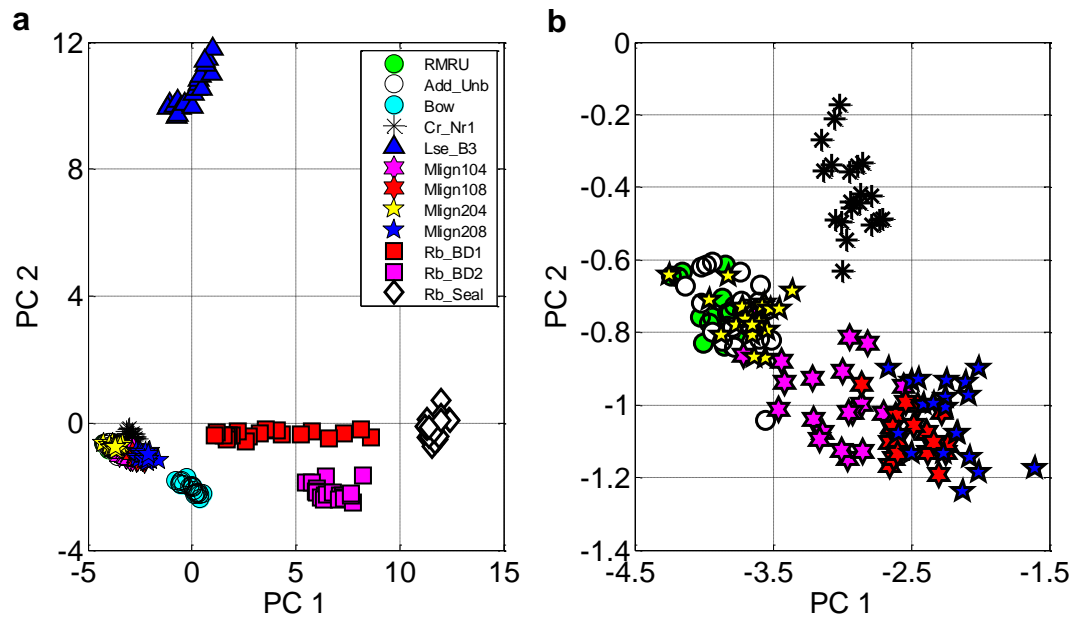


Figure 7.19 Fault diagnosis with ISMF analysis combining FS1 and FS2 at 2400 rev/min (40 Hz) in (a) full view and (b) zoomed view of clustered section with baseline case

7.7.2 Multi-speed multi-foundation (MSMF) analysis on FS1 and FS2

The plots obtained for the MSMF analysis are shown in Figure 7.20. In full view, compared to the previous analyses presented, the largest separation was noted here between the baseline Residual Misalignment with Residual Unbalance case and; Bow, Seal rub and Blade rub (Rb_D1 and Rb_D2). There was also noticeable improved isolation and separation of the different cases tested when compared to the same cases in the ISMF analyses at the different speeds tested. Otherwise, the MSMF approach is comparable to the MSIF Analyses done on FS1 (see Figure 7.14) and FS2 (see Figure 7.16).

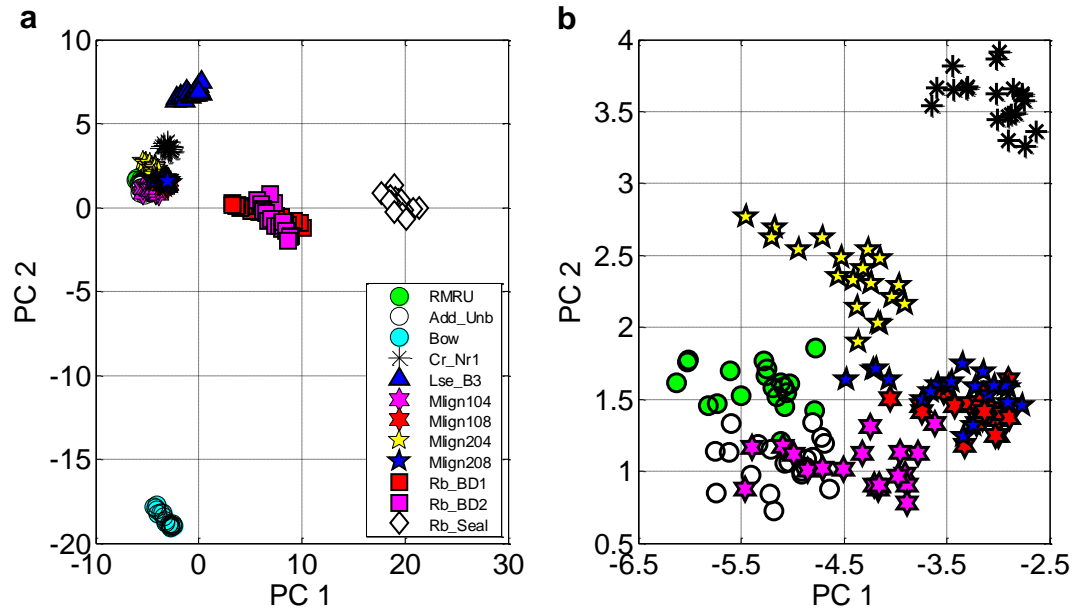


Figure 7.20 Fault diagnosis with MSMF combining FS1 and FS2 at all speeds (20 Hz, 30 Hz and 40 Hz) in (a) full view and (b) zoomed view of clustered section with baseline case

7.8 Global observations

Overall good clustering and separation among the scenarios tested for the previously proposed methods (ISIF and MSIF) and the newly introduced multi-foundation methods (ISMF and MSMF) were noted. In addition to this, some other notable general observations were made. The results of the ISIF analyses on FS1 and FS2 were comparable to findings of Nembhard et al. [123]. The multi-speed techniques (MSIF and MSMF) generated better separation and isolation of the fault conditions compared to the different individual speed techniques (ISIF and ISMF).

This suggests the multi-speed techniques were able to exploit the useful data available across the different steady-state speeds acquired to ascertain a true representation of the state of the experimental rig. PC plots from the newly proposed ISMF and MSMF techniques possessed improved isolation of Crack near Bearing 1 from the misalignment cases tested when compared to techniques done with individual foundation (ISIF and MSIF). Even so, clear isolation of the Crack near Bearing 1 case were noticed at 30 Hz which is approximately $\frac{1}{2}$ the first critical speed for FS1 and the second critical speed for

FS2. Separation of faults from the baseline RMRU case increased with increasing speed. It was apparent that the separation generated could be an indicator for the severity assessment of the different fault conditions. The results of the MSMF confirms the position that the integration of more dynamic features improves the learning process of the tool [132].

The efficacy of the previously proposed individual speed techniques would be confined to the quality and availability of vibration data history, since this would be required in practice for comparison to results from the measured data acquired from the suspect machine. On the other hand, the newly proposed Multi-foundation techniques would not be as susceptible to data history deficiency, since data from a similar machine with different dynamic characteristics could be used to diagnose the suspect machine.

7.9 Summary

The transferability of three previously introduced vibration-based FD techniques: Individual Speed Individual Foundation (ISIF), Multi-speed Individual Foundation (MSIF) and Individual Speed Multi-foundation (ISMF), was investigated in the current study. An innovative “Multi-speed Multi-foundation” (MSMF) FD approach for comparing vibration information collected at different steady-state speeds from similar machines with different dynamic characteristics was also proposed. A previously used experimental rig which had relatively rigid bearing supports was modified to separately accommodate two different sets of relatively flexible supports (FS1 and FS2). Using a single vibration sensor at each bearing, samples of on-bearing vibration data were acquired at various subcritical steady-state speeds for a baseline residual misalignment with residual unbalance (RMRU) case as well as; added unbalance, bow, crack, looseness, misalignment, blade rub and seal rub conditions. One condition was introduced at a time. Commonly used machine health indicators (features) were computed from the measured data and processed by the different techniques tested. The ISIF and MSIF techniques were demonstrated firstly using features computed for FS1 and then for FS2. Afterwards, the ISMF approach, which integrated features computed for both FS1 and FS2 at the same steady-state speed, was explored. Lastly, the features were analysed in the proposed MSMF method.

The results of the ISIF, MSIF and ISMF analyses showed good separation between the different conditions tested, thus suggesting these methods are transferable to machines with different dynamic characteristics for the conditions tested. More encouragingly, the newly proposed MSMF technique gave improved clustering and isolation of the conditions tested; especially for bow, looseness and seal rub. The observations made with the MSMF approach confirm the position that the integration of more dynamic features improves the learning process of the diagnosis tool. Because of their simplicity and demonstrated robustness, these techniques may be useful for practical vibration-based fault diagnosis of rotating machines. However, numerical validation of the results obtained is required to further explore this opportunity.

8 COMPARISON OF EXPERIMENTAL OBSERVATIONS IN ROTATING MACHINES WITH SIMPLE MATHEMATICAL SIMULATIONS

Reformatted version of the following paper:

Title: Comparison of experimental of observations in rotating machines with simple mathematical simulations

Authors: Adrian D. Nembhard and Jyoti K. Sinha

Status: Submitted to Mechanical Systems and Signal Processing

Abstract: Through an earlier experimental study, an integrated fault classification approach was suggested for machines operating at different speeds. The suggested method was observed to separate faults adequately, which can lead to fault diagnosis. However, theoretical understanding of the proposed methods is important to further enhance the confidence of the earlier experimental study. Hence, simplified mathematical simulations of different rotor faults are carried out and used to test the earlier proposed classification technique in this paper. Observations in the orbit, spectra and fault classification diagrams are consistent with the previous experimental case.

Keywords: Vibration analysis; Mathematical simulation; Jeffcott rotor; Fault classification; Data fusion

8.1 Introduction

Vibration-based fault diagnosis (FD) of rotating machinery in industrial systems is a complex process which requires new or continuously improving techniques to meet the

ever burgeoning demand for increased equipment reliability. In the development of new techniques, it may be useful to conduct theoretical simulations to test the utility of the approach and possibly to garner a greater appreciation of the dynamics of faults encountered. The Finite Element Method (FEM) is currently the staple method for the theoretical exploration of the dynamic effects of different faults on rotating machinery [14, 57, 65, 76, 104, 105]. However, FEM is undoubtedly complex and there are instances, such as an initial theoretical investigation of a newly proposed FD technique, in which a simple mathematical model may be preferred.

The Jeffcott rotor is the simplest mathematical method for understanding the dynamic behaviour of rotating machines under different conditions [106]. One of the earliest accounts of the use of the Jeffcott rotor for rotor fault investigation was provided by Jeffcott [107] who investigated the dynamics of an unbalanced shaft. Since then, it has been applied in numerous vibration-related studies with literature accounting extensively for studies on cracks and rotor-stator rub and to a lesser extent other faults.

Jun et al. [108] applied a Jeffcott rotor to identify the characteristics of a breathing crack which opens and closes. Using fracture mechanics it was concluded that the switching crack model with bi-level direct stiffness was mathematically simple but physically sensible when the rotor operated well below the second bending critical speed. Gasch [66] studied the dynamic behaviour of a transverse crack on a Laval rotor that was modelled like a low pressure turbine with weight dominance. Time dependent stiffness variations were based on the hinge model. It was suggested that trend analysis from permanent monitoring would prove helpful to early crack detection. In contrast, Cheng et al. [109] analysed the dynamic response of a Jeffcott rotor with a breathing crack sans the typical weight dominance assumption. Simulations were run near the system's critical speed and shaft breathing was expressed a function of the whirling of the rotor. It was observed that the response of a cracked rotor near its critical speed is similar to those of a healthy rotor. Patel and Darpe [68] cautioned the use of the switching crack model to predict the vibration response of a cracked rotor with deeper cracks. It was found that unbalance phase, unbalance level, crack depth and system damping have significant effect on the vibration response of the rotor with switching crack but have no influence on the rotor with breathing crack. However, Penny and Friswell [110] provided an insightful comparison of the vibration response of a simple Jeffcott rotor with three different crack models, namely;

the hinge model, the Mayes model and the model of Jun et al. and suggested that the differences in the models would be negligible in a crack identification scheme.

Chu and Zhang [111] employed a Jeffcott rotor to examine the nature of rotor to stator rub. Equations of motions of the system were developed and solved via a Runge Kutta integration scheme. It was observed that the rub feature transitioned to three different routes to chaos on increasing rotating speeds. Similarly, Lin et al. [112] was able to study the behaviour of rub-related vibrations with numerical simulations on a Jeffcott rotor model in order to “reveal the nonlinear mechanisms” underlying the chaotic phenomena previously observed in works such as Chu and Zhang [111]. Though simplified, the model was able to capture the rich dynamics of a rotor system rubbing its housing. It was found that there exist threshold values for rotor-stator clearance and friction coefficient above which the bouncing phenomena would not be experienced. It was also suggested that the results of the simulations from such a simple model can be useful for the development of sensitive machinery diagnostic techniques.

Just over a decade ago, Redmond and Al-Hussain [113] and Al-Hussain and Redmond [114] bemoaned the lack of requisite theoretical studies with thorough treatment of the nature of misalignment using “suitably representative models”. Consequently, a coupled twin Jeffcott rotor model was similarly offered by Redmond and Al-Hussain [113] and Al-Hussain and Redmond [114] to provide insight to the dynamic behaviour of machines with coupling misalignment and residual unbalance. The former [113] explored a flexible coupled rotor model, while the latter [114] investigated a rigidly coupled set up. Both studies considered only pure parallel misalignment and solved the system’s equations with the Newmark-Beta method of integration. Redmond and Al-Hussain [113] found that the presence of misalignment caused a radial preload in the rotor system which modified the system vibration amplitude and phase characteristics. More interestingly, Al-Hussain and Redmond [114] did not observe the customary $2\times$ harmonic component in the rigidly coupled system response, therefore leading to the conclusion that other system properties including rotor asymmetry and in some cases coupling kinematics are the sources of higher harmonics in misalignment response.

Though it is opined that the Jeffcott model is too simple and limited to a qualitative understanding of the machine state which does not concur to “real life conditions” [105], the literature reviewed here made observations somewhat contrary to such claims; as the Jeffcott rotor model enabled adequate representation of the dynamic conditions of rotating machine under different conditions. In light of this, the Jeffcott rotor is used in the current study to generate responses of commonly encountered rotor-related faults in order to further test the performance of a previously developed vibration-based FD approach [13] with theoretical data. In the earlier work, the FD method was developed in the Dynamics Lab at the University of Manchester on a small experimental rig. It was intended that modelling of the Jeffcott rotor would preserve the simplicity of the simulation process while yet still producing responses representative of real data.

Five different rotor conditions were simulated in the current study namely; low unbalance, added unbalance, crack, misalignment and rub. To solve the equations of motion developed for the different models the Newmark beta integration scheme [124] is employed. Orbit plots and simple amplitude spectra were compared to check the accuracy of the models. The steady-state time domain response from each model were used to compute condition indicators which were then input to the two classification techniques being tested here; single speed (SS) and multi speed (MS) analysis. The results of classification with both SS and MS analyses had good separation of the conditions tested with the latter having slightly improved separation. The observations made in the current study were consistent with the fault classification done in the earlier experimental study, which suggest the methods perform regardless of data source. The findings made here bode well for the assertion of these vibration-based FD methods as viable.

A brief description of the layout of the paper follows. In Section 8.2 a brief description of the earlier experimental study including a review of the classification technique is provided for reference purposes. Afterwards, in Section 8.3, the simple model of the Jeffcott rotor is derived. Subsequent to this, detailed descriptions of the simulation of different rotor conditions tested are provided in Section 8.4. Section 8.5, presents fault classification with the simulated data in the previously developed technique. Finally, conclusions are drawn in Section 8.6.

8.2 Earlier experimental study [13]

In this section, the previously used experimental rig is presented and experiments done are highlighted. Then, to offer some perspective to the dynamic effects of the different faults tested on the experimental rig, orbit plots representative of the different cases are presented with corresponding simple spectra. Finally, the earlier suggested fault classification approach is briefly introduced. Details of all experiments done and results obtained are provided by [13].

8.2.1 Experimental rig

The experimental rig located in the Dynamics Laboratory at the University of Manchester is shown in Figure 8.1. The rig consists of two rigidly coupled (C2) 20 mm nominal diameter bright mild steel shafts of lengths 1 m (Rotor 1) and 0.5 m (Rotor 2). These form the rotating assembly. The shafts are supported by four identical grease lubricated flange mounted ball bearings (B1–B4). Machined steel sections which act as balancing discs are mounted to each rotor; two discs (D1 and D2) for the long shaft (Rotor 1) and one disc (D3) for the short shaft (Rotor 2). Drive to the system is provided by a 0.7 kW 2800 rev/min 3-phase induction motor. The motor is connected to Rotor 1 via a flexible beam coupling. The first natural frequency of the rig with the set up shown was located at 50.66 Hz. Complete details of the mechanical layout of the rig and instrumentation used are provided by Nembhard et al. [13].

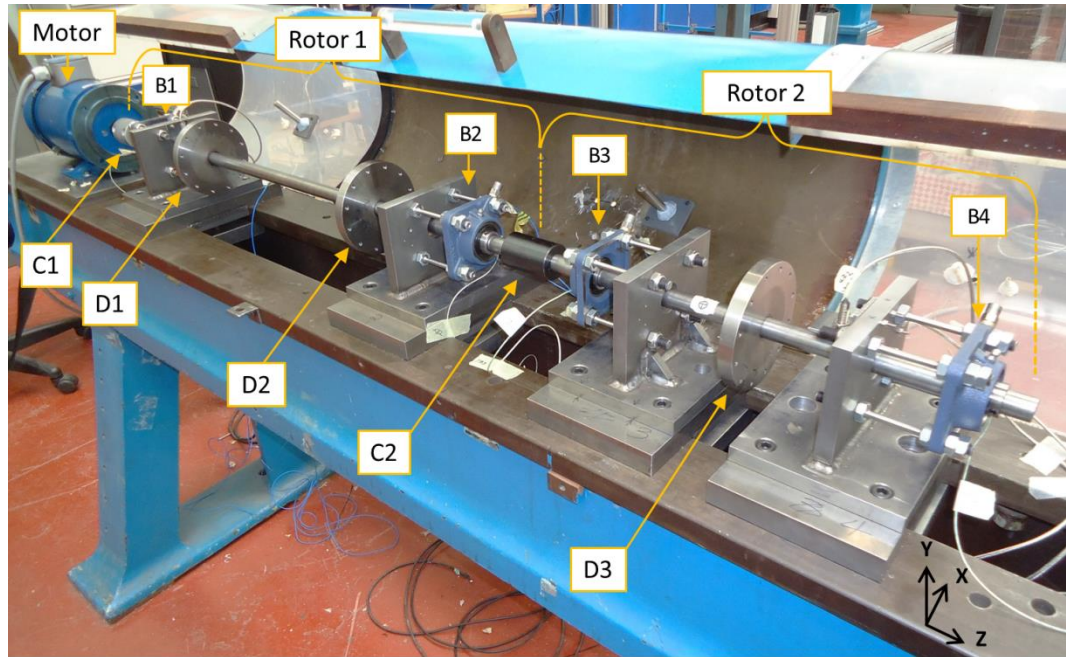


Figure 8.1 Mechanical layout of experimental rig used in earlier study [13]

8.2.2 Experiments conducted

On-bearing steady-state vibration data were collected from the experimental rig for a baseline residual misalignment with residual unbalance (RMRU) condition as well as six different commonly encountered rotor-related fault cases; added unbalance, shaft bow, transverse shaft crack, looseness, parallel misalignment and rub. Three magnitudes of misalignment and three rub cases (two blade rub and one shaft seal rub) were tested. Therefore, a total of 12 scenarios spanning 7 fault conditions were simulated. Experiments were done at three different speeds.

8.2.3 Experimental observations in orbit plots and simple spectra

Prior to performing the proposed fault classification technique, orbit plots and simple spectra were generated from the measured vibration data to observe the dynamic response of the rig during the different conditions tested. The orbits generated that were most representative of the different cases introduced to the experimental rig as well as the corresponding simple spectra are presented in Figures 8.2 and 8.3, respectively, for the

purposes of reference in the current study. The plots show that the experimental rig in the baseline state was characterized by some amount of misalignment as demonstrated by the distorted orbit with a point to the lower left hand corner for the baseline RMRU case in Figure 8.2(a) and the dominant $2\times$ harmonic component in the corresponding RMRU spectra (Figure 8.3(a)). The response of the rig changed with different fault conditions except for the unbalance case which had very little effect on the orbit (Figure 8.2(b)) and spectra (Figure 8.3(b)). As is regularly encountered in literature, crack and misalignment had similar outer looped orbits in Figures 8.2(d) and 8.2(f), respectively, but their spectral content differed (see Figures 8.3(d) and 8.3(f)). As seen in the orbit (Figure 8.2(g)) and corresponding spectrum (Figure 8.3(g)), rotor rub fault generated $0.5\times$ fractional harmonics and its multiples in the response.

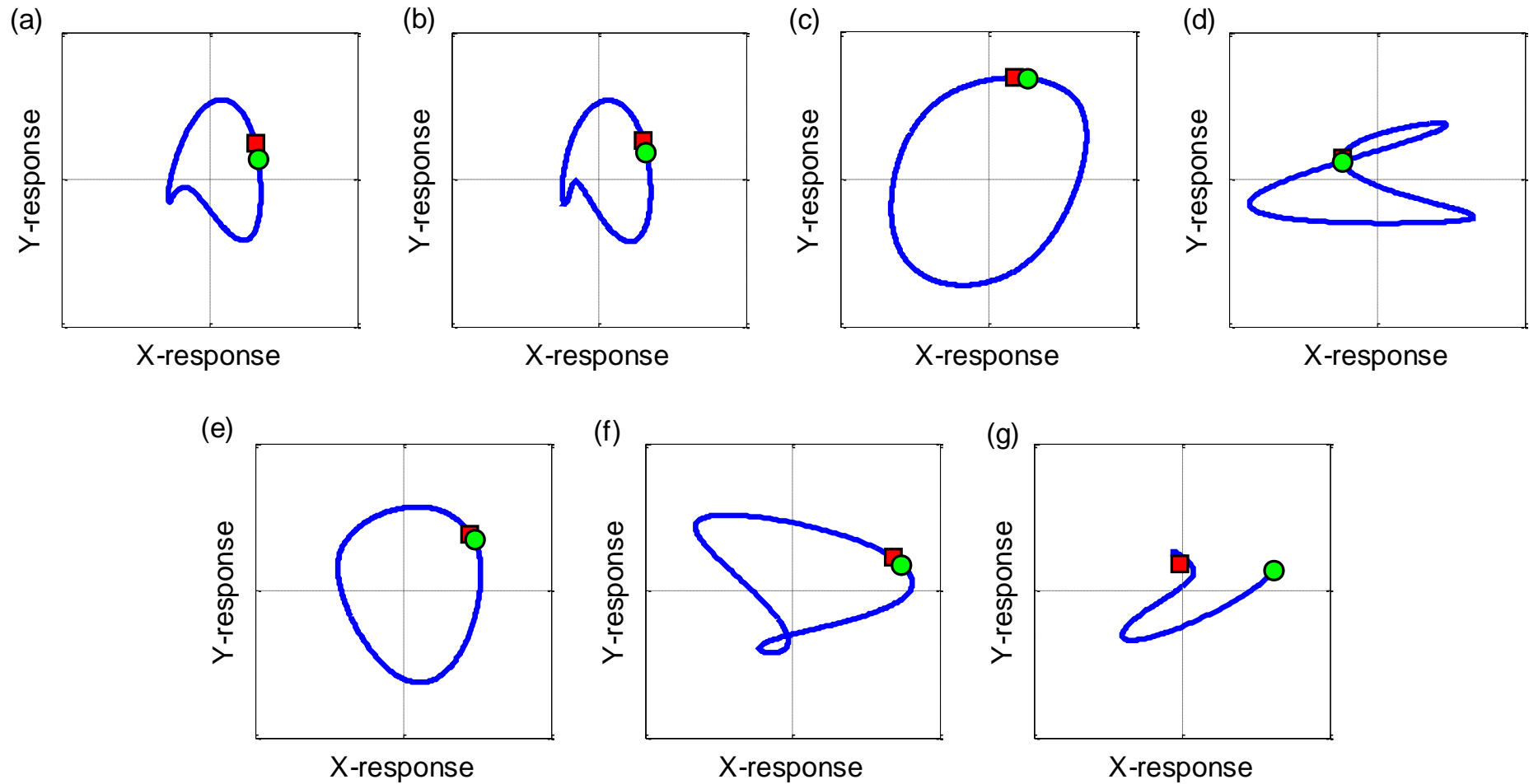


Figure 8.2 Representative experimental orbits at B1 for: (a) RMRU (b) Added unbalance, (c) Bow, (d) Crack, (e) Looseness, (f) Misalignment and (g) Rub

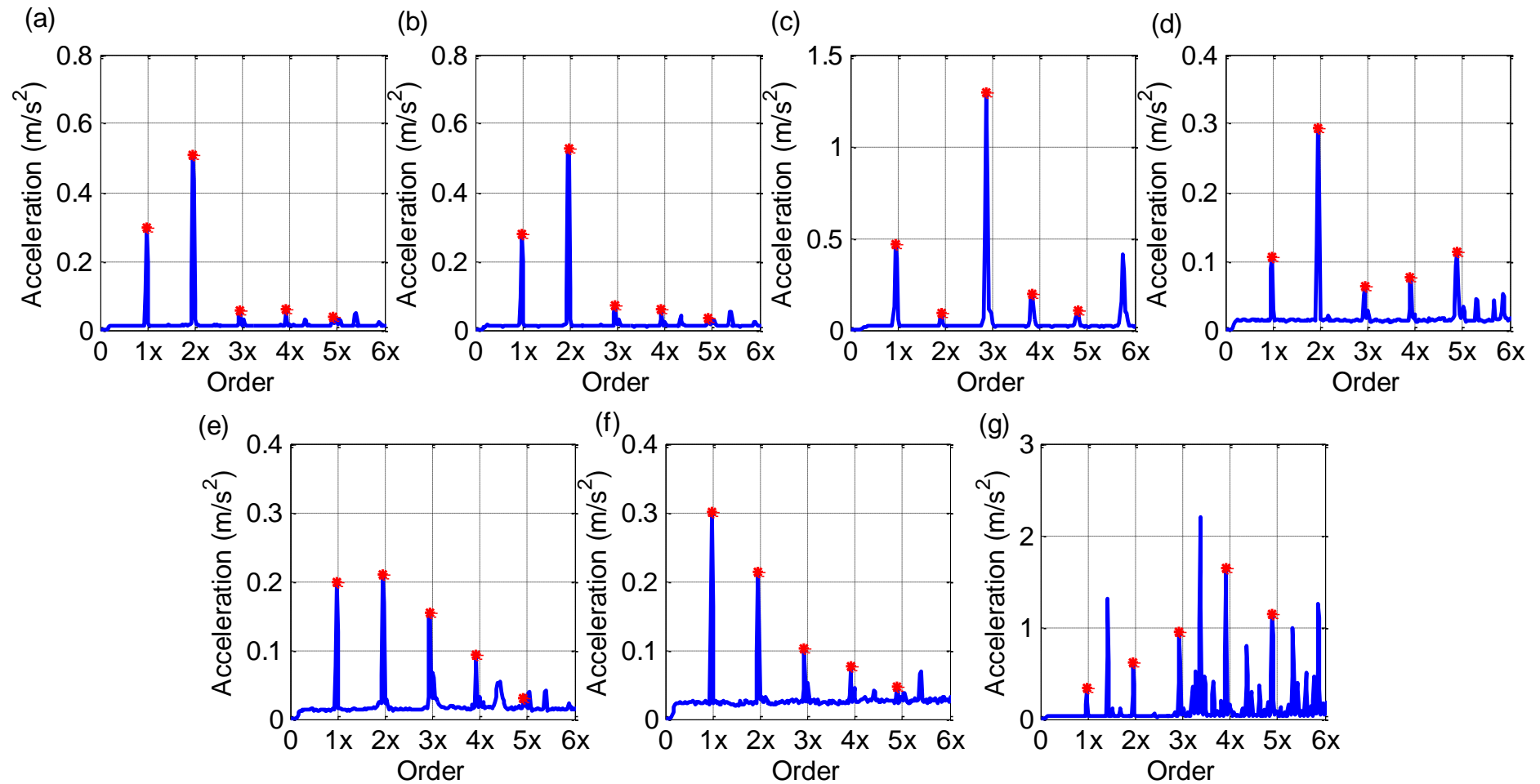


Figure 8.3 Representative experimental spectrum at B1 for: (a) RMRU at 1800 rev/min (30 Hz) (b) Added unbalance at 1800 rev/min (30 Hz), (c) Bow at 1200 rev/min (20 Hz), (d) Crack at 1710 rev/min (28.5 Hz), (e) Looseness at 1800 rev/min (30 Hz), (f) Misalignment at 1800 rev/min (30 Hz) and (g) Rub at 2400 rev/min (40 Hz)

8.2.4 Fault classification method with earlier proposed approach

The earlier proposed method which is being tested in the current study is a pattern recognition approach with Principal Component Analysis (PCA) [121] as its theoretical basis. PCA is a mathematical tool which reduces the dimension of a large inter-related data set by transforming said data to a new set of ordered uncorrelated variables known as Principal Components (PCs). Diagrammatical representation of PCs, such as a plot of the 2nd Principal Component (PC2) against the 1st Principal Component (PC1), allows for exploration of relationships or structures in the original data set, which would have otherwise been difficult to identify [13, 121]. PCA was implemented in the earlier study as part of an algorithm in Matlab software. The algorithm was applied in two different analyses; single speed (SS) and multi-speed (MS). SS analysis was conducted for classification of faults acquired when the rig operated at a steady-state speed, while MS enabled classification of faults by fusion of vibration information acquired from the rig at different rotating speeds.

Widely used vibration condition indicators (hereafter referred to as features); r.m.s. acceleration, amplitudes of $1\times$, $2\times$, $3\times$, $4\times$, $5\times$ harmonic components as well as spectrum energy [124], were computed from the measured vibration data. For a particular condition at a given speed, twenty different vibration samples were collected at each bearing location with one condition introduced to the rig at a time. Features were computed for each data sample and each bearing location was treated as a separate set of features. Therefore, in the SS analysis, the 7 features for the 12 different scenario tested at a given speed for the 4 different bearing locations (see Figure 8.1) were input to the algorithm for classification with a 28×240 matrix, whereas in the MS analysis, features at all 3 speeds tested from the 4 different bearing locations were input to the algorithm via a 84×240 matrix. For purposes of brevity, details of the data input requirement and flow process used are not given here but are, however, provided by Nembhard et al. [13]. The adaption of the data input requirement in the current study is provided in subsequent sections.

A typical sample of the output from the analysis, which is a two dimensional plot of PC2 against PC1, is presented in Figure 8.4. The figure is shown in two parts; “a” gives the results in full view and “b” provides a zoomed view of sections of the plot around the

baseline RMRU condition, respectively. The figure was perused for clustering of similar data points and separation between the different conditions, which is the basis of fault classification. In Figure 8.4(a) it can be seen that bow was completely separated from all other conditions. In the said figure, there was an apparent overlap between all other conditions but on inspection of the zoomed view in Figure 8.4(b) this overlap was not present. The cluster of hexagonal and pentagonal stars was for the same misalignment condition, so this was acceptable. The same overlapping was seen for the rub cases which are essentially the same fault condition. The overlap between RMRU and added unbalance tells us that both cases were very similar, which was in fact congruent with observations made in the orbit and spectra in the previous section (see Section 8.2.3).

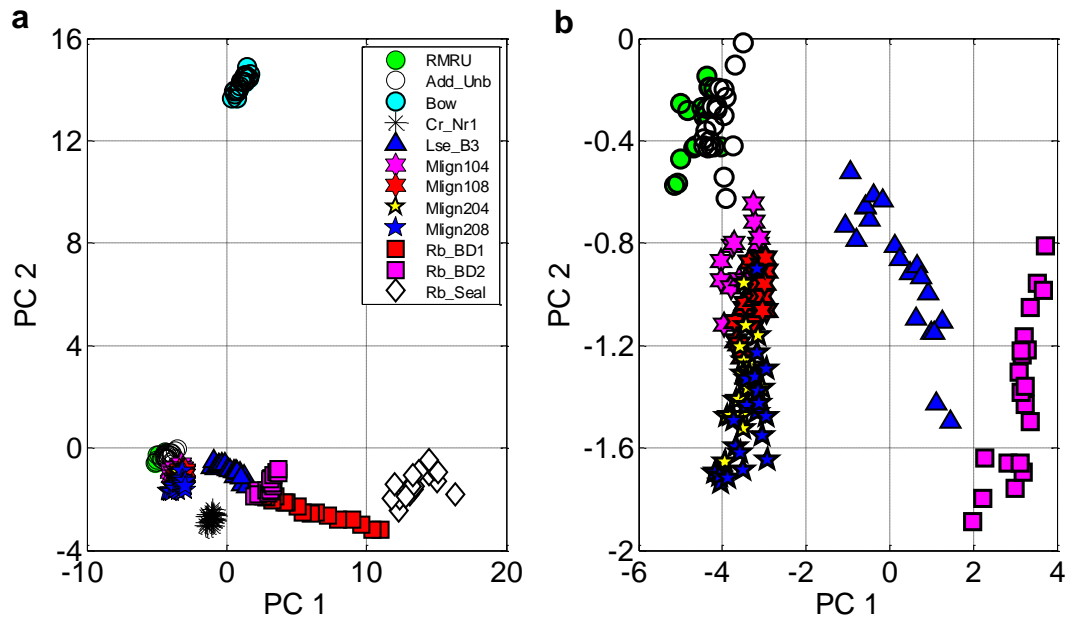


Figure 8.4 Typical output of vibration-based fault classification technique developed in earlier experimental study showing PC plot in: a) full view and b) zoomed view [13]

8.3 Mathematical modelling – Jeffcott rotor

Figure 8.5 shows a diagram of a two degree of freedom horizontal isotropic Jeffcott rotor, which was considered in the present study. The rotor consists of a simply supported flexible shaft of uniform circular cross section with a centrally mounted disc. The displacement of the rotor was characterised by fixed coordinates that were assumed originating at the centre of the disc.

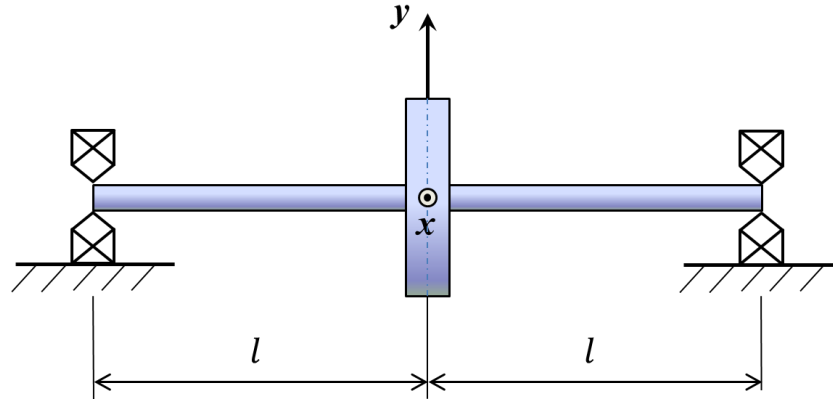


Figure 8.5 Simple Jeffcott rotor model with flexible shaft and centrally located disc on rigid bearing supports

The general motion of the rotor can be defined by a simple time dependent equation as

$$\begin{cases} m\ddot{u} + c\dot{u} + ku = F_x(t) \\ m\ddot{v} + c\dot{v} + kv = F_y(t) \end{cases} \quad (8.1)$$

where u and v are the displacements at the middle of the shaft at the disc location in the x and y directions, respectively, m is the mass of the disc, c is the damping coefficient of the shaft, k is the stiffness of the shaft and F_x and F_y are general forces acting on the system in the x and y direction, respectively, which are functions of time, t . In order to arrive at an equation that includes the system's natural frequency, ω_n and damping ratio, ζ , which is more convenient to implement in the current study than the system damping, c , Equation (8.1) was rewritten as

$$\begin{cases} \ddot{u} + 2\zeta\omega_n\dot{u} + \omega_n^2u = F_x(t)/m \\ \ddot{v} + 2\zeta\omega_n\dot{v} + \omega_n^2v = F_y(t)/m \end{cases} \quad (8.2)$$

The model was created to have the 50.66 Hz natural frequency and similar material properties to the rotor bearing system used in the earlier experimental study [13]. In order

to do this, the rotor was considered; 1000 mm long, 20 mm in diameter, with a modulus of elasticity of $200 \times 10^9 \text{ N/m}^2$ and with density of 7810 kg/m^3 . The disc mass was considered 0.74 kg. These parameters resulted in a bending natural frequency of 50.94 Hz, which was adopted as the natural frequency in the current study. All model parameters used are delineated in Table 1.

8.4 Fault simulation and response

A healthy and four fault conditions were simulated in the current study, namely; added unbalance, transverse crack, misalignment and rub. Therefore, bow and looseness that were tested in the earlier experimental study were not considered here. For each fault condition, it was assumed that the residual unbalance was present on the rotor in addition to the fault conditions. In each case, the equations of motion were developed, excluding gyroscopic effects and cross coupled stiffness. To solve the equations of motion, the Newmark Beta integration scheme, with an alpha value of 0.5, beta value of 0.25 and a time step of 0.1 ms, was implemented in an algorithm in Matlab software. All simulations were for a total response time of 180 sec. which included both transient and steady-state vibration. It was found that 20 sec was sufficient time to allow for the dissipation of transient vibrations and so this was considered the start of the steady region for all simulations. Therefore, the steady-state time domain response for all simulations had a total timespan of 160 sec. (20 sec. to 180 sec.). The iterative steps done in the Newmark integration process is not provided here for brevity, however, a complete treatment of this procedure is provided by Sinha [124]. All initial conditions were assumed to be zero.

Simulations were run for a minimum speed of 600 rev/min (10 Hz) in addition to 1200 rev/min (20 Hz), 1800 rev/min (30 Hz) and 2400 rev/min (40 Hz) [13]. There was the exceptional case of cracked rotor condition which was also simulated at approximately half of the systems natural frequency at 1500 rev/min (25 Hz). The models in each case were configured to recreate, as best as possible, the response observed in the earlier experimental study [13]. The suitability of each model was checked using orbit plots and simple amplitude spectra.

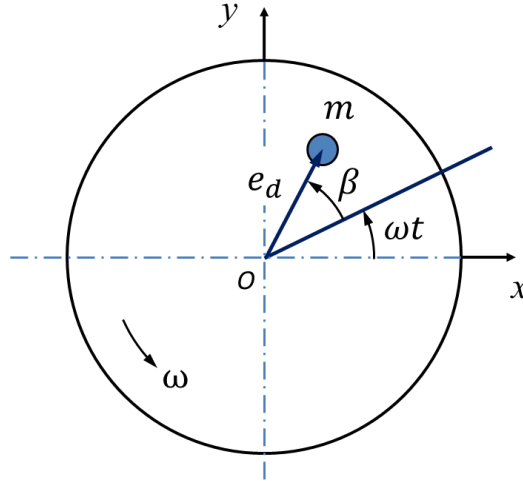
Orbit plots were generated for a single rotation cycle from data from the start of the steady-state region of the time domain response. The data were filtered to include solely the $1\times$ and $2\times$ frequencies. In the earlier study, the amplitude spectra were computed from on-bearing vibration data measured by an accelerometer mounted in 45° position on the bearing. Thus, only a single measurement direction was considered for each bearing. For consistency in the current study, the responses in the x-direction, u and y-direction, v were rotated by 45° using the well-known transformation provided in Equation (8.3) to produce variables u' and v' , respectively. Given only one measurement direction was considered in the earlier study, only the u' direction was considered for subsequent processing in the current study. Afterwards, the simple acceleration spectra were generated. Prior to generating the simple spectra, 20 dB noise was added to the data. The spectra were then computed with a sampling frequency of 1000 Hz, 0.2441 frequency resolution, 95% overlap and a Hanning window. A high pass filter at 5 Hz was applied to remove any undesirable frequencies below this cut off.

$$\begin{Bmatrix} u' \\ v' \end{Bmatrix} = \begin{bmatrix} \cos \omega t & \sin \omega t \\ -\sin \omega t & \cos \omega t \end{bmatrix} \begin{Bmatrix} u \\ v \end{Bmatrix} \quad (8.3)$$

For the purposes of verifying the simulations done the orbit plots are observed for a qualitative evaluation of the different models done. However, the amplitude spectra are examined for some quantitative information.

8.4.1 Healthy

A machine can be considered healthy when the broadband vibration level is acceptable relative to some predetermined standard [1]. However, even in its healthy state unbalance exists. Unbalance in a rotating system occurs when the centre of mass of the system is not coincident with the centre of rotation [135]. Thus, the healthy rotor model was represented as a Jeffcott rotor with low unbalance as shown in Figure 8.6, which shows the centre of rotation, o and m , the centre of mass.

Figure 8.6 Healthy model showing disc with eccentric mass (m)

The equation of motion for the system shown can be written as

$$\begin{cases} m\ddot{u} + c\dot{u} + ku = me_d\omega^2 \cos(\omega t + \beta) \\ m\ddot{v} + c\dot{v} + kv = me_d\omega^2 \sin(\omega t + \beta) - mg \end{cases} \quad (8.4)$$

where m is the mass of the disc, which is the same as the centre of mass of system, e_d is the location of the centre of mass of the disc or its eccentricity, ω , the rotor speed, β , the unbalance phase and g , the acceleration due to gravity. Thus, recalling from Section 8.3, the general forces exciting the rotor is gravity and a harmonic imbalance force of amplitude $me_d\omega^2$ acting at an instantaneous angle of rotation, ωt and phase, β . Equation (8.4) was expressed in terms of natural frequency, ω_n and damping ratio, ζ to obtain Equation (8.5) for solving. The resulting mass, damping and stiffness matrices for processing in the Newmark beta integration algorithm were $\begin{bmatrix} 1 & 0 \\ 0 & 1 \end{bmatrix}$, $\begin{bmatrix} 2\zeta\omega_n & 0 \\ 0 & 2\zeta\omega_n \end{bmatrix}$ and $\begin{bmatrix} \omega_n^2 & 0 \\ 0 & \omega_n^2 \end{bmatrix}$, respectively. A damping ratio of 0.0123 was considered in the current study.

This was obtained from the experimental rig with 10 mm supports [13] using the Half Power Bandwidth method [124].

$$\begin{cases} \ddot{u} + 2\zeta\omega_n\dot{u} + \omega_n^2 u = e_d\omega^2 \cos(\omega t + \beta) \\ \ddot{v} + 2\zeta\omega_n\dot{v} + \omega_n^2 v = e_d\omega^2 \sin(\omega t + \beta) - g \end{cases} \quad (8.5)$$

For the model to be considered healthy, the mass eccentricity had to be small enough to produce broadband root mean square (r.m.s.) vibration amplitudes within an acceptable limit from some standard. Therefore, the r.m.s. velocity vibration limit recommended by ISO 10816 standard [1] for Zone A, 4.5 mm/s, was considered the limit of broadband vibration. By trial and error the eccentricity was adjusted at the maximum speed tested (2400 rev/min) until the r.m.s. velocity vibration amplitude of the system was less than or equal to 4.5 mm/s. It was found that an eccentricity of 0.01592 mm met this criterion, and so this was adopted as the eccentricity for the healthy Jeffcott rotor. The term “healthy” and “residual unbalance” is the same condition and will be used interchangeably for the remainder of the paper.

The orbit plot and simple amplitude spectra for the Healthy Jeffcott rotor system at all speeds simulated are given in Figures 8.7 and 8.8, respectively. As expected, the orbits are circular and the spectra have a solitary synchronous $1\times$ component, which is characteristic of a pure unbalance case. Of course the orbit and spectra seen here are distinctly different from the experimental orbit (Figure 8.2(a)) and spectra (Figure 8.3(a)) earlier shown which was characterised by a residual misalignment condition that additionally created integer multiples of the $1\times$ response. In Figure 8.7 the start and end points of the orbit over one rotation cycle is represented by a green circle and red square, respectively. The same convention applies for orbit plots throughout the remainder of the paper.

The healthy or residual unbalance condition was presented with much detail in the current section. However, the remaining conditions are presented in subsequent sections with less detail, because they were simulated as modifications to the residual unbalance model. Consequently, redundant information was excluded as best as possible. Changes to; the models, equations of motion, orbit plots and spectra will be highlighted with reference to the healthy (residual unbalance) condition.

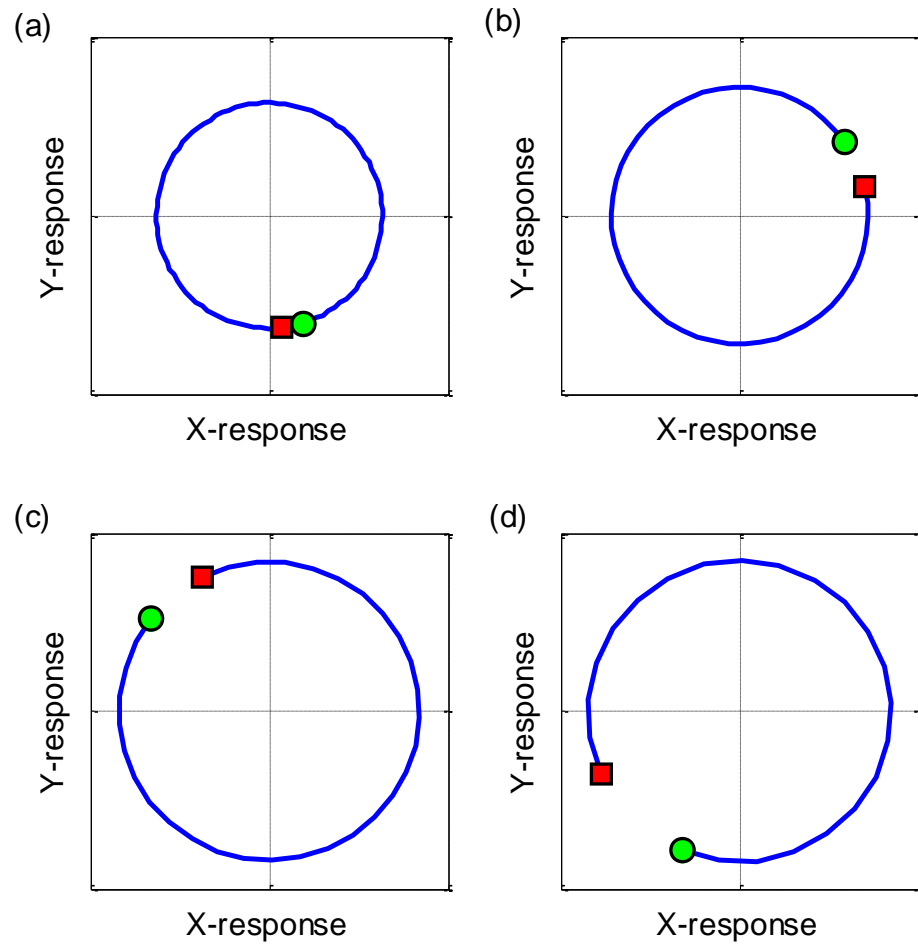


Figure 8.7 Healthy orbit plot; filtered for $1\times$ and $2\times$ at: (a) 600 rev/min (10 Hz), (b) 1200 rev/min (20 Hz), (c) 1800 rev/min (30 Hz) and (d) 2400 rev/min (40 Hz)

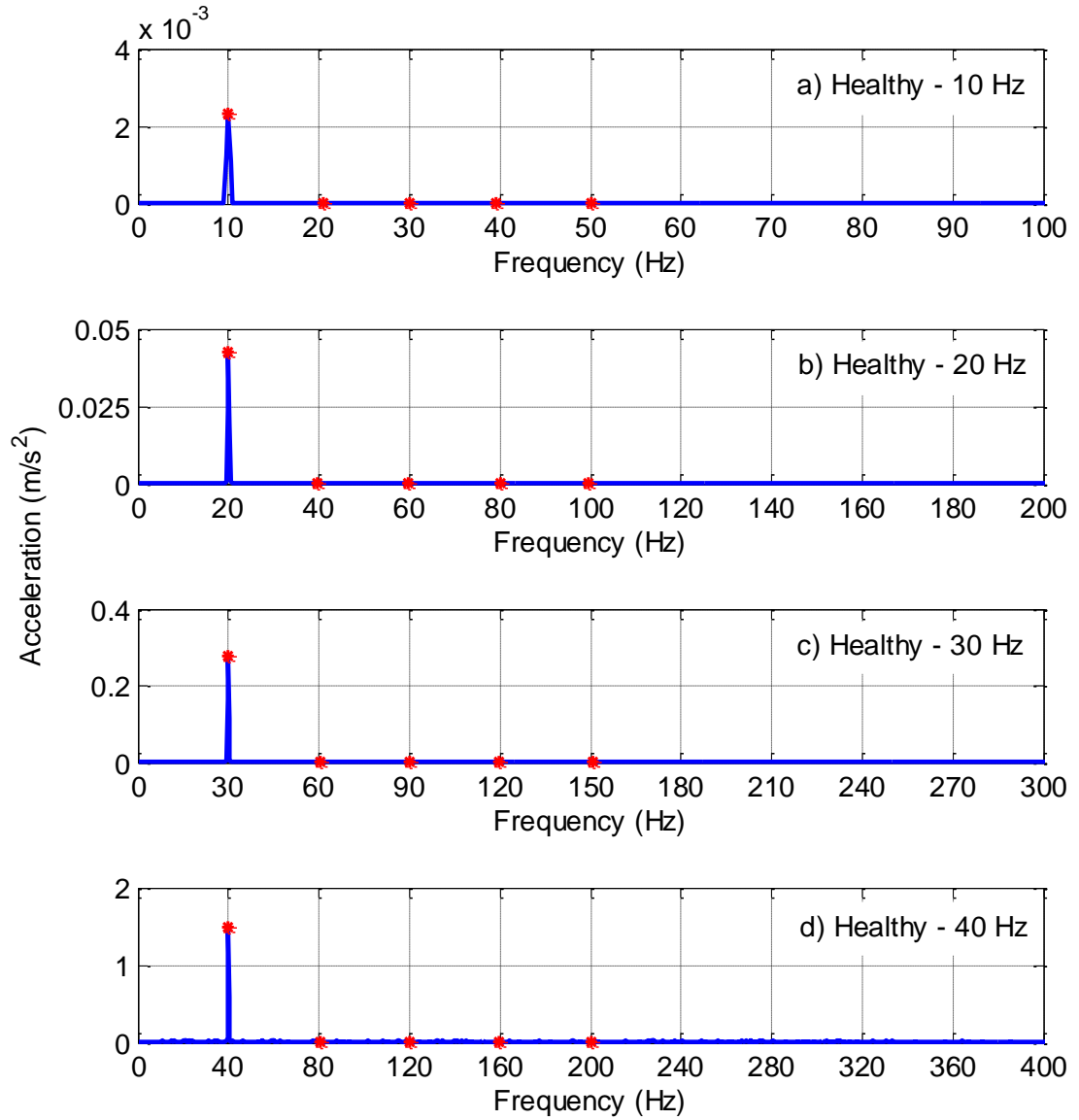


Figure 8.8 Healthy amplitude spectra at 450 for: (a) 600 rev/min (10 Hz), (b) 1200 rev/min (20 Hz), (c) 1800 rev/min (30 Hz) and (d) 2400 rev/min (40 Hz)

8.4.2 Added unbalance

The added unbalance model shown in Figure 8.9 was created by including an additional mass, m_a at an eccentricity, e_a and phase α to the healthy model. The added unbalance is representative of a typical unbalance case that is commonly encountered in practice. The equation of motion for the added unbalance condition can be expressed as

$$\begin{cases} (m + m_a)\ddot{u} + c\dot{u} + ku = me_d\omega^2 \cos(\omega t + \beta) + m_a e_a \omega^2 \cos(\omega t + \alpha) \\ (m + m_a)\ddot{v} + c\dot{v} + kv = me_d\omega^2 \sin(\omega t + \beta) + m_a e_a \omega^2 \sin(\omega t + \alpha) - mg \end{cases} \quad (8.6)$$

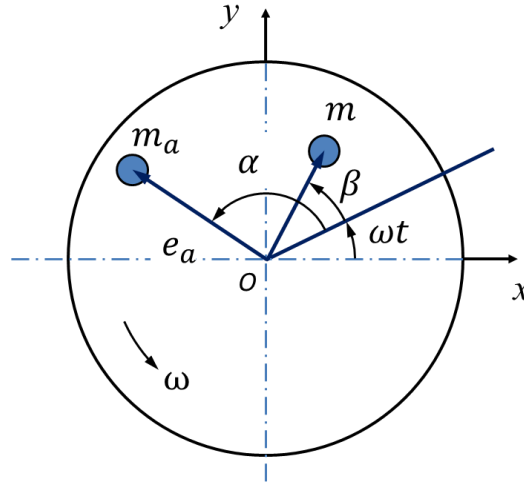


Figure 8.9 Added unbalance model showing mass of disc (m) and added mass (m_a)

The added mass, m_a and its eccentricity, e_a were sized to create the same size unbalance used in the experimental study, which was 1.44×10^{-4} kgm. A mass of 4.8 g at an eccentricity of 30 mm satisfied this condition. The added unbalance and the residual unbalance were assumed in phase.

The orbit plots and simple amplitude spectra for the speeds simulated are shown in Figures 8.10 and 8.11, respectively. The orbits have remained circular across the speed range and the frequency content of the response is purely a $1\times$ synchronous vibration which, again, is characteristic of a pure unbalance case. More interestingly, relative to the healthy spectra at the different speeds tested (Figure 8.8) with the added unbalance spectra (Figure 8.11), it can be seen that the inclusion of additional unbalance mass in phase with the residual unbalance at each speed resulted in an increase in the synchronous ($1\times$) vibration amplitude.

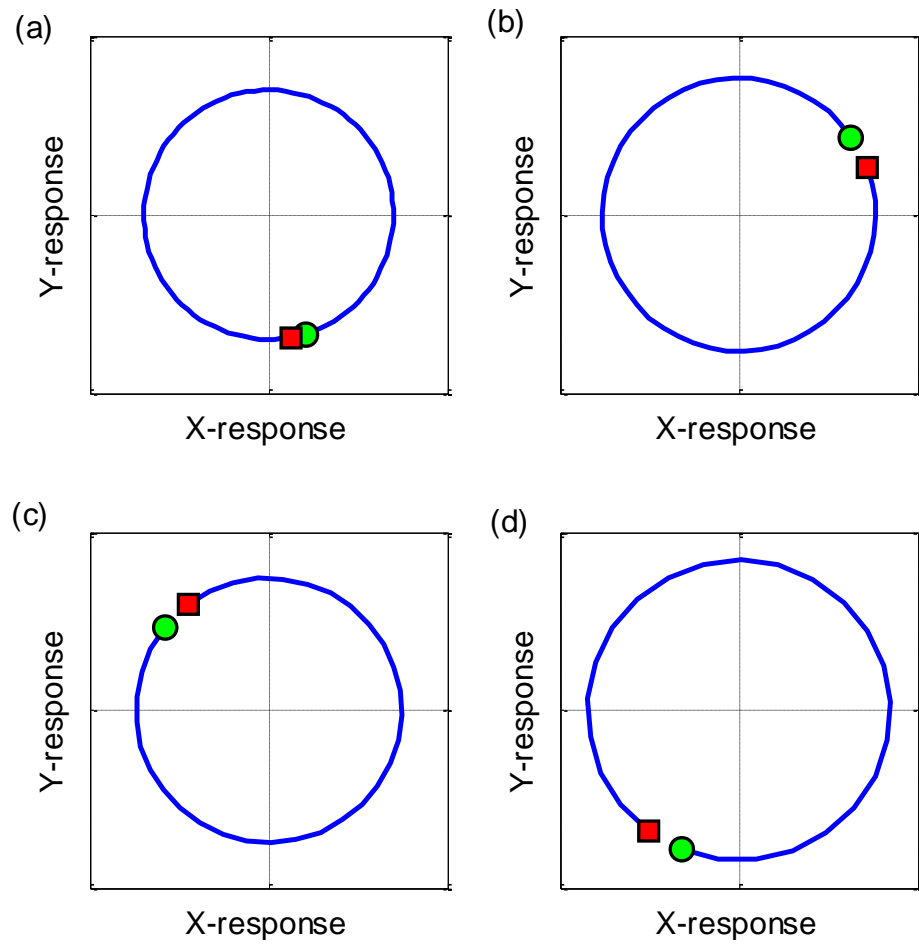


Figure 8.10 Added unbalance orbit plot; filtered for $1\times$ and $2\times$ at: (a) 600 rev/min (10 Hz), (b) 1200 rev/min (20 Hz), (c) 1800 rev/min (30 Hz) and (d) 2400 rev/min (40 Hz)

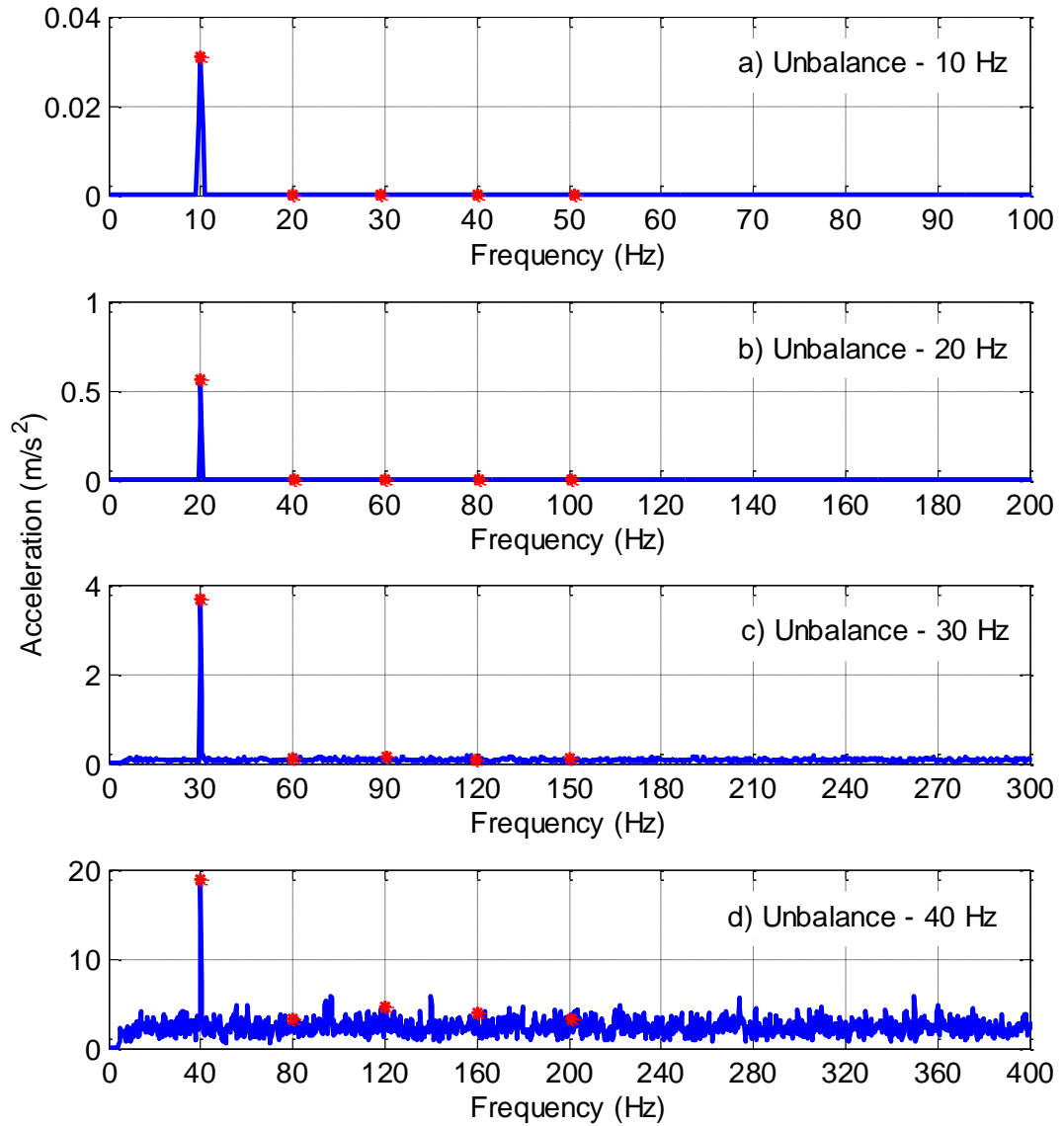


Figure 8.11 Added unbalance amplitude spectrum at 45° for: (a) 600 rev/min (10 Hz), (b) 1200 rev/min (20 Hz), (c) 1800 rev/min (30 Hz) and (d) 2400 rev/min (40 Hz)

8.4.3 Crack

Figure 8.12 presents the Jeffcott rotor with a transverse crack. The model shows a sectional end elevation of the shaft of radius, r_s with a crack of depth, a , that was considered located near the disc at the centre of the shaft. ωt is the instantaneous angle of rotation and β is the angle between the residual unbalance eccentricity and the weak crack direction. The section was taken through the crack, which was assumed to have a straight edge. The equations of motion for the cracked rotor was taken as

$$\begin{cases} m\ddot{u} + c\dot{u} + k(t)u = me_d\omega^2 \cos(\omega t + \beta) \\ m\ddot{v} + c\dot{v} + k(t)v = me_d\omega^2 \sin(\omega t + \beta) - mg \end{cases} \quad (8.7)$$

Equation (8.7) is quite similar to the equation of motion for the healthy case (Equation (8.5)), with the difference being the stiffness term, $k(t)$ which is now time varying and defined by the function given in Figure 8.13. The function shown is a periodic function of time that is based on the hinge or switching crack model [66]. The hinge or switching crack model states that the crack changes abruptly from its open to closed state as the shaft rotates [110]. This behaviour is represented in Figure 8.13 which shows how the stiffness of the shaft in both directions changes as the shaft makes one rotation. It can be seen that the crack remained open for 180° [108]. When the crack is closed its stiffness is equal to that of the uncracked or healthy shaft; which has the same value in the x and y directions. Thus, for a particular direction (x or y) the shaft stiffness is bilinear depending on whether the crack is open or closed.

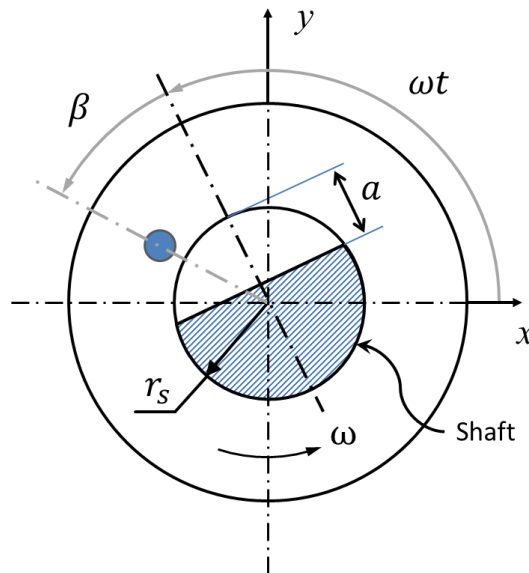


Figure 8.12 Crack model with cracked shaft section

Though criticized as deficient in a direct relationship between the shaft stiffness and crack depth [110], provided that crack depth is less than 25% shaft diameter, it has been

shown that the simple hinge or switching crack model is representative of the response expected of a cracked shaft [136], thus the hinge model was deemed suitable for the current study. The crack depth, a was modelled as 20% of shaft diameter [13]. For simplicity, the open crack stiffness in each direction were computed by considering the difference in the moment of inertia of a circle (shaft cross section) and a segment (crack section) about its x and y axis [137]. The breathing behaviour shown in Figure 8.13 was implemented in Matlab software using the “square” function with frequency, ω . The model considered here is a light rotor and as such, the breathing effect was assumed governed by the vibration response and not weight dominance of the rotor which does not apply in a light rotor case.

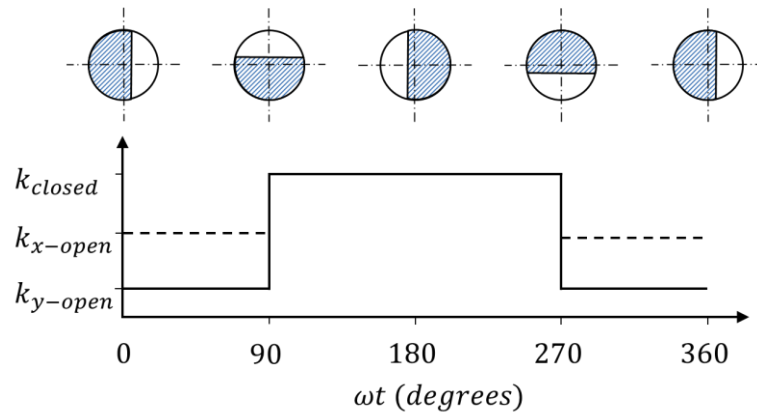


Figure 8.13 Stiffness variation in a switching or hinge crack model

The orbit plots generated from the steady-state region of the time domain response for the different speeds simulated are shown in Figures 8.14 and 8.15 which show plots at the four different speeds simulated and half of the Jeffcott rotor natural frequency, respectively. In Figure 8.14, it can be seen that the orbits were modified from the healthy case seen earlier (Section 8.4.1), but the inner or outer looped orbit that is customary of a cracked rotor case was not noted. It is widely known that the cracked rotor condition generates subharmonic resonances when the system is operated at integer fractions of the natural frequency, especially at half of the natural frequency, due to the presence of higher harmonics in the spectra [69]. Therefore, as seen in Figure 8.15, the selection of the 1500 rev/min rotor speed, revealed the expected crack features in comparison to the orbit plots at the other speeds presented in Figure 8.14.

Compared to the spectra for baseline healthy case (Figure 8.8), it can be seen from the amplitude spectra for the crack case in Figure 8.16, that crack model generated super harmonics. The spectra for crack at 25 Hz (see Figure 8.17) revealed a dominant $2\times$ harmonic component and a $3\times$ component which is widely reported for cracks. A similar outer looped orbit for the cracked shaft condition was noticed in the earlier experimental study [138] close to half of the rig's natural frequency as shown earlier in Figure 8.2(d).

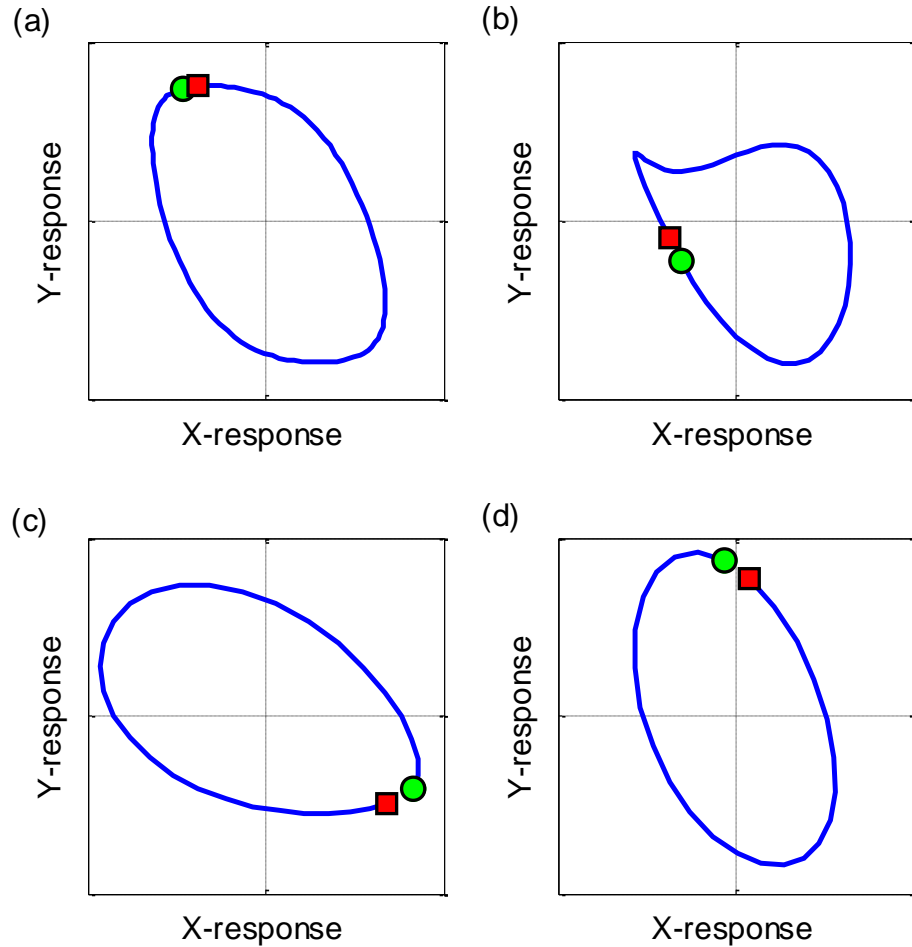


Figure 8.14 Crack orbit plot; filtered for $1\times$ and $2\times$ at: (a) 600 rev/min (10 Hz), (b) 1200 rev/min (20 Hz), (c) 1800 rev/min (30 Hz) and (d) 2400 rev/min (40 Hz)

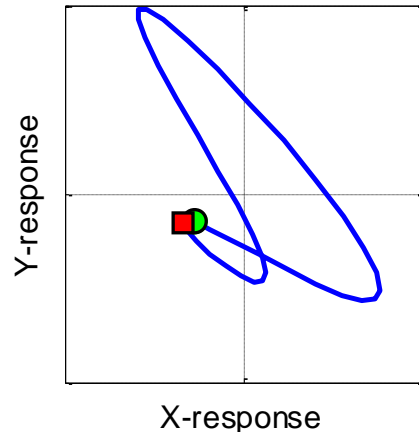


Figure 8.15 Crack orbit plot; filtered for $1\times$ and $2\times$ at half rotor natural frequency; 1500 rev/min (25 Hz)

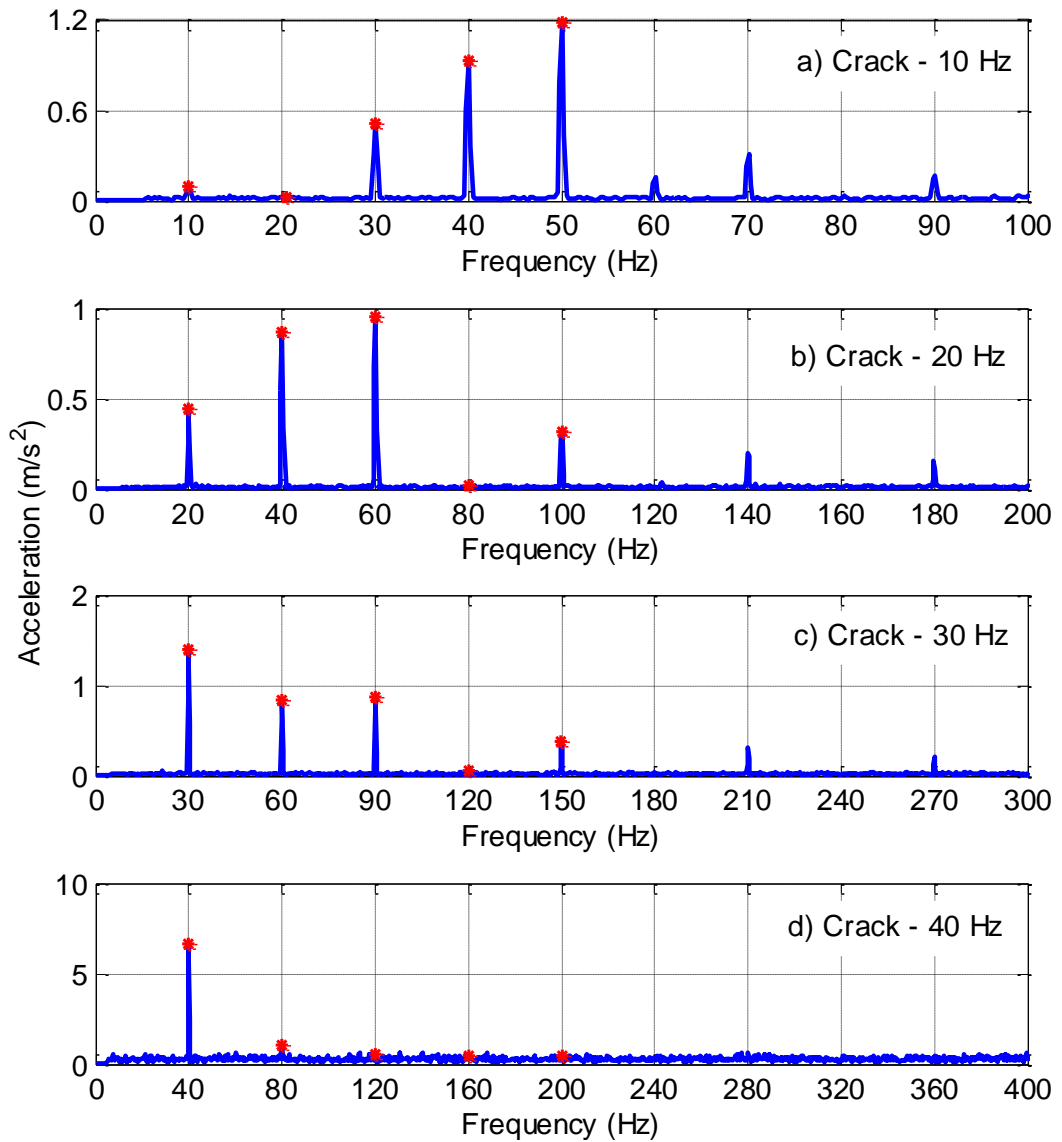


Figure 8.16 Crack amplitude spectra at 45° for: (a) 600 rev/min (10 Hz), (b) 1200 rev/min (20 Hz), (c) 1800 rev/min (30 Hz) and (d) 2400 rev/min (40 Hz)

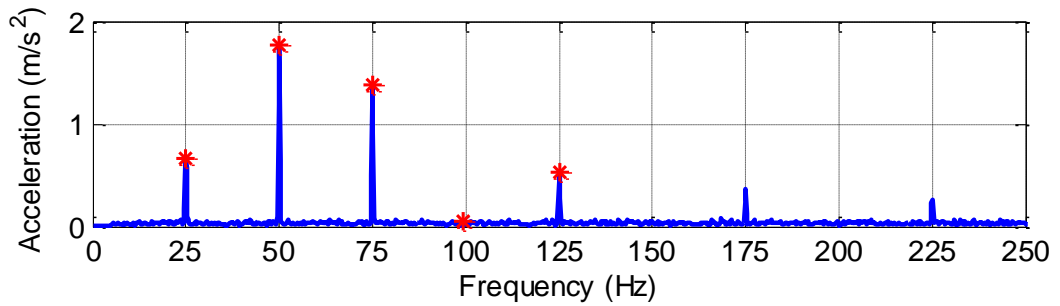


Figure 8.17 Crack amplitude spectra at 450 for half resonant speed; 1500 rev/min (25 Hz)

8.4.4 Misalignment

Misalignment of coupled machine shafts causes reaction forces to be generated in the coupling [139]. Since parallel misalignment was used in the earlier experimental work [13], the treatment of a flexible coupling with parallel misalignment developed by Gibbons [140] was employed in the current study. A schematic of the Gibbons [140] misalignment model is presented in Figure 8.18, which shows two machine centrelines, $Z1$ (driver) and $Z2$ (driven) which are offset both vertically (ΔY) and horizontally (ΔX). At a given speed, the drive rotor is considered subjected to a constant input drive torque, Tq . Also, the driven shaft is considered not to be under load. The figure shows three moments; MX , MY and MZ and three reaction forces; FX , FY and FZ which the coupling exerts on the machine shafts. $Z3$ is the coupling centre of articulation and connects the two shaft centrelines. The reaction forces of the coupling depend on the flexure of the coupling element, which produces an inherent restoring moment due to the spring rate of flexural element.

Even though it is well accepted that different couplings generate different vibration response, the treatment by Gibbons [140] is recognized [135, 139] as a generalized, simplified and acceptable approach to quantifying the forces acting during misalignment. Therefore, the forces and moments for a flexural coupling can be derived as follows [135, 140]

$$\begin{aligned}
\theta_1 &= \sin^{-1}(\Delta X1/Z3), & \theta_2 &= \sin^{-1}(\Delta X2/Z3) \\
\phi_1 &= \sin^{-1}(\Delta Y1/Z3), & \phi_2 &= \sin^{-1}(\Delta Y2/Z3) \\
MX1 &= Tq \sin \theta_1 + K_b \phi_1, & MX2 &= Tq \sin \theta_2 - K_b \phi_2 \\
MY1 &= Tq \sin \phi_1 - K_b \theta_1, & MY2 &= Tq \sin \phi_2 + K_b \theta_2 \\
FX1 &= (-MY1 - MY2)/Z3, & FX2 &= -FX1 \\
FY1 &= (MX1 + MX2)/Z3, & FY2 &= -FY1
\end{aligned} \tag{8.8}$$

where K_b is the bending spring rate for the flexible coupling, which was assumed constant (Sekhar and Prabu, 1995) and taken as $0.31 \text{ }^\circ/\text{Nm}$. To be consistent with misalignment experiments done by Nembhard et al [13], only a positive displacement of 0.8 mm in the y-direction was considered; that is $\Delta Y2 = 0.8 \text{ mm}$. Thus, the condition simulated was one of a parallel misalignment of 0.8 mm in the y direction and therefore; $\Delta X1 = \Delta X2 = \theta_1 = \theta_2 = 0$. The coupling centre of articulation, $Z3$ was taken as 0.024 m. The motor torque was assumed constant at a given speed and was derived from $P = Tq \times \omega$, where P , the motor power is 700 W [13] and ω the motor angular velocity in rad/s.

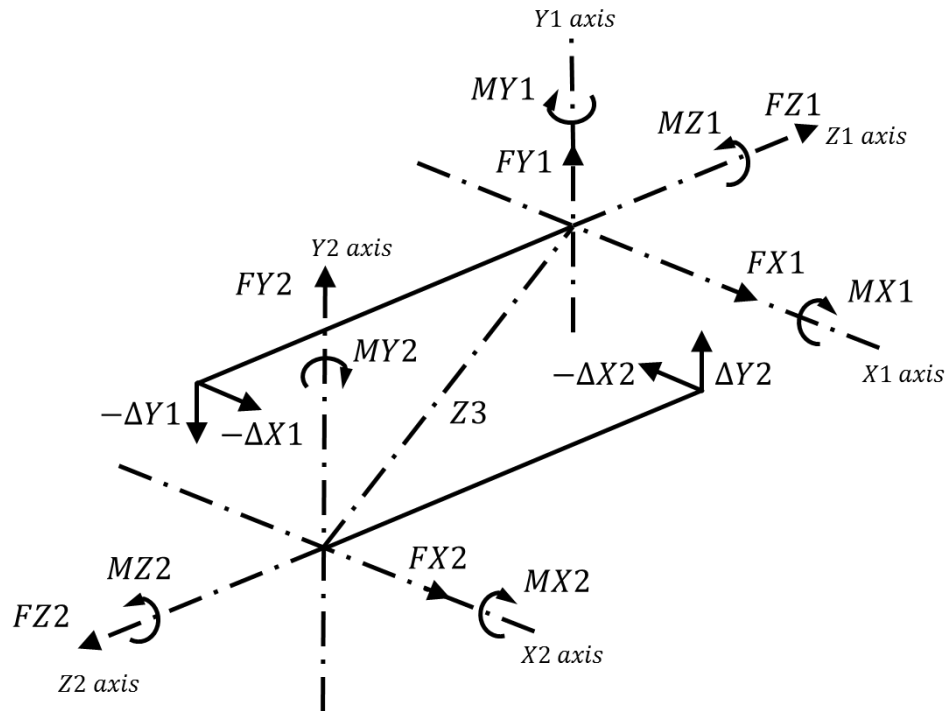


Figure 8.18 Coupling misalignment model for parallel misalignment [140]

The above mentioned forces and moments are the static loads acting on the shaft due to the misaligned coupling. However, for numerical analysis of the rotating shaft, the misalignment forces are assumed to be periodic with only 1ω and 2ω components [135] of the reaction forces acting on the rotor. Thus, the equations of motion for the misalignment case can be written as

$$\begin{cases} m\ddot{u} + c\dot{u} + ku = me_d\omega^2 \cos(\omega t + \beta) + F_{xM} \cos(\omega t + \gamma) + F_{xM} \cos(2\omega t + \gamma) \\ m\ddot{v} + c\dot{v} + kv = me_d\omega^2 \sin(\omega t + \beta) - mg + F_{yM} \sin(\omega t + \gamma) + F_{yM} \sin(2\omega t + \gamma) \end{cases} \quad (8.9)$$

where $F_{xM} = FX2$, $F_{yM} = FY2$ and γ is the misalignment phase angle. Thus, the equations of motion of the healthy condition (Equation (8.4)) have been augmented with the misalignment forces to produce Equation (8.9), which was implemented in the integration scheme and solved for.

The orbit plots of the misalignment response are shown in Figure 8.19 and their corresponding spectra are presented in Figure 8.20. Outer looped orbits (Figures 8.19a-c) were generated for all speeds except at 2400 rev/min (Figure 8.19(d)). It was encouraging to note that orbits for the cracked condition (Figure 8.14) were distinctively different from the orbits seen here for misalignment. As shown earlier in Section 8.2.3, an outer looped orbit was similarly observed when 0.8 mm parallel misalignment (see Figure 8.2(f)) was introduced to the experimental rig in the previous study [138]; albeit with a different loop orientation. Unsurprisingly, the misalignment spectra in Figure 8.20, has only $1\times$ and $2\times$ components, as defined by Equation (8.9) which was confined to the first (1ω) and second (2ω) harmonic components.

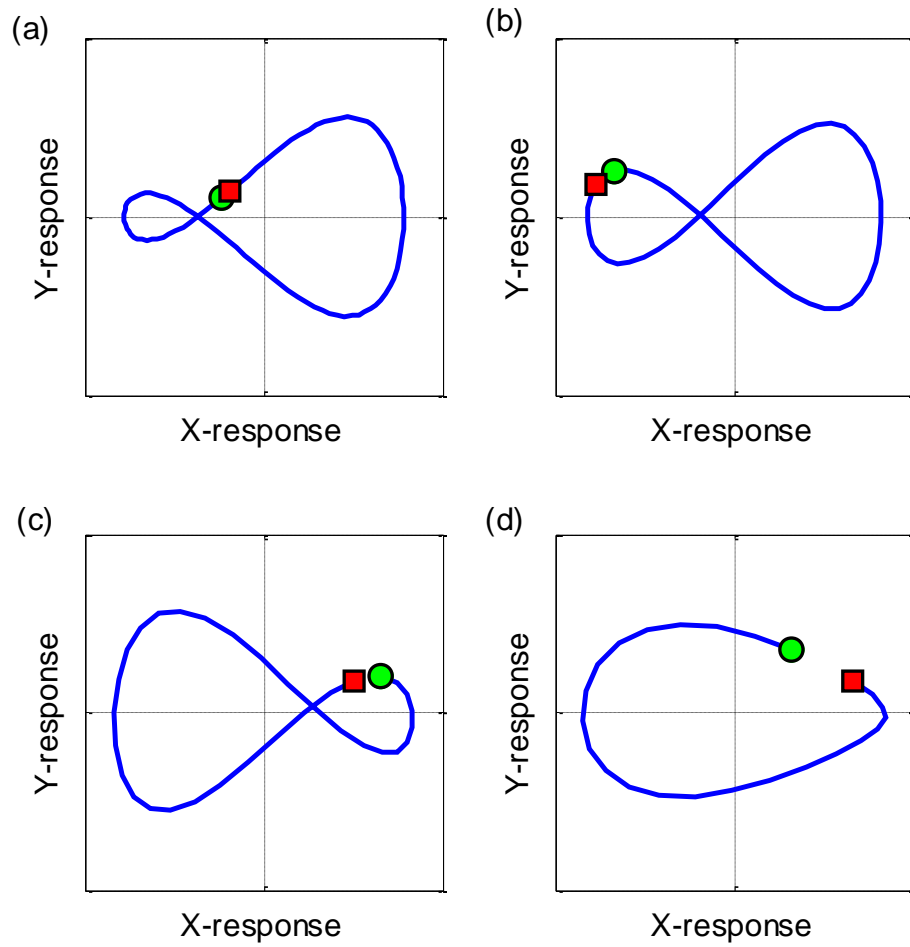


Figure 8.19 Misalignment orbit plot; filtered for $1\times$ and $2\times$ at: (a) 600 rev/min (10 Hz), (b) 1200 rev/min (20 Hz), (c) 1800 rev/min (30 Hz) and (d) 2400 rev/min (40 Hz)

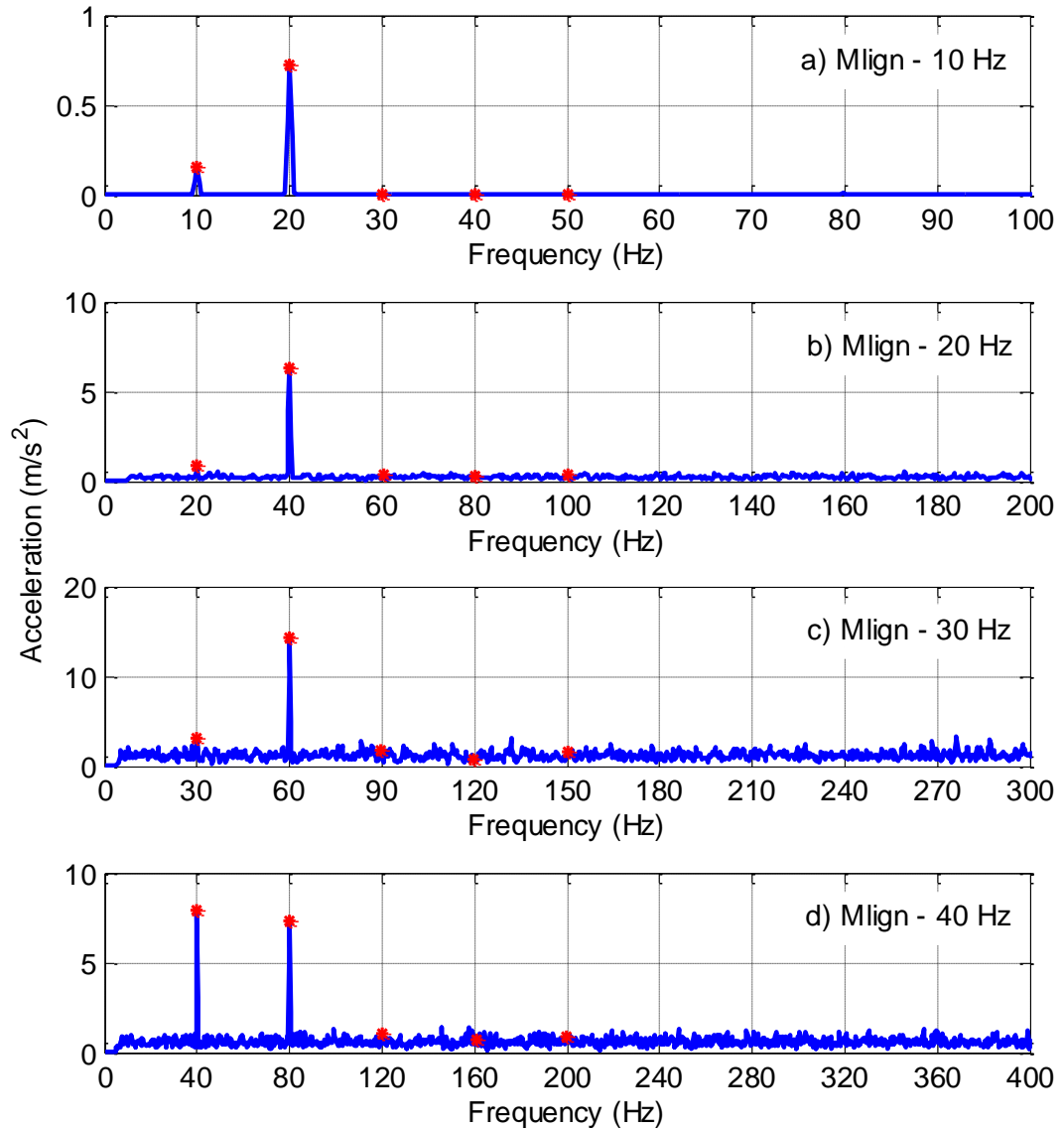


Figure 8.20 Misalignment amplitude spectra at 45° for: (a) 600 rev/min (10 Hz), (b) 1200 rev/min (20 Hz), (c) 1800 rev/min (30 Hz) and (d) 2400 rev/min (40 Hz)

8.4.5 Rub

A contacting rotor stator model is depicted in Figure 8.21. The disc of the Jeffcott rotor rotating at ω rad/s at the point of contact with the stator is shown. Consideration was given to the rotor experiencing intermittent contact with the stator due to an unbalance force. It was assumed the radial clearance between the rotor and the stator, d_0 , was not large enough to accommodate the radial displacement, $d = \sqrt{u^2 + v^2}$, due to the residual

unbalance force. When at rest, the rotor was assumed concentric and centred in the stator without contact. The general equations of motion for the rub-related system are

$$\begin{cases} m\ddot{u} + c\dot{u} + k(t)u = me_d\omega^2 \cos(\omega t + \beta) + F_{xR} \\ m\ddot{v} + c\dot{v} + k(t)v = me_d\omega^2 \sin(\omega t + \beta) - mg + F_{yR} \end{cases}$$

(8.10)

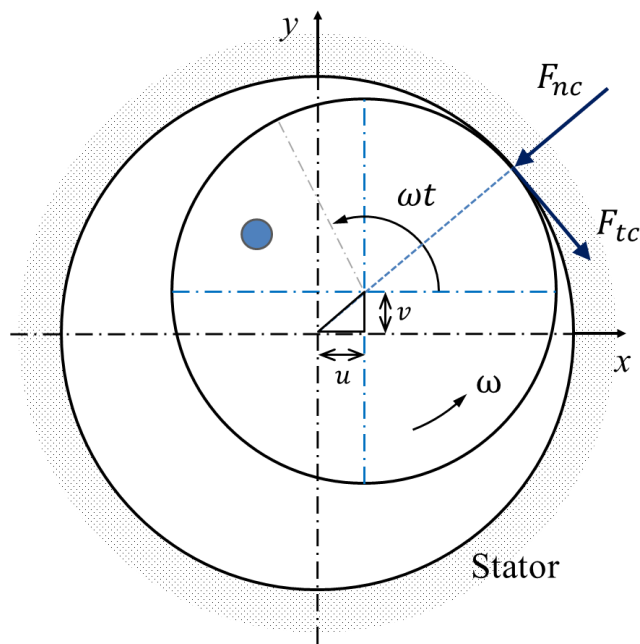


Figure 8.21 Schematic of rub model showing contacting rotor-stator system

where the new additions to the healthy equation (Equation (8.4)), F_{xR} and F_{yR} , denote forces in the x and y direction generated from interactions between the elastic rotor and rigid stator. When the rotor makes contact or rubs the stator, the stator deforms allowing the radial displacement to exceed the radial clearance inside the stator [48]. The stator can be modelled as a spring of stiffness k_c that creates a normal force, F_{nc} and a tangential frictional force, F_{tc} . Coulomb friction (with coefficient of friction μ) is considered for the tangential force at contact. The radial normal contact force and the tangential rub friction contact force can be expressed as [69]

$$F_{nC} = \begin{cases} 0 & \text{for } d < d_0 \\ -k_c(d - d_0) & \text{for } d \geq d_0 \end{cases} \quad \text{and} \quad F_{tC} = \mu F_{nC} \quad (8.11)$$

Therefore, the rub forces acting on the rotor in the x and y direction can be written as [48, 112]

$$F_{xR} = \begin{cases} 0 & \text{for } d < d_0 \\ -k_c(d - d_0)(\cos \theta - \delta_\psi \mu \sin \theta) & \text{for } d \geq d_0 \end{cases} \quad (8.12)$$

$$F_{yR} = \begin{cases} 0 & \text{for } d < d_0 \\ -k_c(d - d_0)(\sin \theta + \delta_\psi \mu \cos \theta) & \text{for } d \geq d_0 \end{cases} \quad (8.13)$$

where $\cos \theta = u/d$, $\sin \theta = v/d$ and δ_ψ , which accounts for the direction of the coulomb friction can be expressed as

$$\delta_\psi = \begin{cases} -1 & \text{for } \psi < 0 \\ 0 & \text{for } \psi = 0 \\ 1 & \text{for } \psi > 0 \end{cases} \quad (8.14)$$

ψ is the velocity of the contact point between the rotor and the stator, which can be derived by adding the velocity of the centre of the rotating disc to the relative velocity of the contact point to the disc centre. Thus, using R as the radius of the disc, ψ can be expressed as (Lin et al, 2001)

$$\psi = \frac{u\dot{v} - v\dot{u}}{d} + R\omega \quad (8.15)$$

More specific equations of motion can be obtained for the rotor-stator rub system considered here by introducing a new delta function, δ_c and combining Equations (8.10), (8.12) and (8.13) to get

$$\begin{cases} m\ddot{u} + c\dot{u} + ku = me_d\omega^2 \cos(\omega t + \beta) - \delta_c k_c (d - d_0)(\cos \theta - \delta_\psi \mu \sin \theta) \\ m\ddot{v} + c\dot{v} + kv = me_d\omega^2 \sin(\omega t + \beta) - mg - \delta_c k_c (d - d_0)(\sin \theta + \delta_\psi \mu \cos \theta) \end{cases} \quad (8.16)$$

where

$$\delta_c = \begin{cases} 0 & \text{for } d < d_0 \\ 1 & \text{for } d \geq d_0 \end{cases}$$

For the current study, the radial clearance was set at the lowest speed simulated (600 rev/min) and assumed constant at for all other speeds simulated. The clearance was taken as 0.0959 mm, which was 99.5% of the maximum response in either x or y direction at 600 rev/min. The stator stiffness was derived from a stiffness ratio, τ , given by $\tau = k/(k_c + k)$ that was assumed to be 0.04 [48]. Lastly, a coefficient of friction of 0.2 was considered.

The rub related rotor orbits are shown in Figure 8.22. The seemingly incomplete orbit at 2400 rev/min (Figure 8.22(d)) that was similar to the experimental rub orbit shown in Figure 8.2(g) was immediately noticeable among the four plots presented. This suggested the presence of fractional harmonics in the response, which was confirmed as the $0.5\times$ fractional harmonic by the presence of multiples of the $0.5\times$ harmonic component in the rub spectrum at 2400 rev/min (Figure 8.24(d)) and the completion of the orbit when generated over two rotation cycles (Figure 8.23). The spectra at 1200 rev/min had similar harmonics of $0.5\times$ but the amplitude of this component was not as prominent. Also, the orbit plots presented were rich in spectral lines of higher harmonics of the fundamental frequency. Consistent with the experimental orbit (Figure 8.2(g)) and observations widely made in literature, spectra rich in spectral lines of higher harmonics of the synchronous speed in addition to generation of the $0.5\times$ fractional frequency and its harmonics are representative of a typical rub case.

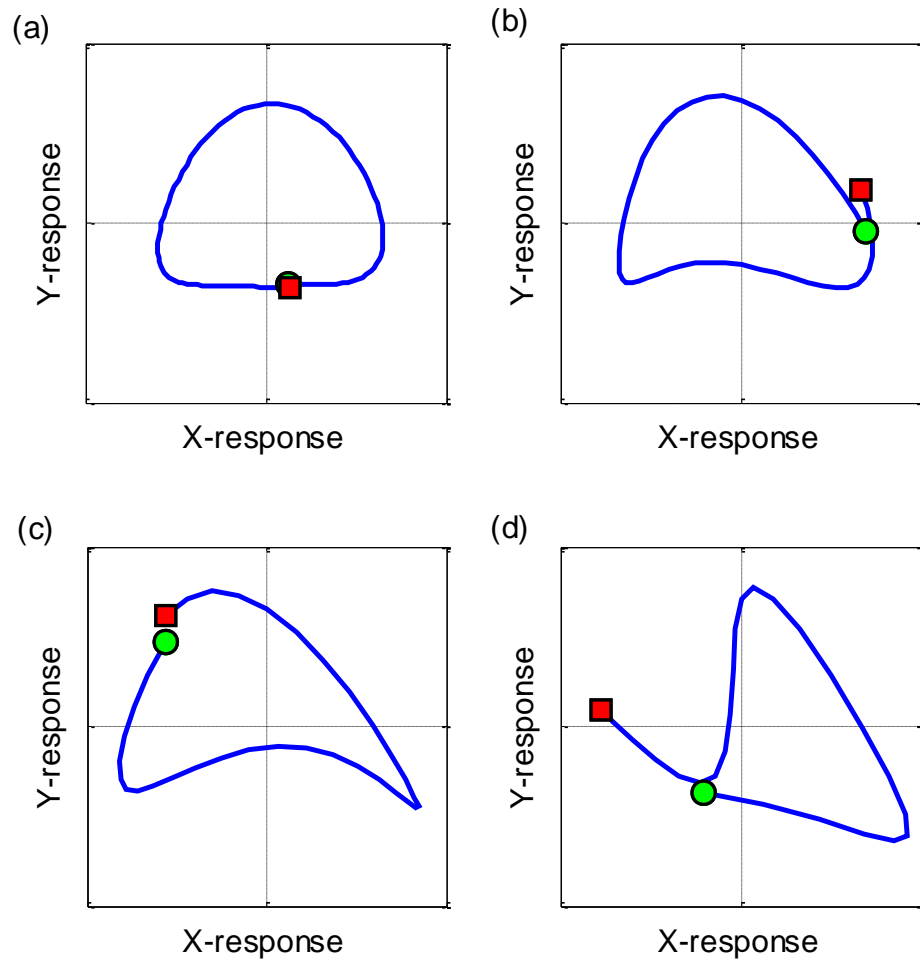


Figure 8.22 Rub orbit plot; filtered for $1\times$ and $2\times$ at: (a) 600 rev/min (10 Hz), (b) 1200 rev/min (20 Hz), (c) 1800 rev/min (30 Hz) and (d) 2400 rev/min (40 Hz)

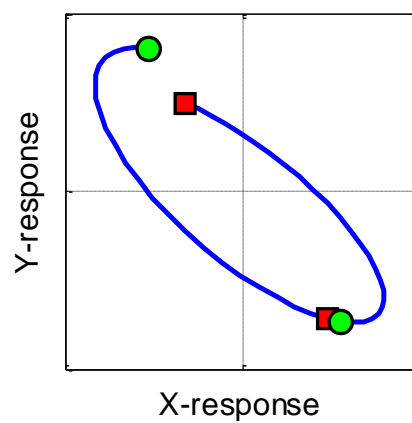


Figure 8.23 Rub orbit plot; filtered for $0.5\times$ component at 2400 rev/min (40 Hz)

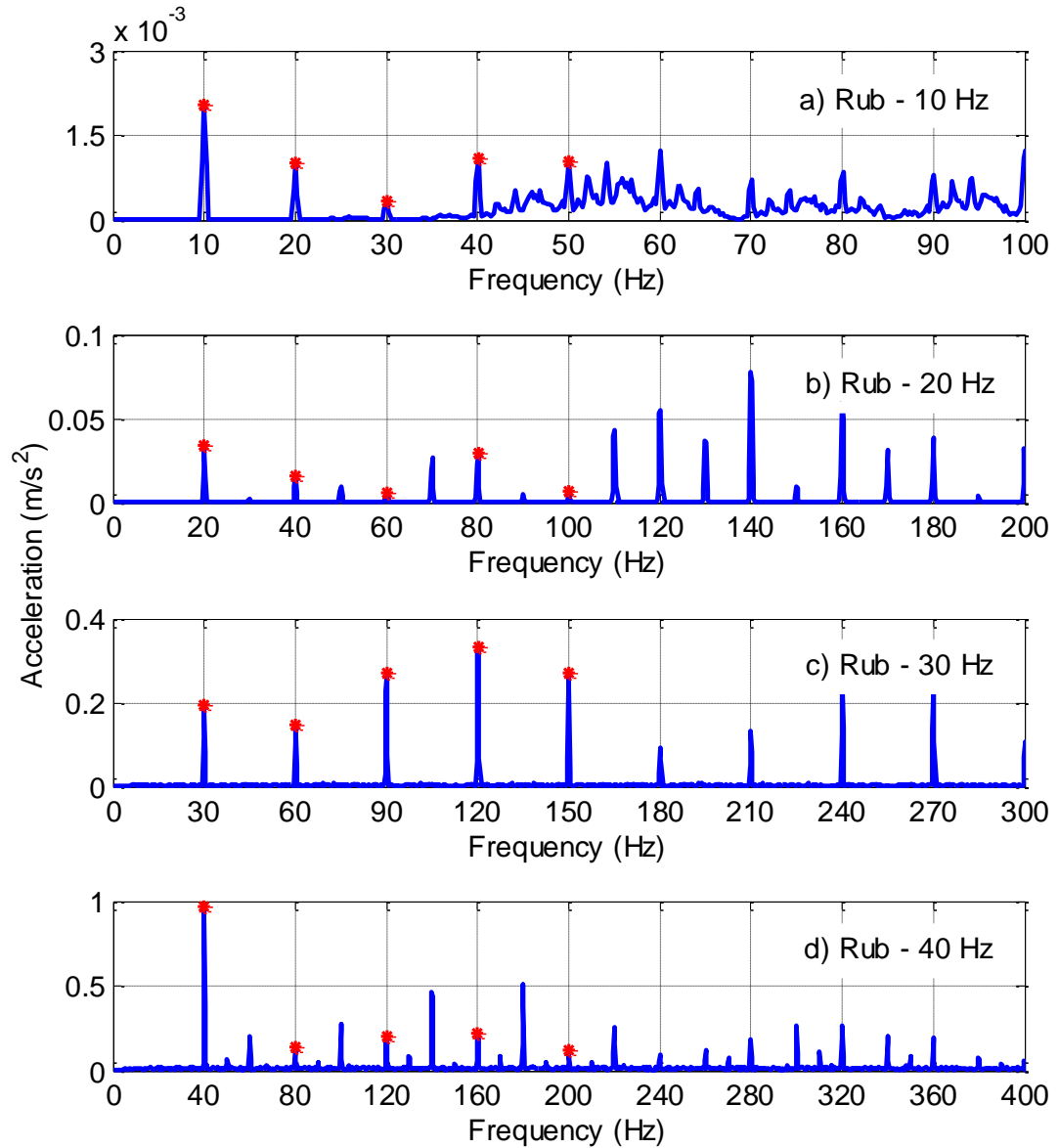


Figure 8.24 Rub amplitude spectra at 450 for: (a) 600 rev/min (10 Hz), (b) 1200 rev/min (20 Hz), (c) 1800 rev/min (30 Hz) and (d) 2400 rev/min (40 Hz)

8.4.6 Summary of fault simulations

To recapitulate, a baseline healthy condition as well as four different rotor faults namely; added unbalance, crack, misalignment and rub, were simulated using a simple Jeffcott rotor model. The healthy case was treated, as would be in a practical machine, as a residual unbalance, and therefore, each fault case was simulated with the fault and residual unbalance condition present on the Jeffcott rotor. To solve the equations of motion, the Newmark Beta integration scheme, with an alpha value of 0.5, beta value of 0.25 and a

time step of 0.1 ms, was implemented in Matlab software. Gyroscopic effects and cross coupled stiffness were ignored. All initial conditions were assumed zero. A summary of the model parameters used for all conditions simulated are provided in Table 1.

Table 8.1 Summary of model parameters

No	Model	Parameter	Symbol	Value	Unit
1	General	Shaft radius	r_s	0.01	m
		Shaft length	L_s	1	m
		Disk mass	m	0.7361	kg
		Damping factor	ζ	.0123	-
		Modulus of Elasticity	E	200×10^9	N/m ²
		Shaft density	ρ	7810	kg/m ³
2	Healthy (Low unbalance)	Unbalance eccentricity	e_d	.01592	mm
3	Added (High) unbalance	Added mass	m_a	4.8	g
		Added mass eccentricity	e_a	30	mm
4	Crack	crack depth ratio	$a/(2 \times r_s)$	0.2	-
5	Misalignment	Misalignment in y-direction	$\Delta X1$	0	m
		Misalignment in x-direction	$\Delta Y1$	8×10^{-4}	m
		Coupling centre of articulation	$Z3$.024	m
		Coupling bending spring rate	K_b	0.31	⁰ /Nm
		Motor power	P	700	W
6	Rub	Radius of disk	R	50	mm
		Stiffness ratio	τ	0.04	-
		Stator clearance	r_0	.0959	mm
		Coefficient of friction	μ	0.2	-

8.5 Fault classification – simulated data

Recall from Section 8.2.4, the method being tested integrated vibration features from data measured at four different bearing locations on the experimental rig. However, given the Jeffcott model provides a single set of response in each coordinate direction, the algorithm used previously was modified to accommodate a single response. The modification done here was analogous to using one of four bearing measurement locations to perform the analysis. Also, the approach requires the number of observations to be significantly more than the number of features [121]. Previously, 20 observations were applied by taking 20 samples of data and the same number of samples is considered here. In order to accomplish this, the response at 45° was treated twenty different times with 20 dB random noise using the “randn” function in Matlab software.

After noise addition, the steady-state time domain responses of the simulations were processed to extract the features used in the study. As done in the earlier study [13], one time domain feature, r.m.s. acceleration and six frequency domain features; amplitudes of $1\times$, $2\times$, $3\times$, $4\times$ and $5\times$ harmonic and spectrum energy [124] were considered in the current study. The parameters for generating the amplitude spectra were the same as provided in Section 8.4. At each speed simulated, the 7 features for each of 20 samples (or observations) for all 5 machine conditions simulated were input to the algorithm using a 7 (features) \times 100 (observations) matrix to perform the SS analysis. The input matrix for the MS analysis was 28 (features) \times 100 (observations), where the rows contained features from each successive speed starting from 600 rev/min.

8.5.1 Single speed (SS) classification with simulated data

The PC plot output from the SS analysis at 600 rev/min, 1200 rev/min, 1800 rev/min and 2400 rev/min are given in Figures 8.25, 8.26, 8.27 and 8.28, respectively. As done in the earlier study, the plots are presented in two parts, “a” and “b”, which shows the PC plot in full view and zoomed view, respectively. The zoomed view puts focus on the healthy condition which is the baseline. At 600 rev/min in the SS analysis, it can be seen that all fault cases were clearly isolated and separated from healthy, except for rub. On closer

inspection of the rub cases in the zoomed view (Figure 8.26(b)) it can be seen that there was little to no separation between the two conditions. There was, however, separation between healthy and rub for the remaining speeds (Figures 8.26 – 8.28) with the largest separation noticed at 1800 rev/min (Figure 8.27). The increased separation at 1800 rev/min could possibly be due to the influence of resonance, since half of the natural frequency occurs at 1500 rev/min. It was quite interesting to note increased separation among the conditions was also observed at 1800 rev/min in the earlier experimental study [13].

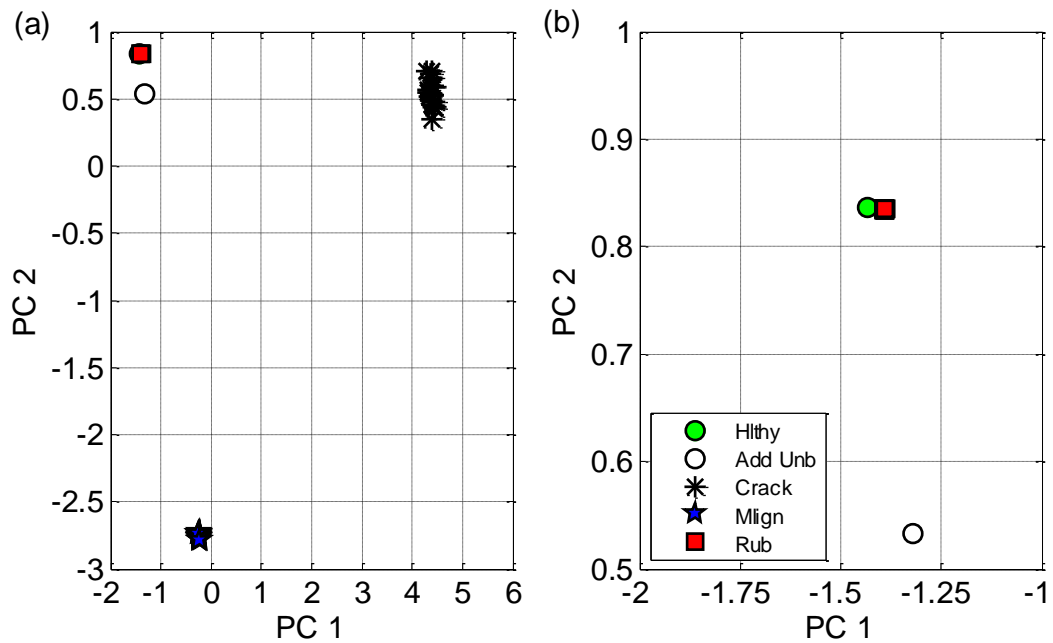


Figure 8.25 Single speed (SS) fault classification with data from mathematical simulations at 600 rev/min (10 Hz) in: a) full view and b) zoomed view

It is not entirely clear why rub was not separated at 600 rev/min, but it was interesting to note that it was the only instance in which the $1\times$ amplitude of the healthy case was larger than the $1\times$ for the fault at the same speed. It was also seen that the r.m.s vibration amplitude for rub at 600 rev/min was just larger than the healthy r.m.s. amplitude and was the lowest amongst the faults at said speed and was only just higher than the healthy case. The behaviour of rub at 600 rev/min prompted a more thorough examination of the r.m.s values for the different faults at the different speeds, and it was apparent that the visible separation of the faults at a given speed was driven by the relative size of the r.m.s. amplitude. Of course, a more detailed quantitative study would be required to confirm this.

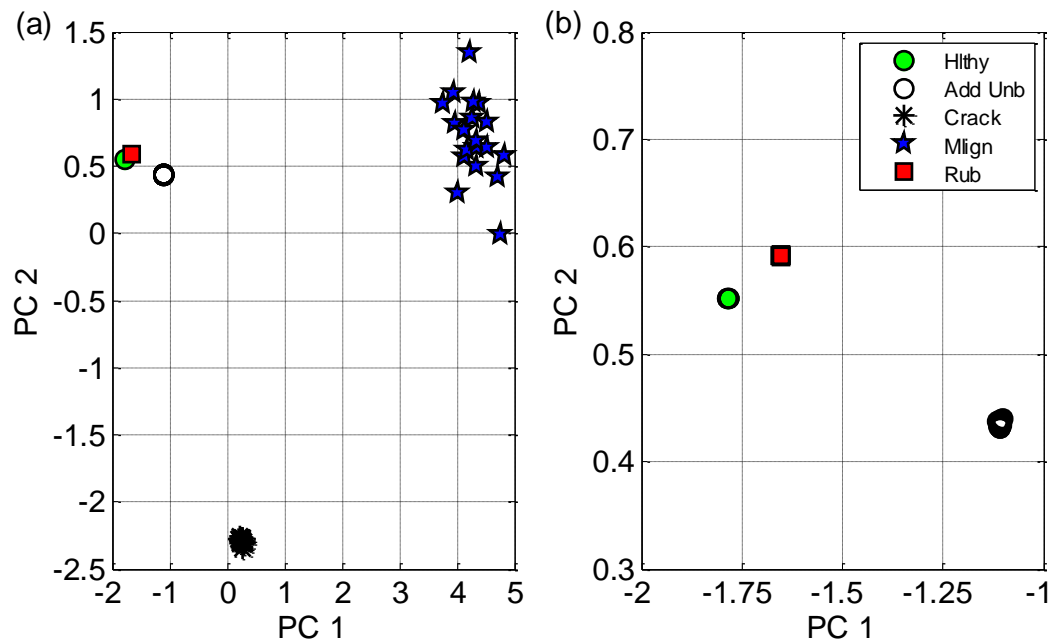


Figure 8.26 Single speed (SS) fault classification with data from mathematical simulations at 1200 rev/min (20 Hz) in: a) full view and b) zoomed view

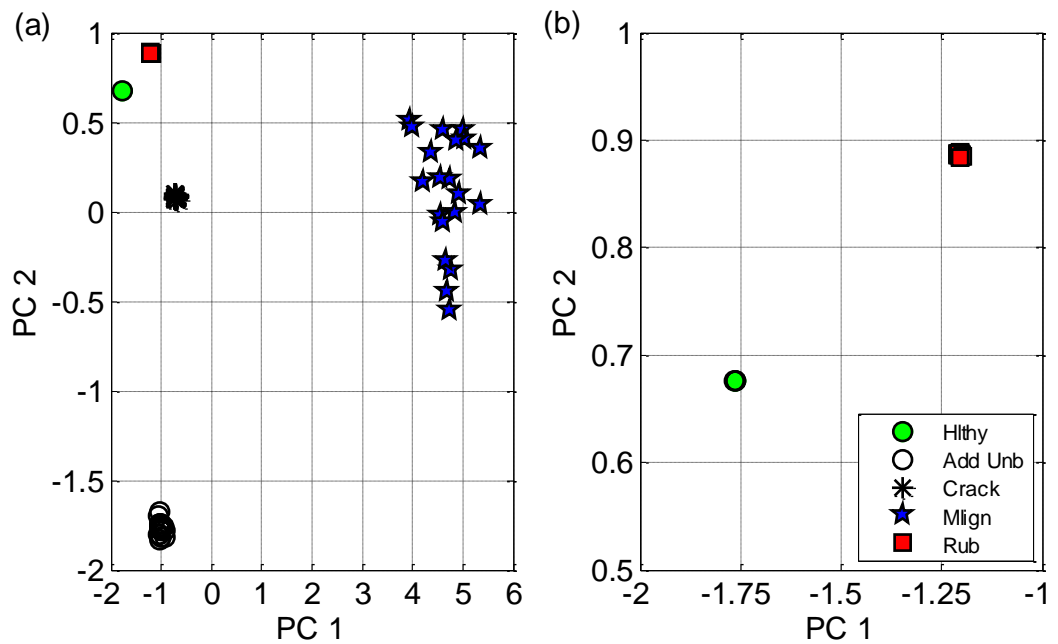


Figure 8.27 Single speed (SS) fault classification with data from mathematical simulations at 1800 rev/min (30 Hz) in: a) full view and b) zoomed view

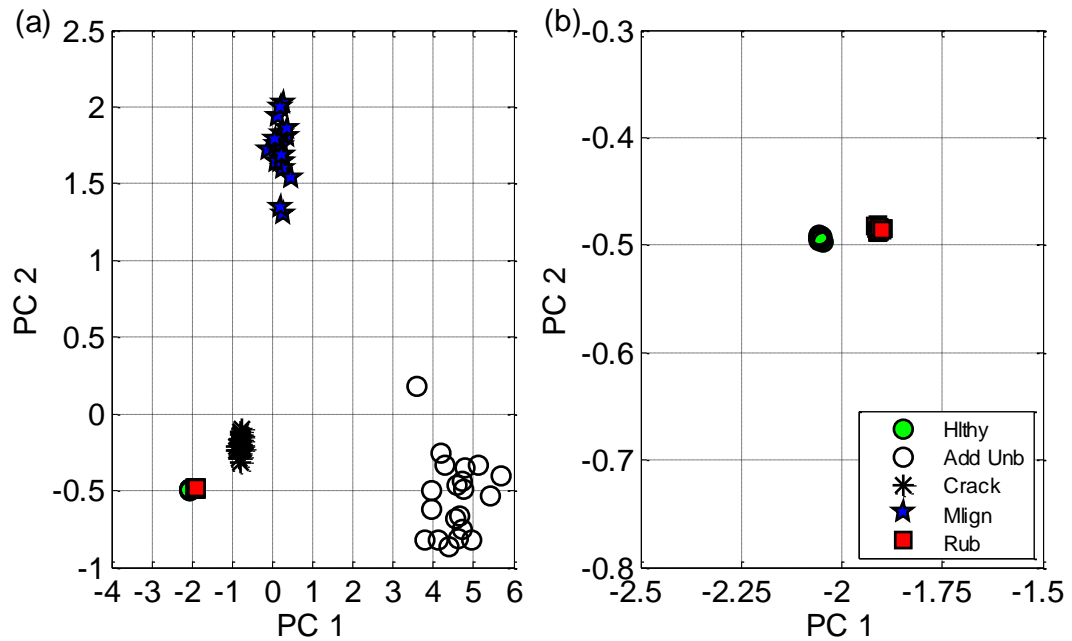


Figure 8.28 Single speed (SS) fault classification with data from mathematical simulations at 2400 rev/min (40 Hz) in: a) full view and b) zoomed view

8.5.2 Multi-speed (MS) classification with simulated data

The output from the MS analysis is shown in Figure 8.29. It can be seen that all fault conditions had conspicuous separation from the healthy case, except for the rub case which appeared to overlap the healthy case in full view (Figure 8.29(a)), but was in fact fully separated from healthy in the zoomed view (Figure 8.29(b)). Consistent with observations made in the earlier study, it was noted that separation of the fault cases in general were improved for the MS analysis when compared to the SS analysis, except for rub in SS at 1800 rev/min. Further investigation would be needed to ascertain why rub performed worst in SS speed at 600 rev/min and best at 1800 rev/min, as this was not evidenced in the earlier experiments [13].

Overall, the observations made here are consistent with those made in the earlier study, which employed experimental data. It is therefore apparent that the simple Jeffcott rotor model was able to accurately represent the dynamics of a rotating machine. The SS analysis showed good isolation and separation between the conditions tested, especially at 1800 rev/min. The close proximity of 1800 rev/min to half the rotor systems resonant

speed (1500 rev/min) suggests that the SS technique performs best at half of the resonant speed, however, further experiments and theoretical exploration would be required to confirm this. Though the earlier study fused data from different bearings whereas the findings here are equivalent to observations at a single bearing, the findings from Nembhard and Sinha [132], who showed that fault classification in the PC plot progressively improved using data from a single bearing to fusion of data from different bearings at a single speed and finally to fusion of data from different bearings at different speeds, would suggest that the results observed here would be improved if different bearing locations were simulated. It would therefore be interesting to develop a detailed finite element model of the rig for this purpose. Notwithstanding, improved separation in MS compared to SS further supports assertions by Nembhard and Sinha [132] that integration of more dynamics improves the efficacy of this diagnostic tool.

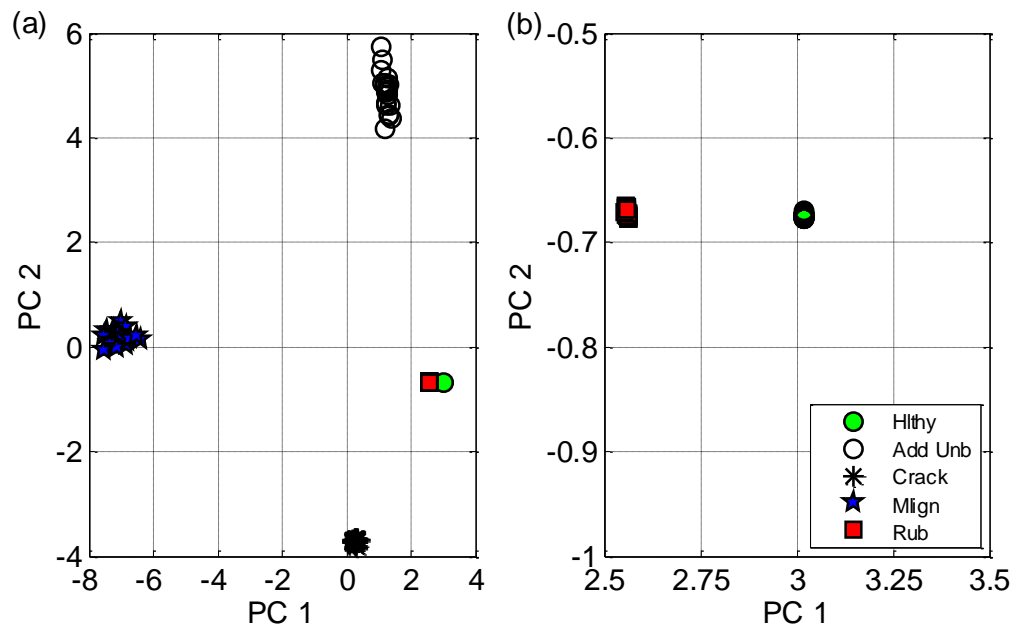


Figure 8.29 Multi-speed (MS) fault classification with data from mathematical simulations from all speeds (10 – 40 Hz) in: a) full view and b) zoomed view

8.6 Summary

Vibration data from simulations on a simple Jeffcott rotor were used to trial the single speed (SS) and multi-speed (MS) vibration-based fault classification techniques that were

proposed in an earlier experimental study. The vibration responses were estimated from the mathematical model of a healthy condition and a number of rotor fault conditions at different subcritical operating speeds. A number of parameters were calculated from the simulated responses and then data classification analyses were carried for the fault diagnosis similar to the experimental study. Different fault classifications were observed good for both SS and MS however, the MS was better able to classify the different conditions simulated as expected. This was similarly noticed in the experimental study. Thus, the results obtained from both analyses were consistent with the earlier experimental study, which suggest SS and MS analyses perform regardless of data source. Given the encouraging results had here, in the future, it would be useful to develop a detailed finite element model of the rig to fully explore the fault severity quantification and fault localization capabilities of the techniques.

9 CONCLUSIONS AND FUTURE WORK

9.1 Conclusions

A novel on-bearing vibration response integration approach for condition monitoring and diagnosis of a wide range of rotor faults irrespective of speed and machine foundation was proposed in the present study. Vibration data were acquired at different sub-critical speeds for crack, misalignment, rub and a baseline condition on a rig with relatively rigid supports. Experiments were then expanded to two different rigs with relatively flexible supports for a wider range of faults, namely: added unbalance, bow, crack, looseness, misalignment, rub and residual misalignment with residual unbalance balance conditions. Two flexible support types that were dynamically different from the rigid set up were deemed flexible support 1 (FS1) and flexible support 2 (FS2). Common time and frequency domain vibration condition indicators (features) were computed from the measured vibration data to be input to the proposed approach for further processing. First, the proposed approach was developed through its application to a the rigid rig at a given speed in a novel Single-Speed FD technique which exploits a single vibration sensor per bearing and fusion of features from different bearings for FD. Initially, vibration data were supplemented with bearing temperature readings with improved classification compared to vibration data alone. However, it was observed that temperature readings are insensitive to faults on the FS1 and FS2 rigs, when compared to vibration features, which were standardised for consistent classification on the different rigs tested. Thus, temperature was not included as final feature in subsequent analyses.

The observed fault classifications on the different flexible support rigs with vibration features alone were encouraging. Thereafter, a novel Unified Multi-Speed FD technique that is based on the initial proposed approach and which works by fusion of vibration features from different speeds and different bearings in a single analysis step for FD on a particular machine was proposed. Then, a novel generic Multi-Foundation Technique (also based on the proposed approach) which allows sharing of vibration data of a wide range of fault conditions between two similarly configured machines with similar speed operation but different foundations was implemented to further mitigate data requirements in the FD process. Afterwards, results from the Single-Speed and Multi-Speed techniques on the FS1 set up were compared to results of the said techniques using data acquired from mathematical simulations order to test the position that the proposed techniques will

perform regardless of data source. A simple Jeffcott rotor was used to model the different rotor fault conditions simulated. The main findings from this study can be summarized as follows:

1. The novel on-bearing vibration integration approach can be applied to rotating machinery fault classification in three novel techniques: Single-Speed analysis technique, Unified Multi-Speed analysis (UMA) technique and a Multi-Foundation Analysis technique.
2. For the novel Single-Speed technique on the rigid set up, fault classification with vibration features alone was good. However, it was seen that the supplementing vibration data with bearing temperature readings improved the efficacy of the fault classification process on the rigid rig.
3. During testing of the transferability of the Single-Speed technique from the rig with rigid supports to the rigs with relatively flexible supports, it was seen that bearing temperature did not affect the results with either flexible support set up. Consequently, temperature was excluded from the set of features used, which were then standardized to the following: r.m.s vibration amplitude; amplitudes of $1\times$, $2\times$, $3\times$ and $4\times$ spectral components; and spectrum energy (SE). Classification with the revised vibration features alone was equally good on both flexible set up.
4. Initially, the Unified Multi-Speed Analysis technique was developed from data obtained on the rigid rig support solely from vibration features as temperature did not have an effect on the classification. Results from the Unified Multi-Speed Analysis (UMA) technique indicated that not enough useful diagnostic information is available at a single bearing location at a single speed, but conversely, fusion of more dynamic features available at different speeds and different bearing locations improve the efficacy of the classification process. Therefore, the Unified Multi-Speed analysis technique would be suitable the diagnosis of fault on variable speed machines that are constantly in transient speed operations.

5. Preliminary analysis revealed that the set of features applied initially for the Single-Speed technique, which included temperature, and the Multi-Speed technique which did not include temperature, did not perform consistently for both flexible supports (FS1 and FS2). Therefore, features used were standardised to the said revised features used in the Single-Speed technique: r.m.s, 1×, 2×, 3×, 4×, 5× and SE. These features performed effectively for both rigid and flexible set up. The test of transferability of the Multi-Speed technique showed good fault classification on both FS1 and FS2; thereby indicating the UMA technique is transferable to different machines with different dynamic characteristics.
6. The results of the novel Multi-Foundation Analysis technique indicated that it was able to accurately classify mixed vibration data from two machines irrespective of speed. Additionally, the results garnered indicated that the method is suitable for mitigating or eliminating the need for unique vibration data histories between similarly configured machines by enabling sharing of vibration data history. The novel Multi-Foundation technique is suitable for situations in which vibration data history for a machine is not readily available, but a similarly configured machine in a different physical location has readily accessible history.
7. Results of the comparison of experimental results on the FS1 set up with simple mathematical simulations indicated that in both the Single-Speed and Multi-Speed analyses, the technique was seen to perform with the simulated data with results consistent to those observed in the experimental studies. The observed results further reinforce the position that the on-bearing vibration response integration approach will perform irrespective of data source.
8. The proposed novel Single-Speed or Multi-Speed techniques would require historical data, from say a database of known healthy and fault data. The historical data would establish healthy and fault clusters (such as clusters of misalignment separate from crack etc.) in the output. As new data become available, these would be fed into the database from which the algorithm mines and generates an input matrix. Continuous classification would be done. Therefore, if a fault does not exist with the machine being monitored, the input data would be grouped into the healthy cluster. This would continue until, say data with a fault occurrence is supplied to

the tool, which would classify and group the fault into one of the predefined fault clusters. There also exists the possibility that new input data is not classified in a predefined healthy or fault clusters. This would therefore mean the fault was not previously classified and would warrant further investigation to ascertain failure cause. This new fault data can then easily be updated to the database as reference for future classification.

9.2 Future Work

In order to exploit the full potential of the proposed approach as a viable vibration-based based condition monitoring and diagnosis approach, the following future work is required:

1. Finite element modelling (FEM) and subsequent analysis of the experimental rigs used in the study to theoretically explore the fault severity quantification and fault localization capabilities of the techniques on machines with ball bearings.
2. Further experimentation to investigate the fault severity quantification and fault localization capabilities of the approach with the fault conditions tested here range of time invariant and time-variant fault conditions.
3. Performance testing of the proposed approach on machines with fluid filled journal bearings by experimenting on rigs with fluid filled journal bearings.
4. Finite element modelling (FEM) and subsequent analysis of the experimental rigs with journal bearings to theoretically explore the fault classification, severity quantification and localization capabilities of the approach on machines with journal bearings.
5. Trialling the proposed approach with data from real machines in industry.

REFERENCES

- [1] British Standards Institution, *BS ISO 10816-1:1995+A1:2009 Mechanical vibration – Evaluation of machine vibration by measurement of on non-rotating parts – Part 1: General guidelines*. 2010, BSI: London.
- [2] British Standards Institution, *BS ISO 18436-2:2014 Condition monitoring and diagnostics of machines - Requirements for qualification and assessment of personnel*, in *Part 2: Vibration condition monitoring and diagnostics*. 2014, BSI: London.
- [3] Patel, T.H. and A.K. Darpe, *Experimental investigations on vibration response of misaligned rotors*. Mechanical Systems and Signal Processing, 2009. **23**(7): p. 2236-2252.
- [4] Sinou, J.-J., *Experimental response and vibrational characteristics of a slotted rotor*. Communications in Nonlinear Science and Numerical Simulation, 2009. **14**: p. 3179-3194.
- [5] Mohamed, A.A., et al., *Monitoring of Fatigue Crack Stages in a High Carbon Steel Rotating Shaft Using Vibration*. Procedia Engineering, 2011. **10**(0): p. 130-135.
- [6] Patel, T. and A. Darpe, *Application of Full Spectrum Analysis for Rotor Fault Diagnosis*, in *IUTAM Symposium on Emerging Trends in Rotor Dynamics*, K. Gupta, Editor. 2011, Springer Netherlands. p. 535-545.
- [7] Behzad, M. and M. Asayesh, *Numerical and experimental investigation of the vibration of rotors with loose discs*. Proceedings of the Institution of Mechanical Engineers, Part C: Journal of Mechanical Engineering Science, 2010. **224**: p. 85-94.
- [8] Taplak, H., S. Erkaya, and İ. Uzmay, *Experimental analysis on fault detection for a direct coupled rotor-bearing system*. Measurement, 2013. **46**: p. 336-344.
- [9] Saavedra, P.N. and D.E. Ramírez, *Vibration analysis of rotors for the identification of shaft misalignment Part 2: Experimental validation*. Proceedings of the Institution of Mechanical Engineers, Part C: Journal of Mechanical Engineering Science, 2004. **218**: p. 987-999.
- [10] Chu, F. and W. Lu, *Experimental observation of nonlinear vibrations in a rub-impact rotor system*. Journal of Sound and Vibration, 2005. **283**(3–5): p. 621-643.
- [11] Sudhakar, G.N.D.S. and A.S. Sekhar, *Identification of unbalance in a rotor bearing system*. Journal of Sound and Vibration, 2011. **330**(10): p. 2299-2313.
- [12] Jordan, M.A., *What are Orbit plots, anyway?*, in *Orbit*. 1993, Bently Nevada Corporation. p. 8-15.
- [13] Nembhard, A.D., J.K. Sinha, and A. Yunusa-Kaltungo, *Development of a generic rotating machinery fault diagnosis approach insensitive to machine speed and support type*. Journal of Sound and Vibration, 2015. **337**(0): p. 321-341.

- [14] Walker, R., S. Perinpanayagam, and I.K. Jennions, *Rotordynamic faults: recent advances in diagnosis and prognosis*. International Journal of Rotating Machinery, 2013. **2013**: p. 12.
- [15] Arebi, L., F. Gu, and A. Ball, *A comparative study of misalignment detection using a novel Wireless Sensor with conventional Wired Sensors*. Journal of Physics: Conference Series, 2012. **364**(1): p. 012049.
- [16] Hashemian, H.M., *Wireless sensors for predictive maintenance of rotating equipment in research reactors*. Annals of Nuclear Energy, 2011. **38**(2–3): p. 665-680.
- [17] Elnady, M.E., J.K. Sinha, and S.O. Oyadiji, *Condition monitoring of rotating machines using on-shaft vibration measurement*, in *IMEchE, 9th International Conference on Vibrations in Rotating Machinery*. 2012, Springer: London, UK.
- [18] Jiang, L.-l., et al., *Fault Diagnosis of Rotating Machinery Based on Multisensor Information Fusion Using SVM and Time-Domain Features*. Shock and Vibration, 2014. **2014**: p. 8.
- [19] Craig, M., et al., *Advanced condition monitoring of tapered roller bearings, Part 1*. Tribology International, 2009. **42**: p. 1846-1856.
- [20] Nembhard, A., *Comparison of Temperature and Vibration Analyses for the Condition Monitoring of Rotating Machines*. MSc. 2011, The University of Manchester.
- [21] Feng, Z., M. Liang, and F. Chu, *Recent advances in time–frequency analysis methods for machinery fault diagnosis: A review with application examples*. Mechanical Systems and Signal Processing, 2013. **38**(1): p. 165-205.
- [22] Lei, Y., et al., *A review on empirical mode decomposition in fault diagnosis of rotating machinery*. Mechanical Systems and Signal Processing, 2013. **35**(1–2): p. 108-126.
- [23] Yan, R., R.X. Gao, and X. Chen, *Wavelets for fault diagnosis of rotary machines: A review with applications*. Signal Processing, 2014. **96**, Part A(0): p. 1-15.
- [24] Worden, K., W.J. Staszewski, and J.J. Hensman, *Natural computing for mechanical systems research: A tutorial overview*. Mechanical Systems and Signal Processing, 2011. **25**: p. 4-111.
- [25] Jayaswal, P., S.N. Verma, and A.K. Wadhwani, *Application of ANN, Fuzzy Logic and Wavelet Transform in machine fault diagnosis using vibration signal analysis*. Journal of Quality in Maintenance Engineering, 2010. **16**: p. 190-213.
- [26] Min, X., K. Fanrang, and H. Fei. *An approach for bearing fault diagnosis based on PCA and multiple classifier fusion*. in *2011 6th IEEE Joint International Information Technology and Artificial Intelligence Conference (ITAIC 2011)*, 20-22 Aug. 2011. 2011. Piscataway, NJ, USA: IEEE.

- [27] Xu, Z., et al., *A novel fault diagnosis method using pca and art-similarity classifier based on yu's norm*. Key Engineering Materials, 2009. **413-414**: p. 569-574.
- [28] Sinha, J.K. and K. Elbhah, *A future possibility of vibration based condition monitoring of rotating machines*. Mechanical Systems and Signal Processing, 2013. **34**: p. 231-240.
- [29] Elbhah, K. and J.K. Sinha, *Vibration-based condition monitoring of rotating machines using a machine composite spectrum*. Journal of Sound and Vibration, 2013. **332**(11): p. 2831-2845.
- [30] Lee, J., et al., *Prognostics and health management design for rotary machinery systems—Reviews, methodology and applications*. Mechanical Systems and Signal Processing, 2014. **42**(1–2): p. 314-334.
- [31] British Standards Institution, *BS ISO 17359:2011 Condition Monitoring and diagnostics of machines – General guidelines*. 2011, BSI: London.
- [32] Barragan, J.M., *Engine Vibration Monitoring and Diagnosis Based on On-Board Captured Data in NATO/RTA AVT, Symposium on AGING MECHANISM AND CONTROL: Part B – Monitoring and Management of Gas Turbine Fleets for Extended Life and Reduced Costs*. 2001: Manchester, UK.
- [33] Grabill, P., J. Seale, and T. Brotherton. *aTEDS: airborne turbine engine diagnostic system*. in *Aerospace Conference, 2004. Proceedings. 2004 IEEE*. 2004.
- [34] Byington, C.S., et al. *False Alarm Mitigation of Vibration Diagnostic Systems*. in *Aerospace Conference, 2008 IEEE*. 2008.
- [35] Wen, Z. and Y. Liu. *Applications of Prognostics and Health Management in aviation industry*. in *Prognostics and System Health Management Conference (PHM-Shenzhen), 2011*. 2011.
- [36] Watson, M., et al., *A Comprehensive High Frequency Vibration Monitoring System For Incipient Fault Detection and Isolation of Gears, Bearings and Shafts/Couplings in Turbine Engines and Accessories*, in *Proceedings of GT 2007, ASME Turbo Expo 2007: Power for Land, Sea and Air*. 2007, ASME: Montreal, Canada.
- [37] Demirci, S., C. Hacıyev, and A. Schwenke, *Fuzzy logic-based automated engine health monitoring for commercial aircraft*. Aircraft Engineering and Aerospace Technology, 2008. **80**: p. 516-525.
- [38] Li, W., et al., *Feature extraction and classification of gear faults using principal component analysis*. Journal of Quality in Maintenance Engineering, 2003. **9**: p. 132-132.
- [39] Brotherton, T., et al. *A testbed for data fusion for engine diagnostics and prognostics*. in *Aerospace Conference Proceedings, 2002. IEEE*. 2002.

- [40] British Standards Institution, *BS ISO 13379-1:2012 Condition monitoring and diagnostics of machines*, in *Data interpretation and diagnostic techniques Part 1: General guidelines*. 2012, BSI: London.
- [41] Nowlan, F.S. and H. Heap, *Reliability-centered maintenance*. 1978, National Technical Information Service, US Department of Commerce: Virginia.
- [42] British Standards Institution, *BS EN 13306:2010 Maintenance*, in *Maintenance terminology*. 2010, BSI: London.
- [43] Moubray, J., *RCM II: Reliability-centered Maintenance*. 2nd ed ed. 1997, Oxford: Butterworth-Heinemann.
- [44] Wowk, V., *Machinery Vibration: Measurement and Analysis*. 1991, New York: McGraw-Hill.
- [45] Mobley, R.K., *An Introduction to Predictive Maintenance*. 2002, Elsevier Butterworth-Heinemann: New York.
- [46] Jiang, S. and H. Mao, *Investigation of the High Speed Rolling Bearing Temperature Rise With Oil-Air Lubrication*. *Journal of Tribology*, 2011. **133**: p. 021101-021101.
- [47] Williams, J.H., A. Davies, and P.R. Drake, eds. *Condition-based Maintenance and Machine Diagnostics*. 1994, Chapman and Hall: London.
- [48] Friswell, M.I., et al., *Dynamics of Rotating Machines*. 2010, New York: Cambridge University Press.
- [49] El-Thalji, I. and E. Jantunen, *A summary of fault modelling and predictive health monitoring of rolling element bearings*. *Mechanical Systems and Signal Processing*, 2015. **60–61**(0): p. 252-272.
- [50] Ewins, D.J., *Modal Testing – Theory, Practice and Application*. 2nd ed. 2000, Baldock: Research Studies Press.
- [51] British Standards Institution, *BS ISO 13374-2:2007 Condition monitoring and diagnostics of machines – Data processing, communication and presentation – Part 2: Data processing*. 2007, BSI: London.
- [52] National Instruments *What is Data Acquisition?* 2013.
- [53] British Standards Institution, *BS ISO 13373-2:2005 Condition monitoring and diagnostics of machines – Vibration condition monitoring – Part 2: Processing, analysis and presentation of vibration data*. 2006, BSI: London.
- [54] Goldman, P. and A. Muszynska, *Application of full spectrum to rotating machinery diagnostics*, in *Orbit*. 1999. p. 17-21.
- [55] Patel, T.H., M.J. Zuo, and A.K. Darpe, *Vibration response of coupled rotor systems with crack and misalignment*. *Proceedings of the Institution of Mechanical Engineers, Part C: Journal of Mechanical Engineering Science*, 2011. **225**: p. 700-713.

- [56] Lu, W.X. and F.L. Chu, *Experimental investigation of pedestal looseness in a rotor-bearing system*. Key Engineering Materials, 2009. **413**: p. 599-605.
- [57] Patel, T.H. and A.K. Darpe, *Vibration response of misaligned rotors*. Journal of Sound and Vibration, 2009. **325**(3): p. 609-628.
- [58] Muszynska, A., *Vibrational Diagnostics of Rotating Machinery Malfunctions*. International Journal of Rotating Machinery, 1995. **1**(3-4): p. 237-266.
- [59] Ehrich, F.F., *High Order Subharmonic Response of High Speed Rotors in Bearing Clearance*. Journal of Vibration and Acoustics, 1988. **110**(1): p. 9-16.
- [60] Darpe, A.K., K. Gupta, and A. Chawla, *Dynamics of a bowed rotor with a transverse surface crack*. Journal of Sound and Vibration, 2006. **296**(4-5): p. 888-907.
- [61] Xiaoyao Shen, Jiuhong Jia, and Mein Zhao, *Numerical Analysis of a Rub-impact Rotor-bearing System with Mass Unbalance*. Journal of Vibration and Control, 2007. **13**(12): p. 1819-1834.
- [62] Jia, J. and T. Hang, *Effect of the Initial Deflection On Vibration Characteristics of the Rub-Impact Rotor System*. Mathematical and Computational Applications, 2010. **15**(5): p. 768-775.
- [63] Darpe, A.K., K. Gupta, and A. Chawla, *Transient response and breathing behaviour of a cracked Jeffcott rotor*. Journal of Sound and Vibration, 2004. **272**(1-2): p. 207-243.
- [64] Gómez-Mancilla, J., et al., *The influence of crack-imbalance orientation and orbital evolution for an extended cracked Jeffcott rotor*. Comptes Rendus Mécanique, 2004. **332**(12): p. 955-962.
- [65] Sinou, J.J. and A.W. Lees, *The influence of cracks in rotating shafts*. Journal of Sound and Vibration, 2005. **285**(4-5): p. 1015-1037.
- [66] Gasch, R., *Dynamic behaviour of the Laval rotor with a transverse crack*. Mechanical Systems and Signal Processing, 2008. **22**(4): p. 790-804.
- [67] Jun, O.S. and M.S. Gadala, *Dynamic behavior analysis of cracked rotor*. Journal of Sound and Vibration, 2008. **309**(1-2): p. 210-245.
- [68] Patel, T.H. and A.K. Darpe, *Vibration response of a cracked rotor in presence of rotor-stator rub*. Journal of Sound and Vibration, 2008. **317**(3-5): p. 841-865.
- [69] Patel, T.H. and A.K. Darpe, *Influence of crack breathing model on nonlinear dynamics of a cracked rotor*. Journal of Sound and Vibration, 2008. **311**(3-5): p. 953-972.
- [70] Al-Shudeifat, M.A., E.A. Butcher, and C.R. Stern, *General harmonic balance solution of a cracked rotor-bearing-disk system for harmonic and sub-harmonic analysis: Analytical and experimental approach*. International Journal of Engineering Science, 2010. **48**(10): p. 921-935.

- [71] Jun, O.S., *Dynamic behavior analysis of cracked rotor based on harmonic motion*. Mechanical Systems and Signal Processing, 2012. **30**(0): p. 186-203.
- [72] Muszynska, A. and P. Goldman, *Chaotic responses of unbalanced rotor/bearing/stator systems with looseness or rubs*. Chaos, Solitons & Fractals, 1995. **5**(9): p. 1683-1704.
- [73] Chu, F. and Y. Tang, *Stability and Non-Linear Responses of a Rotor-Bearing System with Pedestal Looseness*. Journal of Sound and Vibration, 2001. **241**(5): p. 879-893.
- [74] Lee, Y.S. and C.W. Lee, *Modelling and Vibration Analysis of Misaligned Rotor-Ball Bearing Systems*. Journal of Sound and Vibration, 1999. **224**(1): p. 17-32.
- [75] Huang, Z., et al., *Vibration characteristics of a hydraulic generator unit rotor system with parallel misalignment and rub-impact*. Archive of Applied Mechanics, 2011. **81**: p. 829-838.
- [76] Pennacchi, P., A. Vania, and S. Chatterton, *Nonlinear effects caused by coupling misalignment in rotors equipped with journal bearings*. Mechanical Systems and Signal Processing, 2012. **30**(0): p. 306-322.
- [77] Yu, J.J., et al., *Rotor/Seal Experimental and Analytical Study on Full Annular Rub*. Journal of Engineering for Gas Turbines and Power, 2002. **124**(2): p. 340-350.
- [78] Bachschmid, N., P. Pennacchi, and A. Vania, *Diagnostic significance of orbit shape analysis and its application to improve machine fault detection*. Journal of the Brazilian Society of Mechanical Sciences and Engineering, 2004. **26**(2): p. 200-208.
- [79] Pennacchi, P., N. Bachschmid, and E. Tanzi, *Light and short arc rubs in rotating machines: Experimental tests and modelling*. Mechanical Systems and Signal Processing, 2009. **23**(7): p. 2205-2227.
- [80] Ma, H., et al., *Nonlinear dynamic characteristics of a flexible rotor system with local rub-impact*. Journal of Physics: Conference Series, 2013. **448**(1): p. 012015.
- [81] Adewusi, S.A. and B.O. Al-Bedoor, *Experimental Study on the Vibration of an Overhung Rotor with a Propagating Transverse Crack*. Shock and Vibration, 2002. **9**(3).
- [82] Pennacchi, P. and A. Vania, *Diagnosis and Model Based Identification of a Coupling Misalignment*. Shock and Vibration, 2005. **12**(4).
- [83] Cong, F., et al., *Experimental validation of impact energy model for the rub-impact assessment in a rotor system*. Mechanical Systems and Signal Processing, 2011. **25**(7): p. 2549-2558.
- [84] Bently, D.E., *Vibration analysis techniques for detecting and diagnosing shaft cracks*, in *Orbit*. 1986. p. 18-21.

- [85] Bosmans, R., *Shaft Crack Detection Methodology for Reactor Coolant Recirculation Pumps*, in *ORBIT*. 2006. p. 10.
- [86] Hou, S., M. Liang, and Y. Li, *An optimal global projection denoising algorithm and its application to shaft orbit purification*. *Structural Health Monitoring*, 2011. **10**(6): p. 603-616.
- [87] Forland, C., *Why phase information is important for diagnosing machinery problems*, in *Orbit*. 1999, Bently Nevada Corporation. p. 29-31.
- [88] British Standards Institution, *BS ISO 13373-1:2002 Condition monitoring and diagnostics of machines — Vibration condition monitoring — Part 1: General procedures*. 2002, BSI: London.
- [89] Qin, Y., Y. Mao, and B. Tang, *Vibration signal component separation by iteratively using basis pursuit and its application in mechanical fault detection*. *Journal of Sound and Vibration*, 2013. **332**(20): p. 5217-5235.
- [90] Sabnavis, G., et al., *Cracked Shaft Detection and Diagnostics: A Literature Review*. *The Shock and Vibration Digest*, 2004. **36**: p. 287-296.
- [91] Gaberson, H.A. *Rotating machinery energy loss due to misalignment*. in *Energy Conversion Engineering Conference, 1996. IECEC 96., Proceedings of the 31st Intersociety*. 1996.
- [92] Kelch, C.K. and P.E. Grover, *Using thermography to detect misalignment in coupled equipment*. 1996: p. 91-100.
- [93] Larsson, B.r., *Heat Separation in Frictional Rotor-Seal Contact*. *Journal of Tribology*, 2003. **125**(2): p. 600-607.
- [94] Bachschmid, N., P. Pennacchi, and A. Vania, *Thermally induced vibrations due to rub in real rotors*. *Journal of Sound and Vibration*, 2007. **299**: p. 683-719.
- [95] Yong-Wei, T. and Y. Jian-Gang, *Research on vibration induced by the coupled heat and force due to rotor-to-stator rub*. *Journal of Vibration and Control*, 2011. **17**: p. 549-566.
- [96] Malhi, A. and R.X. Gao, *PCA-based feature selection scheme for machine defect classification*. *IEEE Transactions on Instrumentation and Measurement*, 2004. **53**: p. 1517-25.
- [97] He, Q. and R.K.F.D.R. Yan, *Machine condition monitoring using principal component representations*. *Mechanical Systems and Signal Processing*, 2009. **23**(2): p. 446-466.
- [98] Pirra, M., et al. *PC A algorithm for detection, localisation and evolution of damages in gearbox bearings*. in *9th International Conference on Damage Assessment of Structures (DAMAS 2011), 11-13 July 2011*. 2011. UK: IOP Publishing Ltd.

- [99] Liying, J., et al. *Fault detection of rolling element bearing based on principal component analysis*. in *2012 24th Chinese Control and Decision Conference (CCDC), 23-25 May 2012*. 2012. Piscataway, NJ, USA: IEEE.
- [100] Baydar, N., A. Ball, and B. Payne, *Detection of incipient gear failures using statistical techniques*. IMA Journal Management Mathematics, 2002. **13**: p. 71-79.
- [101] Wang, Z. and H. Jiang, *Robust incipient fault identification of aircraft engine rotor based on wavelet and fraction*. Aerospace Science and Technology, 2010. **14**(4): p. 221-224.
- [102] Tumer, I.Y. and A. Bajwa, *A survey of aircraft engine health monitoring systems*, in *35th Joint Propulsion Conference and Exhibit*. 1999, American Institute of Aeronautics and Astronautics. p. 1-7.
- [103] Modgil, G., R.F. Orsagh, and M.J. Roemer. *Advanced vibration diagnostics for engine test cells*. in *Aerospace Conference, 2004. Proceedings. 2004 IEEE*. 2004.
- [104] Al-Shudeifat, M.A. and E.A. Butcher, *New breathing functions for the transverse breathing crack of the cracked rotor system: Approach for critical and subcritical harmonic analysis*. Journal of Sound and Vibration, 2011. **330**(3): p. 526-544.
- [105] Ricci, R. and P. Pennacchi, *Discussion of the dynamic stability of a multi-degree-of-freedom rotor system affected by a transverse crack*. Mechanism and Machine Theory, 2012. **58**(0): p. 82-100.
- [106] Genta, G., *Elementary rotordynamics: The Jeffcott Rotor*, in *Vibration Dynamics and Control*. 2009, Springer. p. 579-614.
- [107] Jeffcott, H., *XXVII. The lateral vibration of loaded shafts in the neighbourhood of a whirling speed.—The effect of want of balance*. The London, Edinburgh, and Dublin Philosophical Magazine and Journal of Science, 1919. **37**(219): p. 304-314.
- [108] Jun, O.S., et al., *Modelling and vibration analysis of a simple rotor with a breathing crack*. Journal of Sound and Vibration, 1992. **155**(2): p. 273-290.
- [109] Cheng, L., et al., *The influence of crack breathing and imbalance orientation angle on the characteristics of the critical speed of a cracked rotor*. Journal of Sound and Vibration, 2011. **330**(9): p. 2031-2048.
- [110] Penny, J. and M.I. Friswell, *Simplified modelling of rotor cracks*. Key Engineering Materials, 2003. **245**: p. 223-232.
- [111] Chu, F. and Z. Zhang, *Bifurcation and chaos in a rub-impact Jeffcott rotor system*. Journal of Sound and Vibration, 1998. **210**(1): p. 1-18.
- [112] Lin, F., M.P. Schoen, and U.A. Korde, *Numerical investigation with rub-related vibration in rotating machinery*. Journal of Vibration and Control, 2001. **7**(6): p. 833-848.
- [113] Redmond, I. and K. Al-Hussain, *Misalignment as a source of vibration in rotating shaft systems*. System, 2001. **1**: p. 47.

- [114] Al-Hussain, K.M. and I. Redmond, *Dynamic response of two rotors connected by rigid mechanical coupling with parallel misalignment* Journal of Sound and Vibration, 2002. **249**(3): p. 483-498.
- [115] Sinha, J., *Significance of vibration diagnosis of rotating machines during installation and commissioning: A summary of few cases*. Noise & Vibration Worldwide, 2006. **37**(5): p. 17-27.
- [116] Sinha, J.K., et al. *Vibration Investigation for Low Pressure Turbine Last Stage Blade Failure in Steam Turbines of a Power Plant*. in *ASME Turbo Expo 2012: Turbine Technical Conference and Exposition*. 2012. American Society of Mechanical Engineers.
- [117] Bai, C., H. Zhang, and Q. Xu, *Subharmonic resonance of a symmetric ball bearing-rotor system*. International Journal of Non-Linear Mechanics, 2013. **50**(0): p. 1-10.
- [118] Muszynska, A., *Misalignment and Shaft Crack-Related Phase Relationship for 1X and 2X Vibration Components of Rotor Responses*, in *ORBIT*. 1989, Bently Nevada. p. 4-8.
- [119] Mountford, R., *Practical uses of various data formats, Routine use of varied plots can lead to improvements in machine train operations*, in *ORBIT*. 1995, Bently Nevada. p. 12-15.
- [120] Jacquet-Richardet, G., et al., *Rotor to stator contacts in turbomachines. Review and application*. Mechanical Systems and Signal Processing, 2013. **40**(2): p. 401-420.
- [121] Jolliffe, I.T., *Principal Component Analysis*. 2nd ed. Springer Series in Statistics. 2002, New York: Springer.
- [122] Nembhard, A.D., et al., *Condition Monitoring of Rotating Machines using Vibration and Bearing Temperature Measurements*, in *International Conference on Condition Monitoring of Machinery in Non-Stationary Operations (CMMNO)*. 2013, Springer: Ferrara, Italy.
- [123] Nembhard, A.D., et al., *Combined vibration and thermal analysis for the condition monitoring of rotating machinery*. Structural Health Monitoring, 2014. **13**(3): p. 281-295.
- [124] Sinha, J.K., *Vibration Analysis, Instruments, and Signal Processing*. 2014, Florida: CRC Press.
- [125] Gauch, H.G., Jr., *Multivariate Analysis in Community Structure*. 1982, Cambridge: Cambridge University Press.
- [126] Palmer, M. *Principal Component Analysis*. 2013; Available from: <http://ordination.okstate.edu/PCA.htm>.
- [127] Borguet, S. and O. Léonard, *Coupling principal component analysis and Kalman filtering algorithms for on-line aircraft engine diagnostics*. Control Engineering Practice, 2009. **17**: p. 494-502.

- [128] British Standards Institution, *BS ISO 2041:2009 Mechanical vibration, shock and condition monitoring — Vocabulary*. 2009, BSI: London.
- [129] Rao, S.S., *Mechanical Vibrations*. 5th ed. 2011, Prentice Hall: New Jersey. p. 23.
- [130] The MathWorks Inc. *kurtosis*. 2015; Available from: <http://uk.mathworks.com/help/stats/kurtosis.html>.
- [131] Chen, G., *A New Rotor-Ball Bearing-Stator Coupling Dynamics Model for Whole Aero-Engine Vibration*. Journal of Vibration and Acoustics-Transactions of the Asme, 2009. **131**: p. 9.
- [132] Nembhard, A.D. and J.K. Sinha, *Unified Multi-speed Analysis (UMA) for the condition monitoring of aero-engines*. Mechanical Systems and Signal Processing, 2015. **2015**.
- [133] Nembhard, A. and J. Sinha, *Vibration-Based Condition Monitoring for Rotating Machinery with Different Flexible Supports*, in *Vibration Engineering and Technology of Machinery*, J.K. Sinha, Editor. 2015, Springer International Publishing, p. 119-127.
- [134] Laws, B., *When you use spectrum, don't use it halfway*, in *Orbit*. 1998, Bently Nevada. p. 23-26.
- [135] Jalan, A.K. and A.R. Mohanty, *Model based fault diagnosis of a rotor-bearing system for misalignment and unbalance under steady-state condition*. Journal of Sound and Vibration, 2009. **327**(3–5): p. 604-622.
- [136] Gasch, R., *A Survey Of The Dynamic Behaviour Of A Simple Rotating Shaft With A Transverse Crack*. Journal of Sound and Vibration, 1993. **160**(2): p. 313-332.
- [137] Roark, J.R., *Formulas for Stress and Strain*. 1975, New York: McGraw-Hill.
- [138] Nembhard, A.D., J.K. Sinha, and A. Yunusa-Kaltungo, *Experimental observations in the shaft orbits of relatively flexible machines with different rotor related faults*. Measurement, 2015. **Under review**.
- [139] Sekhar, A.S. and B.S. Prabhu, *Effects of coupling misalignment on vibrations of rotating machinery*. Journal of Sound and Vibration, 1995. **185**: p. 655-671.
- [140] Gibbons, C.B. *Coupling misalignment forces*. in *Proceedings of the 5th Turbomachinery Symposium, Turbomachinery Laboratory, Texas A&M University, College Station, TX, October*. 1976.